



HAL
open science

Triarylamine based supramolecular polymers : increasing complexity

Flavio Picini

► **To cite this version:**

Flavio Picini. Triarylamine based supramolecular polymers : increasing complexity. Organic chemistry. Université de Strasbourg, 2020. English. NNT : 2020STRAF001 . tel-04961312

HAL Id: tel-04961312

<https://theses.hal.science/tel-04961312v1>

Submitted on 21 Feb 2025

HAL is a multi-disciplinary open access archive for the deposit and dissemination of scientific research documents, whether they are published or not. The documents may come from teaching and research institutions in France or abroad, or from public or private research centers.

L'archive ouverte pluridisciplinaire **HAL**, est destinée au dépôt et à la diffusion de documents scientifiques de niveau recherche, publiés ou non, émanant des établissements d'enseignement et de recherche français ou étrangers, des laboratoires publics ou privés.



UNIVERSITÉ DE STRASBOURG

EDSC
École Doctorale des
Sciences Chimiques

ÉCOLE DOCTORALE 222

UPR 22

THÈSE présentée par :

Flavio PICINI

soutenue le : **24 janvier 2020**

pour obtenir le grade de : **Docteur de l'université de Strasbourg**

Discipline/ Spécialité : Chimie supramoléculaire

**TRIARYLAMINE BASED
SUPRAMOLECULAR POLYMERS:
INCREASING COMPLEXITY**

THÈSE dirigée par :

M. GIUSEPPONE Nicolas

Mme MOULIN Emilie

Professeur, Université de Strasbourg

Chargée de Recherche, Université de Strasbourg

RAPPORTEURS :

M. BASSANI Dario

M. SALLÉ Marc

Directeur de recherche, Université de Bordeaux

Directeur de recherche, Université d'Angers

TABLE OF CONTENTS

ACKNOWLEDGMENTS	iv
ABSTRACT	vi
RESUME EN FRANÇAIS	vii
ABBREVIATIONS AND SYMBOLS	xx
GENERAL INTRODUCTION AND OBJECTIVES	xxv
CHAPTER I. GENERAL BIBLIOGRAPHY	1
A. SUPRAMOLECULAR CHEMISTRY AND SUPRAMOLECULAR POLYMERS	1
1.1 NON-COVALENT INTERACTIONS IN SUPRAMOLECULAR POLYMERS	2
1.1.1 Hydrogen bonding	3
1.1.3 π -interactions	5
1.1.4 Van der Waals forces	6
1.1.5 Hydrophobic interactions	7
1.2 SUPRAMOLECULAR POLYMERS	9
1.2.1 Classification of supramolecular polymers	9
1.2.2 Classification according to the nature of noncovalent forces	10
1.2.3 Mechanisms of supramolecular polymerization	14
1.3 SUPRAMOLECULAR CHIRALITY	21
1.3.1 Generalities	21
1.3.2 Characterization of supramolecular chirality	22
1.3.3 Supramolecular chirality in systems containing chiral molecules	23
1.3.4 Supramolecular chirality in systems containing chiral and achiral molecules	25
1.3.5 Other factors influencing the supramolecular chirality	28
1.3.6 Supramolecular chirality in systems containing just achiral molecules	30
B. MOLECULAR AND SUPRAMOLECULAR CHEMISTRY OF TRIARYLAMINE ..	32
1.4 SYNTETIC STRATEGIES TOWARDS TRIARYLAMINE	32

1.4.1 Historical overview	32
1.4.2 Ullmann Coupling and its modification	33
1.4.3 Palladium-catalyzed couplings.....	36
1.4.4 Aromatic nucleophilic substitution	40
1.5 STRUCTURE AND PROPERTIES OF TRIARYLAMINES.....	41
1.5.1 Structure of the triarylamine core.....	41
1.5.2 Redox and optical properties of triarylamines	42
1.5.3 Oxidation of aromatic amines in chlorinated solvents	48
1.5.4 Charge transfer in systems involving triarylamines	49
1.6 TRIARYLAMINE SELF-ASSEMBLY	50
1.6.1 Light-induced supramolecular polymerization of triarylamines.....	50
1.6.2 Supramolecular polymerization of triarylamine trisamides (TATA).....	53
1.6.3 Supramolecular polymerization of chiral TATAs.....	55
CHAPTER II: TRIARYLAMINE DERIVATIVES WITH SUPRAMOLECULAR POLYMERIZATION INDUCED EMISSION PROPERTIES.....	61
2.1 AGGREGATION INDUCED EMISSION (AIE).....	61
2.1.1 AIE phenomenon and most used AIE luminogens	61
2.1.2 AIE of triphenylamine core.....	63
2.1.3 Supramolecular polymerization induced emission (SPIE).....	65
2.1.4 Application of AIE materials in OLED devices.....	67
2.1.5 Circularly polarized luminescence from chiral AIE molecules and macrostructures.....	69
2.2 INVESTIGATION OF TRIARYLAMINES WITH SPIE PROPERTIES	74
2.2.1 General overview	74
2.2.2 Synthesis of TATA derivatives	75
2.2.3 Properties of 3TPE-TATA	79
2.2.4 Properties of chiral TPE-TATA derivatives.....	83
2.2.5 Circularly polarized luminescence for 1TPE-(S)TATA and 1TPE-(R)TATA	89

2.2.6 Conductivity of 1TPE-(S)TATA based supramolecular polymers.....	94
2.2.7 OLED device based on 1TPE-(S)TATA polymers.....	95
2.3 CONCLUSIONS AND PERSPECTIVES	97
CHAPTER III: TRIARYLAMINE BASED MACROCYCLE	99
3.1 INTRODUCTION.....	99
3.1.1 Self-assembly from conjugated macrocyclic units.....	99
3.1.2 Azacyclophanes.....	101
3.2 TRIARYLAMINE BASED MACROCYCLE	107
3.2.1 General overview	107
3.3 RESULTS AND DISCUSSION	108
3.3.1 Synthesis of hexaaza[1 ₆]para-cyclophane hexakisamide (HCHA): Past attempts and current methodology	108
3.3.2 Characterization of triarylamine based macrocycle 39	120
3.4 CONCLUSIONS AND PERSPECTIVES	131
GENERAL CONCLUSIONS AND PERSPECTIVES.....	133
EXPERIMENTAL PART	135
ANNEXES.....	179
BIBLIOGRAPHY	187

ACKNOWLEDGMENTS

The work described in this manuscript have been carried out in the SAMS group at the Institute Charles Sadron CNRS, University of Strasbourg. The project was funded by the IdEx (Initiative d'Excellence).

Firstly, I would like to express my gratitude to my supervisor Professor Nicolas Giuseppone for giving me the opportunity to work in a stimulating and international environment. During these three years I have been involved in projects that allowed me to grow as scientist and as person. I would like to thank him for the availability he showed during the whole PhD and his kind support.

I own thanks Dr Andreas Jentsch Vargas, his support has been fundamental for the successful outcome of this work and, with his infinite expertise, strongly motivated me to keep learning more and more. I want to thank him for his help in all the practical and theoretical aspects of my work and with the writing of my manuscript.

I am really grateful to Dr Emilie Moulin for helping me whenever I faced a problem, especially for the synthetic part of this work.

A special thanks to Odile Gavot, her precious help and collaboration with the synthesis of the macrocycle have been fundamental. We struggled a lot during these years but, at the end, we have made it.

I thank Gad Fuks for the nice conversations we had during these 3 years and the funny moments we shared during our football matches.

I wish to thank many of my colleagues which have been more or less involved in this work: Professor M. Maaloum for the beautiful AFM images; Professor Dario Bassani and his group, for the collaboration on my first project; Dr E. Wasielewsky and Dr B. Vincent for the help with the NMR experiments; Dr J. M. Strub for the large amount of MALDI measurements; Dr D. Collin who helped me with the light diffusion and the rheology measurements; Dr. S Schneider and Dr. J. Tang, who worked before me on the macrocycle project; Dr A. Osypenko who helped me during the first months of my PhD; Dr S. Tokunaga who will explore new horizons for the macrocycle project. A special thanks to Marie-Celine and Julie for taking care of the laboratories and for have been always nice and friendly to me.

I would like to thank all the members of the SAMS group: Damien, an example of how a colleague can become a good friend, our telepathy on many topics was sometimes incredible, but nevertheless you will never see me eating a French carbonara; Alexis, another example of “friendship beyond borders”, the contrast between your generous and sensible soul and the

conversations we have is fantastic; Melodie, together we started, together we finished and, as Andreas says, together we make a good PhD student; Claire, our peruvian friend; I wish to thank all the other members of the team: Jean-Remy , Joakim , Chuan, Wenzhi, Yali, Raphael, Vasyl, Nicolas, Lara, Cristian, Dr Pierre Lutz. I thank equally the former members of the group I had the pleasure to meet: Chris, Simon, Chloe, Xiaoqin , Cyprian, Martin and all the others. My most sincere gratitude to all the people I met at the ICS with a special thought to Odile Lemble who always helped me with administrative issues; our conversations in Italian were a nice break from work.

A massive thank you to my family, their support during my ten-years journey through the world of chemistry has allowed me to reach my dream. It would not have been possible without their help.

My gratitude goes equally to Vanessa, my partner and friend, we were far but we have always been close. You are able to cheer me up like no one when things get difficult and I love sharing my life with you.

A special thanks to the friends Greg, Karl Heinz, Fabrizio which are far away and make me miss home.

I greatly thank the Italian friends I have met in Strasbourg: Alessandro, Matteoandrea, Riccardo, Livia, Alice, Cosimo, Matteo, Edoardo, Lorenzo, Matilde, and so many others that listing would be too long. Together we enjoyed wonderful moments during these three years, and in many of you, I found true friends.

ABSTRACT

Triarylamine-based materials are extensively known for their extraordinary opto-electronic properties, which have made them the reference materials in several fields. Various recent developments in organic light-emitting devices, xerography, organic field-effect transistors and solar cells have been possible in part by our knowledge on triarylamine systems. In most examples, such materials have been employed in their amorphous phase while a growing interest towards supramolecular systems has showed that reaching a control over the molecular organization at a nanometric scale can lead to materials with new or enhanced properties.

In this regard and during the last ten years, our group has discovered and investigated the self-assembly of amide-substituted triarylaminines in supramolecular polymers observing, for such soft materials, exceptional conducting and plasmonic properties.

In this thesis, we will first introduce the field of the supramolecular chemistry, from the general aspects like the forces involved and the different polymerization mechanisms, to more punctual examples such as the self-assembly of substituted triarylamine molecules.

In the second chapter, we aim to develop triarylamine based supramolecular polymers with luminescence and hole-conductive properties. Different structures will be investigated in order to determine whether we can reach a good control on the morphologies of the self-assemblies and, thus, tune the functional properties of such materials. We will describe how different architectures, based on the same monomer, can behave in various ways and generate new and intriguing properties.

In the third chapter, we explore a relatively new field, in which triarylamine motifs are integrated into a macrocyclic structure. We describe, for the first time, a hexaazapara-cyclophane, functionalized with six amide groups on the periphery, able to form supramolecular polymers forming long mono-columnar structures. We will further expand on the influence that the supramolecular nature of the macrocyclic core is translated to its electrochemical properties, and the consequence in the delocalization of the charge within the cycle.

Overall, in this work, we have further extend the range of functional properties showed by triarylamine-based supramolecular polymers, with the objective of developing highly efficient materials for optoelectronic applications.

RESUME EN FRANÇAIS

La chimie supramoléculaire a été définie comme étant «la chimie au-delà des molécules» par Jean-Marie Lehn, lauréat du prix Nobel de chimie en 1987.. Son concept principal repose sur la possibilité de construire des entités organisées complexes par l'association de simples blocs de construction *via* des interactions non-covalentes. La possibilité de concevoir rationnellement ces éléments constitutifs, en tenant compte des interactions intermoléculaires pour obtenir des structures supramoléculaires bien définies, est un objectif prééminent.² Cette approche a trouvé de nombreux exemples dans les systèmes biologiques, en particulier dans les biomolécules comme les protéines et l'ADN, dont la fonctionnalité dépend étroitement de leur structure tridimensionnelle. La possibilité de construire par approche ascendante des matériaux supramoléculaires avec des propriétés exceptionnelles, comme l'auto-réparation, la réactivité aux stimuli externes ou la dynamique, a attiré les chimistes en raison de la plus grande accessibilité de ces systèmes par rapport aux polymères covalents classiques.

Notre groupe a signalé, il y a quelques années, un comportement unique pour une classe de composés appelée triarylamine. Ces molécules sont bien connues pour leurs propriétés optoélectroniques et sont largement utilisées comme matériaux pour des applications telles que les cellules solaires, les OLED, les OFET, dans les imprimantes laser (procédé Xerox®) et l'absorption et l'émission de deux photons. Bien que les propriétés des triarylamine aient fait l'objet de plusieurs études, rares étaient celles destinées à utiliser ce motif pour former des structures auto-assemblées. Notre groupe a été le premier à décrire l'autoassemblage de triarylamine simples, où le motif central est fonctionnalisé par un groupement amide et deux chaînes alkyles;¹³ ce modèle de substitution spécifique est crucial pour conduire son organisation. Le processus d'autoassemblage est amorcé par la lumière visible dans les solvants chlorés en produisant une quantité catalytique de radicaux triarylammonium qui favorisent l'empilement de molécules chargées et neutres; en conséquence, un réseau de nanofibres à base de triarylamine est formé.

Ces assemblages présentent des propriétés électroniques particulières. Lorsque les nanofibres sont cultivées entre deux électrodes en or espacées de 80 nm, elles présentent un comportement métallique avec des conductivités de $5 \times 10^3 \text{ S m}^{-1}$. À partir de ces résultats, nous avons développé une deuxième génération de triarylamine portant trois groupes amidiques en périphérie (TATA). Ces dérivés s'autoassemblent, par liaisons hydrogène et interactions d'empilage π , en de longues structures hélicoïdales mono-colonnes. Contrairement à la génération précédente de triarylamine, il n'est pas nécessaire dans ce cas d'utiliser un stimulus

lumineux pour favoriser l'autoassemblage, qui se produit spontanément. L'exposition des fibres préformées à la lumière visible entraîne une diminution du nombre de défauts des structures supramoléculaires, et l'étude spectroscopique montre une délocalisation des polarons dans les assemblages nanoscopiques. Depuis nos premières publications, de nombreux progrès ont été réalisés concernant la chimie supramoléculaire de la triarylamine. Les mécanismes de la polymérisation supramoléculaire ont été élucidés pour les triarylamine trisamides chirales et achirales, ce qui a permis de mettre en lumière leurs propriétés intéressantes et leurs applications en tant que guides d'ondes plasmoniques. Dans le but d'élargir le champ d'application des dérivés de la triarylamine, nous avons conçu de nouvelles architectures qui devraient présenter des propriétés améliorées par rapport à celles déjà présentées.

Comme premier objectif, nous nous sommes inspirés du phénomène d'émission induite par agrégation (AIE), décrit en 2001 par le groupe de Tang, pour développer des polymères supramoléculaires à base de triarylamine aux propriétés AIE et de transport de trous. L'exploitation de nos connaissances sur l'autoassemblage de la triarylamine devrait permettre d'obtenir un contrôle précis des molécules à l'échelle nanométrique, et l'introduction de la chiralité dans nos systèmes peut amener nos polymères supramoléculaires à présenter une luminescence à polarisation circulaire (CP) pour le développement de nouvelles OLED (CP-OLED).

Comme deuxième objectif, une nouvelle classe de molécules à base d'oligoarylamines macrocycliques a été développée, dont la présence simultanée de multiples centres redox et la possibilité d'ajuster la taille et la nature chimique de la cavité font de ces composés un motif prometteur en chimie supramoléculaire et des matériaux (**Figure R 1**) La structure proposée devrait pouvoir s'auto-assembler, puisqu'il s'agit d'un dérivé macrocyclique de la triarylamine, et permettrait ainsi la génération d'une structure nanotubulaire de grande taille, qui posséderait des propriétés électromagnétiques intéressantes en raison d'une double délocalisation de la charge radicalaire, à la fois à l'intérieur de l'assemblage tubulaire ainsi que dans le macrocycle lui-même. La combinaison de ces propriétés électromagnétiques avec la possibilité d'attacher plusieurs groupes fonctionnels à la périphérie du macrocycle pourrait conduire à des applications comme les OLED, les capteurs et la microélectronique.

La possibilité qu'une telle molécule interagisse par le biais de six liaisons hydrogène et d'interactions van der Waals devrait favoriser sa propension à l'autoassemblage. Les optimisations DFT sur le macrocycle ont montré que les cycles aromatiques voisins au sein de la structure sont inclinés les uns par rapport aux autres, ce qui donne une structure globalement

plane dans laquelle les cycles aromatiques opposés sont parallèles entre eux (**Figure R 1**). Cette architecture plane est avantageuse pour l'assemblage unidirectionnel de plusieurs macrocycles et favoriserait ainsi la formation de structures nanotubulaires. De plus, les orbitales HOMO et LUMO calculées révèlent une délocalisation électronique étendue des orbitales moléculaires sur toute la structure du noyau aromatique (**Figure R 1**).

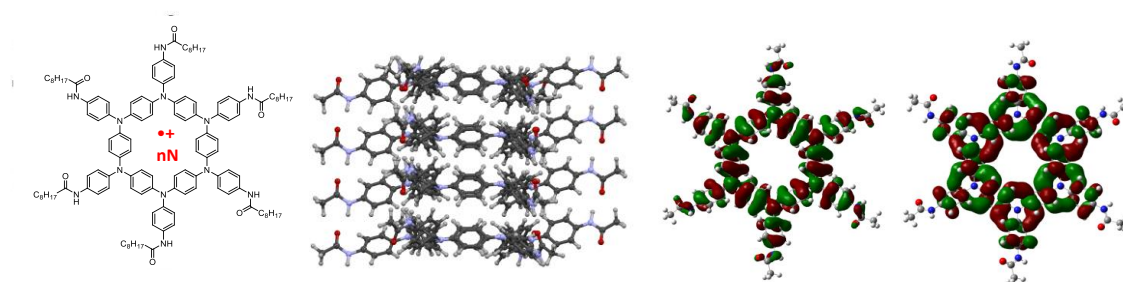


Figure R 1 | De gauche à droite: structure chimique du macrocycle ; représentation schématique en vue latérale de plusieurs unités empilées dans un ensemble en colonnes ; optimisation des HOMO et LUMO du macrocycle avec des chaînes alkyles courtes C2 selon la méthode DFT M06-2X/6-31G.

Dans notre premier projet portant sur les propriétés d'AIE, quatre structures ont été obtenues en combinant le motif central de triarylamine trisamide avec un nombre variable d'unités tétraphényléthylène (TPE), bien connues pour leurs fortes propriétés AIE, et de chaînes chirales (**Figure R 2**).

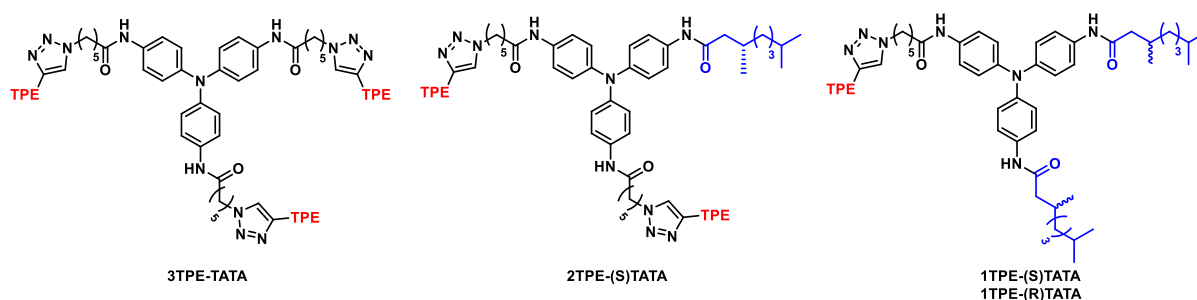


Figure R 2 | Quatre dérivés obtenus en combinant un noyau TATA avec des unités TPE et des chaînes chirales

Le premier composé possède un noyau TATA relié à trois unités TPE (**3TPE-TATA**). Les gels obtenus à partir de ce dérivé dans le chlorobenzène ont été étudiés plus en détail par

microscopie à transmission électronique (TEM), révélant un réseau de fibres (**Figure R 3**). Le gel présente une forte fluorescence sous irradiation UV, confirmant le caractère AIE attendu des agrégats qui a été confirmé par spectroscopie de fluorescence à température variable sur la solution et le gel (**Figure R 3**). Les spectres UV-Vis ont montré un décalage hypsochrome lors du refroidissement d'une solution chaude en phase gel, indiquant le rôle clé joué par les interactions aromatiques pendant le processus d'autoassemblage (**Figure R 3**). Malgré ces résultats prometteurs, les tentatives visant à contrôler la morphologie des structures assemblées ont échoué. Même si la molécule s'agrège en fibres ordonnées, ce processus s'accompagne d'une forte précipitation amorphe et nous n'avons pas été en mesure d'optimiser le processus. L'unité TPE peut être responsable de l'agrégation vers le précipité amorphe, en augmentant le degré de désordre du système.

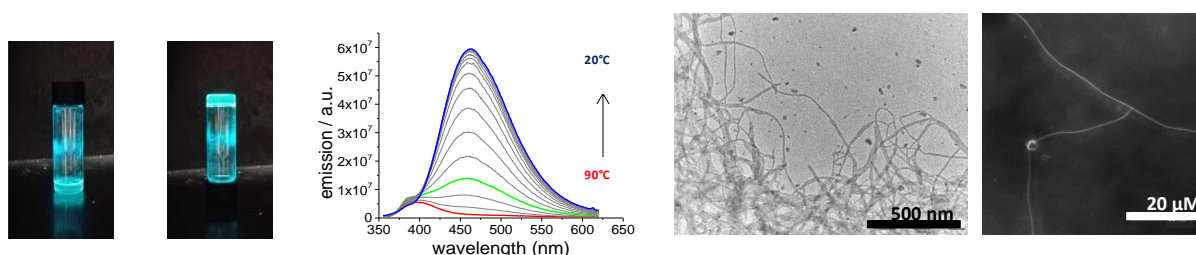


Figure R 3 | De gauche à droite : Photographies d'un gel de 1 mM de **3TPE-TATA** dans du toluène sous irradiation UV, $\lambda_{exc} = 254$ nm; Spectre de fluorescence à température variable enregistré lors du refroidissement d'un gel de 3 mM de B dans du toluène, $\lambda_{exc} = 322$ nm; images TEM et microscopie par fluorescence des fibres.

Un comportement similaire a été observé pour le second composé dans lequel une unité TPE a été remplacée par une chaîne chirale. Le troisième composé a été construit en reliant un TPE et deux chaînes chirales au noyau central TATA; les deux énantiomères **1TPE-(S)TATA** et **1TPE-(R)TATA** ont été synthétisés. Ces dérivés ont montré la formation de structures fibrillaires dans les solvants aromatiques comme le toluène et le dichlorobenzène, et la spectroscopie par fluorescence a confirmé les propriétés AIE de ces composés. L'apparition d'un effet Cotton dans le spectre du dichroïsme circulaire (CD) lorsque la polymérisation supramoléculaire a lieu démontre que la présence de centres chiraux sur les chaînes latérales permet un transfert de chiralité des monomères vers la structure supramoléculaire (**Figure R 4**). Il est intéressant de noter que le signal et la forme du spectre de CD changent en fonction de la vitesse de refroidissement : le refroidissement rapide (5 °C/min) conduit à des signaux

CD faibles, tandis que le refroidissement lent ($0,1\text{ }^{\circ}\text{C}/\text{min}$) conduit à un effet Cotton intense (**Figure R 4**). L'analyse TEM d'échantillons obtenus à partir de ces deux régimes a montré que les échantillons refroidis rapidement sont principalement constitués de fibres longues, minuscules et molles, avec une certaine quantité de matière non organisée, alors que les échantillons refroidis lentement ont montré des faisceaux de fibres plus épais avec des longueurs persistantes plus longues et des degrés d'organisation plus élevés (**Figure R 4**).

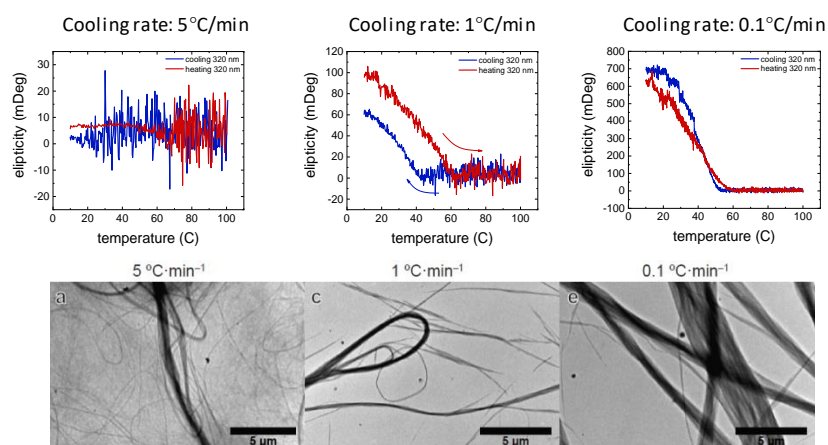


Figure R 4 | Evolution du signal CD enregistré à 320 nm à partir de $100\text{ }^{\circ}\text{C}$ pour un cycle de refroidissement/chauffage d'une solution à $0,1\text{ mM}$ de **1TPE-(S)TATA** dans le toluène à différentes vitesses de refroidissement et images TEM des fibres obtenues de l'échantillon correspondant.

Nous avons étudié plus avant les propriétés de l'autre énantiomère, le composé **1TPE-(R)TATA**, et nous avons effectué des mesures de CD à température variable pour comparer les résultats à ceux obtenus à partir du composé **1TPE-(S)TATA**. Comme la chiralité des chaînes est inversée, nous nous attendions à ce que ces polymères supramoléculaires présentent une hélicité opposée à celle des polymères de **1TPE-(S)TATA**. Cette hypothèse a été confirmée par le spectre CD d'un échantillon de **1TPE-(R)TATA** refroidi rapidement, qui apparaît comme l'image miroir de son énantiomère (**Figure R 5a**). Cela indique que les monomères s'agrègent en fibres avec une hélicité opposée sous l'influence de la chiralité moléculaire. De façon surprenante, un comportement différent a été observé sur les polymères supramoléculaires obtenus par un lent processus de refroidissement. Ici, les deux énantiomères ont donné un spectre CD presque identique qui peut être traduit en structures supramoléculaires avec la même chiralité (**Figure R 5b**). Nous avons émis l'hypothèse que, lors du refroidissement d'une solution de monomères dispersés moléculairement, le système commence d'abord à nucléer dans des structures primaires, dont l'hélicité est contrôlée par la chiralité des chaînes latérales. Ces assemblages primaires peuvent ensuite s'agréger, sous l'effet

d'interactions latérales, dans des structures hiérarchiques comme les superhélix, qui sont favorisées sur le plan thermodynamique. À ce stade, la chiralité, démontrée par ces polymères, n'est plus influencée par la chiralité moléculaire mais par l'enchevêtrement des structures primaires. Ainsi, au cours d'un processus de refroidissement rapide, des structures primaires se forment qui n'ont pas le temps de s'auto-organiser dans des architectures plus complexes et aboutissent ainsi à des structures cinétiquement piégées. De plus, ces assemblages se sont avérés stables pendant plusieurs mois. D'autre part, un refroidissement lent permet aux structures primaires de s'équilibrer et de s'auto-assembler en superstructures hiérarchiques.

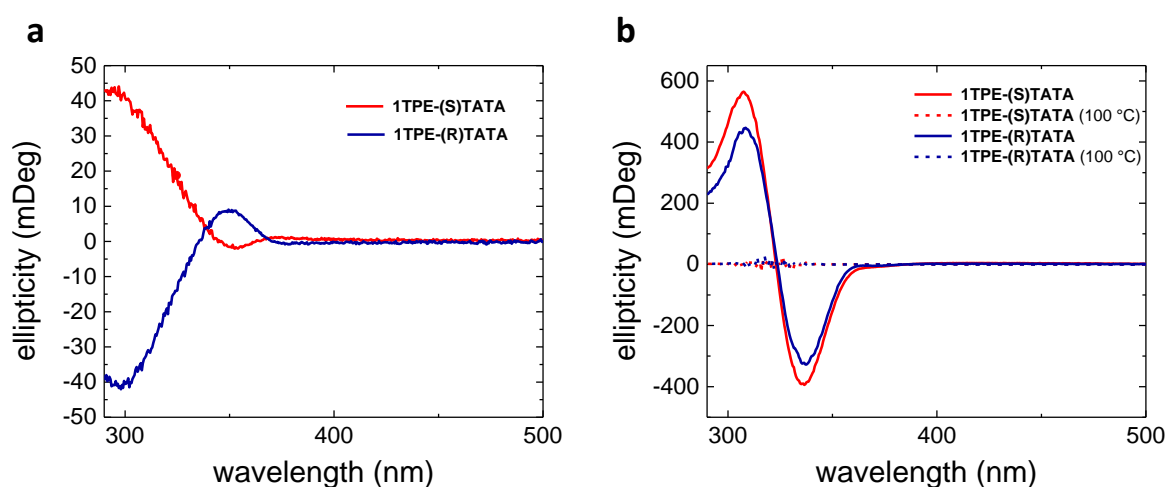


Figure R 5 | a) Spectres CD après refroidissement rapide de solutions de 0,1 mM de **1TPE-(S)TATA** (rouge) et de **1TPE-(R)TATA** (bleu) ; b) spectres CD pour les systèmes à dispersion moléculaire (lignes pointillées) et après refroidissement lent (0,1 °C/min; ligne pleine) de solutions de 0,1 mM de **1TPE-(S)TATA** (rouge) et de **1TPE-(R)TATA** (bleu).

Étant donné la forte émission et le dichroïsme circulaire de **1TPE-(S)TATA** et **1TPE-(R)TATA**, nous avons décidé d'étudier la luminescence polarisée circulairement (CPL) des deux composés sous les deux régimes extrêmes (lent et rapide) décrits pour préparer les matériaux auto-assemblés. Comme on peut le voir sur la **Figure R 8a**, un fort signal CPL a été observé pour le **1TPE-(S)TATA** refroidi lentement, avec des valeurs de luminescence aussi élevées que $15 \cdot 10^{-3}$. Malheureusement, le même échantillon a également montré une valeur non négligeable de luminescence polarisée linéaire (LPL) (**Figure R 8b**), probablement due à la présence de faisceaux de fibres longs et épais. La présence d'une telle LPL indique que la CPL observée peut être, au moins partiellement, due à un artefact de la mesure. D'autre part, les polymères supramoléculaires obtenus par un processus de refroidissement lent d'une solution de **1TPE-(R)TATA** ont montré un signal CPL moins important mais, du bon côté,

une intensité beaucoup plus faible de la LPL correspondante. Ces deux résultats combinés indiquent que, bien que nous ne puissions pas négliger la contribution de la luminescence polarisée linéairement à la CPL détectée, il est certain que nos polymères supramoléculaires peuvent agir comme des émetteurs polarisés circulairement. Les échantillons préparés selon le protocole de refroidissement rapide, pour les deux composés **1TPE-(S)TATA** et **1TPE-(R)TATA**, ont montré des valeurs plus faibles de LPL et de CPL, ce qui est cohérent avec les degrés d'organisation plus faibles conduisant à des fibres plus douces et plus fines avec une courte longueur de persistance.

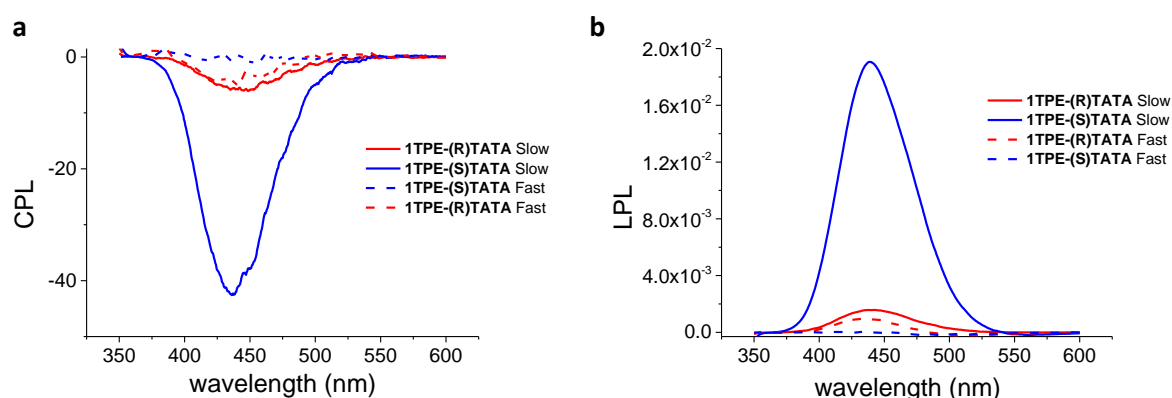


Figure R 6 | a) Émission polarisée circulaire pour les échantillons refroidis lentement et rapidement de **1TPE-(S)TATA** et **1TPE-(R)TATA** (0,2 mM, toluène); **b)** Luminescence polarisée linéairement pour les mêmes échantillons (voir légendes).

Il est important de mentionner que, comme déjà observé dans les expériences sur les CD, les spectres CPL des deux énantiomères ont montré le même signe et non, comme prévu, l'image miroir l'un de l'autre. Cette découverte a confirmé notre hypothèse sur les facteurs qui déterminent la chiralité supramoléculaire: l'hélicité des structures hiérarchiques supérieures (c'est-à-dire les faisceaux de fibres) n'est que faiblement influencée par la chiralité moléculaire, mais surtout par la conformation en hélice adoptée par le noyau de triarylamine dans l'assemblage. Une autre conclusion importante, obtenue à partir de nos expériences sur les CD, qu'il convient de souligner dans le contexte de la CPL, est qu'il est possible de réduire - voire d'inverser - la LD détectée de l'échantillon par une action mécanique (cabossage, agitation) sans affecter de manière significative l'intensité du signal CD détecté.

Dans l'ensemble, nous avons observé des valeurs significatives de luminescence polarisée circulairement pour des échantillons à refroidissement lent. Il n'est pas possible d'exclure la présence d'artefacts en raison de la luminescence polarisée linéairement et, par conséquent,

d'extrapoler les valeurs précises de la morosité. Néanmoins, la tendance générale est confirmée, à savoir que la présence d'assemblages hiérarchiques dans les échantillons à refroidissement lent conduit à des signaux CPL plus forts par rapport aux polymères supramoléculaires des échantillons à refroidissement rapide.

Nous avons ensuite imagé les fibres par microscopie confocale polarisée pour les échantillons à refroidissement lent et rapide, en irradiant les échantillons à 375 nm et en détectant au-dessus de 405 nm. Nous avons observé une lumière fortement polarisée émise par les faisceaux de fibres dans tous les échantillons (**Figure R 7**), tandis que le matériau amorphe ne présentait aucune polarisation significative.

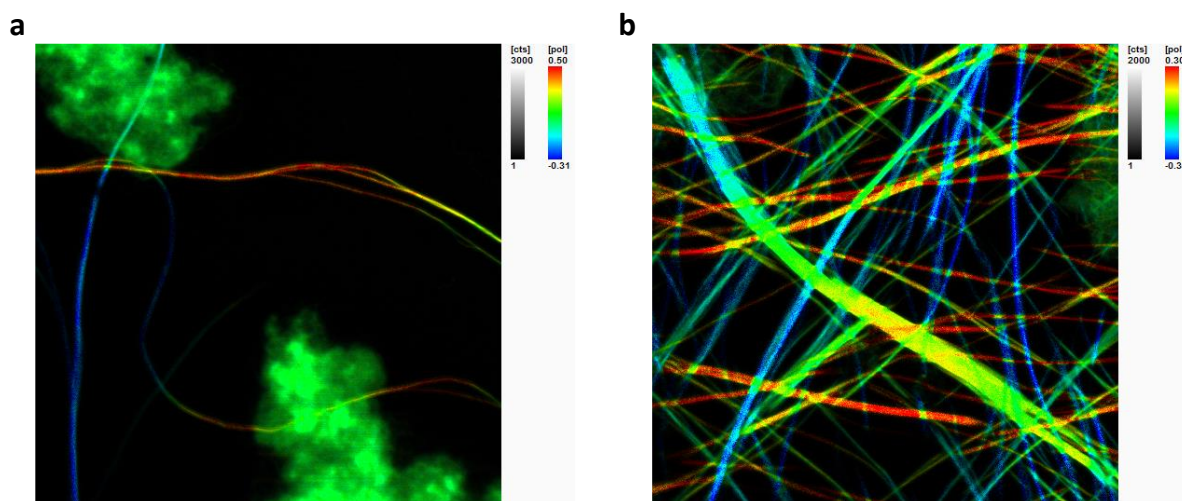


Figure R 7 | Images de microscopie confocale à fluorescence d'échantillons à refroidissement rapide (a) et lent (b).

Le deuxième projet concerne la synthèse d'un hexaazaparacyclophane, où une voie synthétique efficace vers le macrocycle a été développée (**Figure R 8**), afin de pouvoir tester ses propriétés.

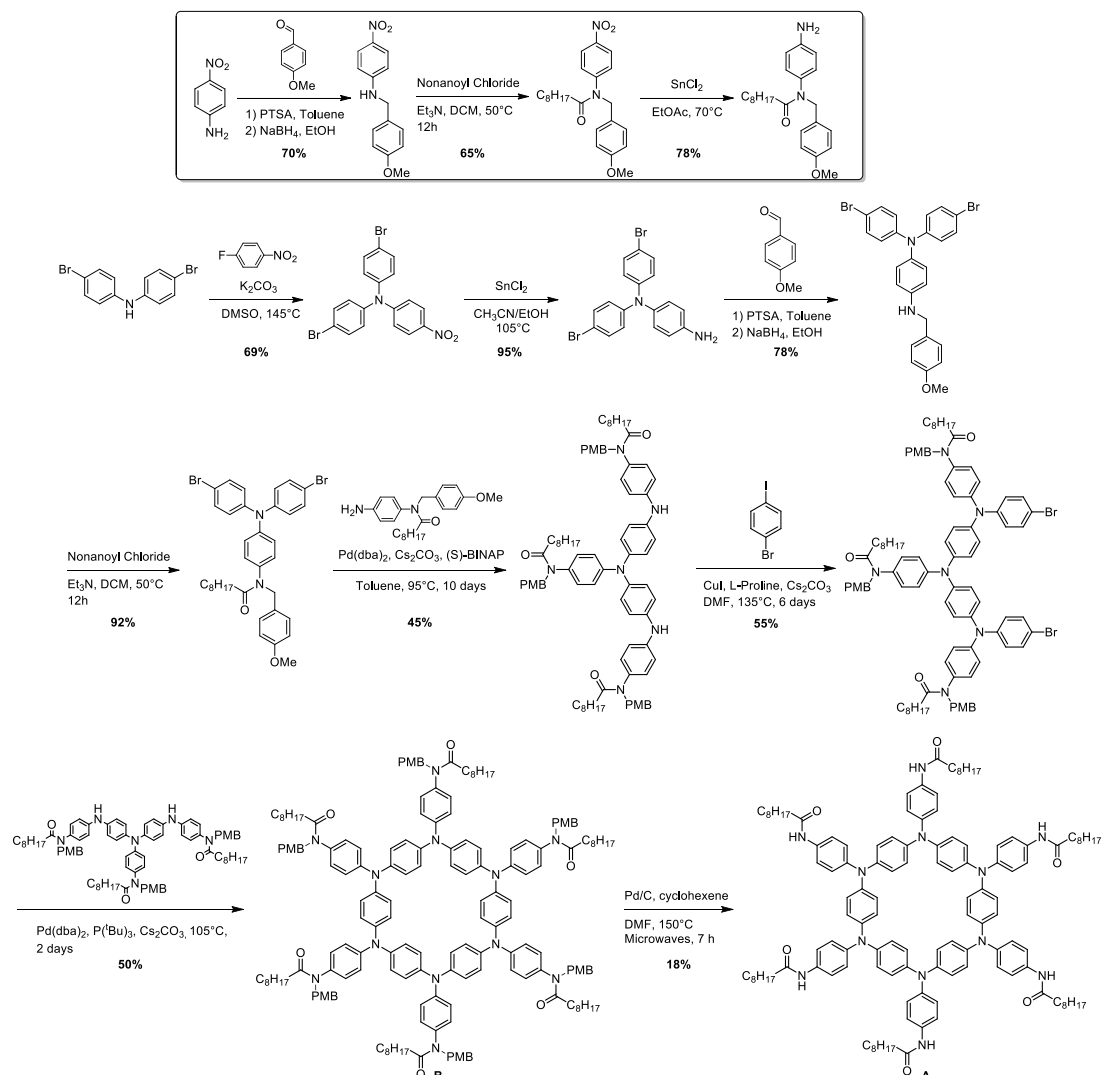


Figure R 8 | Voie synthétique vers le composé A

L'étude comparative des propriétés électrochimiques des composés **A** et **B** permet de mettre en évidence les différences découlant de l'aptitude du composé **A** à établir une liaison hydrogène. La voltampérométrie cyclique et la voltampérométrie à ondes carrées montre qu'il existe deux voies d'oxydation différentes pour les deux composés. Le précurseur **B** montre deux ondes d'oxydation, correspondant chacune à un transfert di-électronique pour un total de quatre électrons retirés du macrocycle. Le composé **A** présente trois pics d'oxydation principaux, correspondant chacun à un transfert mono-électronique. Ces différences peuvent

être expliquées par les conformations qui peuvent être adoptées par les deux molécules, **B** adoptant une conformation de chaise tandis que **A** présente une conformation planaire, conforme à nos attentes. Les spectres UV-Vis acquis au cours du processus électrochimique ont montré, pour les deux molécules, l'apparition d'une bande de transfert de charge inter-valence autour de 1400 nm pour **B** et 1700 nm pour **A**, indiquant une nature plus délocalisée du cation radicalaire pour le macrocycle **A**. En augmentant la tension, la forme du spectre reste relativement inchangée pour le composé **B**, alors qu'un déplacement hypsochrome est observé pour le composé **A** (**Figure R 9**). Cette observation peut être rationalisée par la délocalisation possible des radicaux entre molécules chargées et molécules neutres en solution qui s'assemblent en petits agrégats ; un comportement similaire a été observé pour les triarylamines empilées.

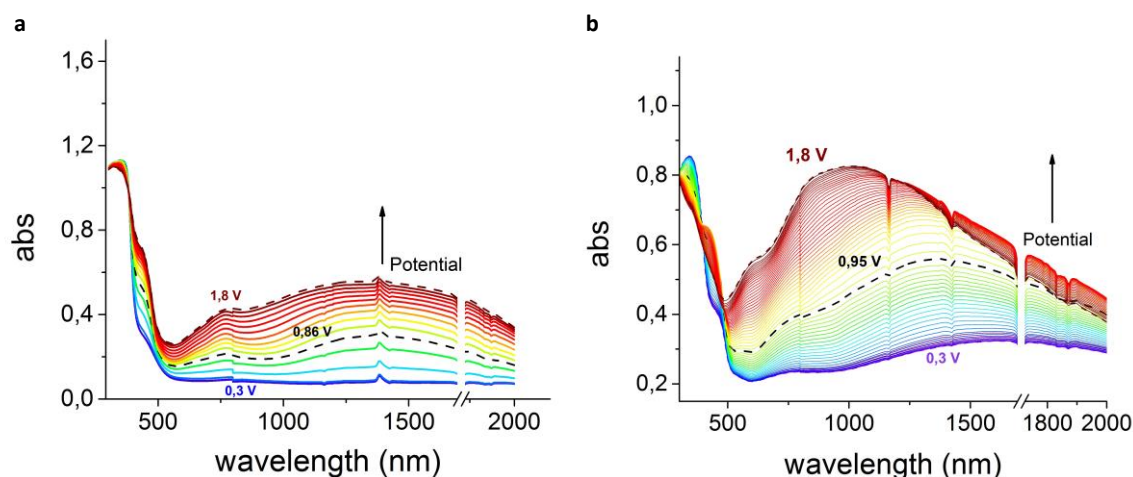


Figure R 9 | Spectres UV-Vis-NIR enregistrés pendant l'oxydation électrochimique progressive d'une solution de TCE 0,5 mM de **B** (a) et **A** (b).

Nous avons également étudié l'auto-assemblage de **A** par le TEM dans plusieurs autres solvants. À cette fin, nous avons testé trois concentrations différentes (0,05 mM, 0,5 mM, 1 mM) dans trois solvants différents : le toluène, le chlorobenzène et le dichlorobenzène. Nous avons observé une agrégation amorphe pour toutes les concentrations, principalement en raison de la faible solubilité du macrocycle dans ce solvant. Le chlorobenzène a permis d'améliorer légèrement l'auto-assemblage du composé **A** puisque certaines fibres étaient visibles avec de grandes quantités de précipitations amorphes. Passant à l'o-dichlorobenzène, plus polaire, les images TEM ont montré une quantité assez importante de matériau auto-organisé formant de courts assemblages fibrillaires avec quelques points de précipitation non organisée.

Malheureusement, pour toutes les concentrations en o-dichlorobenzène, nous n'avons pas pu minimiser l'agrégation amorphe. Nous pensons que les monomères interagissent fortement entre eux en solution. Il est donc difficile de briser les forces intermoléculaires avant d'amorcer la polymérisation supramoléculaire, ce qui explique les différences observées entre les trois différents solvants, dont le point d'ébullition croissant (du toluène à l'o-dichlorobenzène), permet d'atteindre une meilleure solubilité dans l'o-dichlorobenzène, et donc des degrés d'organisation plus élevés. Plusieurs tentatives ont été faites pour améliorer l'ordre du système dans ce solvant, comme le reflux de la solution pendant des heures et l'exécution de rampes de refroidissement lentes, mais aucune n'a apporté d'amélioration.

Afin de maximiser la quantité de matériaux auto-assemblés, nous avons testé d'autres solvants et mélanges binaires. En utilisant des systèmes solvants/non-solvants, nous espérons réduire la force des interactions intermoléculaires permettant aux monomères de s'auto-assembler de manière contrôlée. Compte tenu de la grande solubilité du **A** dans les mélanges toluène/méthanol, nous avons essayé d'obtenir des assemblages à partir de plusieurs échantillons avec différents rapports toluène/méthanol. Malheureusement, ce choix s'est avéré infructueux car aucune structure supramoléculaire n'a été observée. Nous avons ensuite essayé de mélanger du méthanol et de l'o-dichlorobenzène et nous avons obtenu de petits assemblages avec un matériau encore amorphe, probablement en raison du faible point d'ébullition du méthanol qui ne permettait pas de chauffer suffisamment l'échantillon. Nous avons décidé de continuer avec l'o-dichlorobenzène comme non solvant, et nous avons choisi le DMF comme bon solvant pour son point d'ébullition élevé. En refroidissant une solution de 2 mM de **A** dans de l'o-dichlorobenzène/DMF (9:1), nous avons finalement observé la formation de polymères supramoléculaires à haut degré d'organisation. L'imagerie par AFM de ces fibres nous a permis d'identifier des fibres individuelles d'un diamètre d'environ 2,5 nm, cohérent avec le diamètre calculé du macrocycle qui est d'environ 2,1 nm (**Figure R 10**). Ce résultat a confirmé nos attentes concernant l'auto-assemblage du macrocycle dans des structures nanocolonnes.

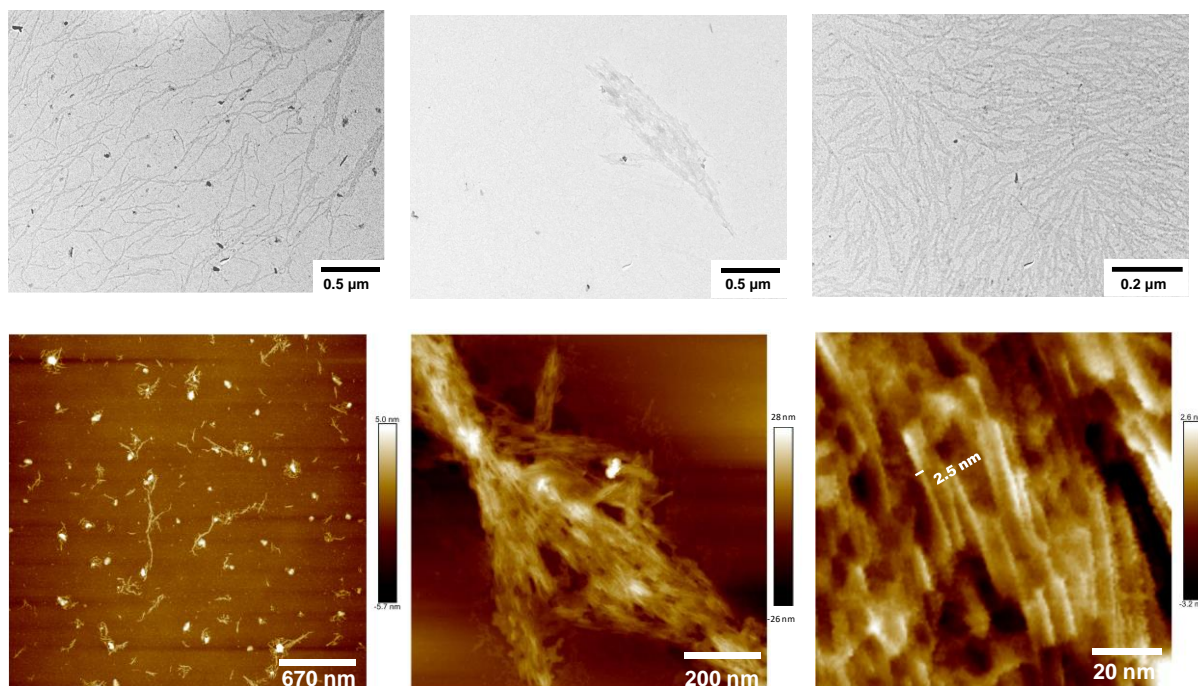


Figure R 10 | Images TEM (en haut) et AFM (en bas) des polymères supramoléculaires obtenus à partir d'une solution de 2 mM de **A** dans un mélange o-dichlorobenzène/DMF ; en bas à droite : image avec le diamètre d'une seule fibre.

En conclusion, dans ce travail, nous visions à développer des systèmes supramoléculaires basés sur la triarylamine, capables de montrer des propriétés qui ne sont pas accessibles avec de simples molécules de triarylamine. Les connaissances que nous avons acquises au cours des dernières années sur ces systèmes peuvent être exploitées, maintenant, pour élargir le champ vers des applications de polymères supramoléculaires à base de triarylamine.

Dans le *Chapitre II*, nous avons étudié de nouveaux dérivés de triarylamine trisamide, portant un nombre variable de fragments tétraphényléthylène et de chaînes chirales, pour obtenir des polymères supramoléculaires capables de présenter à la fois des propriétés d'émission induite par polymérisation supramoléculaire et de transport de trous. Pour les composés chiraux, nous avons observé la formation d'assemblages avec une hélicité préférentielle et, pour l'un d'entre eux, nous avons pu obtenir un contrôle élevé des morphologies des polymères supramoléculaires en réglant simplement la vitesse de refroidissement appliquée au système. Des degrés d'organisation élevés ont été atteints pour les échantillons à refroidissement lent, dont les assemblages ont montré des propriétés améliorées en termes de luminescence et de conductivité à polarisation circulaire, par rapport aux échantillons à refroidissement rapide. D'autres études seront menées pour tester ces matériaux dans des dispositifs optoélectroniques

afin de déterminer si un haut niveau d'organisation, à l'échelle nanoscopique, peut conduire à une amélioration majeure de l'efficacité des dispositifs.

Dans le *chapitre III*, nous avons décrit la synthèse du premier macrocycle à base de triarylamine capable de former des polymères supramoléculaires au moyen de six liaisons hydrogène simultanées. Grâce à la présence de six centres de triarylamine et de son noyau conjugué, ce macrocycle peut être oxydé plusieurs fois et la charge délocalisée dans l'anneau. La formation d'assemblages nanoscopiques devrait conduire à une délocalisation supplémentaire des radicaux le long de l'axe du polymère supramoléculaire, conférant à ce matériau des propriétés électromagnétiques intrigantes. Nous émettons l'hypothèse que la nature fortement donneuse d'électrons de ce composé, associée à la capacité de s'assembler en polymères supramoléculaires, est avantageuse pour son application comme matériaux de transport de trous. D'autres expériences seront menées afin de démêler les propriétés électromagnétiques des polymères supramoléculaires basés sur le macrocycle et de les tester pour de futures applications.

Pour conclure, nous avons la ferme conviction que le progrès technologique, qui est de plus en plus orienté vers la réduction d'échelle des dispositifs, peut être stimulé par l'approche ascendante que seule la chimie supramoléculaire fournit, et qui n'est pas possible avec les approches classiques. Dans cette optique, la recherche de polymères supramoléculaires aux propriétés fascinantes comme la luminescence, la conductivité, le guidage des ondes plasmoniques, la réactivité aux stimuli, la piézoélectricité, etc. est de la plus haute importance pour découvrir de nouveaux champs d'application et faire progresser ceux qui existent déjà.

ABBREVIATIONS AND SYMBOLS

°C	Celsius degree
A	ampere
Å	angstrom
ACQ	aggregation caused quenching
ACW	anticlockwise
ACN	acetonitrile
AEM	arylene ethynylene macrocycle
AFM	atomic force microscopy
AIE	aggregation induced emission
AIEgens	AIE luminogens
BAT	benzene-1,3,5-tricarboxamide
BINAP	2,2'-bis(diphenylphosphino)-1,1'-binaphthyl
Bn	benzyl
Boc	<i>tert</i> -butyloxycarbonyl
BODIPY	4,4-difluoro-4-bora-3a,4a-diaza-s-indacene
CBT	carbonyl-bridged triarylamine trisamides
CD	circular dichroism
CPL	circularly polarized luminescence
CP-OLED	circularly polarized organic light emitting device
CT	charge transfer
CTAB	cetyltrimethyl bromide
CV	cyclic voltammetry
CW	clockwise
d	day
DAC	diaminocyclohexane
dba	dibenzylideneacetone
DCE	1,2-dichloroethane
DCM	dichloromethane
DDQ	2,3-Dichloro-5,6-dicyano-1,4-benzoquinone
DFT	density functional theory
DIBAL	diisobutylaluminium hydride
DLS	dynamic light scattering

DMF	dimethylformamide
DMSO	dimethylsulfoxide
DNA	deoxyribonucleic acid
DOSY	diffusion ordered spectroscopy
DPPF	1,1'-Bis(diphenylphosphino)ferrocene
EL	electroluminescence
EPR	electron paramagnetic resonance
ESI	electron spray ionization
ESP	electrostatic potential
ESR	electron spin resonance
ET	electron transfer
EWG	electron withdrawing group
FFTEM	freeze fracture transmission electron microscopy
FGFR3	fibroblast growth factor receptor 3
FTIR	fourier transform infrared spectroscopy
G	Gibbs free energy
g_{lum}	luminescence dissymmetry factor
h	hour
HCHA	hexaaza[1 ₆]para-cyclophane hexakisamide
HF	Hartree Fock
HOMO	highest occupied molecular orbital
HPS	hexaphenylsilole
HRMAS	high-resolution magic angle spinning
HTL	hole transporting layer
ICT	intramolecular charge transfer
IR	infrared
ITO	indium tin oxide
IV-CT	inter valence charge transfer
K	kelvin
LC	liquid chromatography
LD	linear dichroism
LUMO	lowest unoccupied molecular orbital
LPL	Linearly polarized emission
MALDI	matrix assisted laser desorption ionization

MCH	methylcyclohexane
min	minute
mM	millimolar
MNB	<i>p</i> -methoxy- <i>o</i> -nitrobenzyl
MO	molecular orbital
MS	mass spectroscopy
MSP	metallo-supramolecular polymer
MV	mixed valence
NBS	N-bromosuccinimide
NIR	near infrared
nm	nanometers
NMR	nuclear magnetic resonance
OFET	organic field-effect transistor
OLED	organic light emitting device
OPE-TA	oligo- (phenylene ethynylene)-based tricarboxamides
OPV	p-oligo(phenylene vinylene)
PEDOT:PSS	poly(3,4-ethylenedioxythiophene) polystyrene sulfonate
PBI	perylene bisimide
PCC	Pyridinium chlorochromate
Ph	phenyl
PL	photoluminescence
PMB	<i>p</i> -methoxybenzyl
PMDETA	N,N,N',N'',N''-pentamethyldiethylenetriamine
PMMA	polymethylmethacrylate
PTSA	<i>p</i> -toluenesulfonic
PSS	poly(styrene sulfonate)
PEI	polyethyleneimine
QY	fluorescence quantum yield
r.t.	room temperature
RIM	restriction of intramolecular motion
RIR	restriction of intramolecular rotation
RIV	restriction of intramolecular vibration
SAXS	small-angle X-ray scattering
SEM	scanning electron microscopy

SOMO	singly occupied molecular orbital
SP	supramolecular polymer
SPIE	supramolecular polymerization induced emission
STM	scanning tunneling microscopy
SW	square wave voltammetry
TAA	triarylamine
TATA	triarylamine trisamides
TBABF ₄	tetrabutylammonium tetrafluoroborate
TBACN	tetrabutylammonium cyanide
TBAP	tetrabutylammonium perchlorate
TCE	tetrachloroethane
t_e	elongation temperature
TEA	triethylamine
TEM	transmission electron microscopy
TFA	trifluoroacetic acid
$T_{g/s}$	gel-sol transition temperature
THF	tetrahydrofuran
TLC	thin layer chromatography
TMPPD	N,N,N',N'-tetramethyl- <i>p</i> -phenylenediamine
TMSA	trimethylsilylacetylene
TPA	triphenylamine
TPBi	2,2',2''-(1,3,5-Benzinetriyl)-tris(1-phenyl-1-H-benzimidazole)
TPE	1,1,2,2-tetraphenylethylene
$T_{s/g}$	sol-gel transition temperature
TTPS	meso-tetrakis(4-sulfonatophenyl)porphyrin
UV	ultraviolet
VCD	vibrational circular dichroism
VdW	Van der Waals
Vis	visible
VB-FNPD	9,9-Bis[4-[(4-ethenylphenyl)methoxy]phenyl]-N2,N7-di-1-naphthalenyl-N2,N7-diphenyl-9H-Fluorene-2,7-diamine
WAXS	wide-angle X-ray scattering
XRD	X-ray diffraction
y	yield

Abbreviations and Symbols

α_{agg}	degree of aggregation
η_{ext}	external quantum efficiency
λ_{det}	detection wavelength
λ_{exc}	excitation wavelength

GENERAL INTRODUCTION AND OBJECTIVES

The possibility to obtain supramolecular polymers, which are polymer-like materials of precise architectures and advanced dynamic properties, from simple building blocks gained enormous attention over the last decades. Our group has focused much attention in this field since we discovered, in 2010, the self-assembly of amide functionalized triarylamine molecules. Since then, we have gained detailed knowledge of the supramolecular chemistry of triarylamine based systems, unravelling its polymerization process and numerous intriguing properties for those materials (e.g. metal-like conductance, active-plasmonic waveguiding).

In this work, our objective is to explore new triarylamine-based supramolecular polymers with attractive properties like fluorescence, circularly-polarized luminescence, extended radical delocalization and hole transporting properties. The need for materials showing such characteristics is in constant growth, notably with regards towards nanotechnology, and we believe that it is of paramount importance to develop supramolecular polymers beyond proof-of-concepts to create the materials of the future.

In the first part of this thesis, we will combine the well-known phenomenon of *aggregation induced emission* by using the tetraphenylethylene motif, with the self-assembling properties of triarylamine trisamides, to obtain fluorescent supramolecular polymers with hole-conducting properties. Further introduction of chiral moieties should lead our materials to show circularly polarized emission. In addition, we will try to control the polymerization process in order to tune the morphologies of the assemblies and the related properties. More in general, we aim to demonstrate that a supramolecular approach towards luminescent materials can be an ideal strategy towards the development of functional materials with tuneable properties controlled by their polymerization process.

In our second project, we have envisioned the synthesis of a triarylamine-based macrocycle made by of a hexaaza[1₆]para-cyclophane core and surrounded by six nonaamido chains. The proposed macrocyclic core, in which the aromatic rings are connected to the nitrogens at their para- position, permits the highest extent of delocalization. On the other hand, the presence of six amide groups endow the system with the ability of establishing hydrogen bonding and is expected to drive the self-assembly towards mono-columnar self-assemblies. The synthesis that will be developed will join the small number of reported synthetic methodologies towards hexaaza[1₆]para-cyclophanes and will be the first ever report of a hydrogen-bond driven self-assembling cyclophane. The electrochemical and self-assembling properties will be explored.

Both projects are developed within the context of functional supramolecular materials and are expected to provide new insights in the possibilities of triarylamine-based supramolecular polymers, notably with regards to their electronic properties.

CHAPTER I. GENERAL BIBLIOGRAPHY

A. SUPRAMOLECULAR CHEMISTRY AND SUPRAMOLECULAR POLYMERS

Supramolecular chemistry has been defined as “the chemistry beyond the molecules” by Jean-Marie Lehn, Nobel Prize in chemistry in 1987.¹ The main concept of supramolecular chemistry relies on the possibility to build organized entities of higher complexity through the association of simple building blocks by non-covalent interactions. Considering the generality of this assumption, many phenomenon occurring in chemical science can be considered to be a part of supramolecular chemistry: The term “host-guest chemistry”, in which the association of one or more small molecules (guest) to the binding sites of a larger molecule (host) leads to the formation of complexes or aggregates, is of particular interest in the field.² Molecular self-assembly, where monomeric units associate via noncovalent interactions forming discrete (micelles, spheres, cages, *etc.*) or infinite (fibers, networks, *etc.*) objects, represents a large domain in supramolecular chemistry.³ In many cases, molecules are linked together only due to mechanical constraints (mechanically-interlocked molecules) such as catenanes, rotaxanes, molecular knots, and others.⁴

In supramolecular chemistry, the possibility to rationally design the building blocks, taking into account the intermolecular interactions, to prepare well-defined supramolecular structures is a preeminent goal.⁵ This approach can be observed in numerous examples in biological systems and in particular using biomolecules such as proteins and DNA whose functionality is strongly dependent on their tridimensional structure.^{6,7} The noncovalent interactions among the simple building blocks, such as amino acids and nucleotides in the sequence, is responsible for determining the organization of the entire “biopolymer” in the tridimensional space. Therefore, every single small modification that may occur in the monomers’ sequence is reflected in a modification of the whole structure and, consequently, on the impairment of the original function. In nature, there are plenty of examples of how much a small modification in an amino acid sequence can affect the final folding of the protein leading to sever dysfunction. A notable case is that of achondroplasia: a genetic disorder originating from a mutation in the gene encoding for the fibroblast growth factor receptor 3 (FGFR3) and which is the most common cause of dwarfism.⁸ In particular the mutation in the gene results in the substitution of an arginine residue for a glycine at position 380 of the final protein (**Figure 1**), this change forces an additional hydrogen bonding between two arginine side chains which stabilize the FGFR3 in the activated form leading to complications with bones and cartilage production.⁹

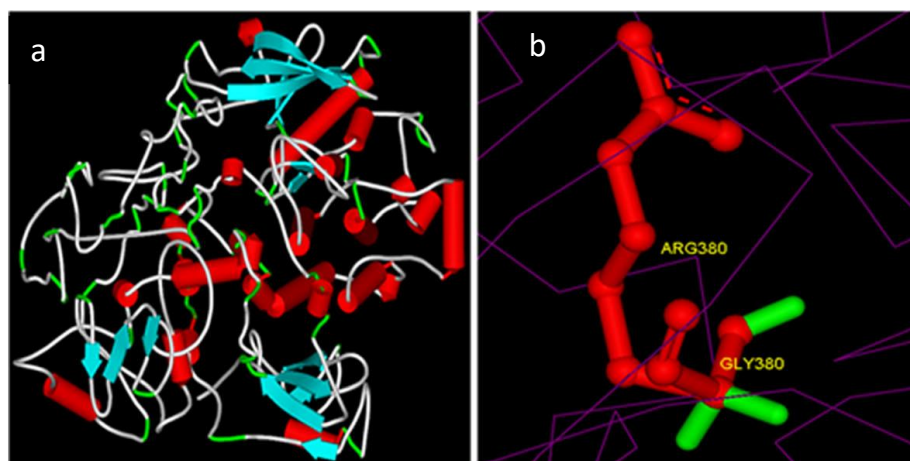


Figure 1 | **a**) Three-dimensional structure prediction of wild-type FGFR3 using I-Tasser. Red cylinders showing α -helix, flattened cyan color arrows showing β - Sheets and rest tube like features are coils. **b**) Superimposed three-dimensional structures of wild-type and mutant highlighting the substituted amino acid. Superimposed structures represented by purple wire display style while red ball and stick model is representing arginine which got substituted by glycine (green color stick display style) at the 380 amino acid position. (Reproduced from⁹).

In order to achieve a good understanding of the field of supramolecular chemistry, which is behind all the projects presented in this work, we will start describing more in detail the non-covalent forces involved. We will then explore how these interactions can build and mold supramolecular polymers, which represent an alternative family to the classical covalent polymers but introduce a few new properties and characteristics. We will present the different types of supramolecular polymers with a succinct description of the various mechanisms for their self-assembling. We will discuss how chirality can arise from supramolecular systems and we will then focus on a specific family of conductive supramolecular polymers based on the triarylamine motif. These supramolecular polymers have been introduced and investigated by the group of professor Nicolas Giuseppone and constitute the molecules of interest for the projects described in this work.

1.1 NON-COVALENT INTERACTIONS IN SUPRAMOLECULAR POLYMERS

Covalent and non-covalent interactions are considerably different for their origins and for the energies involved. Covalent bonds are mainly formed from the overlapping of partially occupied orbitals with a pair of electrons which is shared between the atoms and normally act on distances shorter than 2 Å. Non-covalent interactions arise most prominently from the electromagnetic interactions between different types of multipole: permanent multipole,

induced multipole and instantaneous time variable multipole; these typology of attractions can act on distances up to tens of angstrom. The energies engaged in the two cases range from 1 to 200 $\text{kJ}\cdot\text{mol}^{-1}$ for the non-covalent interactions, in general smaller when compared to the energy of a covalent bond which is about $400 \text{ kJ}\cdot\text{mol}^{-1}$.^{10,11}

Ion-ion, Ion-dipole and dipole-dipole, interactions are electrostatic attractions between charged ions or molecules which possess a dipolar moment. Considering the nature of this forces, it follows that these interactions becomes stronger with an increase of the charges involved, which is high in the case of fully charged ions and weaker for partially charged dipoles. The relationship governing the force between charged particles can be expressed by the Coulomb law, defined as:

$$F = \frac{kq_1q_2}{r^2} \quad (1)$$

Where k is the Coulomb's constant, q_1 and q_2 the magnitude and the charges, and r the distance between the charges. It follows that the Coulombic interactions decrease exponentially with increasing distance between the charged species.¹² Interactions between ions differ from those between dipoles also regarding the directionality: while ion-ion interactions are non-directional, dipoles have to be aligned to have an efficient attraction (**Figure 2**).¹¹

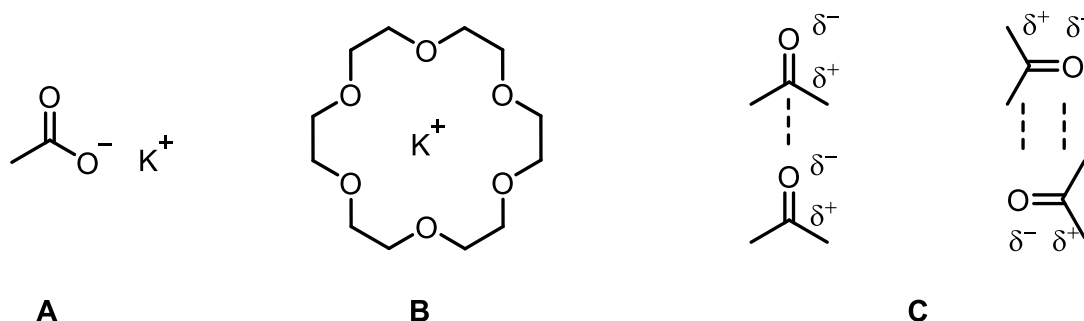


Figure 2 | Electrostatic interactions: A) Ion-ion interactions; B) Ion-dipole interaction; C) Dipole-dipole interaction.

1.1.1 Hydrogen bonding

The hydrogen bond is a type of dipole-dipole interaction between a group called *hydrogen bond donor* (D), which is constituted by a hydrogen atom usually covalently bonded to an electronegative atom, and a *hydrogen bond acceptor* (A) which is typically another electronegative atom. Despite the energy for a single hydrogen bond being normally weak, with values between 5 and 30 $\text{kJ}\cdot\text{mol}^{-1}$,¹³ they hold a prominent place in supramolecular

chemistry thanks to their directionality and versatility.¹⁴ Moreover, the possibility to combine several hydrogen bonds in a functional unit increases the strength of these interactions. Multiple hydrogen bonds can be arrayed to create a hydrogen-bonding array whose strength depends on many factors: the number and nature of the hydrogen bonds involved, the solvent used as medium, and the order of the *donor* and *acceptor* in the array.¹⁴ The possibility to tune the strength and directionality of the hydrogen bonds that can be obtained through the array of multiple hydrogen bonds is shown for the case of a linear array of three hydrogen bonding sites (**Figure 3**).

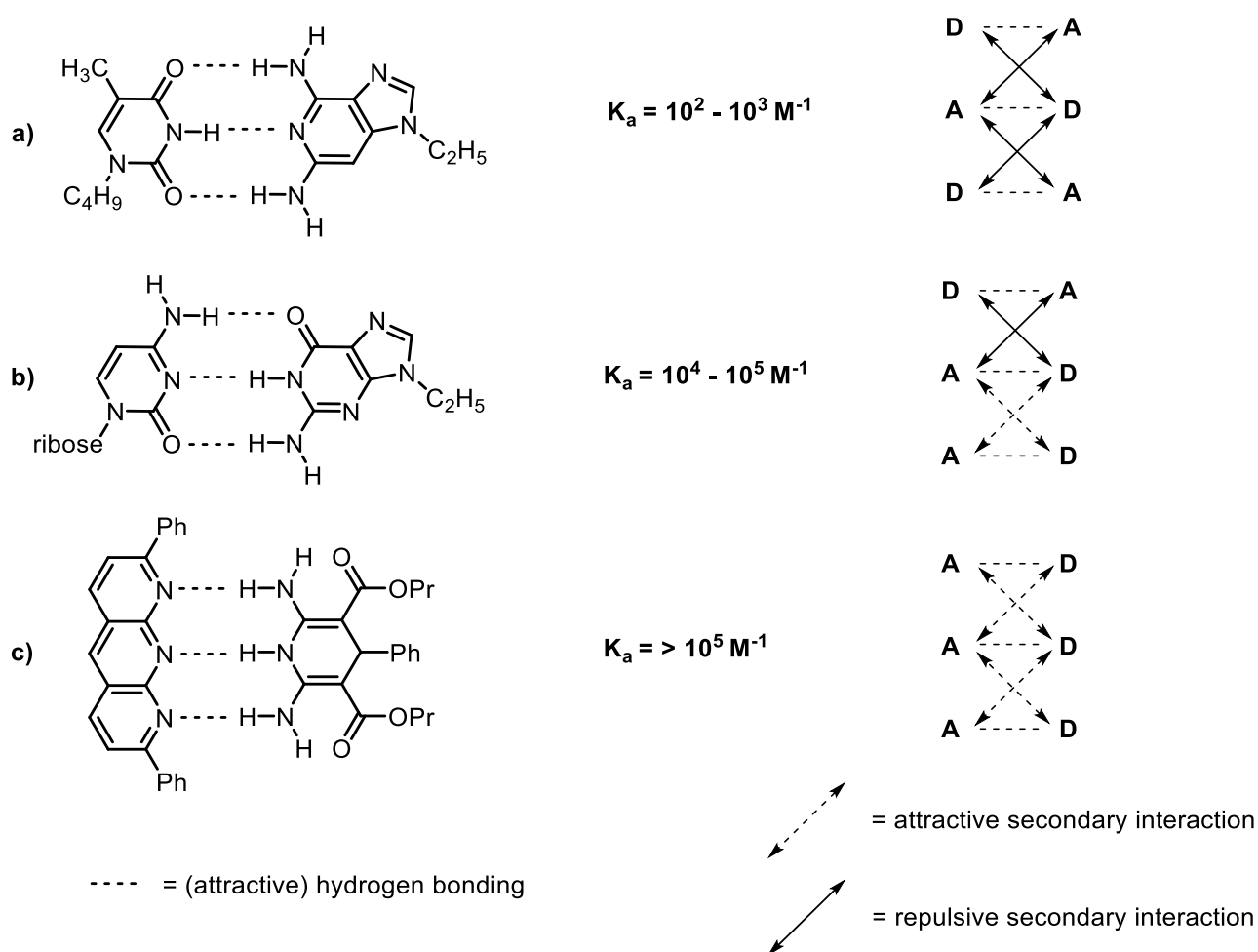


Figure 3 | Stability of complexes with different hydrogen-bonding motifs. (Reproduce from¹⁴).

Although the number of hydrogen bonding remains the same in all the cases, for the first arrangement (DAD – ADA) the association constant, in chloroform, is around 10^2 M^{-1} ; the association constant increases for the DAA – ADD arrangement reaching value around 10^4 M^{-1} and it exceeds the value of 10^5 M^{-1} for the AAA – DDD array. This trend is explained taking into account the secondary interactions between diagonally opposed sites: these interactions

are of attractive type when the sites are disparate, whereas they are repulsive when the sites are of the same kind. In the DAD array, all the secondary interactions are repulsive minimizing the association constant, while in the AAA motif the attractive secondary interactions are maximized resulting in the highest association constant. Following this approach, it has been possible to build even more stable multiple-hydrogen-bonding arrays with higher association constant than those of triple-hydrogen-bonding arrays. In one textbook example, reported by the group of Bert Meijer, a quadruple-hydrogen-bonding array based on ureidopyrimidone unit showed a dimerization constant of $6 \times 10^7 \text{ M}^{-1}$ in chloroform. This very high constant was achieved thanks to the AADD sequence of *donor/acceptor* units in the array.¹⁴

1.1.3 π -interactions

The term π -interaction includes non-covalent interactions between two aromatic units or between an aromatic unit and a cation or an anion. The first one, called π - π *stacking* consist in the mutual attraction between two stacked aromatic rings. The easiest way to describe the π - π stacking is to consider the system constituted by a benzene dimer. For such a system, the molecules can interact with each other through three different configurations (**Figure 4**).

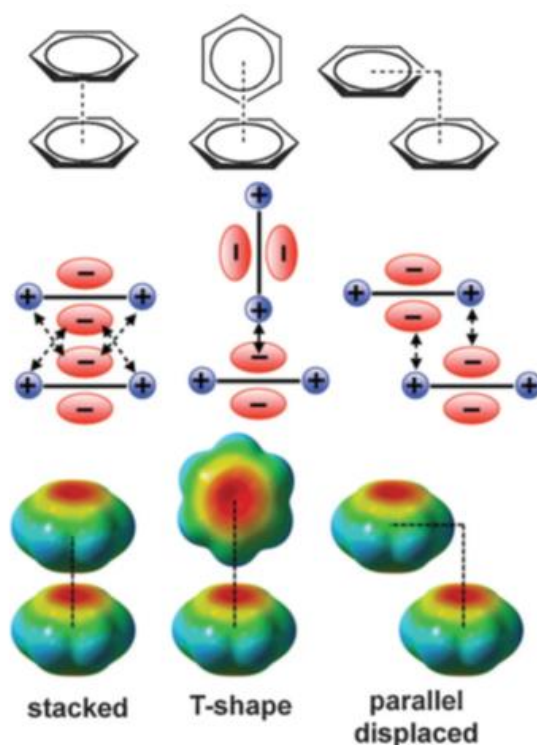


Figure 4 | Geometries, quadrupole moments and ESPs (blue is positive and red is negative) of typical π - π aromatic interactions. (Reproduced from ¹⁵).

The first one, called *face to face*, in which the two aromatic rings are parallel, the second one, called *edge-face* or *T-shape*, where the two aromatic rings are perpendicular, and the third one, called *offset*, in which the benzene rings are parallel displaced.^{15,16} The stability of these structures can be rationalized if we consider the quadrupolar moment for each aromatic ring which generate a partial negative charge on both faces of the π system and a partial positive charge around the aromatic ring. It follows that the *T-shape* and the *offset* are the most stable configurations owing to the attractive electrostatic interactions between the rings while the *face to face* is the less favored due to the repulsion between the negatively charged π electron cloud of the aromatic ring.¹⁷

The π -*cation* and the π -*anion* interactions works in a similar way, (**Figure 5**) with the positively charged ion sitting above the aromatic ring, and the negatively charged ion which sits in the plane on the periphery of the aromatic ring. In the last case, the preference of the anion can be reversed if the aromatic ring is electron deficient (ex. C_6F_6).^{15,18}

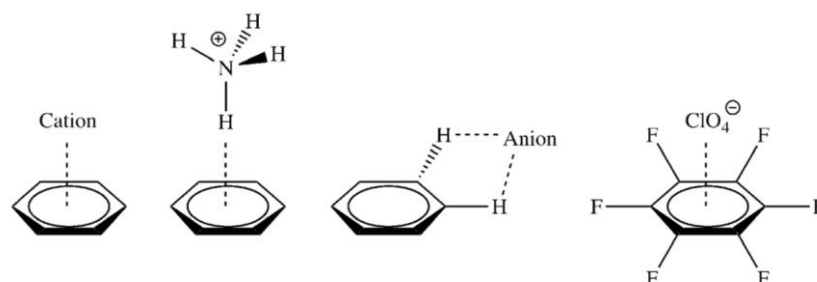


Figure 5 | Different possibilities for cation-anion interactions with aromatic ring. (Reproduced from¹⁵).

The energies involved in these kind of interactions are generally weak, ranging from 4 to 50 $\text{kJ}\cdot\text{mol}^{-1}$ depending on the units.¹⁶

1.1.4 Van der Waals forces

The Van der Waals (VdW) forces are the weakest interactions among the non-covalent interactions, with interaction energies typically lower than $4 \text{ kJ}\cdot\text{mol}^{-1}$. Nevertheless, they are the most ubiquitous at the nanoscale and they arise from the transient concentration of electrons in one region of a molecule which temporarily polarizes the electron shell, thus inducing an

opposite polarization on the nearby electron shell resulting in a transient attractive force. They act at typical distances of about 0.4 nm below which the overlap between the orbitals prevent the molecules to approach further. Increasing the distance between the units results in a rapid loss of energy which makes this forces very easy to break.¹⁶

1.1.5 Hydrophobic interactions

The hydrophobic effect can be described as the tendency of hydrophobic units to segregate from water and aggregate in nonpolar cluster. According to several models, the release of water molecules in this way leads to an increase in the entropy of the system and to more cohesive interactions between water molecules through hydrogen bonding leading to an overall gain in enthalpy. On the other side, hydrophobic molecules can be attracted by van der Waals and π - π interactions.¹⁹

We can distinguish two different energy contributions to this process: an *enthalpic hydrophobic effect* and an *entropic hydrophobic effect*. The *enthalpic hydrophobic effect* is relevant in the case of a guest replacing the water present in the cavity of a host, the water extruded can now replace the weak interactions with the hydrophobic cavity with stronger hydrogen bonding with molecules in the bulk solvent (**Figure 6a**).¹¹

The *entropic hydrophobic effect* takes place, for instance, for several hydrophobic objects dispersed in water: each single object constitutes a hole in the water network which is solvated.

When two objects cluster together the two holes merge in one hole and the solvation free energy decreases resulting in a favorable driving force for the aggregation (**Figure 6b**).^{11,20}

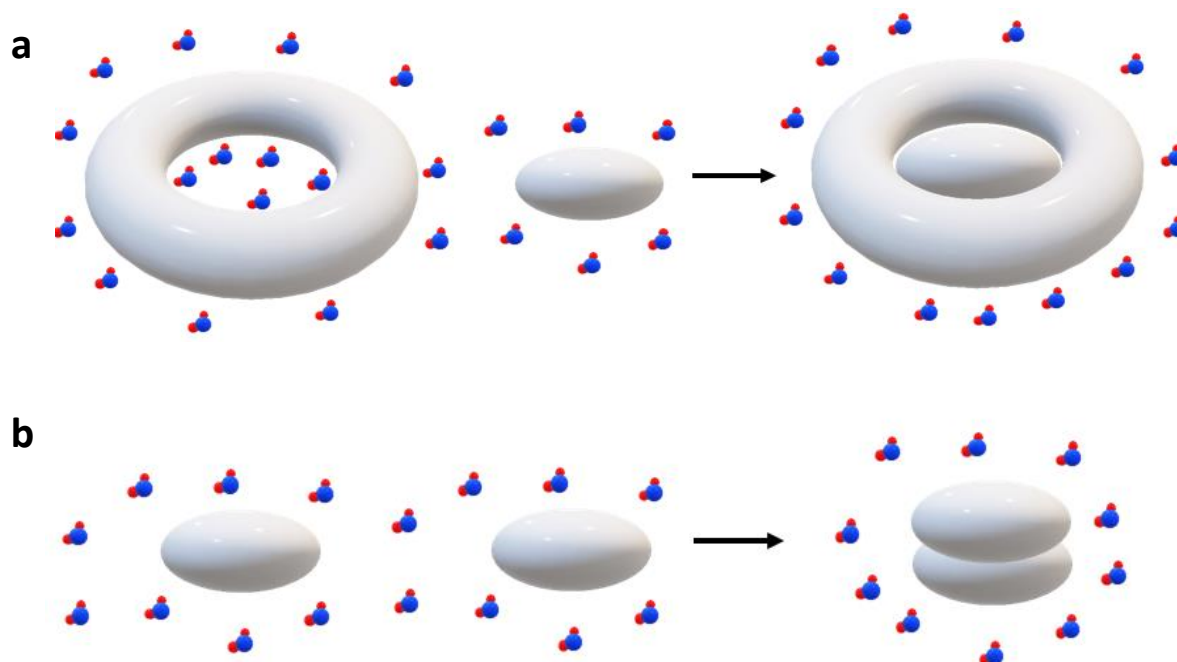


Figure 6 | a) The displacement of water molecules from a hydrophobic cavity is responsible for the enthalpic hydrophobic effect; **b)** Two organic molecules surrounded by water molecules forms two holes in solvent network, upon aggregation just one hole is present which lead to the entropic gain.

1.2 SUPRAMOLECULAR POLYMERS

According to the general definition of a polymer as a large molecule, or macromolecule, composed by many repeating units, a supramolecular polymer (SP) is, in simple terms, a long sequence of units (*i.e.*, monomers, polymers) connected by noncovalent interactions.²¹ Due to the reversible and directional nature of the supramolecular bonds, new and attracting properties arise for such polymers in solution: a degree of polymerization that depends on the monomer concentration and the respective association constant, self-healing properties, and stimuli responsiveness properties among others.^{22,23} Such characteristics have contributed, during the last decades, to rise the interest in these materials, and many studies have revealed the mechanisms behind their formation. The possible use of supramolecular polymers in materials sciences has received much attention not only with regards to new materials but to contribute to the improvement of existing materials by controlling their supramolecular interactions.

1.2.1 Classification of supramolecular polymers

Since the inception of supramolecular polymers (SP), several ways to classify the different types of SPs have been developed. However, the high heterogeneity of this class of compounds for the constituent monomer, the non-covalent interaction involved, the different mechanisms of polymerization and the properties of the obtained materials, make this task a challenging endeavor and have led to different ways to classify them.

According to different principles, three main classifications can be summarized: *(i)* the physical nature of the non-covalent interactions responsible for the monomers aggregation; *(ii)* the type of monomers forming the polymer; *(iii)* The evolution of the Gibbs free energy during the supramolecular polymerization process.²⁴

In this manuscript we will describe shortly the original classification according to the various types of interaction that act as driving force. Despite its utility in having an overview on the different families of SP, it neglects the mechanistic details that have become relevant in recent years, hence, we will outline more in detail the “thermodynamic classification” according to the mechanisms proposed and the ways to assess them.

1.2.2 Classification according to the nature of noncovalent forces

a) Supramolecular polymers formed from hydrogen bonding arrays

As it was mentioned above, the relatively weak nature of the hydrogen bonding can be increased by combining units with multiple *acceptor/donor* sites. The group of Lehn reported, in 1990,²⁵ one of the first example of supramolecular polymers based on hydrogen bonding. This system, based on the molecular recognition between complementary components, sees a tartaric acid functionalized with an uracil (U) on each side, establish three hydrogen bonding per site with another tartaric acid functionalized with two 2,6-diacetylamidopyridine (P). The two precursors, mixed in chloroform, self-assembled in a supramolecular polymer which forms a liquid crystalline phase made by helical structures as seen by electron microscopy^{25,26} (**Figure 7**).

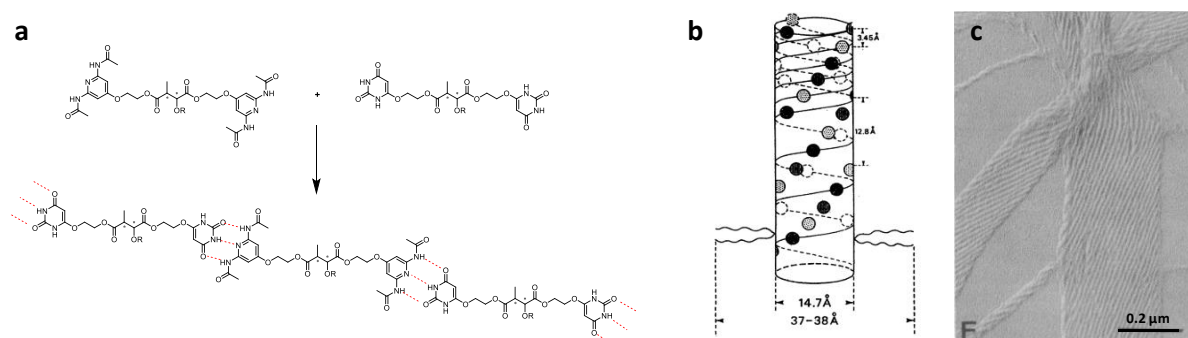


Figure 7 | a) Formation of the triple hydrogen bonding between the *donor* and the *acceptor* synthons leading to the supramolecular polymerization; b) Schematic representation of the columnar superstructure suggested by the X-ray data, spots of the same type belong to the same helical strand of a triple helix; c) SEM image after drop-casting on a TEM grid. (Reproduced from^{25,26}).

b) Ionic and coordination (metal – ligand) polymers

The incorporation of ionic and metal – ligand interaction in supramolecular polymers opens the door to a wide class of materials with many advantages compared to other class of supramolecular systems (*e. g.*, $\pi - \pi$ or host guest interaction) because of the highly directional nature of the coordinative bond and the possibility to easily vary the ligand structure.^{27,28} The general structure for a metallocupramolecular polymer (MSP) sees an alternance between organic ligand molecules and metal ions (**Figure 8**). In this highlight, is important that the association between the metal and the ligand is strong enough to preserve the polymer chain in solution.

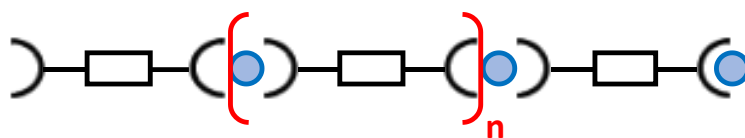


Figure 8 | General structure for a linear metallosupramolecular polymer: the blue spheres represent the metal ion while the black box represents the organic spacer equipped with two receptors. (Reproduced from²⁷).

The strength of the metal to ligand interaction, and therefore, the stability of the supramolecular polymer in solution, can be tuned in two main way: by increasing the affinity between the ligand and the metal, or by using multidentate chelators. An example of how the latter approach can enhance the stability of the complex is demonstrate by using pyridine-based ligands (**Figure 9**): The binding constant increase from $K = 10^3 \text{ M}^{-1}$ for a Zn^{II} -pyridine complex to the $K > 10^8 \text{ M}^{-1}$ for a Zn^{II} -terpyridine complex.²⁸

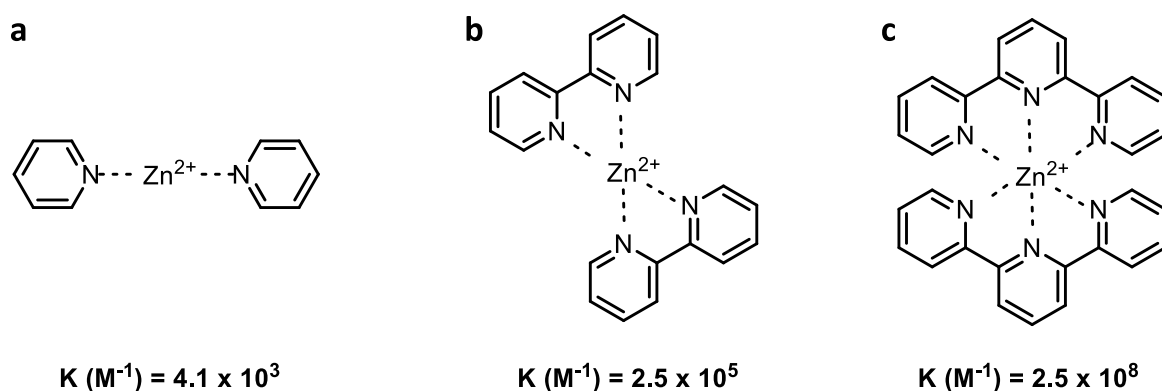


Figure 9 | Representation of a series of Zinc complexes with pyridine-based ligands of increasing denticity; (values of the constant are reported from²⁷).

A simple example of a metallosupramolecular polymer which exploited the high stability of terpyridine complex as building block for hierarchical self-assembly, was reported by the group of Kurth (**Figure 10**). They succeeded in obtaining a polyelectrolyte film in two steps: firstly the association between ligand **1** and iron ions allow to form a metallosupramolecular polymer positively charged **2**; in a second step, the alternating adsorption of the MSP and the negatively charged poly(styrene sulfonate) (PSS) leads to the generation of the ultrathin polyelectrolyte interfaces.²⁹

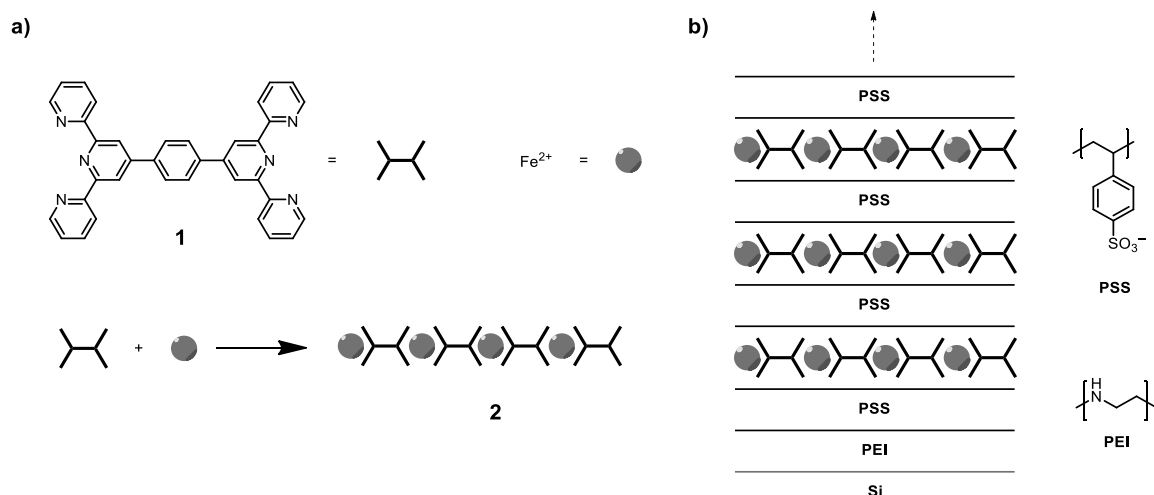


Figure 10 | a) Metallosupramolecular polymer **2** formed by equal ratio of ligand **1** and metal ions; **b)** Multilayers deposition of oppositely charged polyelectrolytes. (Reproduced from ²⁹).

c) Polymers based on host – guest interactions

The term “host – guest interaction” does not refer to a specific noncovalent interaction but is the result of a synergistic effect of multipole noncovalent interactions, like hydrogen bonding, hydrophobic interactions, electrostatic interactions, and Van der Waals forces. A host – guest complex is normally formed by an organic molecule, guest, whose size perfectly fits the cavity of a host molecule and which is non-covalently bonded to this latter. Among the large number of host – guest systems reported in the literature, the most common complexes used in the fabrication of supramolecular polymers include cyclodextrins (CDs), crown ethers, cucurbit[8]urils and calixarenes (**Figure 11**).¹³

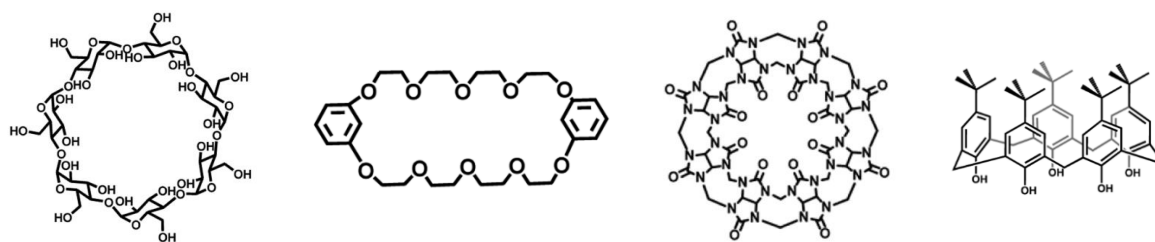


Figure 11 | From left to right: a β -cyclodextrin, a crown ether, a cucurbit[8]uril and a calixarene.

For each of these hosts, a specific guest molecule is needed to bind the cavity like adamantane or the coumarin for cyclodextrin, viologen or a charged amine for crown ethers, methyl viologen or anthracene for cucurbit[8]uril and alkanes with charged substituents for calixarene. This approach is really advantageous towards the development of functional materials, like the

photoswitchable CD-based supramolecular polymer reported by the group of Tian.³⁰ In their work, a supramolecular polymer is formed by mixing γ -CD with a viologen moiety bringing two terminal coumarins. The large cavity of the γ -CD can accommodate two coumarin units providing the host – guest complex responsible for the formation of the supramolecular polymer network (**Figure 12**). Moreover, the reversible photodimerization of the active coumarins allows the switching between the noncovalent and the covalent polymer.

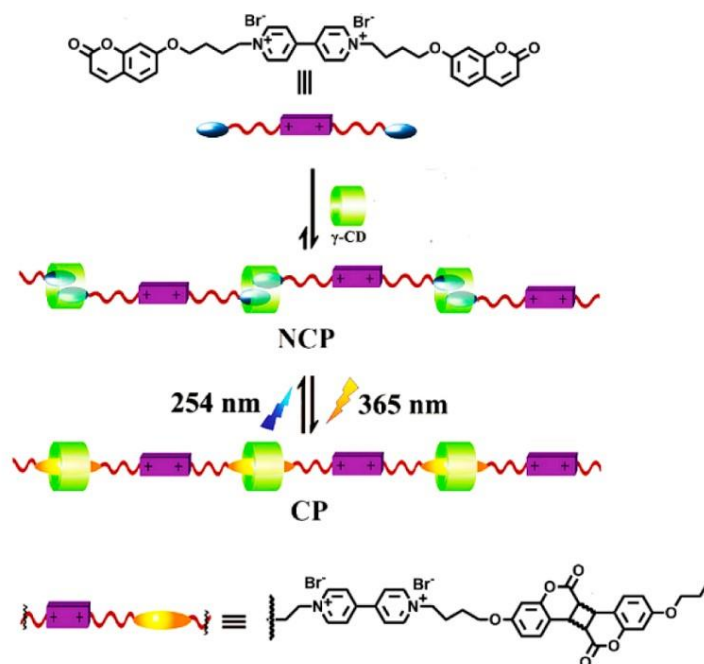


Figure 12 | Schematic representation of the synthesis of the supramolecular noncovalent polymer (NCP) and photoswitching to the covalent polymer (CP). (Reproduced from¹³).

d) Supramolecular polymer based on arene-arene interactions

Supramolecular polymers, based on π - π interactions, are normally constructed by the stacking of small or large aromatic systems such as: triphenylene,³¹ phthalocyanines,³² porphyrins,³³ helicenes,³⁴ *m*-phenylene ethynylene,³⁵ *etc.*

Despite the possibility to have supramolecular polymers based only on aromatic interactions (**Figure 13**),³⁶ it is often the case that those interaction are too weak and not directional enough to drive the self-assembly process alone, therefore, the integration of additional driving forces, like hydrogen bonding, are employed to promote the supramolecular polymerization.¹³

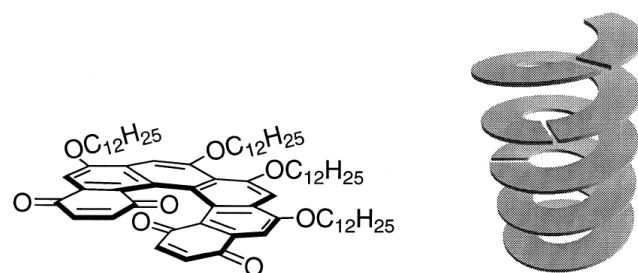


Figure 13 | From left to right: liquid crystalline disc-shaped helicene and its mode of association into helical columns.

A particular property, for this class of supramolecular polymers, arise when aromatic donor (D) and aromatic acceptor (A) molecules are alternating in a columnar stacking (**Figure 14**). This configuration can lead the material to show excellent conducting properties³⁷.

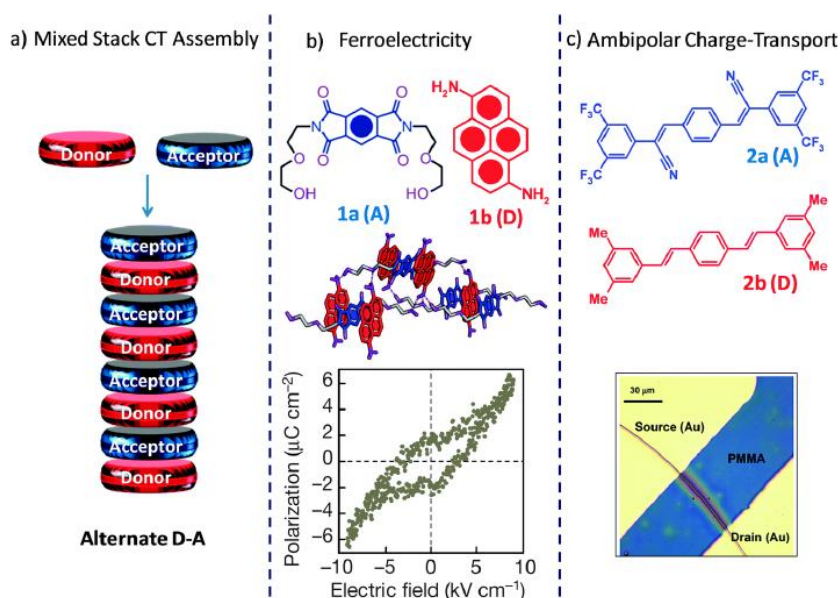


Figure 14 | **a)** Schematic representation of alternated D and A units in a columnar assembly; **b)** ferroelectricity, at room temperature, showed by a co-crystal of pyrromellitic diimide acceptor and pyrene donor units; **c)** ambipolar charge transfer of the assembly of distyrylbenzene and dicyano disyrylbenzene units. (Reproduced from³⁷).

1.2.3 Mechanisms of supramolecular polymerization

As mentioned above in this chapter, the supramolecular polymerization, due to the nature of the forces involved, is a dynamic process in which monomers and polymers are in equilibrium. Because of this, the degree of polymerization is influenced by different thermodynamic parameter like: concentration, temperature and pressure.²⁴ To elucidate how those parameters influence the evolution of the Gibbs free energy during the growth of the supramolecular

polymer, many theoretical models have been proposed. Among them, three major growth mechanism can be highlighted: isodesmic, cooperative and ring-chain growth (**Figure 15**).³⁸ In the following section we will describe in detail the first two mechanisms.

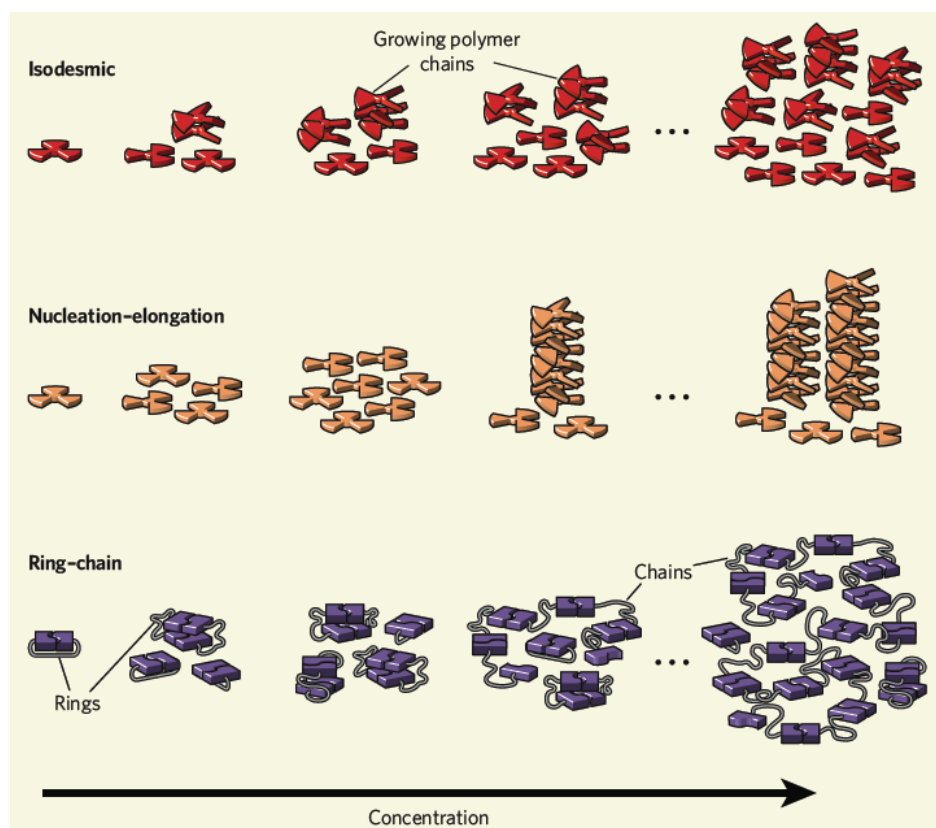


Figure 15 | Main mechanisms of supramolecular polymerization: isodesmic, cooperative (nucleation-elongation) and ring-chain. (Reproduced from³⁸).

a) Isodesmic model

The principle of “equal reactivity”, stated by Flory for a step-by-step reversible polycondensation, assert that the reactivity of the functional groups remains unaffected during the polymerization process.³⁹ This principle, enounced for covalent polymerization, can be extended to the isodesmic model for supramolecular polymerization. Following this principle, an isodesmic growth consist of a series of reversible steps in which each incorporation of a monomer into the polymeric chain happens with the same kinetics and thermodynamics. The result is a constant decrease of the Gibbs free energy during the polymer growth (**Figure 16a**). A convenient consequence it that the process can be characterized by a single binding constant (K) for each reversible monomer addition, with the reactivity of the terminal group on the polymeric chains equal to that of monomers in solution (**Figure 16b**).²⁴

The equivalence of the binding constant for each step, implies the absence of a critical concentration or a critical temperature to initiate the supramolecular polymerization process.^{40,41,42,43}

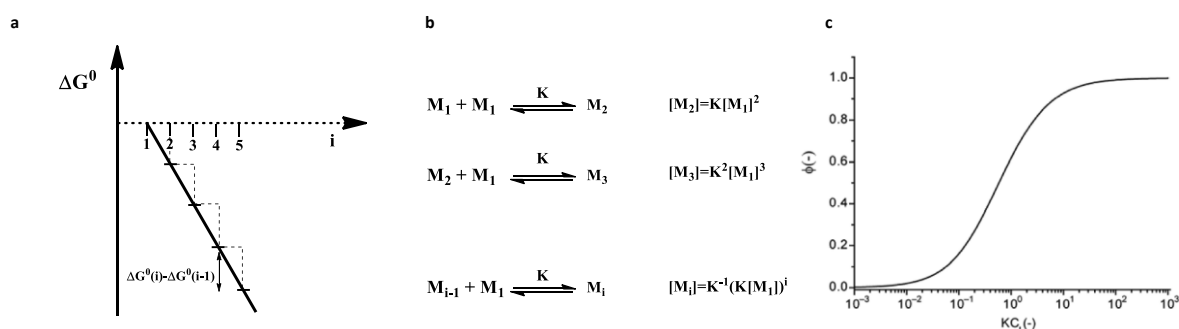


Figure 16 | a) Schematic depiction of the Gibbs free energy variation (ordinate) during the isodesmic supramolecular polymerization (abscissa); **b)** Scheme of polymer formation by monomer addition; **c)** Fraction of polymerized material as a function of concentration showing the typical sigmoidal shape for the isodesmic model. (Reproduced from²⁴).

In an isodesmic supramolecular polymerization, the size and the number of the assemblies increase gradually during the process and high degrees of aggregation become possible only for strong association constants or highly concentrated solutions. Therefore, the possibility to obtain the value of the association constant (K), and thus, information on the extent of the polymerization becomes attractive. In this regard, many spectroscopic techniques have allowed researchers to access the degree of polymerization. Examples include UV-Vis,⁴⁴ Infrared,⁴⁵ NMR,⁴⁶ fluorescence,⁴⁷ and circular dichroism.⁴⁸

In a typical example, the extrapolation of the K value from experimental UV-Vis data and the relative fitting with the isodesmic model was demonstrated in the group of Prof. Würthner using a perylene bisimide that assembles in π - π stacks (**Figure 17**). Their study reveals the characteristic sigmoidal shape associated to the isodesmic model (**Figure 17b**).⁴⁹

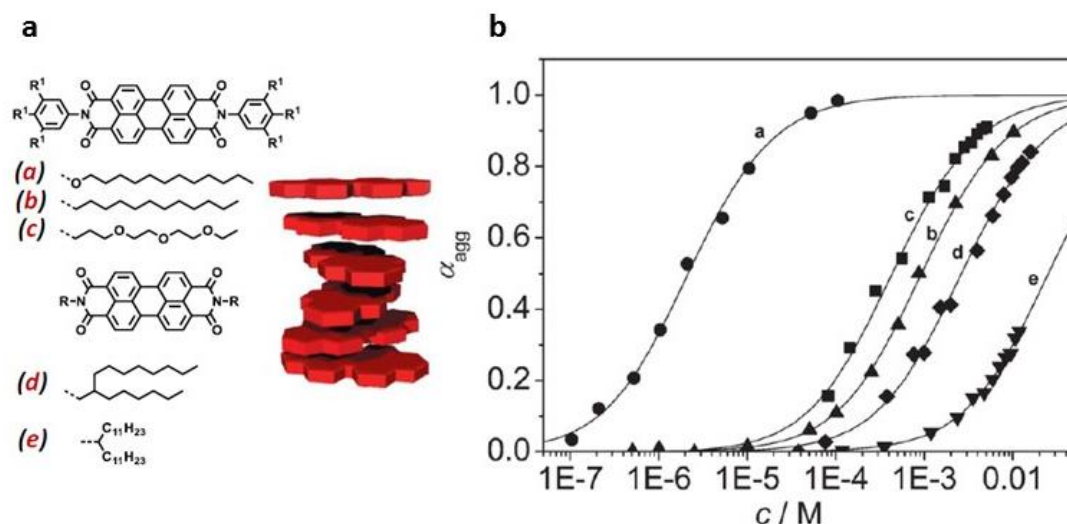


Figure 17 | (a) Chemical structure of various perylene bisimides (PBI) molecules studied by concentration dependent UV-Vis spectroscopy. (b) Molar fraction of aggregated molecules α_{agg} as a function of concentration of the PBI dyes (a – e) in tetrachloromethane. The lines were obtained by fitting the concentration-dependent UV-Vis data with the isodesmic model. (Reproduced from⁴⁹).

b) Cooperative model

In a cooperative supramolecular polymerization, the model for the growth of a supramolecular polymer postulates that it is possible to identify (at least) two different regimes occurring with (at least) two different association constants. A first approximation for this model is to consider only two regimes that can be described as two isodesmic supramolecular polymerizations: the first one occurring until the formation of a nucleus of degree of polymerization s , and the second one starting thereafter. The rate of the first process is identified by a nucleation equilibrium constant K_n , while for the second process by an elongation constant K_e . A logical consequence is that three different sub-classes of cooperative supramolecular polymerization can be differentiated: nucleated, downhill and anti-cooperative growth.²⁴

i) Cooperative nucleated mechanism

A cooperative nucleated supramolecular polymerization is characterized by an initial stage in which a nucleus, of a given degree of polymerization is formed and constitute a maximum in the free energy diagram. Following this stage, the polymerization becomes energetically favorable (**Figure 18**). Therefore, in such a case, the nucleus represents the less energetically stable species and hence its formation limits the rate of the whole process. From this follows

that for a cooperative nucleated mechanism there is a delay in the supramolecular polymerization process which can be circumvented by seeding the solution with preformed nucleus. In contrast to the isodesmic model, in a nucleated mechanism, there is a critical temperature and a critical concentration for which the monomer and the polymer are in equilibrium.⁵⁰

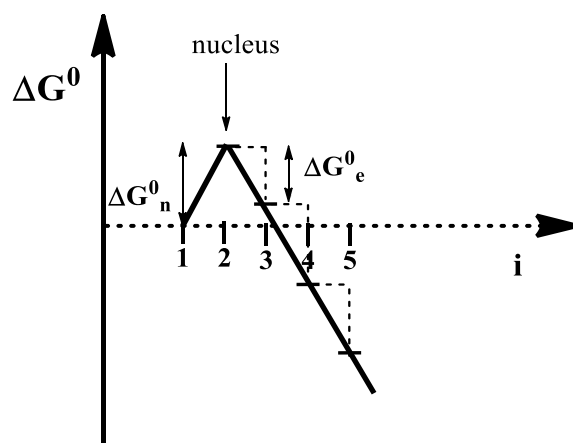


Figure 18 | Schematic diagram of the Gibbs free energy variation (ordinate) during the cooperative nucleation supramolecular polymerization (abscissa). (Reproduced from²⁴).

ii) Cooperative downhill supramolecular polymerization

In a cooperative downhill supramolecular polymerization, the monomer is the specie with the higher Gibbs free energy.⁵¹ The supramolecular polymerization occurs, in a first step, with an initial association constant (nucleation) until a nucleus is formed, at that point, the slope of the Gibbs free energy diagram, suddenly increase and the supramolecular polymerization continue with a larger association constant (elongation) (**Figure 19**).^{51,24}

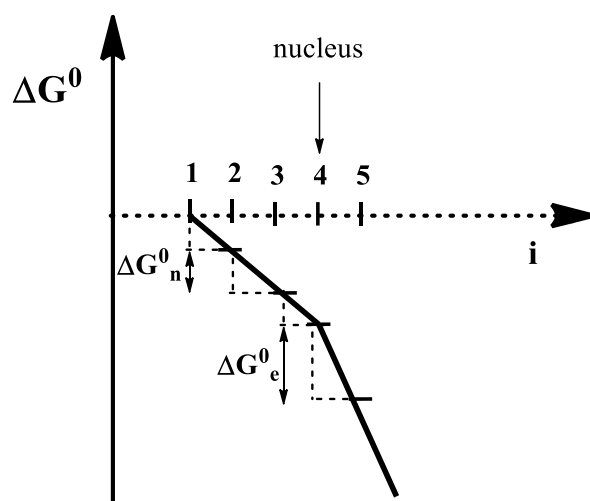


Figure 19 | Schematic diagram of the Gibbs free energy variation (ordinate) during the cooperative downhill supramolecular polymerization (abscissa) (reproduced from²⁴).

It is noteworthy that the nucleation and downhill growth are interchangeable and both depend from the monomer concentration in a way that the first one can become the latter for high values of monomer concentration.⁵²

iii) Anticooperative supramolecular polymerization

As opposed to downhill growth, in an anticooperative supramolecular polymerization, the formation of the nucleus occurs with a higher association constant than the following elongation process (**Figure 20**). This diminishes the polydispersity of the objects that are formed as compared to the high polydispersity index found for the cooperative counterpart.²⁴

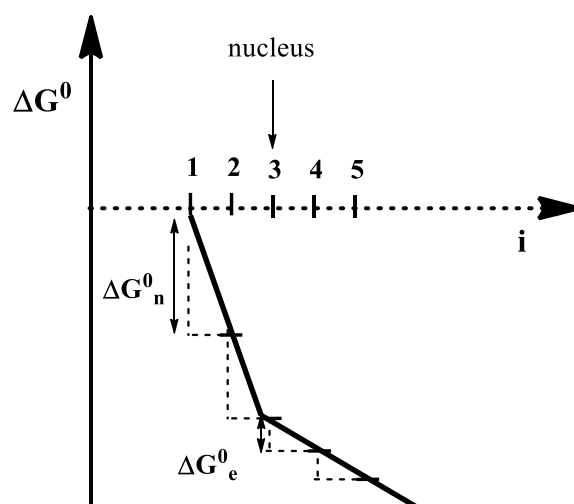


Figure 20 | Schematic diagram of the Gibbs free energy variation (ordinate) during the cooperative downhill supramolecular polymerization (abscissa) (reproduced from²⁴).

It has been shown that the main driving force for the anticooperative effect originates from a combination of intrinsic repulsions (steric and electrostatic),⁵³ which increase with the polymer size and, thus, constrains the supramolecular polymer to a maximal finite size.

In a recent example, Würthner and coworkers⁵⁴ reported an example of seeded supramolecular polymerization of a perylene bisimide derivative: a system related to the one presented in **Figure 17** but differing from it by the presence of hydrogen-bond donors and acceptors in the structure. This difference in structure is reflected on the supramolecular polymerization mechanism that the molecules undergo. As opposite to the previous example, in this case a cooperative nucleated mechanism was found (**Figure 21**), and the authors further showed that it is possible to seed pre-formed nucleus to the system to initiate the supramolecular polymerization.

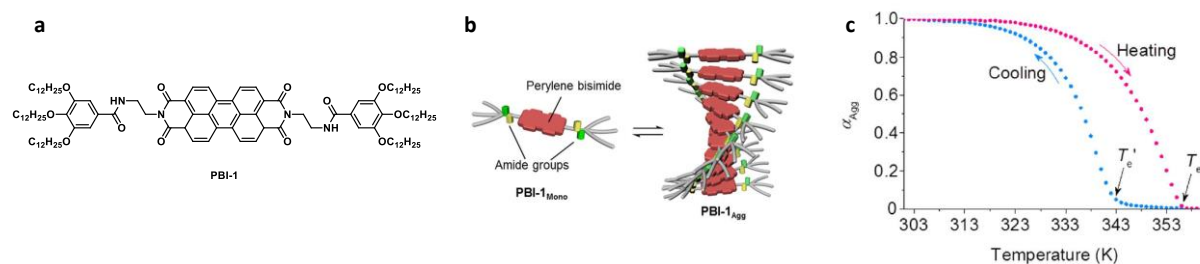


Figure 21 | a) Chemical structure of **PBI-1**; **b)** Schematic representation of the monocolumnar self-assembly of **PBI-1**; **c)** Temperature-dependent degree of aggregation α_{agg} at $\lambda = 525$ nm for a heating-cooling cycle at a $1^\circ\text{C}/\text{min}$ rate of a 10^{-5} M solution in methycyclohexane/toluene (2:1, v/v), the plot shows the typical non-sigmoidal shape for a cooperative nucleated supramolecular polymerization. (Reproduced from⁵⁴).

1.3 SUPRAMOLECULAR CHIRALITY

1.3.1 Generalities

Chirality is a recurring theme in the world as we know it, being an intrinsic characteristic of living matter. Despite its diversity, nature displays only one preferential chirality, and the origin of this asymmetry remains still unclear. Spreading over all hierarchical levels, chiral systems are present from subatomic level, like the left-handed helical neutrino, up to the macroscopic level like some helical plants, bacteria and seashell.^{55,56}

An object is defined to be chiral if it is not superimposable with its mirror image. This general definition also applies to molecules and the two mirror images of an asymmetric molecule are called S- and R- enantiomers. The two enantiomers show the same physical and chemical properties with the only difference that a polarized light, passing through a sample of one of the two enantiomer, rotates the plane of polarization clockwise or anticlockwise in respect to the other enantiomer.⁵⁵

Molecules can have different *types* of chirality which relate to the element which is at the origin of the asymmetry of the system. For instance, a molecule in which a carbon is attached to four different substituents is a stereocenter and is responsible for the point chirality of the molecule; in other cases, molecules which possess non-coplanar rings which are dissymmetric and whose rotation around the chemical bond connecting them is avoided, shows planar chirality; in a similar way, the non-planar arrangement of four group about an axis lead to the axial chirality; in a last example, molecules which are twisted in a cork-screw fashion show helical chirality.

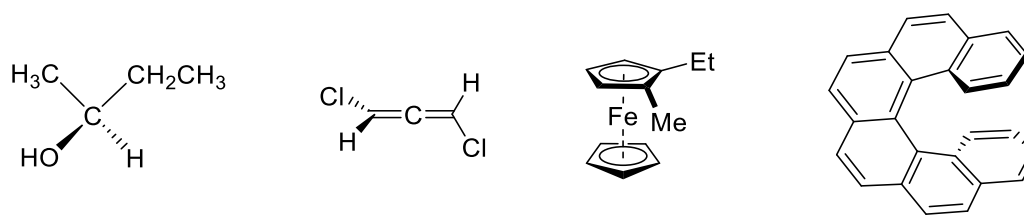


Figure 22 | Example of the different types of molecular chirality, from left to right: A stereogenic carbon showing point chirality; An allene representing a typical system for the axial chirality; a disubstituted ferrocene showing planar chirality; An hexahelicene in a cork-screw conformation responsible for the helical chirality.

Similar to simple molecules, supramolecular systems can have an intrinsic chirality arising from the asymmetric assembly of molecules via noncovalent interactions. Supramolecular chirality is strongly related with the arrangement of the monomers in the system and it is directly influenced by the molecular chirality of the building blocks. Hence, most of the systems built by means of chiral molecules show supramolecular chirality but, as we will show afterwards in this chapter, supramolecular chirality is also possible from mixture of chiral and achiral molecules or even from just achiral monomers.⁵⁶

1.3.2 Characterization of supramolecular chirality

Characterizing the chirality of a supramolecular system is been of fundamental interest since the early days of this field. Towards this task, chemists can rely on many techniques to accomplish this job. Among all the possible techniques available, two main groups can be identified and perfectly fit this purpose: on one hand there is microscopy, like STM, AFM, SEM and TEM; and, on the other hand, spectroscopies, like circular dichroism (CD), vibrational CD, and Raman optical activity.⁵⁶

Although the morphological analysis of supramolecular objects allows for the direct observation of chiral structures (**Figure 23a**),⁵⁷ no information can be obtained on the self-assembly event, which is a dynamic process where both aggregation and disaggregation take place. In light of this, spectroscopic techniques, in particular CD, are more useful to obtain information on the supramolecular polymerization mechanisms, on the interaction between the species composing the chiral nanostructures and on the response of the system to external stimuli.⁵⁸

For example, the group of Meijer,⁵⁹ demonstrated, through a combination of CD and UV-vis spectroscopy, the self-assembly of dimers of p-oligo(phenylene vinylene)s (OPV)

functionalized with ureido-*S*-triazine units in a chiral supramolecular stacks. Variable temperature CD experiments allowed the determination of the melting temperature for the supramolecular polymer (**Figure 23b**).

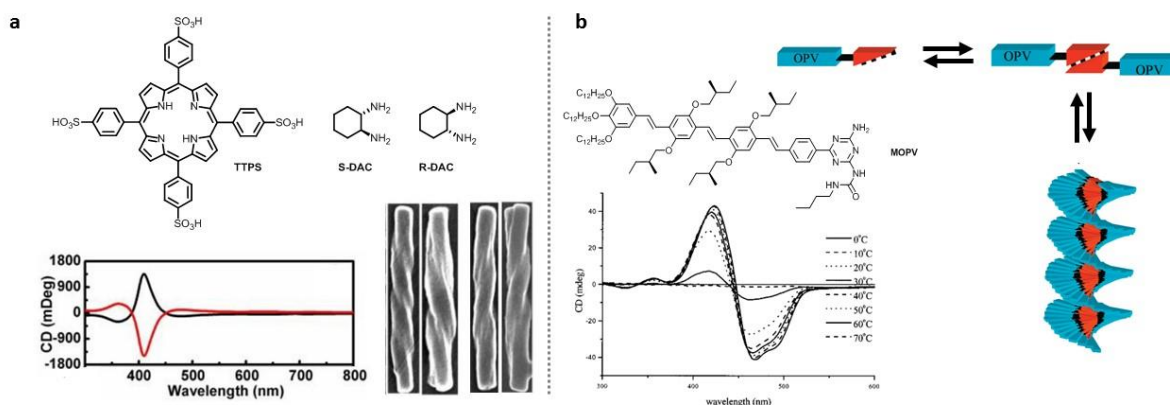


Figure 23 | a) On top: structure of TPPS and *R/S*-DAC, bottom left: CD spectra of the dispersion of TPPS obtained in the presence of *R*-DAC (black) and *S*-DAC (red), bottom right: SEM images of the chiral assemblies of TPPS in presence of *R*-DAC and *S*-DAC; (reproduced from⁵⁷) **b)** Structure and schematic representation of the self-assembly of MOPV in dodecane; Bottom left: variable temperature CD spectrum of MOPV in dodecane. (Reproduced from⁵⁹).

1.3.3 Supramolecular chirality in systems containing chiral molecules

The mechanism by which the molecular chirality is reflected at a supramolecular level is called *chirality transfer*. The bridge between the molecular level and higher hierarchical levels is represented by noncovalent forces which allow the propagation of the information through the assemblies. The self-assembly of chiral monomers normally lead to chiral nanostructures even if many parameters can influence the chirality transfer, for instance, the distance between the core of the assembly and the chiral center is a main factor that can directly affect this process. As introduced before, CD spectroscopy is often used to assess the emergence of chirality in a supramolecular system. There is, however, the limitation that it requires the presence of a chromophore in the supramolecular structure to detect the helicity by CD. Typically, if the chiral center and the assembly site are far enough, the monomers, in their dispersed state, do not show any Cotton effect but, upon self-assembly, the chiral moieties influenced special arrangement of the aromatic, light absorbing, rings in a way that the chromophores have a preferred chiral conformation which is then detected by CD spectroscopy.⁵⁶

The structure of a molecule is directly responsible for its self-assembling behavior and thus, for those which are chiral, for the transfer of chirality. Many families of compounds have shown, in recent decades, the formation of chiral supramolecular systems like amphiphile

molecules,^{60,61,62,63} π -conjugated derivatives like pyrene,⁶² hexa-peri-hexabenzocoronene,⁶⁴ perylenebisimide,^{65,66} porphyrin,⁶⁷ oligo- and polythiophenes⁶⁸ and so on. Among these families of molecules known to form supramolecular helical structures, one of the most studied, thanks to the easy way of functionalizing it and for the good self-assembling properties, is the one of derivatives of benzene-1,3,5-tricarboxamide (BTA). The intrinsic flat nature of the central aromatic ring together with the capability of establish three hydrogen bonding per units, leads to the formation of columnar supramolecular architectures. The eventual chirality, of the substituents surrounding the BTA core, can be transferred to the whole assembly.

BTA derivatives can be divided in two families according to the different ways to connect the amide to the central aromatic ring: C=O centered and N centered (**Figure 24a**). Those two derivatives show similar self-assembly behavior aggregating into helical assembly (**Figure 24b**) but, with a different amplification of the chirality, that turn-out to be higher for the supramolecular structures obtained from C=O centered BTAs. An explanation to this came from the higher energetic barrier found for the rotation around the Ph-NH bond compared to the Ph-CO bond which make the self-assembly of N-BTA less cooperative with respect to the C=O centered one, this may lead to a lower amplification of the chirality.⁶⁹

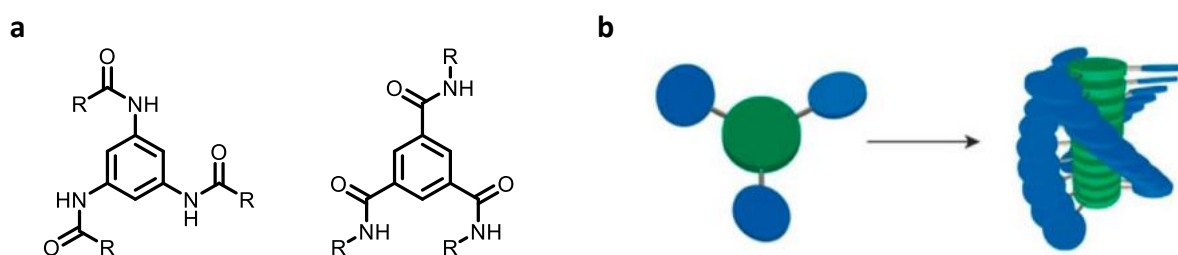


Figure 24 | **a)** General structure of N- and C=O centered BTAs; **b)** Helicoidal assembly of BTA units.

In another example, Sanchez and coworkers, investigated the influence of the central core on the chiral amplification to the self-assembly. For this purpose they compared two series of organogelators based on the **BTA** core and the oligo- (phenylene ethynylene)-based tricarboxamides motifs (**OPE-TAs**) motifs (**Figure 25a**).⁷⁰ Unexpectedly, for the chiral **BTA** derivative, no CD signal was recorded upon self-assembly; on the other hand, for the chiral **OPE-TA**, an intense Cotton effect was detected upon self-assembly (**Figure 25b**). The authors explain the silent nature of chiral **BTA** by considering that the outer amide groups of a molecule are too far apart to interact, through hydrogen bonding, with those of a neighboring stacked

molecule. They conclude that the amide functionalities are involved in hydrogen bonding network but without forming helical structures and thus, chiral supramolecular polymers.

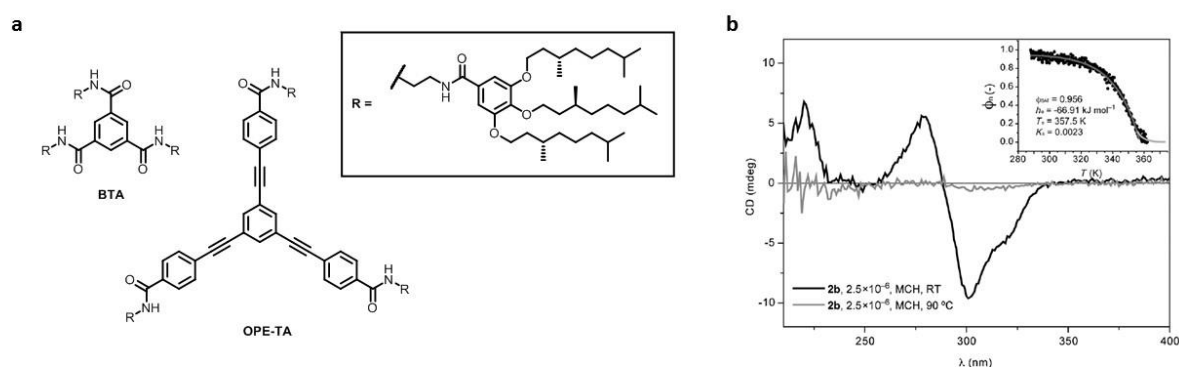


Figure 25 | a) Structure of **BTA** and **OPE-TA** units; **b)** CD spectra of **OPE-TA** derivatives in methylcyclohexane at room temperature and at 100 °C: at high temperature, the system is molecularly dispersed and no cotton effect is detected, upon cooling down, the molecules assemble in chiral helicoidal architectures and a CD signal is observed. (Reproduced from⁷⁰).

Interestingly, the group of Meijer observed on a similar **OPE-TA** based system that by retaining the configuration of the stereogenic centers but changing the connectivity of the amidic bond (N-centered instead of C=O centered), it is possible to reverse the helicity of the assembly and thus, obtain the same CD spectra but opposite in sign.⁷¹ All those results give an indication on how small changes can affect the chirality transfer from chiral molecules to supramolecular polymers. At the time of writing, this still represents a very active field of research.

1.3.4 Supramolecular chirality in systems containing chiral and achiral molecules

Obtaining chiral supramolecular polymers from pure enantiomers is a straightforward way to transfer the chirality to a higher hierarchical level. Despite its apparent simplicity, the synthesis required to afford enantiopure molecules is often tricky. Hence, there has been a strong interest focused on transfer of chirality between mixed achiral/chiral molecules. Such a situation allows for the usage of a small percentages of a chiral molecule to express chirality in an achiral environment.

According to the so-called *sergeant and soldier* principle, if the chiral (*sergeant*) and the achiral (*soldier*) molecules interact in a proper way, by means of noncovalent interactions, the chirality can be transferred to the achiral units and to the whole assembly.

The *sergeant and soldier* principle has been exploited, for instance, by the group of Sanchez on OPE based trisamides system,⁷² the achiral derivative, in MCH at room temperature, is CD silent, this means that an equal amount of the right- and left- handed helices is formed. Upon addition of an increasing percentage of the (*R*)- or the (*S*)- enantiomer, the system starts to self-organize with a preferential helicity that reflect those of aggregates obtained with the pure enantiomer. Upon the addition of the sergeant, the CD response increase in a non-linear way, reaching a maximum value at 20% of enantiomer (**Figure 26**).

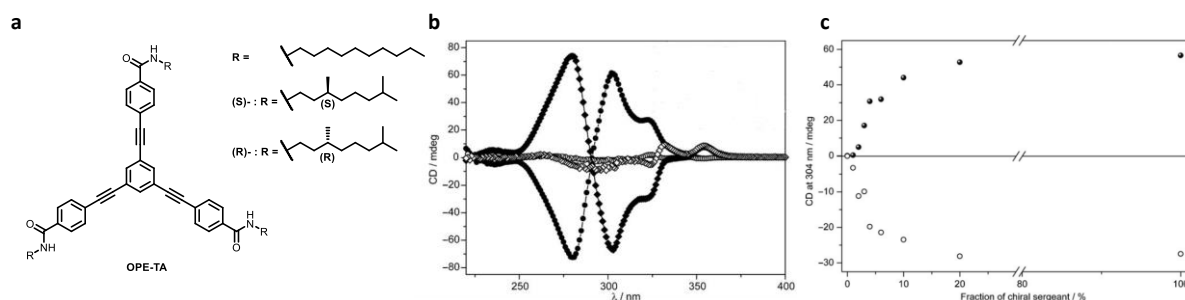


Figure 26 | a) Structure of the **OPE-TA** derivatives; b) CD spectra of the (*R*)- (◆) and (*S*)- (●) enantiomers (MCH, 1.5x10⁻⁵M); c) Amplification of chirality experiments for the achiral **OPE-TA** in MCH (298 K, 1x10⁻⁵ M) at different percentage of chiral (*S*)- (top) and (*R*)- (bottom). (Reproduced from⁷²).

In some interesting cases, it has been possible, to induce the chirality by using simple and commercial small molecules. Chiral diamines turn out to be excellent sergeants in guiding the self-assembly of achiral tetracarboxymetallophthalocyanine in a mixture of DMSO and chloroform (**Figure 27**).⁷³ The possibility to use a wide number of different diamines, together with the possibility to vary the ratio of the binary solvent system, permit to tune the chirality transfer and to obtain different supramolecular chiralities from the same achiral precursor.

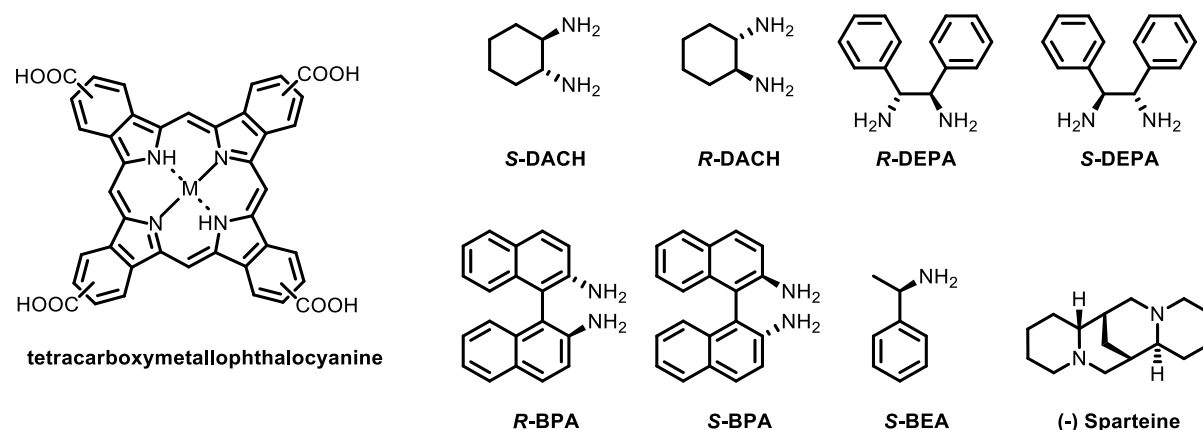


Figure 27 | General structure of the tetracarboxymetallophthalocyanine used as soldiers, and the several chiral diamines that have been used as sergeants. (Reproduced from⁷³).

We have already shown that an efficient chirality transfer is possible between achiral and chiral molecules even though the chiral one has no structural similarities with the achiral. There are even instructive cases in which the chirality is transferred from a chiral solvent to achiral molecules in solution. For instance, Meijer and coworkers,⁷³ reported an example in which achiral derivatives of oligo(*p*-phenylenevinylene) (**Figure 28a**) self-assembled in an helicoidal column in apolar solvents without any chiroptical activity, underlining a racemic organization within the stacks (**Figure 28b**). By changing the solvent with pure (*R*)-citronellol, the supramolecular polymers, show a bisignated Cotton signal (**Figure 28c**), indicating a chirality transfer from the solvent to the assemblies. Moreover, the CD spectra shows the mirror image when (*S*)-citronellol is used confirming the solvent is at the origin of the transfer of chirality.

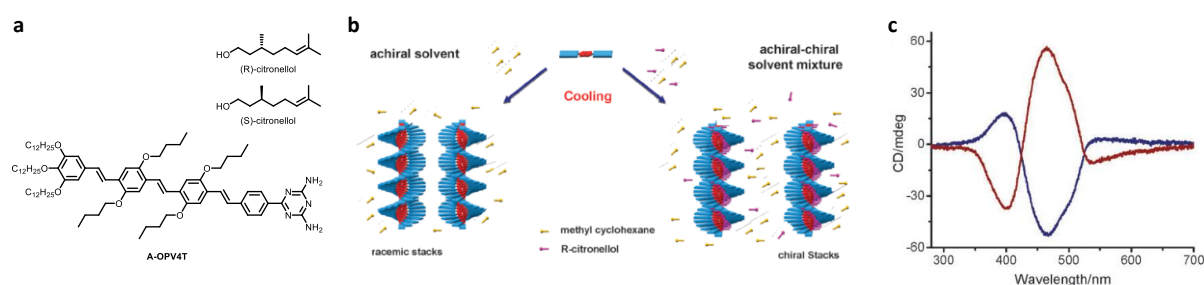


Figure 28 | **a**) Structure of the achiral oligo(*p*-phenylenevinylene) derivative; **b**) Schematic representation of self-assembled structures in achiral and chiral environments; **c**) CD spectra of A-OPV4UT in chiral solvents (*R*-citronellol, blue line; *S*-citronellol, brown line. (Reproduced from⁷⁴).

1.3.5 Other factors influencing the supramolecular chirality

Considering what we have described in the previous paragraphs, it is evident that supramolecular chirality is not determined by few elements, but it is the result of a synergistic effect depending on several factors. These include but are not limited to: the structure and the chirality of the monomers composing the system, the non-covalent interactions which allow the chirality transfer, the eventual chirality of the solvent media and so on. Despite this, there are many other known, and certainly other unknown, parameters that play important roles in governing supramolecular chirality.

Supramolecular polymerization is often induced upon cooling a hot solution of the monomer in a proper solvent. The transition from the molecularly dispersed to the aggregate state is strictly related to the speed of the process, which can, sometimes, undertake different paths according to different cooling rates. Wan and collaborators,⁷⁵ reported an example where a sugar-based gelator forms reversible gels in different aqueous and organic solvents, helical ribbons were observed by TEM and SEM and a different helicity was found depending on the cooling rate (**Figure 29c**). In particular, for a fast-cooled sample right-handed ribbons were observed showing negative Cotton effect, and for slowly-cooled samples they observed left-handed ribbons and a positive Cotton effect (**Figure 29b**). The authors ascribe this phenomenon to the formation, at high temperature, of a metastable nucleus with a preferred helicity, upon slow cooling, the metastable state evolves to a more stable form with a reversed orientation. For the fast-cooling process, the system has no time to perform this rearrangement and the assemblies grow retaining the configuration of the metastable state.

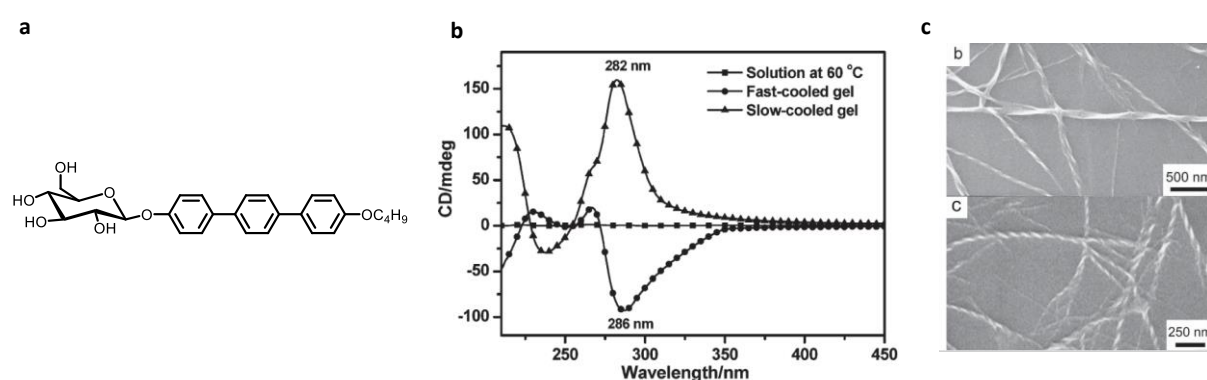


Figure 29 | **a**) Structure of the sugar-based organogelator; **b**) CD spectra for the two cooling regimes; **c**) SEM images of a slowly-cooled sample (top) and for a fast-cooled sample (bottom). (Reproduced from⁷⁵).

Among all the external stimuli that have been used to influence supramolecular self-assembly, light, is an easy and non-invasive stimuli often utilized by chemists to tune the structure of self-assembled systems.⁵⁶ Liu and coworker investigated an azobenzene-based organogelators which self-assemble in a wide range of solvents. Even though the molecule shows no CD response in its dispersed state, supramolecular chirality was found in the gel state. This system showed to be affected from many factors like the polarity of the solvent, which can switch the chirality of the helices; the temperature, regulating the sol-gel transition temperature and, thus, the chiroptical activity. The presence of the photoswitchable azobenzene introduced another variable to the system: the irradiation of the gel using UV light promotes the isomerization of the azobenzene and the collapse of the gel network with a decrease in CD signal; further irradiation with visible light promotes the back-isomerization of the azobenzene and the recovery of the gel state with an increase in CD signal close to the original one (**Figure 30**).⁶²

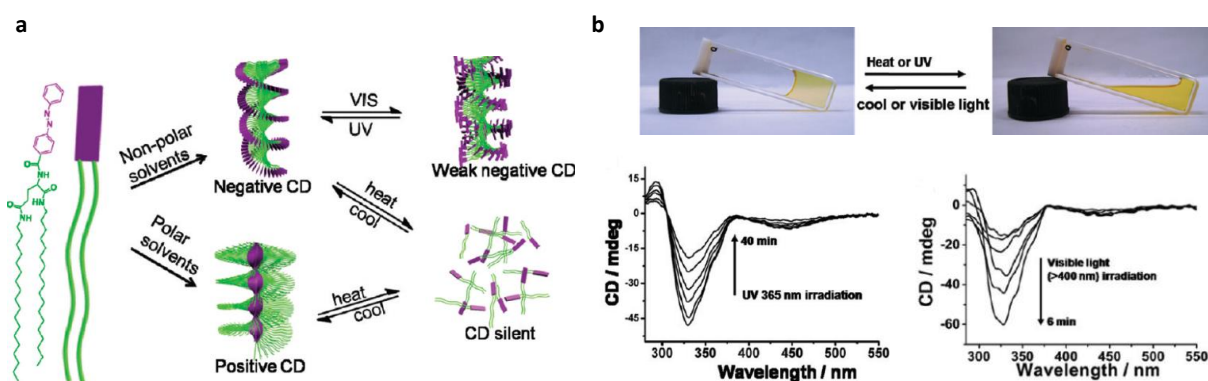


Figure 30 | a) Schematic representation of multi-responsive self-assembly of azo-benzene organogelator; b) Photographs of the reversible photo/thermo sol-gel transition (top), CD spectra during UV (bottom left) and visible light (bottom right) irradiation. (Reproduced from⁶²).

Sonication is a common technique often used to break and homogenize noncovalent interactions among monomers, this can lead to morphological changes and, thus, changes to the supramolecular chirality.

We already mentioned the perylene motif for its excellent self-assembling properties and, in this example, was used by Kawai and coworkers that investigated a system composed by a perylene bisimide moiety which self-assembled in chiral aggregates and whose morphology and chirality were controlled according to the method of preparation. The nanostructures obtained by varying the temperature result in well-ordered and with an excellent chiral amplification properties; on the other hand, samples obtained by ultrasonication, showed a less ordered arrangement within the assembly with an inversion of chirality with respect to the

sample prepared thermally (**Figure 31**). These differences can be explained by the formation of thermodynamically more stable nanostructures upon cooling process compared to the aggregates obtained by the fast ultrasonication process.⁷⁶



Figure 31 | Schematic representation of the structural differences according to the method of preparation that lead to the reversal of supramolecular chirality. (Reproduced from⁷⁶).

1.3.6 Supramolecular chirality in systems containing just achiral molecules

Beyond chirality transfer from chiral molecules, or achiral/chiral mixtures, to supramolecular systems, also achiral molecules can self-organize to form chiral nanostructures by the phenomenon called *spontaneous symmetry breaking*. Although, in most cases, a chiral environment is needed for breaking symmetry, in this paragraph we are interested in those examples where symmetry breaking occurs without chiral conditions or additives.

One of the first groups reporting an example of symmetry breaking was the group of Young, which described the formation of a nematic liquid crystal from a stilbene derivatives. Even though they used racemic stilbene mixtures, they found small cholesteric liquid crystalline regions under polarized light.⁷⁷

Still in the field of liquid crystal, Tschierske and colleagues investigated achiral, banana-shaped, molecules founding, in the liquid-crystalline phase, chiral domains. They further observed an inversion of the chirality depending on the temperature.⁷⁸

In homogeneous solutions, achiral monomers lead to the formation of an equal mixture of left- and right-handed helices, which are globally silent in CD spectroscopy. Nevertheless, cases have been reported where an unequal ratio of opposite helices arise from achiral monomers leading to symmetry breaking and, thus, to the detection of a CD signal. The first paper reporting the formation of chiral aggregates from achiral molecules in solution was published by Dahne and collaborators. They reported a dye molecule with long alkyl chains that

undergoes self-assembly with a preferential chirality. They speculate that the lateral hydrophobic interactions between the alkyl chains are responsible for J aggregation leading to herringbone structure with chiral properties.⁷⁹

Recently, the group of Meijer found that achiral partially fluorinated benzene-1,3,5-tricarboxamide derivatives (**Figure 32a**) could self-assembled in chiral nanostructures through symmetry breaking.⁸⁰ Investigating the supramolecular polymerization by UV and CD spectroscopy they observed a unique behavior. As already described earlier in this chapter, the classical cooperative growth for BTA based system shows two regimes: a first nucleation, followed by an elongation in which an equimolar amount of left- and right-handed helices are formed. Intriguingly, fluorinated benzene-1,3,5-tricarboxamide derivatives showed a further transition where a CD signal start to be detected (**Figure 32b**). Some extra studies indicated that first the system assembles in a racemic mixture of one-dimensional helices driven by hydrogen bonding and then, a secondary nucleation occur, in which, the peripheral hydrogen of the CF₂-H group in the BTA stacks interact with the fluorine of another column leading to hierarchical assemblies(**Figure 32c**). The presence, even in traces, of chiral impurities, is strongly amplified during the secondary nucleation.

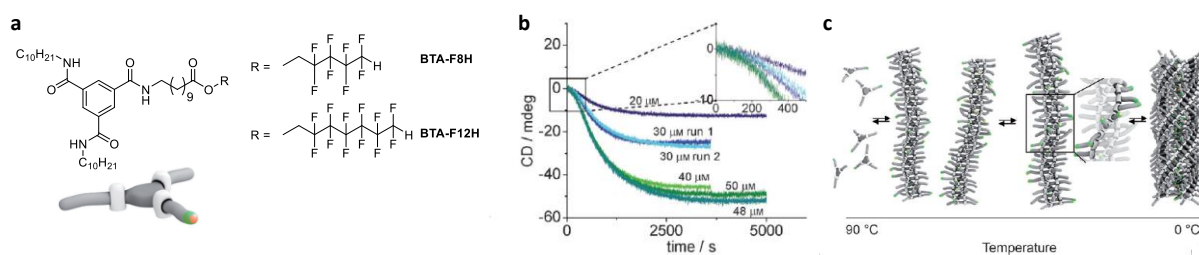


Figure 32 | **a**) Structures of the two partially fluorinated BTA derivatives; **b**) Evolution of the CD signal ($\lambda = 223$ nm) during stopped flow CD spectroscopy upon injection, in MCH (non-solvent), of different solutions of **BTA-F8H** in DCM (solvent); **c**) Schematic representation of the proposed self-assembly process. (Reproduced from⁸⁰).

Emergence of chirality via symmetry breaking has also been observed in gel systems. For instance, Liu and coworkers synthesized a benzene-1,3,5-tricarboxylate with a cinnamate appendix (**Figure 33a**) which shows optimal gelation properties in various organic solvents. Considered the achiral nature of the precursors, no gels exhibited supramolecular chirality except when MCH was employed and symmetry breaking occurred. In that case, the authors observed different chiralities for several samples, indicating a random distribution of the predominant handedness of the assembly in the different batches (**Figure 33b**). Given the

absence of other possible non-covalent interactions between the monomers, they further attributed to the π - π stacking interactions the driving force for the symmetry breaking.⁸¹

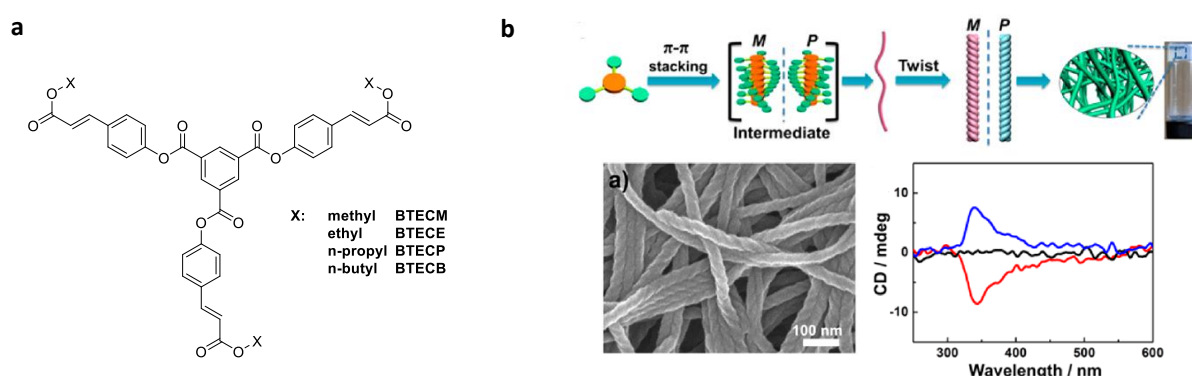


Figure 33 | a) Chemical structures of benzene-1,3,5-tricarboxylate derivatives; **b)** Mechanisms beyond the gel formation in MCH (top), helicoidal bundles of fibers observed by SEM (bottom left); CD spectra of different gels showing a random distribution of Cotton effects. (Reproduced from⁸¹).

B. MOLECULAR AND SUPRAMOLECULAR CHEMISTRY OF TRIARYLAMINE

Triarylamines derivatives constitute a wide family of molecules with an enormous range of applications. They have been widely employed in organic photovoltaic and perovskite solar cells,⁸² in OLEDs as hole conductive⁸³ and electroluminescent materials,^{84,85} in laser printers (Xerox[®] process)⁸⁶ and for two photon absorption and emission.⁸⁷

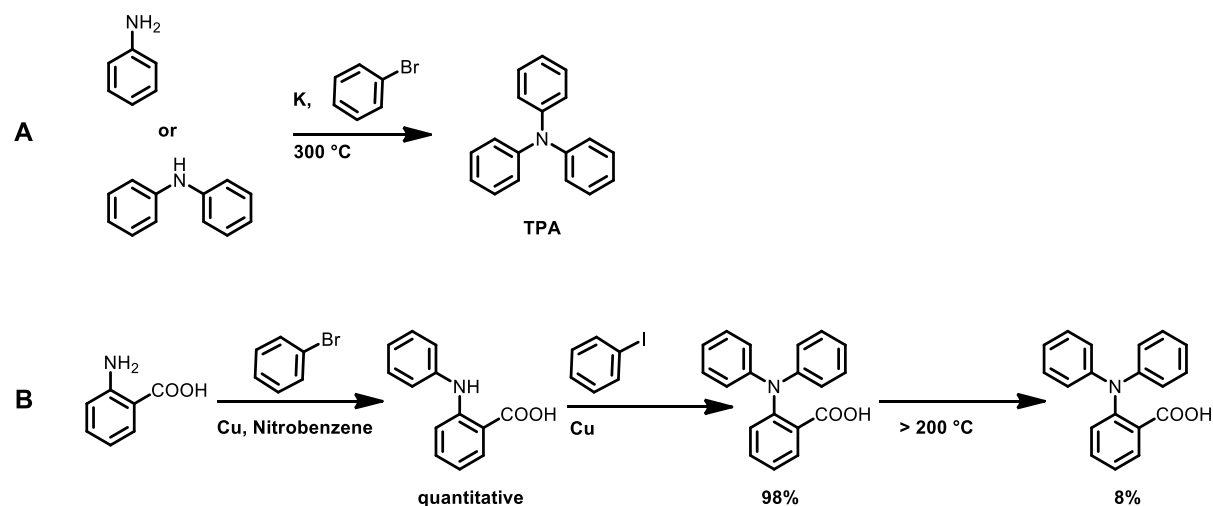
Beside those applications, in the last decade much interest was given to their self-assembly properties, notably for functionalized triarylamines. In this section, we will firstly focus on synthetic strategies for the preparation of triarylamine derivatives, then we will investigate the properties of the triphenylamine core and finally we will have an overview on the self-assembly of amide-functionalized triarylamine which constitute an important domain for the work described in this manuscript.

1.4 SYNTHETIC STRATEGIES TOWARDS TRIARYLAMINE

1.4.1 Historical overview

The first reported synthesis of a triphenylamine (TPA) molecule is dated 1873 when Merz and Weith reacted aniline or diphenylamine with bromobenzene in presence of potassium obtaining a triphenylamine in very low yield (**Scheme 1A**).⁸⁸ In a further attempt, by Goldberg and Nimerovsky in 1907, a triphenylamine was obtained after a three steps synthesis involving subsequent Ullman couplings starting from anthranilic acid (**Scheme 1B**).⁸⁹ This latter

approach promoted more than one century of synthetic efforts in triarylamine synthesis and copper-catalyzed couplings, and still represent one of the main approach to produced complex triarylamine architectures.

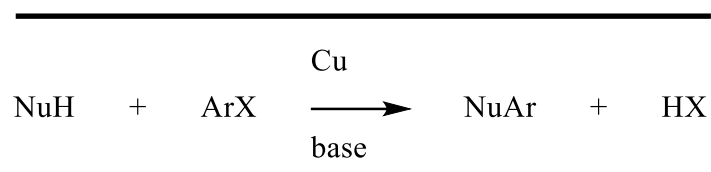


Scheme 1 | A) First synthesis of TPA reported by Merz and Weith; **B)** Multistep synthesis of TPA according to Goldberg and Nimerovski. (Reproduced from⁸⁸).

In the following section, we will present the main synthetic strategies to afford triphenylamine molecules which are commonly used; they can be summarized in three principal families: copper- and palladium-catalyzed coupling, and nucleophilic aromatic substitution. In most of the cases, for preparing a given target molecule, there is not a unique approach that can be successful, but different paths can be undertaken. Thus, in our classification, we will focus on describing the advantages and disadvantages for each methodology. Moreover, according to the substitution of the triarylamine derivative, the presence of specific functional groups, and their stability, can make one methodology to be preferred with respect to another.

1.4.2 Ullmann Coupling and its modification

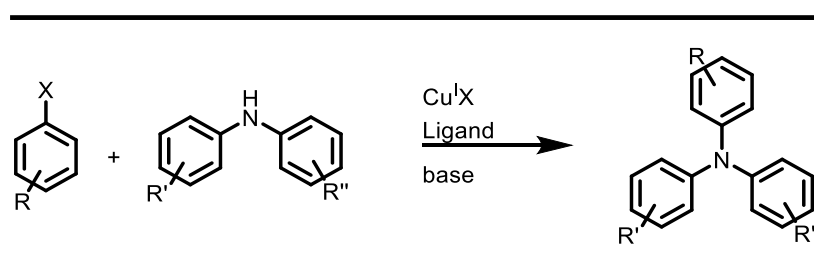
The nucleophilic substitution of an aryl halide mediated by copper represent the oldest, and still very efficient, way to prepare triarylamine derivatives.



Scheme 2 | General scheme for an Ullmann coupling.

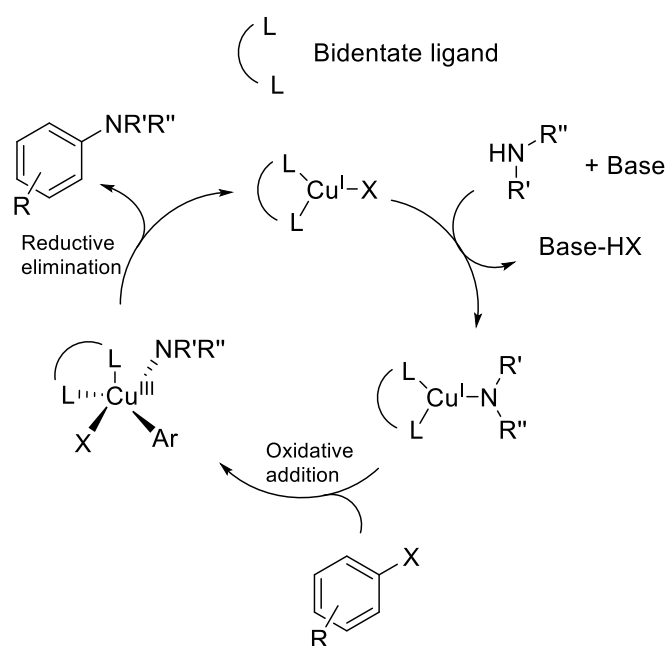
The choice of a phenylamine or a diphenylamine as nucleophile leads to a triphenylamine as product. The first described protocols needed to be carried out in very harsh conditions, by using copper powder in stoichiometric amount at about 200 °C with sodium or potassium carbonate or hydroxide as base. Coupling reactions performed under these conditions were not efficient since low yields were typically obtained as well as many side products during the long-lasting reactions. Over the past decades, many studies addressed to understand the influence of the solvent, the base and the catalyst have been reported with the aim of improving the efficiency of this reaction.

As consequence, recent methodologies, which typically involved the usage of a bidentate ligand, have been developed. The presence of a ligand, which helps solubilizing and stabilizing the catalyst in organic medium, allows to increase the catalyst activity, decrease its amount (< 10%) together with a decrease of the temperature needed to perform the reaction.⁹⁰ This modification goes under the name of *modified Ullmann coupling*.



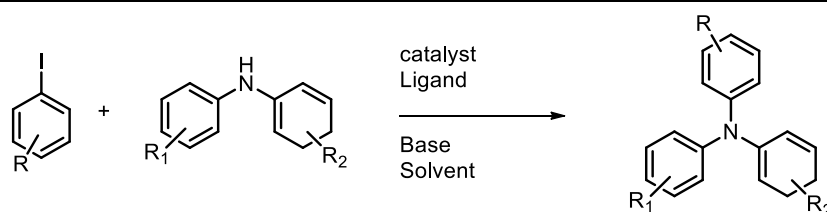
Scheme 3 | Scheme for a general modified Ullmann coupling for triarylamine derivatives synthesis

Despite the wealth of scientific literature on Ullmann couplings, many mechanistic details remains still unknown, several experiments confirm the existence of different steps in the catalytic cycle (**Scheme 4**).⁹¹ The bottle neck of the whole process has been identified to be the release of the halide from the substrate which constitute the rate-determining step, hence the highest reactivity is found to be as follows: I > Br > Cl > F.



Scheme 4 | General mechanism proposed for the modified Ullmann coupling

The difficulties in fully understanding the general mechanism makes the choice of proper conditions quite difficult. Thus, for the optimization of a specific reaction, a screening of different combinations of bases, ligands, solvents, and temperature is needed in order to maximize the yield or the reaction. Nevertheless, the Ullmann coupling have been widely employed for the synthesis of simple triphenylamine and functionalized triarylamines as reported in **Table 1**.

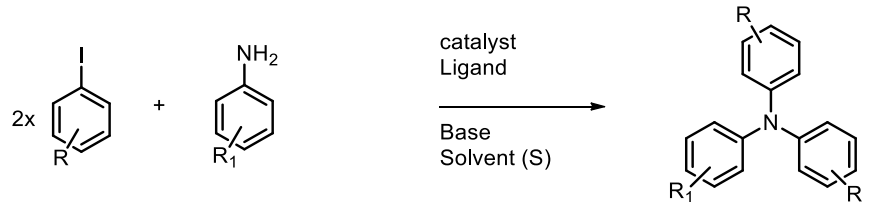


Entry	R	R1	R2	Catalyst	Ligand	Base	S	T (°C)	Time (h)	Yield (%)
1	H	<i>p</i> -Me	<i>p</i> -Me	CuCl	2,20-bipyridine	NaO ^t Bu	Tol	110	5	80
2	<i>p</i> -OMe	H	H	Cu(neocup)(PPh ₃)Br		KO ^t Bu	Tol	110	6	88
3	H	H	H	Cu(neocup)(PPh ₃)Br		KO ^t Bu	Tol	110	6	78
4	<i>p</i> -Cl	H	H	CuCl	8-Hydroxyquinoline	K ₃ PO ₄	DMF	120	24	89
5	<i>o</i> -COOCH ₃	H	H	CuCl	8-Hydroxyquinoline	K ₃ PO ₄	DMF	120	24	49

Table 1 | entry (1)⁹²; (2,3)⁹³; (4,5)⁹⁴

Considering the existence of many procedures for the synthesis of asymmetric diphenylamine ($R_1 \neq R_2$), the approach described above allows to synthesize triarylamine with three different groups on the periphery.

Triarylamine can also be synthesized starting from aniline, by reacting it with two equivalents of iodobenzene (**Table 2**); this one-pot approach, allows the synthesis of triarylamine derivatives bearing two identical groups. Noteworthy, the presence of bromo substituents on one of the reagents (entry 4), does not affect the reaction since the higher reactivity of the iodine allows a good chemoselectivity. Hence, the possibility of synthesizing triarylamine with bromo substituents is of utmost interest since it enables further modification taking advantages from the chemistry of palladium-catalyzed coupling.



Entry	R	R1	Catalyst	Ligand	Base	S	T (°C)	Time (h)	Yield (%)
1	H	H	CuCl	8-Hydroxyquinoline	K ₃ PO ₄	DMF	120	24	68
2	<i>p</i> -Cl	H	CuCl	8-Hydroxyquinoline	K ₃ PO ₄	DMF	120	24	76
3	<i>p</i> -Cl	<i>p</i> -OCH ₃	CuCl	8-Hydroxyquinoline	K ₃ PO ₄	DMF	120	24	79
4	<i>p</i> -Me	<i>p</i> -Br	CuCl	1,10-phenanthroline	KOH	Tol	125	5	85
5	<i>p</i> -Me	<i>p</i> -Me	Cu(I)-DAB complex		KO ^t Bu	Tol	90	8	87

Table 2 | Entry 1,2,3⁹⁴; 4⁹⁵ 5⁹⁶

In conclusion, copper catalyzed coupling represents a suitable way to synthesize triarylamine derivatives. Although it presents several drawbacks like: lower yields if compared with other metal-catalyzed couplings, mechanistic details still unclear and the virtual impossibility to predict the outcome of the reaction, poor substrate scope, *etc.* Conversely, it also presents many advantages like: lower price for the catalysts and the ligands employed as compared to the reagents used in other couplings and lower sensitivity to air and humidity.⁹⁷

1.4.3 Palladium-catalyzed couplings

The drawbacks of copper catalyzed couplings outlined in the previous paragraph and the need for a more efficient strategy for triarylamine synthesis, pushed scientists to find alternative

ways to the modified Ullmann coupling, which could allow higher yields, milder reaction conditions and higher reactivity towards other halides as well as aryl-iodide.

In two early reports, the group of Buchwald⁹⁸ and Hartwig⁹⁹ reported the aryl amination of aryl bromides and iodides catalyzed by palladium complexes with ligands like: P(*o*-tolyl)₃, BINAP, and DPPF. This methodology goes under the name of *Buchwald-Hartwig coupling* and, despite it allowing the synthesis, in good yields, of diarylamines derivatives, the first extensive report on palladium-catalyzed triarylamines synthesis was published by the group of Yamamoto in 1998.¹⁰⁰ The authors employed a mixture of Palladium diacetate, Pd(OAc)₂, with a sterically bulky trialkyl phosphine like P(^tBu)₃ to react aryl halides (I, Br, Cl) with diarylamines in the presence of NaO^tBu to obtain triarylamines in excellent yield (**Table 3**).

		Product	Yield (%)
Arylbromide	Diarylamine		
			99
			80
			77
			92
			92

Table 3 | Reproduced from¹⁰⁰

Using this methodology, the authors were able to synthesize simple triaryl amines but also more complex structures, like dendrimers, which are fundamental hole-transport materials. Noteworthy, they revealed the importance of using a bulky and basic ligand like $P(tBu)_3$ to be able to access triaryl amines.

A further development in palladium-catalyzed triarylamine synthesis was brought by Hartwig and his collaborators. They observe an increase in reaction rates by using $Pd(dba)_2$ instead of

$\text{Pd}(\text{OAc})_2$ which allows some difficult couplings between aryl amine and aryl bromide to occur even at room temperature (**Table 4**).¹⁰¹

Entry	X	R	R1	R2	T (°C)	Time (h)	Yield (%)
1	Br	H	H	H	r.t	1	91
2	Br	<i>o</i> -Me	H	H	r.t	4	97
3	Br	<i>p</i> -CN	H	H	r.t	1	97
4	Br	<i>p</i> -OMe	<i>p</i> -OMe	<i>p</i> -OMe	r.t	1	94
5	Br	<i>p</i> -Br	H	H	r.t	1	85
6	Cl	<i>p</i> -OMe	H	H	70	16	97
7	Cl	<i>p</i> -CN	H	H	rt	5.5	89

Table 4 | Adapted from ¹⁰¹

The authors observed very fast reactions, at room temperature, when coupling an aryl bromide with a diphenylamine (e.g. entries 1 - 4) with high yields obtained, in some cases, within 15 minutes. Upon reacting the *para*-dibromo benzene with two equivalents of diphenylamine (entry 5) both the bromine functionalities were substituted allowing the synthesis of a triarylamine dimer. The less reactive aryl chloride was successfully coupled at 70 °C with longer reaction times as compared to the bromo analogous (entry 6) but, activated aryl chlorides, reacted also at room temperature (entry 7).

Despite most of the coupling reactions between aryl halide and diphenylamine showing faster rates when NaOtBu is used as base in stoichiometric amounts, many functional groups, like esters, nitro group, enolizable hydrogens, N-H and O-H protic groups, show a low tolerance to this strong alkoxide. To overcome this issue, the use of a weaker base like: Cs_2CO_3 , K_3PO_4 , K_2CO_3 or the sterically hindered lithium bis(trimethylsilyl)amide can extend the scope of substrates.^{102,103}

Taking advantage from the different reactivity between aryl bromides and aryl chlorides, Buchwald and coworkers, developed a one pot strategy to synthesize unsymmetrical triaryl amines as follows: a simple aniline is mixed in 1:1:1 ratio with an aryl bromide and an aryl chloride; upon addition of palladium catalyst, a diarylamine is formed in situ and

subsequently reacted with the co-present aryl chloride to generate the corresponding triarylamine (**Table 5**).¹⁰⁴

Entry	R	R1	R2	Yield (%)
1	<i>p</i> -OMe	<i>o</i> -OMe	<i>m</i> -OMe	74
2	<i>m</i> -Me	<i>p</i> -OMe	<i>p</i> -NMe ₂	91
3	<i>p</i> -Me	<i>o,p</i> -2Me	<i>m,m</i> -2Me	84
4	<i>p</i> -Me	<i>p-n</i> Bu	<i>p</i> -OMe	85

Table 5 | Adapted from¹⁰⁴

1.4.4 Aromatic nucleophilic substitution

Copper and Palladium catalyzed couplings represent an excellent way to synthesize triarylamine; the high yields, the good tolerance to different substituents and the possibility to use mild conditions, make of these reactions the first choice for triphenylamine synthesis. Despite all these advantages, metal-catalyzed couplings are limited in their applications by the price of catalyst and ligands, and by the often strict reaction conditions required.

An alternative, metal-free, strategy to prepare triarylamine is the aromatic nucleophilic substitution. A fluorobenzene substituted, in the *para* position, with an electron withdrawing group like nitro or cyano, can be reacted with an aniline or a diphenyl aniline to afford triarylamine in good yields (**Table 6**).

In this section, we present several strategies that have been successfully employed to prepare triarylamine synthons; most of the structures are accessible in different ways, each presenting advantages and drawbacks. The possibility of preparing substituted triarylamine, in few steps, provides a convenient way to use them as starting materials to synthesize more complex structures. Dimers, trimers and dendrimers of triarylamine are well-known materials in optoelectronic devices and, despite their complex architectures, aromatic nucleophilic substitution, allows for their synthesis with high yields.

Most of the molecules that will be presented in this work are based on the triarylamine core, hence, they have been prepared according to protocols that can be ascribed to one of the three

main methodologies described above. Moreover, the previous experience in our group, during years of research on triarylamine molecules, allowed us to further optimize those conditions.

Entry	Arylamine	Product	Base	Solvent	Temp (°C)	Time (h)	Yield (%)
1			NaH	DMAc	100	1	92
2			K ₂ CO ₃	DMSO	145	12	64
3			NaH	DMAc	100	3	92
4			NaH	DMAc	100	3	54
5			K ₂ CO ₃	DMSO	90	72	94

Table 6 | Entry 1¹⁰⁵, 2¹⁰⁶, 3,4¹⁰⁷, 5¹⁰⁸

1.5 STRUCTURE AND PROPERTIES OF TRIARYLAMINES

1.5.1 Structure of the triarylamine core

The molecular structure of the triphenylamine core has been the object of a long controversy since Branch and Calvin proposed a flat conformation for this molecule.^{109,110} This hypothesis was strongly contraposed to the general knowledge on trialkyl-substituted amines which

normally possess a tetrahedral C_3 -symmetry, like triethylamine. Surprisingly, according to crystallographic data, the CNC angle was found to be 119.6° , very close to the 120° typical of a sp^2 hybridization (**Figure 34a,b**).¹¹¹ According to this finding, the lone pair of the nitrogen occupies the nitrogen p orbital favoring the p- π intramolecular interactions. Furthermore, *ab initio* HF calculations, revealed that the lone pair is 59% localized on the central nitrogen and, the reminding electronic density is to be located on the benzene rings.¹¹²

The dihedral angle between the plane containing the central NCCC atoms and those formed by the aromatic rings was found to be comprised between 37.0° and 50.5° with a mean of 44° , depicting a propeller shape conformation for the molecule in crystalline state (**Figure 34c**).¹¹¹ Gas-phase electron diffraction, FTIR analysis of triarylamine in gas phase, and the subsequently comparison with DFT calculations, confirmed the similar geometry of the free molecule with that obtained from crystallographic data.^{113,114}

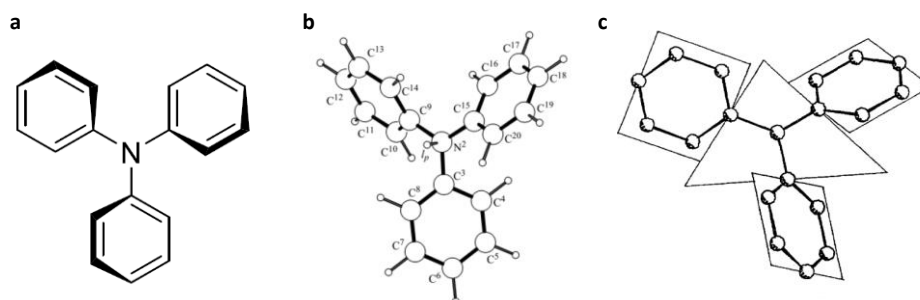


Figure 34 | **a)** Chemical structure of TPA; **b)** Conformation of triphenylamine and atom numbering scheme; **c)** Representation of the dihedral angle between the central CNN and the aromatic rings planes. (Reproduced from^{112,113}).

1.5.2 Redox and optical properties of triarylamines

The first extensive investigation on the redox and optical properties of triarylamine molecules was reported by the group of Lambert.¹¹⁵ They investigated, by cyclic voltammetry and UV-vis spectroscopy, a group of 10 triarylamines bearing different substituents (Cl, OMe, Me) (**Table 7**).

	R ₁	R ₂	R ₃	E _{1/2} , mV DCM	λ _{max} , nm (neutral TAA) MeCN (DCM)	λ _{max} , nm (radical TAA) MeCN
1	OMe	OMe	OMe	109	296 (300)	718; 633
2	Me	Me	Me	332	299 (303)	667; 576
3	Me	OMe	OMe	180	296 (300)	725; 590
4	Me	Cl	Cl	576	301 (304)	681; 573
5	OMe	Me	Me	250	297 (301)	706; 575
6	OMe	Cl	Cl	463	300 (302)	717; 578
7	Cl	Me	Me	460	299 (302)	677; 569
8	Cl	OMe	OMe	290	294 (300)	748; 590
9	Cl	Cl	Cl	691	304 (307)	684; 590
10	Cl	OMe	Me	359	296 (300)	715; 578

Table 7 | Structures of the ten triarylamine molecules investigated and its corresponding oxidation potentials; maxima of UV-vis absorption, for both neutral and radical TAA, in different solvents. (Adapted from¹¹⁵).

The cyclic voltammetry for compound **1** and **10** (**Figure 35**) show a first, reversible, oxidation peak for both the molecules and, in addition, molecule **1**, shows a second oxidation wave at higher potential. Interestingly, this second oxidation step, was only observed in the case of tri-4-anisyl-amine. The presence of substituents on the aromatic rings, affect the redox potential of the triarylamine derivatives in the following way: chloro- substituents move the redox potential to higher values as compared to the methyl substituted triarylaminines, while the methoxy group decreases it.

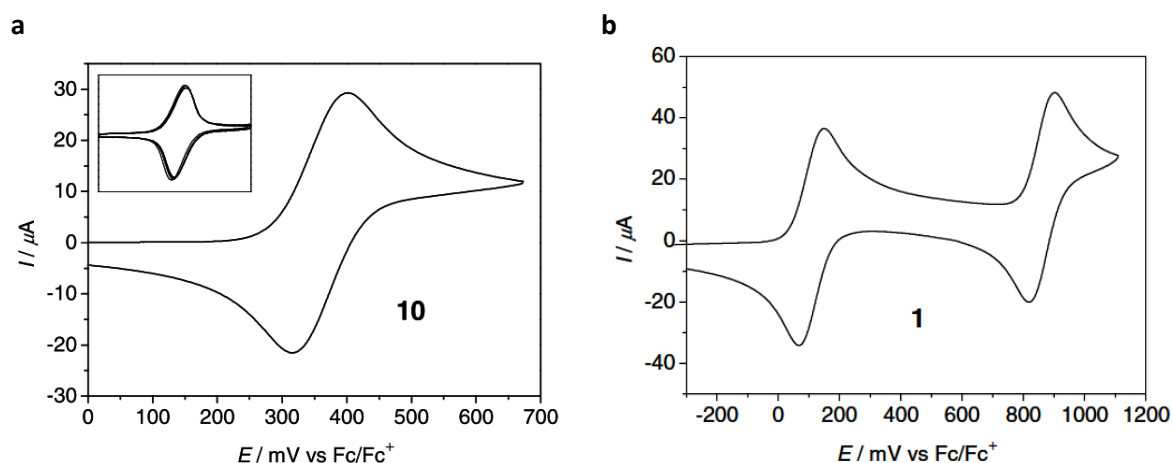


Figure 35 | Cyclic voltammograms of **10** (a) and **1** (b) in DCM. (Reproduced from¹¹⁵).

The UV-vis spectra for neutral **1** and **9** in dichloromethane show an intense absorption around 300 nm ($33\,000 - 34\,000\text{ cm}^{-1}$). Changing substituent from methyl- to methoxy- leads to a bathochromic shift, while for chloro- substituents, a hypsochromic shift is observed. Spectra, recorded in polar solvents, like acetonitrile, show broader absorption bands which are slightly blue shifted indicating a minor CT character of the electronic transition.

The origin of the absorption for symmetric neutral TAA, can be ascribed to the $\pi\text{-}\pi^*$ transition with an electron being promoted from the HOMO to the LUMO ($S_0 \rightarrow S_1$) and the excitation into a degenerate (E) S_1 state. For asymmetric derivatives, in which the C_3 -symmetry is broken, the degenerate state is split into two states, leading to a second transition HOMO \rightarrow LUMO + 1 corresponding to ($S_0 \rightarrow S_2$) excitation.

The triarylamine radical cation $\text{TAA}^{+\bullet}$ shows three characteristic absorption bands: a first and intense one comprised between 670 – 730 nm ($13\,000 - 14\,990\text{ cm}^{-1}$), a broad and less intense band around 570 – 630 nm ($15\,300 - 17\,570\text{ cm}^{-1}$), and a high energy one near 350 nm ($28\,570\text{ cm}^{-1}$).

$\text{TAA}^{+\bullet}$ having a C_3 axis should show only one transition from the double degenerate HOMO to the SOMO ($D_0 \rightarrow D_1$) with the excitation to a degenerate D_1 (E) state. Despite this, both symmetric and asymmetric molecules show two absorption maxima; this can be explained by the absence of the C_3 axis for the asymmetric ones, and the symmetry breaking caused by the interaction with the solvent for symmetric molecules. This leads to the splitting of the degenerate HOMO in two levels, hence, a double transition HOMO \rightarrow SOMO and HOMO-1 \rightarrow SOMO is possible corresponding to $D_0 \rightarrow D_1$ and $D_0 \rightarrow D_2$ transitions respectively

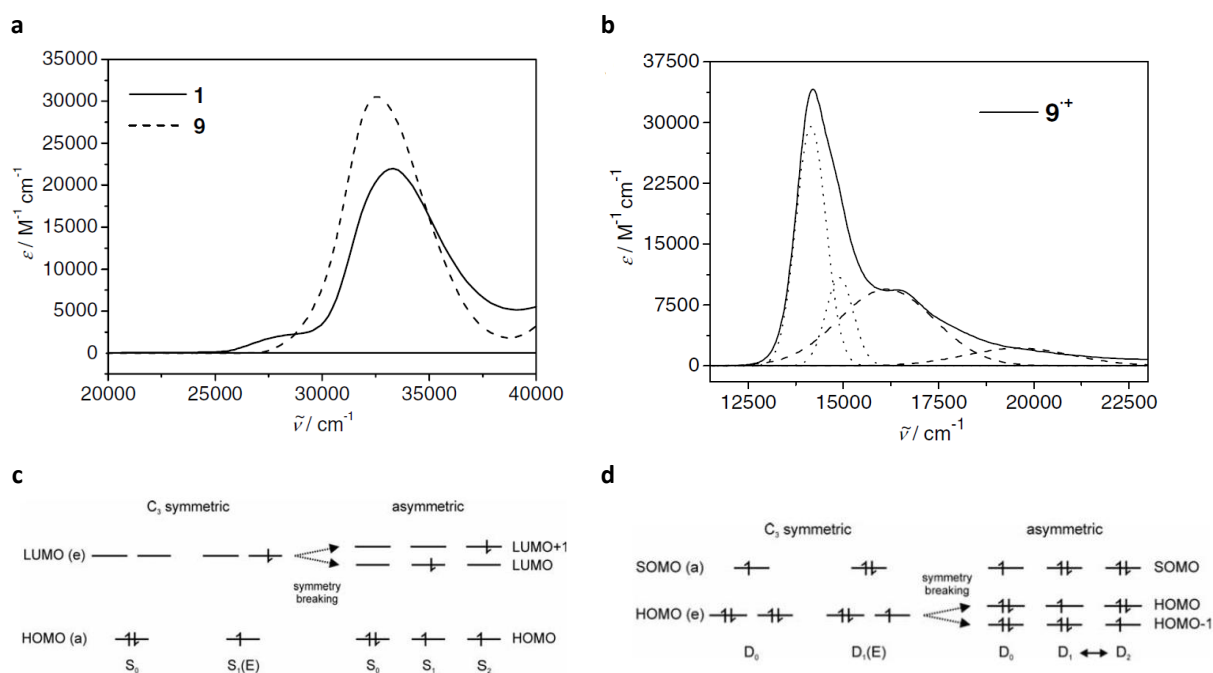


Figure 36 | **a)** UV-vis spectra of **1** and **9** in DCM; **b)** UV-vis spectrum of TAA radical cation of **1** and **9** in DCM with the deconvolution ($D_0 \rightarrow D_1$ dotted lines, $D_0 \rightarrow D_2$ dashed lines); **c)** Configuration diagram for the ground state and excited state of a neutral symmetric TAA and the ground state and excited states of an asymmetric TAA. **d)** Configuration diagram for the ground state and excited state of a symmetric TAA⁺ radical cation and the ground state and excited states of an asymmetric TAA⁺ radical cation. (Reproduced from¹¹⁵).

The group of Audebert investigated the fluorescence of different triarylamine derivatives containing various substituent on para position such as: halides, cyano, methoxy, carbonyl, aryl (**Table 8**).¹¹⁶ The photophysical properties were investigated for both the neutral molecule and the radical cation; the latter was obtained upon electrochemical or chemical oxidation.

All triarylamines in neutral state show fluorescence under UV irradiation with maximum of the emission band comprised between 300 and 550 nm according to the different substitutions. (**Figure 37a**). The quantum yields, using quinine sulfate in sulfuric acid as reference, are near 0.05, with the exception of compound **f** which show a higher quantum yield at 0.37 due to the increase in conjugation length with the introduction of phenyl rings as substituents. By increasing the electron withdrawing nature of the substituents, the intramolecular charge transfer between the nitrogen and the EWG group is reduced leading to a blue shift of the absorption and emission bands (e.g. going from compound **a** to compound **c**)

	R_1	R_2	λ_{abs}	λ_{em}	Φ
a	Br	CHO	353	531	0.06
b	I	CHO	355	532	0.04
c	Br	CN	311	447	0.09
d	OMe	OMe	283	384	0.06
e	Me	OMe	301	382	0.03
f	<i>p</i> -MeOPh	<i>p</i> -MeOPh	357	418	0.37

Table 8 | Structure of the triarylamine investigated; maxima of the UV-vis absorption and emission and quantum yields (Adapted from¹¹⁶).

Opposite to the neutral TAAs, upon oxidation, triarylamine radicals show essentially no fluorescence. Compound **d**, **e**, and **f** were oxidized by titration, in acetonitrile, with $\text{Cu}(\text{ClO}_4)_2$, a mild one-electron oxidant, which is silent, at low concentrations, in UV-vis and fluorescent spectroscopy.

During the titration of **f**, the UV-vis spectrum, show the gradual appearance of the radical cation, identified through the increasing bands at 450 and 980 nm, together with the decreasing of the band at 357 nm consistent with the consumption of the neutral species. The presence of two isosbestic points (307 and 374 nm) proves the existence of an equilibrium between the neutral and the oxidized molecule (**Figure 37b**).

On the other hand, the fluorescence shows a gradual quenching as soon as the amount of oxidant is increased, reaching a plateau for 1.05 equivalent of $\text{Cu}(\text{ClO}_4)_2$ added (**Figure 37c**).

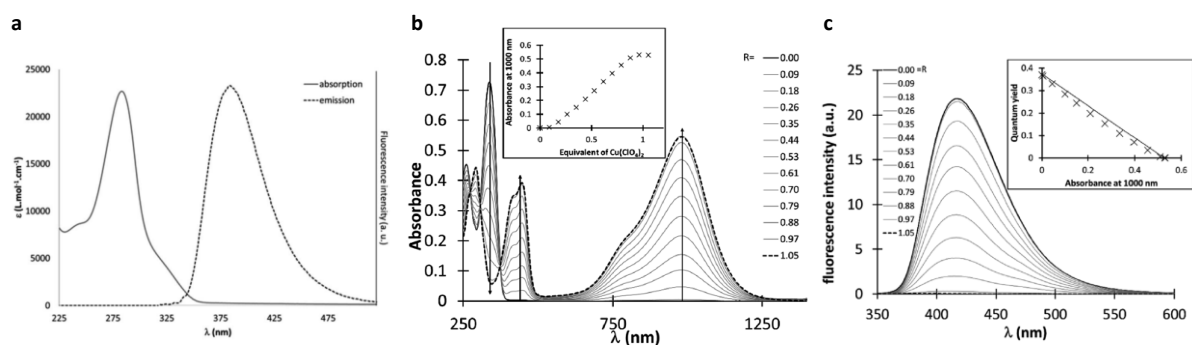


Figure 37 | **a**) Comparison of absorption (solid line) and emission (dashed line) spectra for compound **d** $\lambda_{\text{ex}} = 309 \text{ nm}$; **b**) Evolution of UV-vis spectrum during titration of **f** with $\text{Cu}(\text{ClO}_4)_2$; **c**) Evolution of emission spectrum upon titration, $\lambda_{\text{exc}} = 307 \text{ nm}$. (Reproduced from¹¹⁶)

The eventual reversibility of the process was investigated for compound **a**, **b** and **c** using spectroelectrochemistry. For compound **c**, by increasing the potential applied to the cell, the absorption of the neutral specie at 310 nm slowly disappears and is replaced by the absorption of the $\text{TAA}^{+\cdot}$ radical cation with peaks at 370 and 710 nm (**Figure 38a**). Further reduction of the system demonstrates that the process is reversible, showing the gradual quenching of the bands ascribe to the radical and the recovery of the original signal (**Figure 38b**).

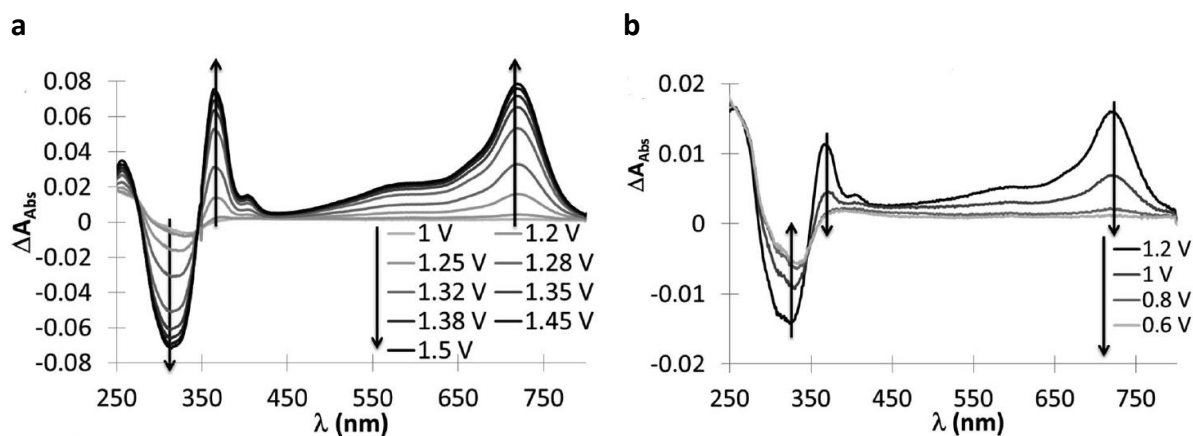
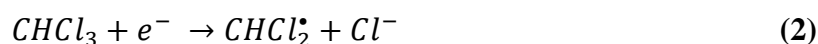


Figure 38 | Evolution of UV-vis spectrum, upon electrochemical oxidation, of **c** for both oxidation (**a**) and reduction (**b**) process, the open circuit spectrum is used as the background and subtracted from all the other subsequent spectra.

1.5.3 Oxidation of aromatic amines in chlorinated solvents

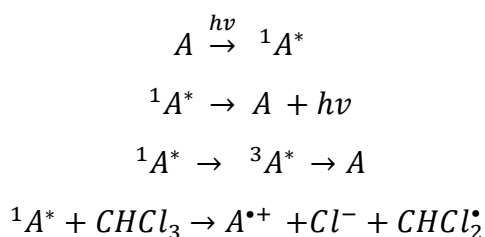
In the previous section, the oxidation of triarylamines to their respective triarylammonium cations, can be carried out in an electrochemical cell or by means of chemical oxidation with a selected oxidant (e.g. Cu^{II}). Beyond these possibilities, over the past sixty years, the oxidation of aromatic amines has been pursued also *via* photooxidation.^{117,118} In an early study, Meyer, investigated the photooxidation of N,N,N',N'-tetramethyl-*p*-phenylenediamine (TMPD) in liquid solution, and, aiming at understanding the role of the solvent in the process, a screen of several solvents was done. He concluded that photooxidation only happens in halogenated solvents and without correlation with the dielectric constants.¹¹⁸

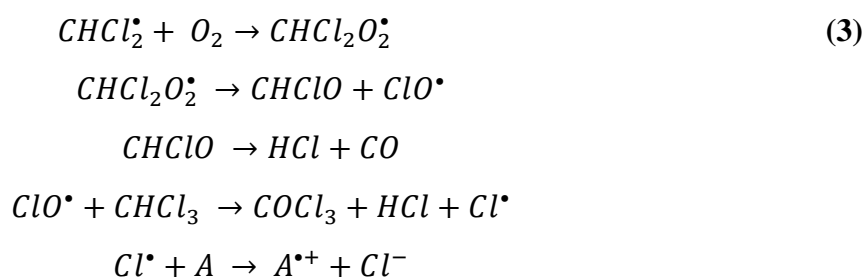
A more complete understanding on how the phenomenon works came from the group of Richtol that investigated the oxidation of a series of aromatic amines in chloroform or carbon tetrachloride. Interestingly, they observed, that the photooxidation occurs using a UV light with lower energy (3.5 eV) than the ionization potentials of the target amines (~ 6 eV). This led to the consideration that another process should supply the remaining energy. Further experiments proved that the dissociative electron attachment reaction (2), which occurs with halogenated solvents, provides the required energy. In particular, for chloroform, this contribution is exothermic by 16 kcal/mol.



The authors observed a contribution of the oxygen dissolved in solution on the oxidation quantum yield: the latter increases about two times for air-saturated systems as compared to the degassed ones. This suggests that oxygen plays an important role in the photooxidation process. They further found that oxidation occurs even in a mixture ethanol/chloroform, with a correlation between the oxidation quantum yield and the amount of chloroform in the mixture. The analysis of the byproducts, produced during the photooxidation, revealed that for each mole of amine oxidized, 1 mol of H^+ is produced; moreover, phosgene and chloride ions were identified as side products.

According to these findings, the authors, proposed the following mechanism for the photooxidation of aromatic amines (A):





1.5.4 Charge transfer in systems involving triarylaminines

Electron (ET) or charge (CT) transfer is a phenomenon that can occur, among other systems, in organic mixed valence (MV) compounds. Such systems are characterized by the presence of two or more redox centers which can act, respectively, as electron donors and acceptors. This allows the electron, or hole, to be transferred from one site to the other through a saturated or unsaturated bridge. When CT is possible for a given molecule, it leads to the observations of the so-called intervalence charge transfer band (IV-CT) in the NIR part of the absorption spectrum.^{119,120,121} Most of our understanding on CT mechanism comes from the theory of Marcus-Hush for the analysis of the IV-CT band.^{122,123} The interpretation of the IV-CT band aims to evaluate the electronic coupling V which is a measure of the strength of the interaction between the two redox centers. According to this, organic mixed valence molecules, can be ascribed to three different classes: redox centers which are completely localized and non-interacting with each other belong to class I; redox centers which are partially coupled and partially localized belong to class II; redox centers which are strongly coupled and possess a completely delocalized nature belong to class III. While the Marcus-Hush theory allows to determine the V value and, thus, the class of a MV system, the nature of the electronic coupling between the redox centers can also be estimated by a qualitative analysis: provided there is interaction between the donor and the acceptor, and increase in interaction is accompanied by a decrease in the symmetry of the IV-CT band. Hence, molecules belonging to class II with small electronic coupling exhibit a Gaussian shape for the characteristic band, while compounds in which the charge is fully delocalized, show an asymmetric band.¹²⁰ Another consequence of the Marcus-Hush theory is that the IV-CT band of class II molecules is strongly affected from the polarity of the solvent while class III compounds show a IV-CT which is completely solvent-independent.¹²⁴

The group of Lambert investigated the CT in a series of triarylamine derivatives containing two redox centers connected by different bridges. Upon chemical oxidation, they obtained the radical mono-cations and, thus, the organic mixed valence compounds, in which, the two

identical redox centers, have different oxidation states. The analysis of this species, by UV-Vis-NIR spectroscopy, revealed, for molecules **b**^{•+} and **c**^{•+}, a broad and symmetric IV-CT band which is consistently blue shifting absorption upon changing solvents from DCM to ACN; this permits to assign both compounds to a class II system. On the other hand, compound **a**^{•+} shows an asymmetric absorption, which is slightly influenced by the solvent, and, which is consistent with a class III system (**Figure 39**).

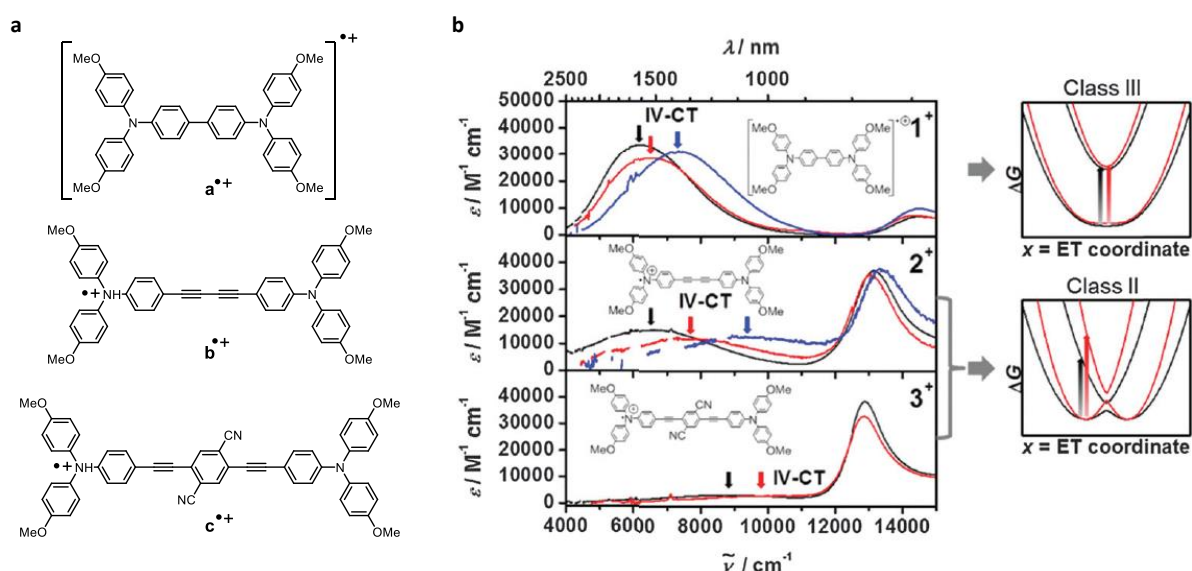


Figure 39 | **a**) Chemical structures of the three MV compounds containing two triarylamine moieties linked by three different bridges; **b**) Vis-NIR absorption spectra of the three compounds in different solvents: black (DCM), red (PhNO₂), and blue (ACN), the arrows indicates the maximum of the IV-CT band. The diagrams on the right-hand side represent the Gibbs potential energy surface for low (black) and high (red) reorganization energy for a Class III situation (top) and a Class II situation (bottom). IV-CT absorptions are indicated by black and red arrows. (Reproduced from ¹¹⁹).

1.6 TRIARYLAMINE SELF-ASSEMBLY

1.6.1 Light-induced supramolecular polymerization of triarylamines

Although the several studies have addressed the properties of triarylamines, few of them have aimed at using this motif to form self-assembled structures.^{125,126}

Our group was the first to describe the self-assembly of *simple* triarylamines on a system composed by a triarylamine core functionalized with an amide group and two alkyloxy chains.^{127,128} We found that this specific substitution pattern is crucial in driving the self-organization. The first indication came from the observation that a solution of **A** (**Figure 40a**) in deuterated chloroform shows a flattening of the aromatic and amidic NMR signals after exposure to visible light, which is accompanied by a change in the color of the solution which towards green. Interestingly, the signals could be recovered after heating the solution overnight

at 60 °C. We found that this phenomenon occurs only in chlorinated solvents (CDCl_3 , DCM-d_2 , TCE-d_4) since no flattening was observed in other deuterated solvents. No degradation of the product was observed after several cycles of light exposure – heating, and the two NMRs remains unchanged even after one week in the dark, underlining the stability of both states.

UV-vis and EPR analysis show the formation of a radical cation typical for triarylamine molecules and we further determined, after 1 h of visible light irradiation (20 W), that 11% of the total number of molecules could be oxidized. Following exposure to visible light, we observed a great stability of those radicals, as detected by EPR, even after one week in the dark at room temperature (**Figure 40d**). This made us guess that a particular mechanism was enhancing the radical stability in solution. Thanks to a combination of HRMAS, DLS and AFM, we demonstrated the formation of self-assembled structures following the photooxidation (**Figure 40c**). Hence, the flattening observed in the NMR spectra was due to a combination of the paramagnetic effect of the radical species and to the formation of dense assemblies. The radicals were strongly stabilized within the self-assembled structures and heating was needed to break the assemblies and allow the solvent to quench the remaining radicals.

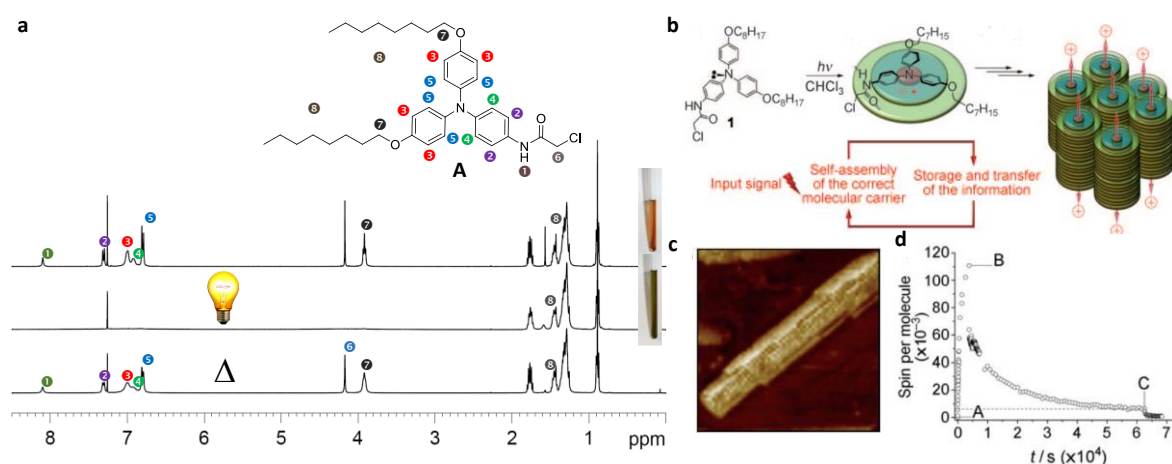


Figure 40 | **a**) Structure of triarylamine **A** with corresponding NMR spectra before and after light irradiation, bottom: NMR spectrum after one night at 60 °C; **b**) Schematic representation of the light-induced self-assembly process; **c**) High resolution AFM image of a single supramolecular fiber; **d**) EPR signal evolution for a TAA solution during light irradiation (A-B), after light irradiation in the dark (B-C) and after heating at 60 °C for 2h (C). (Reproduced from¹²⁷).

Further experiments and simulations were addressed to fully disclose the mechanism leading to the formation of nanostructures upon photooxidation since no self-assembly was detected in absence of light irradiation.¹²⁹ The inner molecular organization of the nanowires was resolved

owing to a combination of high-resolution AFM, X-ray diffraction measurements and DFT and molecular mechanics calculations showing a bicolumnar “snowflakes” stacks of triarylamine (**Figure 4II**). The mechanism proposed, supported by EPR, NMR, UV-vis kinetics and simulations, sees an early step in which triarylaminines are photooxidized to the triarylamonium radical cation following a mechanism similar to the one already described for aromatic amines. As consequence of the oxidation, we observed a flattening of the TAA core with a reduction of the dihedral angle of the aromatic rings. This situation is advantageous towards the stacking of several radicals. The TAA^{•+} produced at that stage, can form a stable CT complex with the Cl⁻ present as side product of the amine oxidation (**Figure 4IIb**). Several of these complexes, attracted by electrostatic forces between the dipoles, can assemble in two arrangements according to the position of the chloride in respect to the triarylamine: a loose chain when the chloride is in between two triarylaminines, and a tight chain with the chloride in the off-axis position (**Figure 4IIc-h**). In an early stage, the CT complexes self-organizes in a loose conformation, but as soon as, the chain reaches a certain length, the chloride moves to yield the tight conformation which allows a better π - π stacking and, thus, more stable. In a second step, the stacking of CT complexes reaches a critical length and two columns assemble and are stabilized by lateral interactions (Hydrogen bonding) (**Figure 4IIi**). At this point, neutral triarylaminines are attracted as well, and continue the growth on the nanostructures from both sides of the stack (**Figure 4IIj**) until, above a certain length, the main chain breaks, and more tips are generated. At that point the mechanism became auto-catalytic.

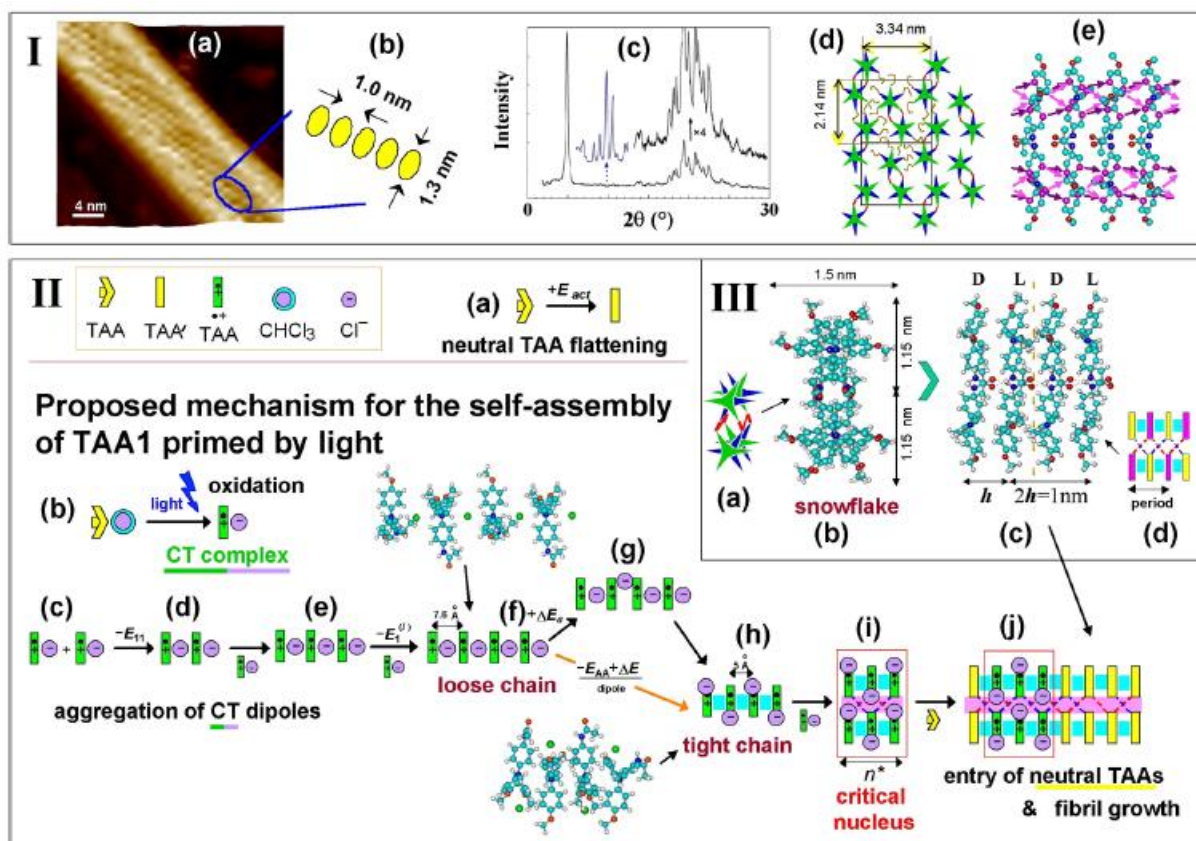


Figure 41 | I (a, b) AFM image of maize-like structures formed in 1 mM solution of TAA (A) in chloroform; (c) The original XRD pattern (bottom, black) accompanied by its magnification in the WAXS range (top, black) and in the SAXS range (top, blue); (d) The proposed internal molecular organization of TAA fibrils (in the plane normal to the c-axis) based on the XRD; (e) The simulated all-atomic structure of snowflake double column; **II** Light-induced aggregation kinetics in TAA solutions; (a) Highly improbable spontaneous flattening of isolated neutral TAA molecule; (b) Photooxidation of neutral TAA molecule to TAA^{•+} radical and Cl⁻ anion; (c,d) Two CT complexes attract each other head-to-tail; (e,f) the stack of radicals grows; (f,g,h) Transition from loose chain to tight chain; (i) Two columns assemble together stabilized via hydrogen bonding; (j) Neutral TAA are attracted at the tips of the assembly, fibril growth; **III** Arrangement of molecules in bicolumnar “snowflake” stacks of neutral TAA: (a) Representation of alternating molecular orientation in the columns. (b) The top view (along the main axis), and (c) the side view of the structure; (d) Highlight of the hydrogen bonding connecting the columns. (Reproduced from¹²⁹).

1.6.2 Supramolecular polymerization of triarylamine trisamides (TATA)

We further extended our interest to triarylamine bearing three amidic chains on the aromatic rings. Increasing the number of hydrogen bonding that each molecule can establish may increase their tendency to self-assemble. We investigated three triarylamine trisamides with different alkyl chains (**Figure 42a**).¹³⁰ Similar to the case of the triarylamine bearing one amide group, we found that it is possible to trigger self-assembly by white light irradiation of a solution in a mixture toluene / methanol (5:3) with a 5% of chloroform. The broadening of the

aromatic signals was then observed as consequence of the formation of radicals and self-assembly (**Figure 42a**). By expanding the range of solvents employed, we demonstrated that self-assembly was possible, in pure solvents, without light irradiation. FTIR spectroscopy confirmed the primary role of hydrogen bonding in driving the self-assembly. At a macroscopic level, and for concentration above a certain value, organogels were formed. The direct observation of the nanostructures by freeze fracture transmission electron microscopy (FFTEM) for the gel state, and AFM for dropcasted films from dilute solution, revealed the formation of long fibers with high persistence lengths (**Figure 42b**). The single fiber, obtained from self-assembly of TATA **1**, shows a diameter of about 16 Å with a twisted pattern. More structural details were obtained by X-ray scattering (SAXS, WAXS) including: a period of 29.1 Å for the helices, a distance of 4.85 Å between the central nitrogen atoms and of 3.2 Å between aromatic rings. Moreover, the dihedral angle between two stacked molecules was about 20° (**Figure 42c**).

Intriguingly, upon light irradiation of preformed fibers in chloroform, the UV-vis spectrum shows the appearance of an IV-CT band in the NIR region ($\lambda_{\text{max}} = 1100$ nm) whose shape and intensity vary as a function of the irradiation time (**Figure 42d**). Considering the nature of the molecules employed, the only way to justify such absorption is by an intermolecular through-space charge transfer. The localized or delocalized nature of the charge can be determined by considering the shape of the IV-CT band and its evolution during the irradiation. For the first 30 minutes of light exposure, the NIR band shifted and shows an increase in asymmetry suggesting a transition from a partially delocalized (mixed population of class II and class III) to a fully delocalized (single population of class III) nature. Simultaneously, after 5 minutes of irradiation, the absorption of the localized radical at 800 nm appears and, for long irradiation times, it becomes predominant while the IV-CT band decrease. This is due to the fact that when a large number of radicals are generated, the electrostatic repulsion becomes sufficiently strong, that the system displays a fully localized nature (single population of class I). These results were further confirmed by EPR spectroscopy.¹³⁰

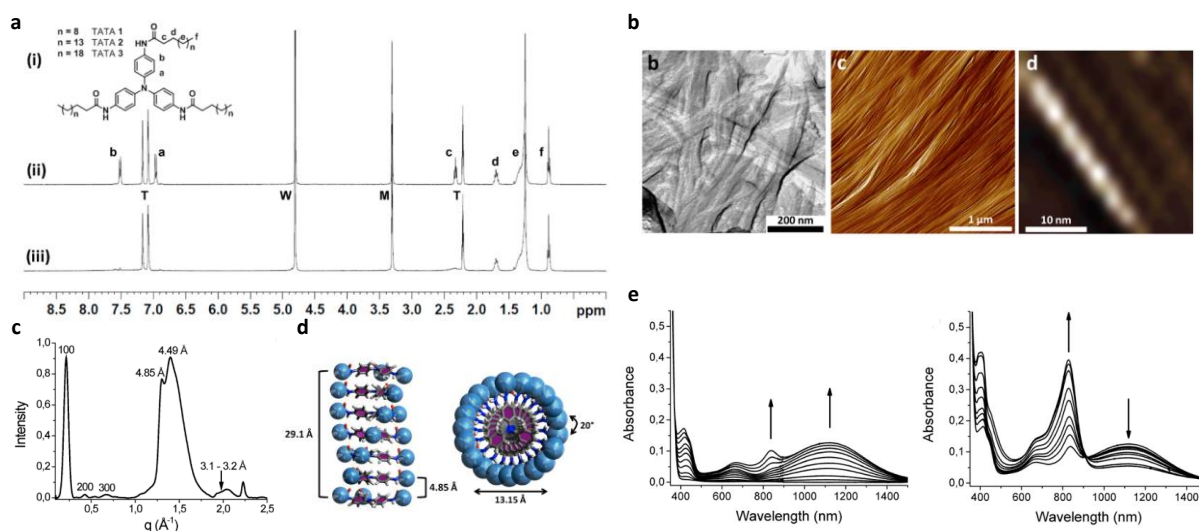


Figure 42 | **a**) Triarylamine structures (i) and NMR before (ii) and after (iii) white light irradiation; **b**) From left to right: freeze-fracture TEM image of TATA **1** showing its native form in chloroform; AFM imaging of TATA **1**; nanometer scale for a single fiber obtained from a chloroform solution drop cast on mica; **c**) X-ray scattering of a thin film of TATA **1**; **d**) Side view and top view of the proposed stacking structure of TATA **1** according to DFT optimization; **e**) Left: evolution of UV-vis spectrum during the first 5 minutes of irradiation, right: evolution of UV-vis spectrum between 7 and 73 minutes of light irradiation. (Reproduced from¹³⁰).

1.6.3 Supramolecular polymerization of chiral TATAs

We already discussed how triarylamine trisamides self-assemble in supramolecular helices. Upon integration of a new monomer in the assembly, the conformation of the propeller-shaped core, which can normally show (*P*)- or (*M*)- chirality, is forced in a preferential one according to the handedness of the helices in which it assembles. This leads, for achiral monomers, to a racemic mixture of right-handed and left-handed helices.¹³¹

The group of Aida and Miyajima demonstrated that the propeller conformation of the TAA core, strongly influences the chiral amplification.¹³¹ To show this, they prepared chiral (**C₃(R)**) **C₃(S)**) and achiral (**A**) TATA derivatives able to form nanostructures (**Figure 43a**), as shown by variable temperature DLS. According to CD spectroscopy, **A** was found to form a racemic distribution of both handed helices while **C₃(R)** and **C₃(S)** showed the formation of just one preferential helicity (**Figure 43d**). VCD experiments, confirmed that the conformation of the TAA core, within the assemblies, is related to the handedness of the helices, as shown by the VCD peaks in correspondence of the IR absorptions of the amidic group (1639, 1584 cm⁻¹) (**Figure 43c**).

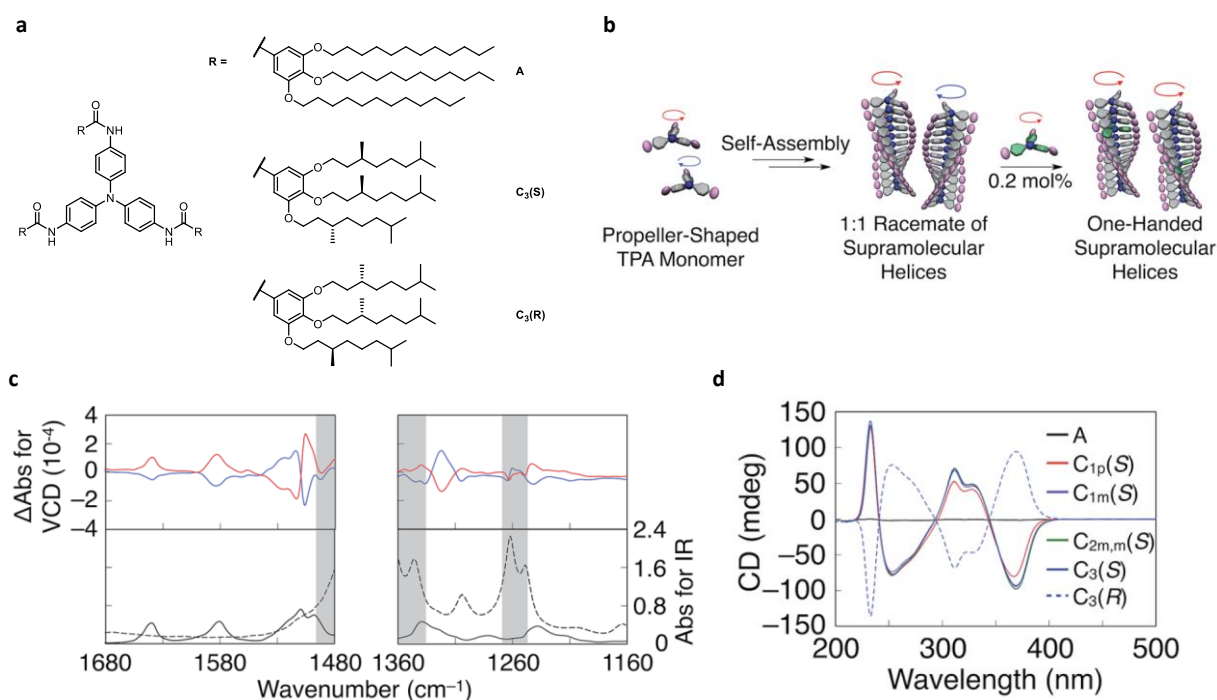


Figure 43 | **a**) Structures of **A**, **C₃(S)** and **C₃(R)**; **b**) Representation of TATAs assembling in a racemate of supramolecular helices (left) and, upon addition of small amount of sergeant (green), in one-handed helices; **c**) VCD (top) spectra of **C₃(S)** (blue line) and **C₃(R)** (red line) 5 mM solutions in MCH; IR spectra (bottom) of a 1:1 **C₃(S)** / **C₃(R)** mixture in MCH; the dashed line corresponds to the absorption of the solvent; **d**) CD spectra of **A** (black line), **C₃(R)** (dashed line) and **C₃(S)** (blue line). (Reproduced from¹³¹).

To further prove the key role of the handedness of the helices in guiding the propeller chirality of TAA, they conducted sergeants and soldiers experiments with quite surprising results: For mixed systems of **A** / **C₃(R)** or **A** / **C₃(S)** in a 9:1 ratio, the VCD shows almost identical spectra to those of the pure enantiomers (**Figure 44a**). Moreover, they found that extremely low amounts of chiral molecules were needed to drive the chiral assembly, with one sergeant being able to influence the helicity of 500 soldiers (**Figure 44b**) (the average in the literature is of about 1 sergeant for 100 soldiers^{132,133}). This underlines the synergistic effect of the molecular chirality in influencing the helicity of the assembly, and the handedness of the helices in influencing the chirality of the propellers.

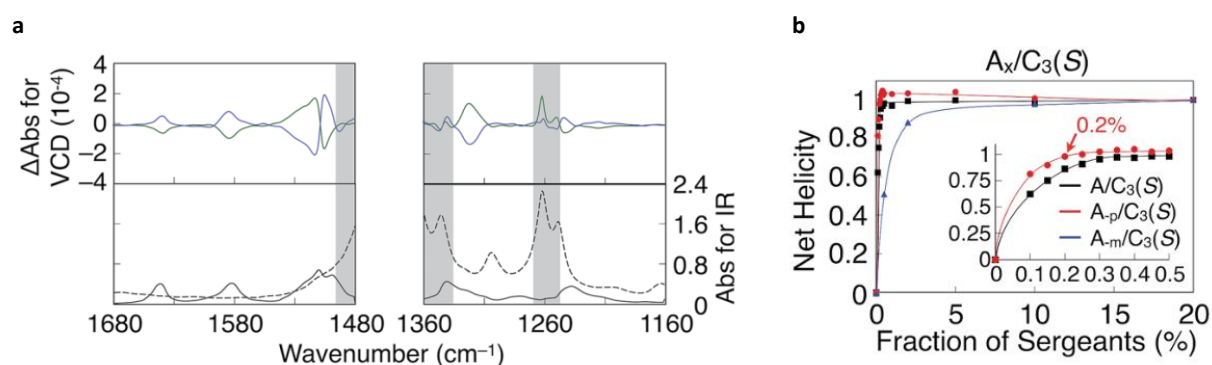


Figure 44 | **a**) VCD (top) spectra of 9:1 mixture of **A** / **C₃(S)** (blue line) and **A** / **C₃(R)** (green line) in MCH; IR spectra (bottom) of a 1:1 **C₃(S)** / **C₃(R)** mixture in MCH; the dashed line corresponds to the absorption of the solvent; **b**) Net helicity as function of the amount of sergeant added **C₃(S)** (black line). (Reproduced from¹³¹).

Recently, our group, investigated the hierarchical supramolecular polymerization of triaryl amines bearing achiral and chiral chains.¹³⁴ We designed and synthesized three derivatives (**Figure 45a**) which show the formation of physical organogels in chlorinated and aromatic solvents like toluene and dichloroethane. By microscopic analysis (TEM, SEM) we observed the formation of a network of fibers (**Figure 45c**) with some differences in length and thickness between the samples: comparing the fibers formed using *S*-TATA and C9-TATA, which show short and rigid fibers, C14 shows longer and thinner fibers. FTIR and AFM allowed to prove that all the derivatives assemble in a monocolumnar stack with a diameter, for the single fiber, about 1.5 nm (**Figure 45b**). Upon studying the supramolecular polymerization mechanism for *S*-TATA in toluene, by means of variable temperature UV-vis spectroscopy, we observed a clear non-sigmoidal shape of the curves showing a thermal hysteresis during heating cooling cycles (**Figure 45def**). Furthermore, the increase of the elongation temperature (t_e) with increasing concentration provides an additional proof of the high cooperativity of the process.

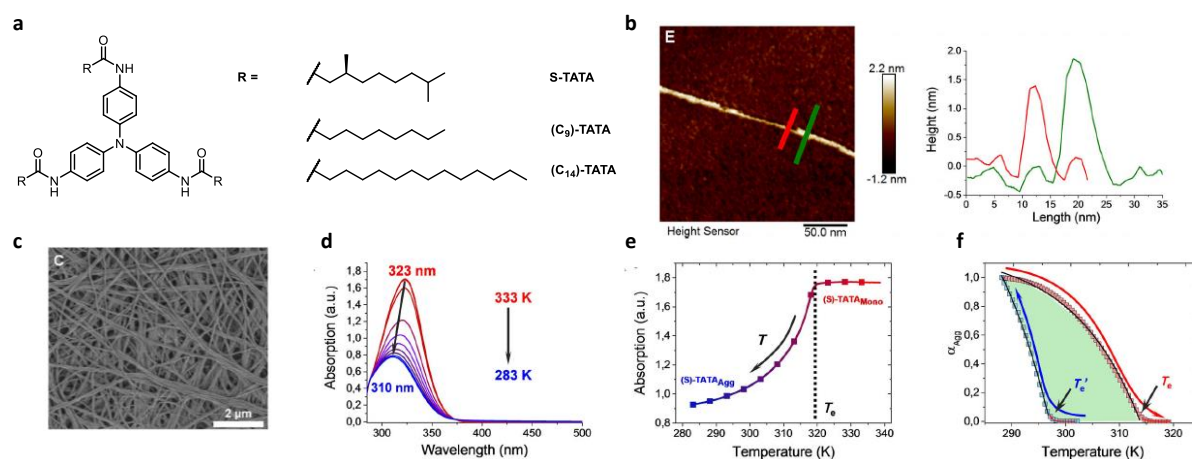


Figure 45 | a) Chemical structure of TATA derivatives; b) AFM image and height profiles of (S)-TATA supramolecular polymers prepared at a concentration of 0.1 mM in toluene; c) SEM image of (S)-TATA supramolecular polymers prepared at a concentration of 1 mM in toluene; d) Variable temperature UV spectra upon cooling a solution of **S-TATA** ($c = 0.5$ mM in toluene); e) Evolution of the degree of aggregation (α_{agg}) during heating-cooling processes. (Reproduced from¹³⁴).

Intriguingly, while exploring the supramolecular chirality of the structures obtained from **S-TATA** in toluene, we observed a quite unique behavior: At concentration around 0.5 mM, we found that different helicities were observed when changing the cooling rate in a way that slowly cooled (1 K/min) solutions show a positive Cotton effect, while fast cooling (10 K/min) yields a negative Cotton effect (**Figure 46a**). In dilute solutions (0.1 mM), a negative signal was detected independently from the cooling rate, while for concentrated solution (1 mM) a positive Cotton effect was obtained for both the regimes (**Figure 46b**). The explanation of this phenomenon arises from the existence of a hierarchical self-assembly pathway. In a medium range of concentration, upon cooling a hot solution, primary nucleation occurs which leads to the formation of *P*-helical fibrils. At this stage, according to the cooling rate, the system can proceed under two different pathways: for slow cooling, the short monocolumnar stacks assemble together, stabilized by lateral interactions, entering in a superhelical growth regime leading to the formation of *M*-superhelices which represent the thermodynamic product and show a positive cotton effect. In fast cooling regime, single *P*-helices are formed which then coagulate in fibers, the fast process does not allow the system to equilibrate and initiate the secondary nucleation, the system is then trapped and the kinetic product is obtained (showing a negative Cotton effect) (**Figure 46c**).

In dilute solution, only the formation of *P*-helices is observed without secondary nucleation for all cooling rates, with few superhelices observed after slow cooling. On the other hand, for

concentrated solutions, the formation of *M*-superhelices is always observed for both fast and slow cooling.

These results were further confirmed by AFM imaging of the assemblies obtained following both procedures, where the already mentioned structures could be observed (**Figure 46d**).

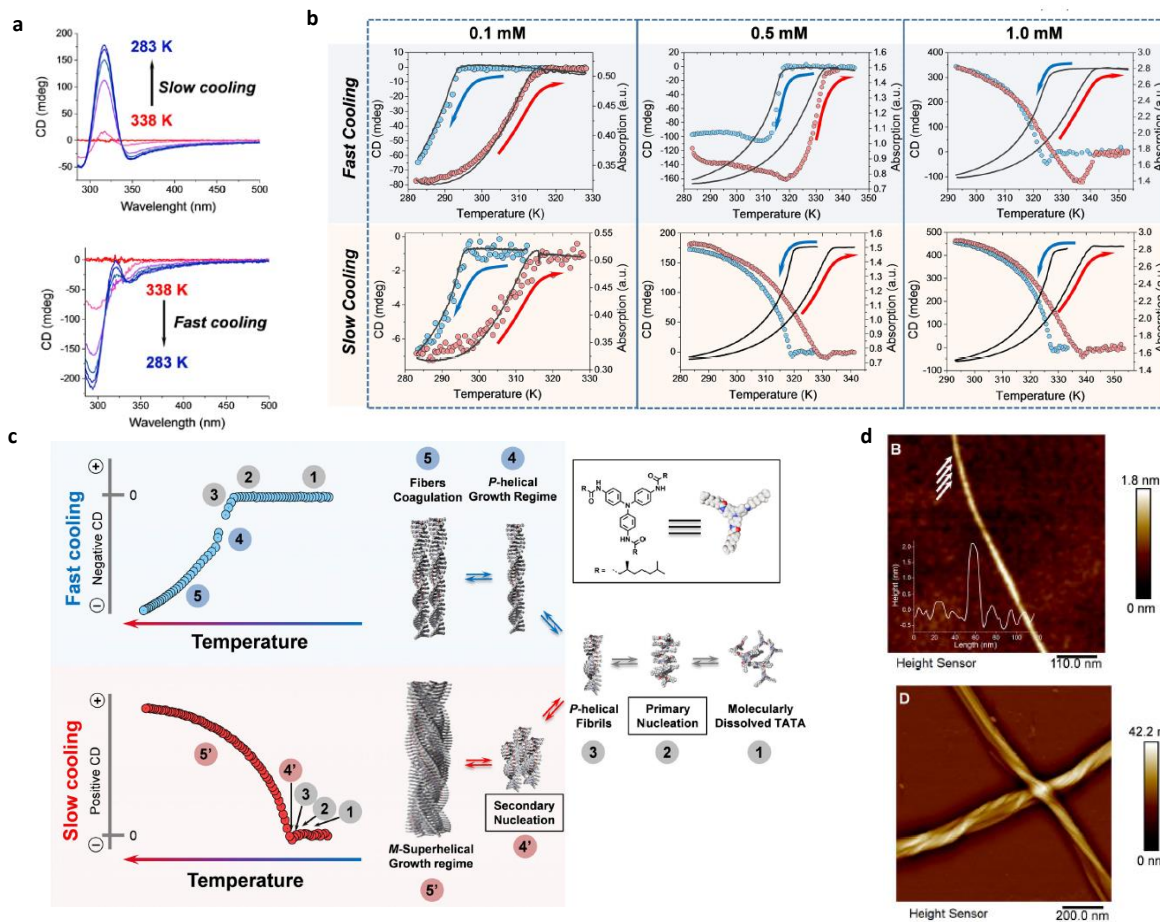


Figure 46 | **a**) Evolution of the CD spectra during the slow (top) and fast (bottom) cooling of a 0.5 mM solution of **S-TATA** in toluene; **b**) Variable temperature CD (blue and red circles) and UV (grey solid lines) curves recorded for **S-TATA** in toluene at various concentrations and for different cooling regimes; **c**) Schematic representation of the two pathways for the self-assembly; **d**) AFM images of: single fibril with a *P*-helicity (top) obtained from a 0.1 mM solution of **S-TATA** in toluene, *M*-superhelices obtained from slow cooling of a 0.5 mM solution of **S-TATA** in toluene (bottom). (Reproduced from¹³⁴).

CHAPTER II: TRIARYLAMINE DERIVATIVES WITH SUPRAMOLECULAR POLYMERIZATION INDUCED EMISSION PROPERTIES

2.1 AGGREGATION INDUCED EMISSION (AIE)

2.1.1 AIE phenomenon and most used AIE luminogens

Luminescent materials have become highly attractive considering their wide range of applications, ranging from biological probes and chemical sensing to stimuli responsive and optoelectronic systems. Despite the possibility to use such materials in their gaseous, liquid and solid state, most of the practical applications employ them as thin solid films and aggregates. Furthermore, in biological applications, the hydrophilic environment makes it necessary to rely on the hydrophobic luminophores to form nanoscopic assemblies. Therefore, reaching high efficiency in light emission from molecules in the solid state has become of utmost importance in order to improve the performances of the related application. In this regard, a phenomenon called aggregation caused quenching (ACQ), which affect most aromatic luminophores, strongly limits their applications. Molecules, which show the ACQ effect, are strongly emissive in dilute solution while, upon aggregation, their fluorescence is switched off. The main reason explaining such phenomenon arise from the intermolecular π - π stacking interactions established among the luminogens, which provide a preferential non-radiative decay of the excited state, resulting on a quenching of the observed luminescence (**Figure 47a**).¹³⁵ A way to circumvent this problem was found in 2001 by the group of Tang,¹³⁶ during the investigation of new, highly emissive, linear and hyperbranched polymers. They observed that a hexaphenylsilole (HPS) was non-emissive when solubilized in a good solvent while, upon adding a non-solvent to induce the aggregation, the fluorescence was switched on. (**Figure 47b**) They called this phenomenon *aggregation induced emission* (AIE). Looking for an explanation to this unusual behavior, they concluded that in dilute state the six aromatic rings (rotors) of the HSP are free to rotate dissipating the energy of the excited state through a non-radiative pathway. On the other hand, upon aggregation, the rotors are frozen in a propeller shape which prevents the unfavorable π - π stacking interaction, allowing the excited state to relax in a radiative way. This mechanism goes under the name of *restriction of intramolecular rotation* (RIR) (**Figure 47b**).^{137,138} Further advances in this field, with the discovery of new AIE luminogens (AIEgens) without rotatable units, demonstrated that is not only the RIR mechanism that is responsible for the AIE phenomenon but an alternative restriction of the

intramolecular vibration (RIV) can also lead to an enhanced in fluorescence in the aggregate state. Thus, given the difficulty to attribute RIV and RIR mechanisms, the general name of restriction of intramolecular motion (RIM) is typically applied.¹³⁵

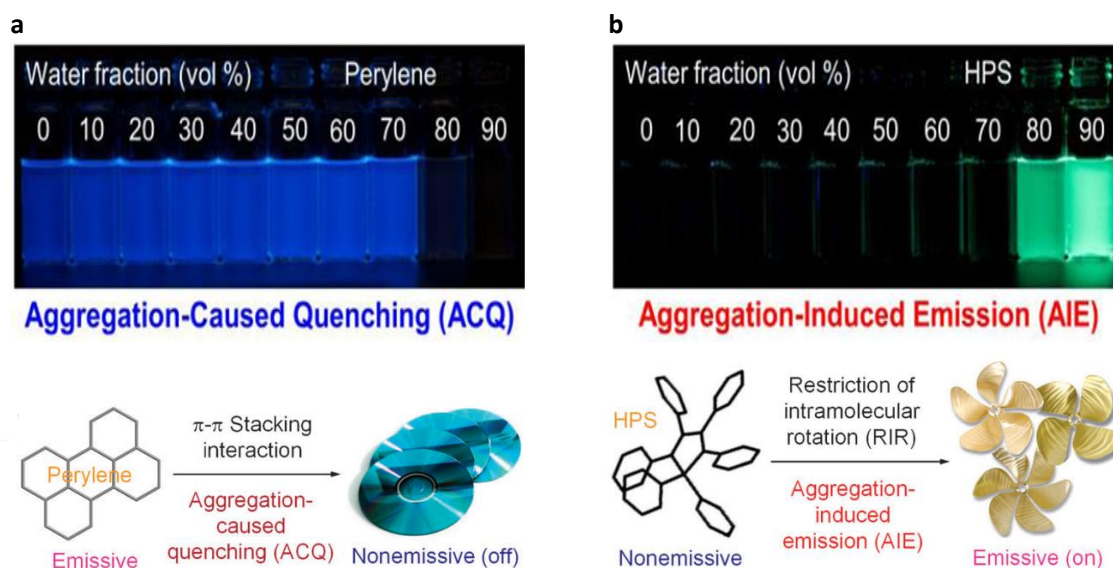


Figure 47 | **a**) Fluorescence of solutions of perylene in THF with an increasing amount of water showing a typical ACQ effect, the mechanism is depicted below; **b**) Fluorescence of solutions of HPS in THF with an increasing amount of water showing the AIE effect, the RIR mechanism is depicted below. (Reproduced from references^{135,137}).

During the last twenty years an incredible number of AIE systems have been described,¹³⁵ from simple hydrocarbons¹³⁹ to molecules containing heteroatoms like nitrogen,^{140,141,142} phosphor,¹⁴³ boron,^{144,145} sulfur,¹⁴⁶ silicon,^{136,147} germanium,¹⁴⁷ metallo-organic complexes,^{148,149} functional groups like nitrile^{150,151} and imine;¹⁵² systems whose intramolecular motion is reduced via hydrogen bonding,¹⁵³ and polymeric materials¹⁵⁴. Within this new growing world, some AIEgens have become of primary importance owing to their simple chemical structure and the possibility to include them in more complex architectures to achieve fluorescent functional materials in a relatively easy way. One of those system is the 1,1,2,2-tetraphenylethylene (TPE) moiety. It has a propeller shape in which the four aromatic rings can freely rotate around the σ bonds in dilute solution but, upon aggregation or in the solid state, the constriction of the rotation boosts the fluorescence. Because of these characteristics, TPE moiety, has been successfully employed for many applications, like cell imaging,¹⁵⁵ chemical sensors,¹⁵⁶ biological probes,^{157,158} and OLED devices (**Figure 48**).¹⁵⁷

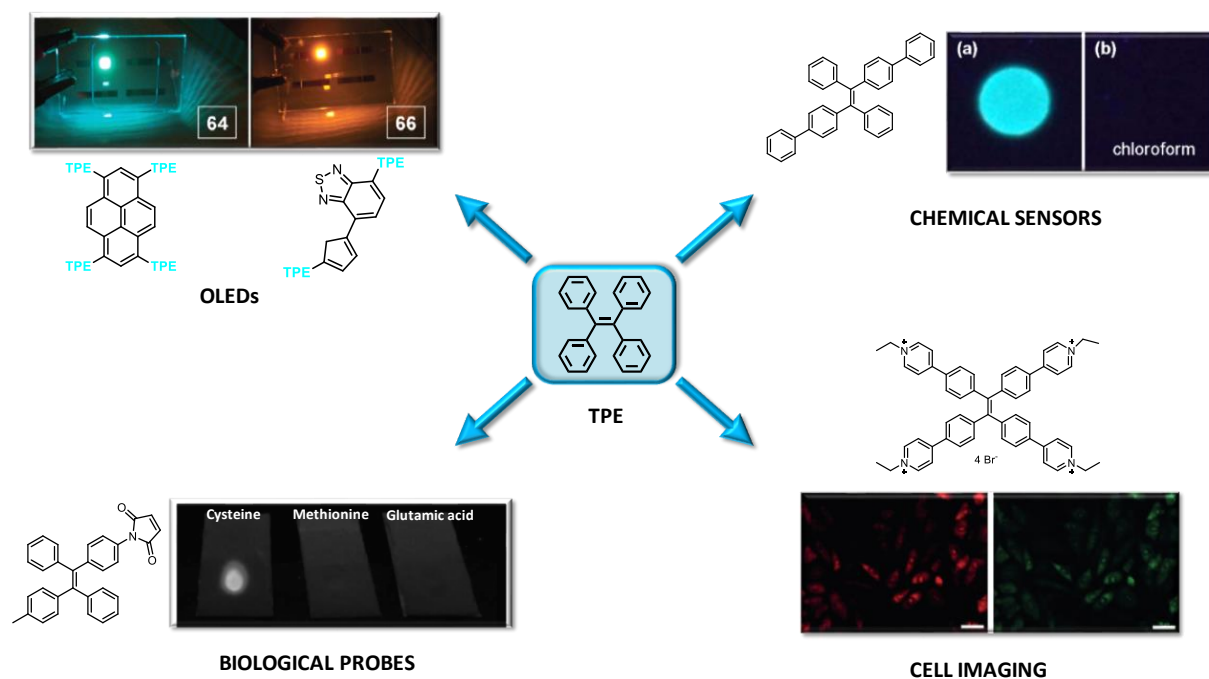


Figure 48 | Examples of different applications for TPE derivatives (Reproduced from references¹⁵⁵⁻¹⁵⁸).

In light of the well-known properties of the tetraphenylethylene moiety, as exhaustively reviewed by Tang,¹⁵⁷ we decided to use this AIE luminogen for the synthesis of triarylamine derivatives with aggregation induced emission properties.

2.1.2 AIE of triphenylamine core

As described in the first chapter of this manuscript, the conformation of the triphenylamine core is not planar and the presence of three phenyl rotors may help in the relaxation process of the excited state in solution. Furthermore, the twisted structure of the molecule, could reduce the stacking of the aromatic rings in the solid state, allowing TPA derivatives to show AIE properties. In many cases, because of its electron rich nature, TPA moieties are linked with electron deficient units to form D-A derivatives with special properties like solvatochromism, two photon absorption and AIE. A similar approach has been described by Zhao et al,¹⁵⁹ who reported the synthesis of a sensor for cyanide in aqueous media combining a triphenylamino moiety with two dicyanovinyl groups. The presence of the bulky diphenylamino group on the terphenyl units permits reaching strong emission in the solid state. The dicyanovinyl groups, acting as a strong electron-accepting units, induce an intramolecular

charge transfer (ICT) but also act as the reactive part of the sensor (**Figure 49a**). In water, the molecule displays a strong fluorescence at 590 nm, upon addition of a cyanide solution, the consequent nucleophilic attack of cyanide to the dicyanovinyl group, induces the blue shift of the emission at 450 nm (**Figure 49b**).

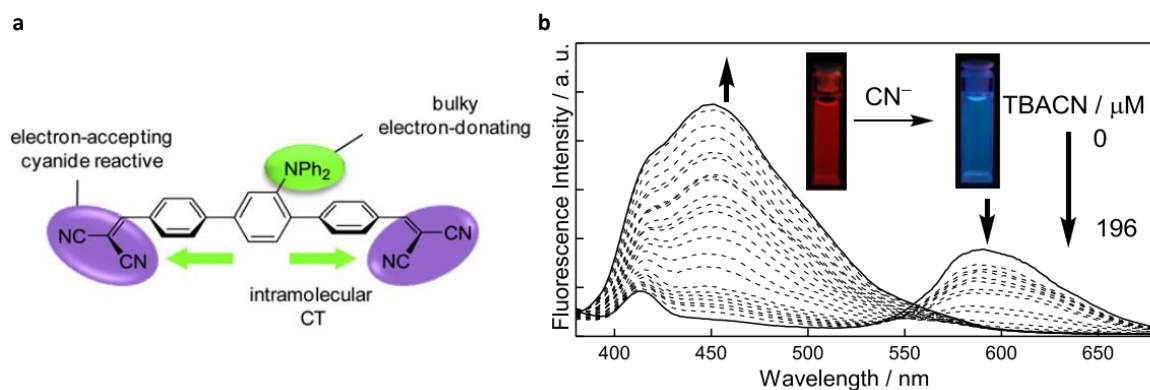


Figure 49 | a) Molecular structure of the chemical sensor; b) Fluorescence spectra change of a solution of sensor (2.80 mM) in 2 mM CTAB micellar solution upon addition of TBACN ($\lambda_{\text{exc}} = 370$ nm). Inset: emission color change upon addition of TBACN. (reproduced from¹⁵⁹).

By a similar approach, several TPA based AIEgens, have been synthesized, with the possibility to tune the emission wavelength by changing the electron deficient units. Upon combining TPA with imidazolium, blue emission was achieved (**Figure 50a**);¹⁴¹ when two lateral TPAs are linked to a central thienopyrazine, through silicon bridges, a green emitter is obtained (**Figure 50b**);¹⁶⁰ finally, red emission is obtained by combining the triphenylamino moiety with BODIPY units (**Figure 50c**).¹⁶¹ The latter showed also a strong solvatofluorochromism as represented below.

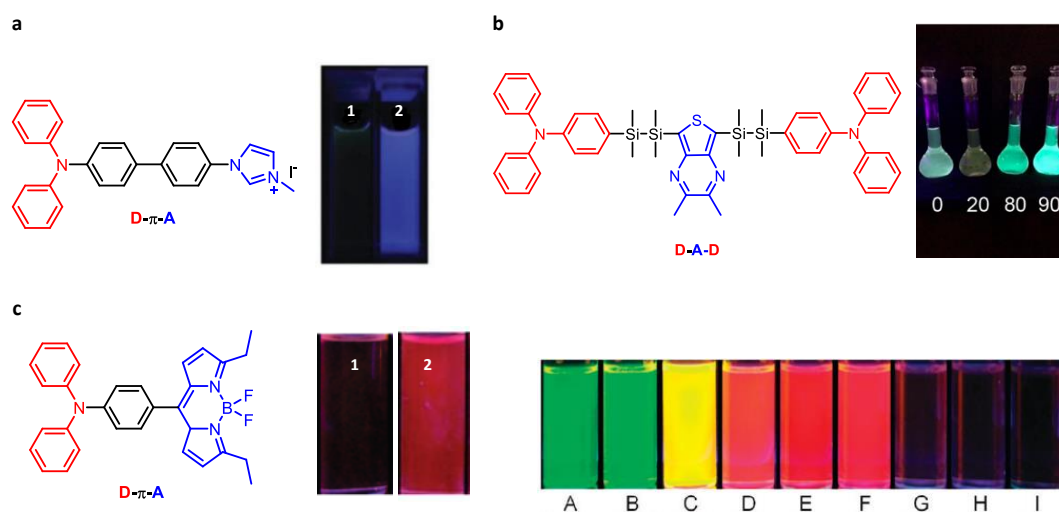


Figure 50 | a,b,c) Examples of triarylamine based AIEgens and fluorescence of solutions in THF before and after inducing the aggregation upon addition of water; bottom right: solvatofluorochromism for the TPA linked to BODIPY units (bottom left): (A) hexane, (B) cyclohexane, (C) toluene, (D) chloroform, (E) ethyl acetate, (F) THF, (G) ethanol, (H) acetonitrile, and (I) methanol (Reproduced from^{141,160,161}).

2.1.3 Supramolecular polymerization induced emission (SPIE)

In the systems described so far, fluorescence is achieved in the solid state (powder), but also in small aggregates dispersed in solution. The last are normally formed upon reducing the solubility of the target AIEgen by adding a non-solvent to the system. In the most typical case, a mixture in THF/water is increased in its water content. The aggregation in such cases is mainly amorphous, mostly driven by hydrophobic interaction and occurs without a precise organization of the molecules in nano- and micro- structures. Despite this simple approach being quite useful for certain applications like for chemo and bio sensors, other applications may take advantage from a more precise organization of the molecules in supramolecular structures. For example, 1D nanowires are of great interest for their small size, high flexibility, and simple tunability of the photoelectric properties. Hence, the possibility to obtain fluorescent nanowires exploiting the AIE phenomenon may increase the opportunities for such materials in nanoscale photonic and optoelectronic. The aggregation induced emission obtained from well-organized structures will be addressed from this point on as *supramolecular polymerization induced emission* (SPIE) to differentiate it from its amorphous counterpart. For instance, the group of Tang, reported the self-assembly of a tetraphenylethylene functionalized with (S)-(+)-2-(6-methoxy-2-naphthyl)propionic acid through ester bonds (**Figure 51a**).¹⁶² Beside the classic AIE behavior showed by this derivative in THF/water mixture, the authors

found the formation of self-assembled structures in DCM/methanol mixtures. SEM analysis of the samples revealed the formation of small nanowires with a diameter of about 50 nm, and lengths in the order of a few μm . The nanowires were further assembled in thin films which emit bright greenish-blue light under UV irradiation, as showed by fluorescence microscopy (**Figure 51b**).

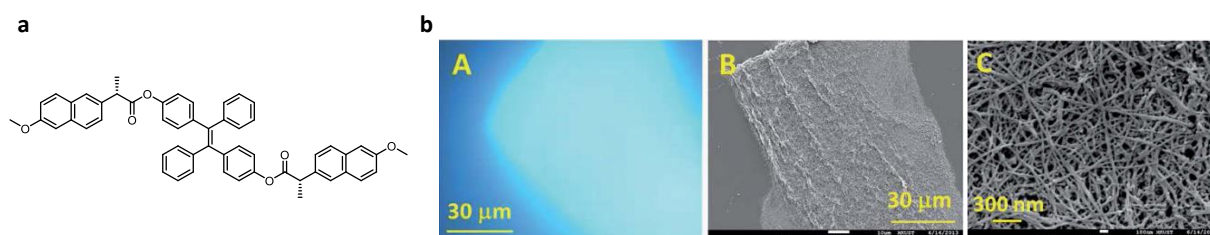


Figure 51 | a) Chemical structure of the TPE derivative; **b)** From left to right: Fluorescence microscopy image of the thin film; SEM image of the thin film; self-assembled nanowires under SEM microscopy. (Reproduced from¹⁶²).

The same group reported, in 2012, the SPIE for perylene bisimide derivatives. This class of compounds are well known for their electron-transporting properties and for their fluorescence in dilute solution. Unfortunately, upon self-assembly the interaction between the stacked aromatic rings quenched the fluorescence limiting their applications. To overcome this problem, the authors functionalized the PBI moiety with TPE units (**Figure 52a**) achieving fluorescence in solid state. Moreover, they found the formation of micro-fibers (**Figure 52b**) in various mixtures such as hexane/DCM, methanol/DCM and water/THF with small changes in length and size distributions among the systems. The self-assembled structures appear to be strongly red emitting under confocal fluorescence microscopy (**Figure 52b**)

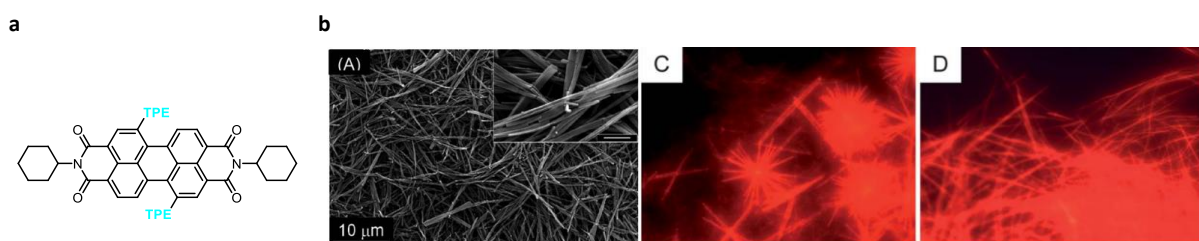


Figure 52 | a) Chemical structure of the perylene bisimide derivative; **b)** From left to right: SEM image of micro-fibers obtained in methanol/DCM mixture; Confocal fluorescence microscopy image of fibers formed in a methanol/DCM mixture; Confocal fluorescence microscopy image of fibers obtained from a water/THF mixture.

Supramolecular polymerization induced emission has also been achieved by host-guest chemistry as recently reported by Cao and coworkers.¹⁶³ The host-guest interactions between a cucurbit[8]uril (CB[8]) and tetra(1-carboxyethylpyridinium) tetraphenylethylene derivatives, in water, led to the formation of primary planar or curved layers, which goes under secondary hierarchical self-assembly in cuboids and spheroids. Small differences in the pyridinium(vinyl) arms allow to drive the aggregation process towards a selected architecture between the cubical and the spheroidal nano-objects. Moreover, the fluorescence of the supramolecular structures shows a large red-shifts of the maximum emission peaks, which can be turn OFF or ON as response to an external stimuli, such as a competitive guest (**Figure 53**).

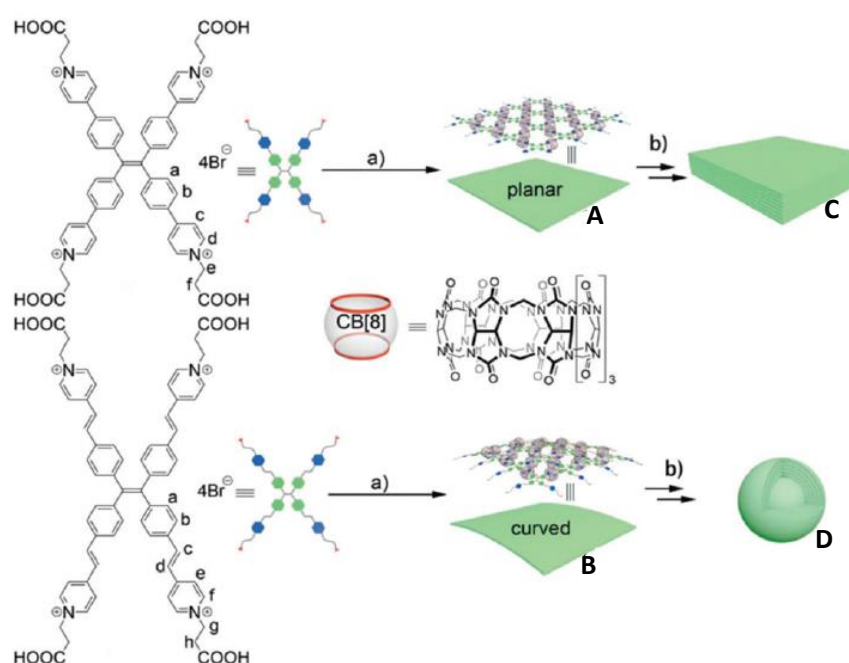


Figure 53 | Representations of the hierarchical formation of the supramolecular layers (**A** and **B**) and frameworks (**C** and **D**): (a) host-guest complexation; (b) stacking or aggregating. (Reproduced from¹⁶³)

2.1.4 Application of AIE materials in OLED devices

As we have mentioned several times in this chapter, materials showing AIE properties are becoming more and more important in many domains, like OLEDs, OFETs, optical waveguides, liquid crystals, photovoltaic and so on.¹⁶³ In particular, the research around OLED display devices, has grown tremendously in the last decades, as possible alternative to classic inorganic led devices. Despite many efforts and advances have been pursued there are still

some drawbacks which limit the efficiency of such technology, mostly the degradation of the materials employed, thus, the short lifetime of the organic materials.¹⁶⁴ One of the biggest challenges, for developing full-color displays, is to improve the performances of the blue OLEDs whose band gap of relative light emitter is high and, thus, contribute to lower the efficiency (20% red, 19% green, and 4–6% blue are the usual external quantum efficiencies (η_{ext}) reported in literature).¹⁶⁴ For this purpose, the TPE moiety, has been employed to design blue emitting AIEgens to improve the OLEDs efficiency by reducing the ACQ effect. For example, a TPE dimer (***p*TPE-*p*TPE**) connected through its para position was employed in a multilayer OLED showing good efficiency ($\eta_{\text{ext}} = 3.17\%$) and brilliant luminance (up to 11180 cd/m^2 at 15 V).¹⁶⁵ During the past years, in an attempt to construct new blue AIE luminogens, good results have been obtained by modulating the degree of conjugation and increasing the twisting of the molecules.¹⁶⁶ Thus, the introduction of bulky groups, like triphenylamine may positively affect the extent of conjugation and increase the dihedral angles. Moreover, the TPA units being remarkable hole transporters, it could confer to the luminogens hole transporting properties. Many structures combining TPE and TPA have been designed with various ratios between the two units and employing different linking motifs. For instance, the group of Li,¹⁶⁶ reported high efficiencies, up to $\eta_{\text{ext}} = 3.99\%$, for a series of triphenylamines and methyl-substituted triphenylamines decorated with three TPE moieties (**Figure 54; MethylTPA-3MethylTPE**). In some cases, TPE-TPA derivatives have been employed to build simple OLED devices with a reduced number of layers, taking advantages from the double nature of these materials as light emitters and charge carriers. In this regard, Tang and coworkers,¹⁶⁷ have built a monolayer device in which a triphenyl amine functionalized with a TPE moiety (**Figure 54; TPATPE**) acts as both hole transporting and emitting layers reaching an external quantum efficiency of 1.1%. Despite this value being consistently lower than that obtained by employing **TPATPE** in a multilayer device, it underlines the potential double nature of such materials. The same group reported, some years later, a monolayer device based on two triarylamine-bridged by a TPE unit (**Figure 54; DATE**), which showed an efficiency even higher if compared to the device with additional hole transporting layers.¹⁶⁸

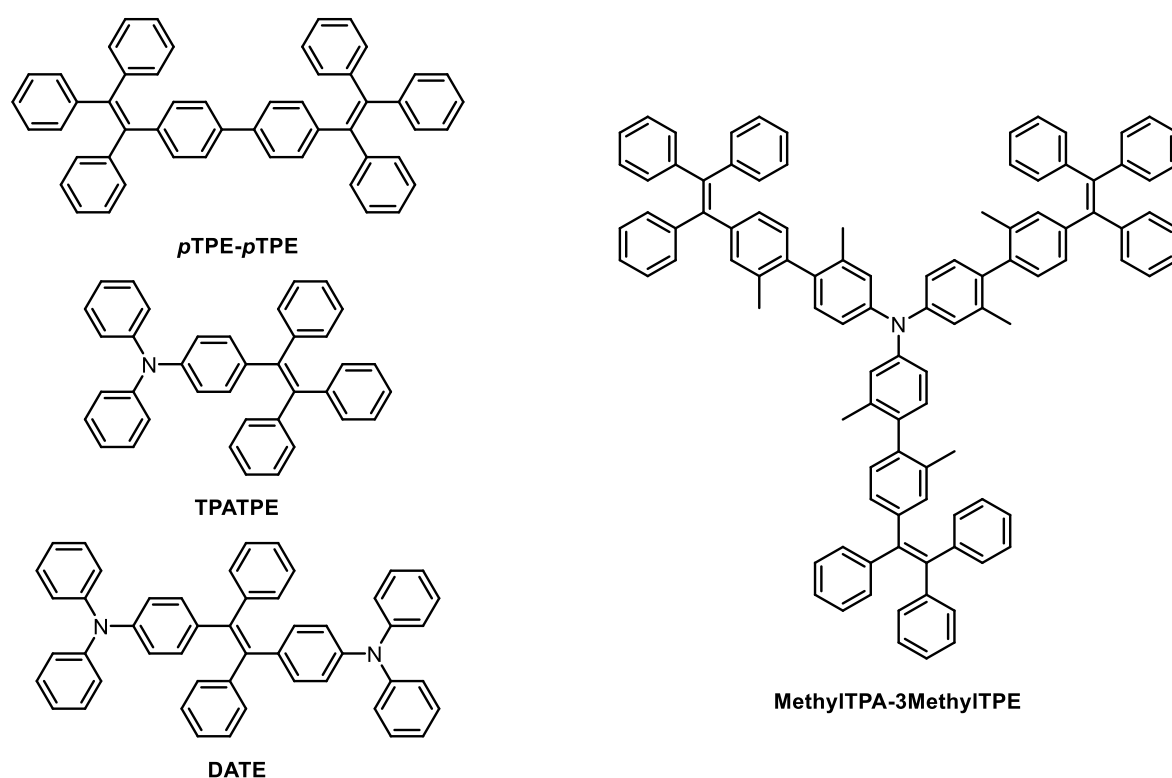


Figure 54 | TPE and TPA derivatives used as examples of OLEDs applications (Reproduced from¹⁶⁵⁻¹⁶⁸).

In this section, we have highlighted the advantages of combining TPE with TPA units in order to obtain materials which show fluorescence in the solid state but, additionally, are capable to act as hole-transporting materials. The optimization of the properties of such derivatives would allow to simplify the architectures of the devices without affecting the efficiencies. It is noteworthy to point out that, in all cases, the materials are employed in their amorphous states. It is only natural to wonder whether gaining control on the supramolecular structures of the materials used, through a bottom up approach, may improve the characteristics of the devices.

2.1.5 Circularly polarized luminescence from chiral AIE molecules and macrostructures

We highlighted in chapter I how supramolecular systems build through the assembly of chiral, chiral/achiral, and in some cases purely achiral monomers, can show a difference in absorptivity of left and right circularly polarized light. This Cotton effect constitutes a fundamental feature for the characterization of such systems. Circularly polarized luminescence (CPL) is another related property that can arise in systems that show a preferential absorption of the polarized light and are luminescent. By analogy, it consists in the

differential emission of right- and left-circularly polarized light from simple chiral molecules or assemblies (**Figure 55a**), and it can be quantified by the luminescence dissymmetry factor (g_{lum}) according to Equation 4

$$g_{\text{lum}} = \frac{2(I_{\text{L}} - I_{\text{R}})}{I_{\text{L}} + I_{\text{R}}} \quad (4)$$

With I corresponding to the intensity of the left (L) and right (R) circularly polarized emission. Hence, the maximum value for $|g_{\text{lum}}|$ is 2 which correspond to a fully circular polarized light. Despite many chiral fluorescent organic molecules emitting circularly polarized light in their monomeric form, supramolecular systems normally show higher g_{lum} values due to their higher transition dipole moment vectors.^{169,170} Thus, AIEgens which are normally fluorescent silent in solution, can show CPL if integrated in asymmetric supramolecular structures. Three main approaches allow to combine fluorescence and chirality in self-assembled structures: in a first case, the chiral moiety is fluorescent itself, or is covalently attached to a luminophore, forming a monomer that can self-assemble transferring the chirality to the whole structure (**Figure 55b; i**); in a second alternative, a chiral monomer co-assembles with an achiral luminophore, and the chirality is transferred to the luminophore and the assembly (**Figure 55b; ii**); in the last case, an achiral luminophore assembles forming supramolecular structures, and chirality is generated through symmetry breaking (**Figure 55b; iii**).

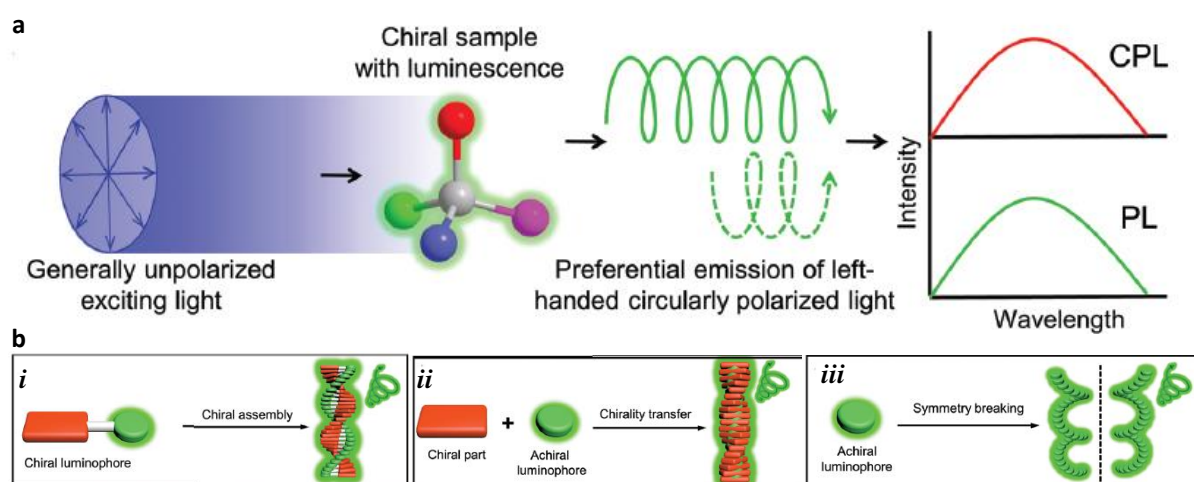


Figure 55 | a) General scheme of CPL from a chiral molecule; **b)** Schematic representation of the three possible approaches to have CPL from supramolecular systems. (Reproduced from¹⁷⁰).

For instance, the first approach, has been employed by the group of Liu¹⁷¹ to design a chiral AIEgens made by two mannose units bridged by a tetraphenylsilol moiety (**Figure 56a**).

Solutions of such derivative, at different concentrations in DCM, show no Cotton effect indicating the monomeric state of the molecules in solution (**Figure 56b**). Upon adding a non-solvent like hexane, they observed the emergence of a CD signal suggesting a chirality transfer from the mannose to the silole assembly (**Figure 56c**). In a similar way, solution in pure DCM shows almost no fluorescence, while, above 80% of hexane added to the system, the fluorescence increases drastically as consequence of the restriction of the intramolecular motion (**Figure 56d**). Both the properties indicate a possible CPL for such derivative, so several samples were tested to determine whether the light emitted was circularly polarized. The solution in DCM showed no CPL as result of the good solubility of the molecules in this solvent. On the other hand, thin films obtained upon drop-casting from DCM solution, solid dispersion in DCM/hexane mixture, or aggregates dispersed in a PMMA matrix at 10 wt% show CPL with g_{lum} values comprised between -0.08 and -0.13. Interestingly, the samples obtained upon evaporating a DCM/toluene solution of the molecule in Teflon-based microfluidic channels showed an enhanced CPL signal as compared to the previous samples, with a g_{lum} of -0.32 (**Figure 56e**). The authors concluded that the inner structure of the microchannels increases the packing of the molecules leading to a higher CPL effect.

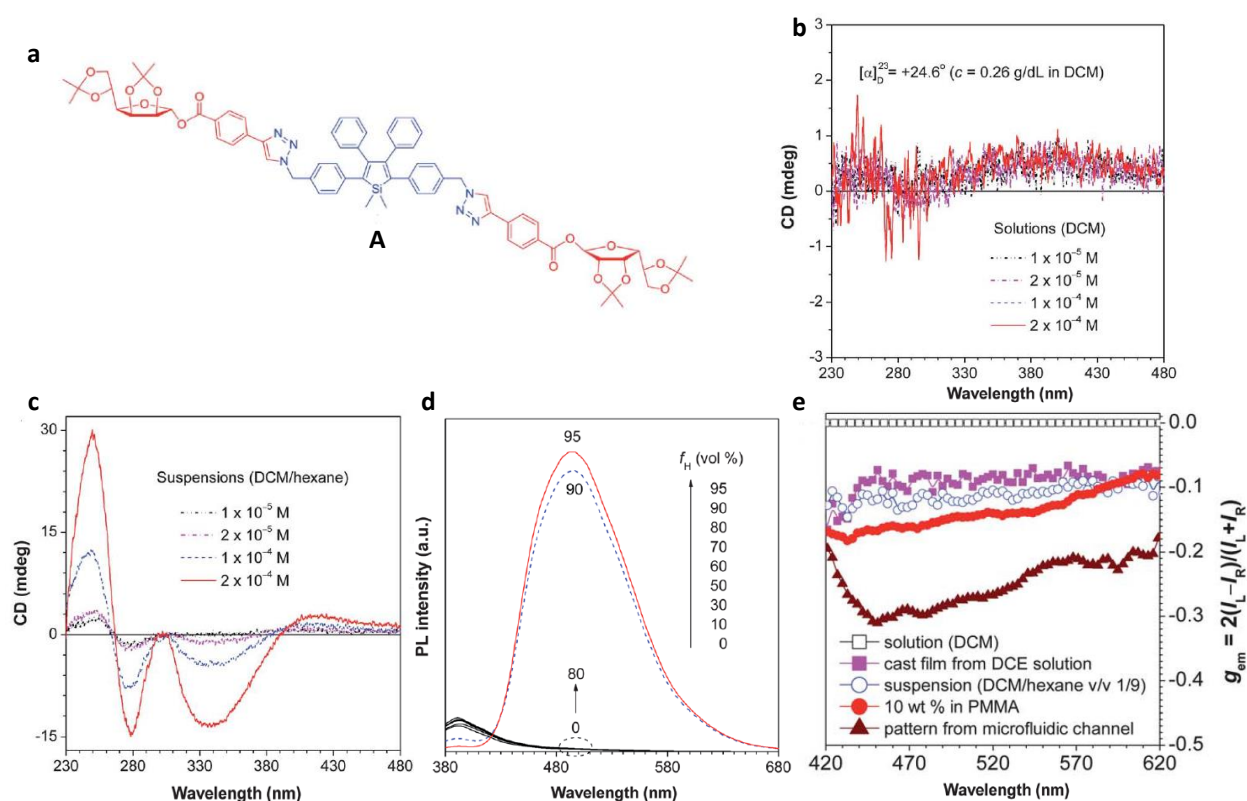


Figure 56 | a) Chemical structure of **A**; b) CD spectra of a solution in DCM of **A** at different concentrations; c) CD spectra of solutions of **A** at different concentrations in a DCM/hexane mixture (1:9); d) Fluorescence spectra of solutions of **A** by increasing the ratio of hexane in DCM; e) Different samples showing different CPL spectra. (Reproduced from¹⁷¹).

Recently, the group of Meijer investigated the supramolecular polymerization processes for chiral carbonyl-bridged triarylamine trisamides (CBT) derivatives.¹⁷² In particular, by following through spectroscopic techniques the self-assembly of compound **S-CBT** (**Figure 57a**), they observed that two stable states were obtained at the same conditions of temperature and concentration, but after two different self-assembly pathways. The first state, **A**, was obtained upon cooling, from 80 °C to 7 °C, a solution of **S-CBT** in *o*-dichlorobenzene. The system showed, upon cooling, the appearance of a negative Cotton effect in the CD spectrum as result of the organization of the monomers in helices with a preferred handedness (**Figure 57b**). A second state, **B**, was obtained upon undercooling the solution from 80 °C to -5 °C. The CD signal showed, in the range from 7 °C to -5 °C, a transition from negative to positive values indicating a morphological rearrangement and the formation of the new state **B**. Upon further heating to 7 °C, state **B** remains stable, thus, making it possible to have the two states under the same conditions. Both the states showed photoluminescence, with higher intensity for state

A (Figure 57c) but, state **B** exhibited strong circularly polarized luminescence with a positive g_{lum} value while state **A** showed weak CPL with negative g_{lum} (**Figure 57d**). This example clearly shows that reaching a high control of the self-assembly process should allow us to select one morphology over others and, at the same time, gain control over the emerging properties of the so-formed supramolecular structures. Since the properties of supramolecular materials are strongly related to the organization of the monomers at all hierarchical levels, it is clear that controlling the supramolecular polymerization is necessary to optimize the properties of these materials.

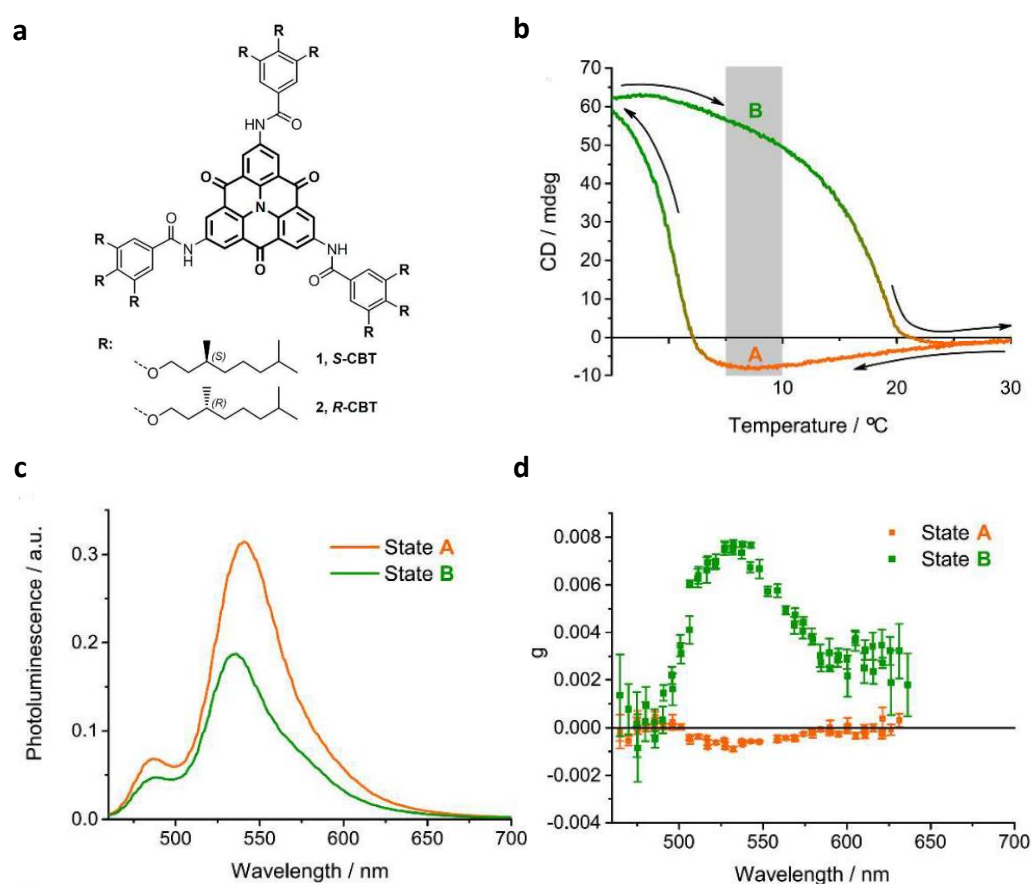


Figure 57 | a) Chemical structures of the **R-CBT** and **S-CBT**; b) Evolution of CD signal at 490 nm for a cooling / heating cycle (0.2 K/min) of a 5×10^{-5} M solution of **S-CBT** in *o*-dichlorobenzene; c) Photoluminescence spectra of the two different states; d) Circular polarization of the photoluminescence spectra of the two different states. (Reproduced from¹⁷²).

The interest around this kind of systems, exhibiting CPL properties, has grown consistently in the recent period owing to the major availability, as compared to the recent past, of the instrument to evaluate it. At the same time, the applications for CPL materials developed as

well. The attractiveness of this phenomenon is particularly addressed to the OLED applications since OLED displays suffer from the reflection of the external light and, in order to reduce reflectance, a polarizer and a quarter-wave plate are employed as antiglare filter. A drawback of this solution is that 50% of the non-polarized light emitted from the device is absorbed by the filter, with a consequent reduction of the performance. Thus, employing CPL materials in OLED (CP-OLED), would avoid this loss of efficiency.¹⁷³ Moreover, 3D displays with high-contrast, can be developed with CP-OLEDs.¹⁷⁰

2.2 INVESTIGATION OF TRIARYLAMINES WITH SPIE PROPERTIES

2.2.1 General overview

Triarylamine based materials are widely used in electronic devices (OLEDs, OFETs, solar cells) because of their outstanding hole transporting properties.⁸² With a focus on OLED applications, TPA based hole transporting layers (HTL) are, nowadays, commercially available. Besides their employment as HTL, triphenylamines have been also used as emitting layers (EL) and as host materials for phosphorescent OLEDs.^{84,174} As we mentioned previously in this chapter, during last years, the interest around materials able to accomplish a dual function has raised. Triarylamine, functionalized with AIEgens have shown promising properties as emitting materials with hole transporting properties. Despite this approach having led to good results, especially regarding the number of active layers needed, the efficiencies remain relatively low when compared to more complex architectures. Thus, optimizing the characteristic of these materials would allow us to simplify the structures of the devices, their manufacturing, and reduce the costs. To the best of our knowledge, TPA derivatives with AIE properties have always been employed in their amorphous form without control over their organization. On the other hand, some reports indicate that achieving a good control at a nanometric scale, i.e. controlling the morphology, of the materials can strongly boost the efficiencies of the devices with respect to their non-organized counterpart.¹⁷⁵ Based on this knowledge, the goal of the work described in this chapter is the preparation of triarylamine based supramolecular polymers with supramolecular polymerization induced emission (SPIE) properties. Towards this purpose, we designed three derivatives by functionalizing a triarylamine trisamides (TATA) with a variable number of TPE units and chiral chains (**Figure 58**). In such a configuration, the central TATA core would drive the supramolecular polymerization while the TPE units on the periphery would act as AIE by the restriction of

intramolecular rotation turning on the fluorescence. Moreover, the presence of the chiral chains is intended to induce the monomers to assemble with a preferential helicity leading to chiral supramolecular structures having circularly polarized luminescence.

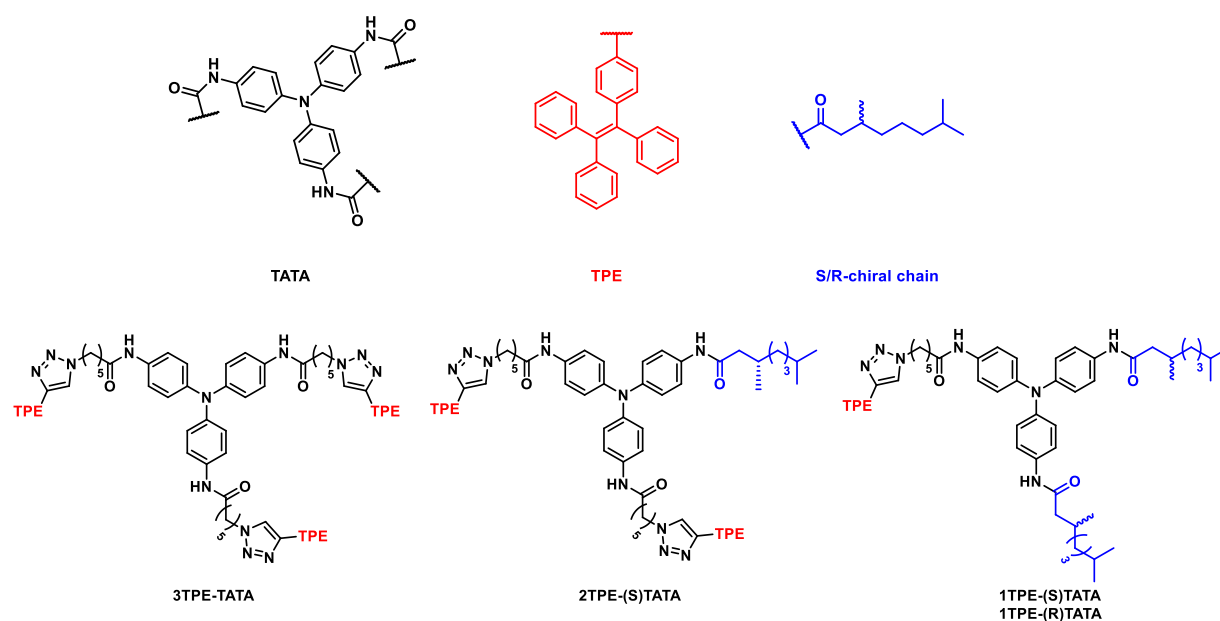


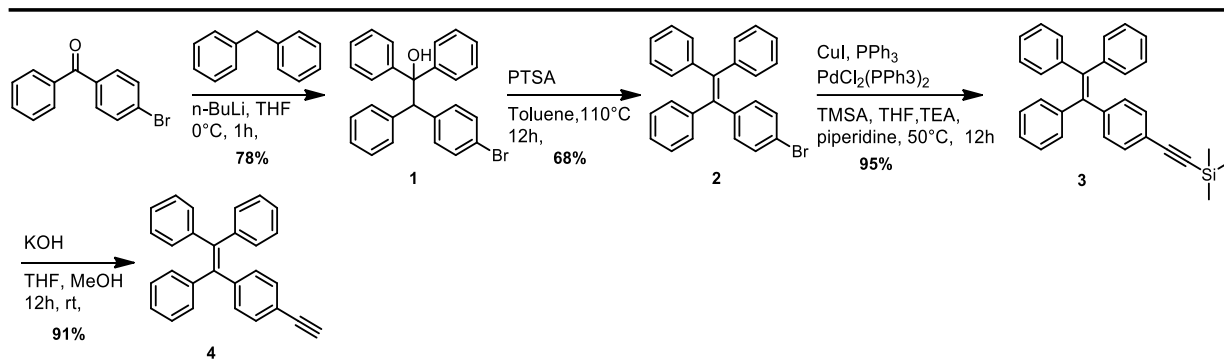
Figure 58 | TATA derivatives synthesized in this work.

The first derivative we designed was compound **3TPE-TATA** in which the TATA core is linked, through a five carbons chain ending with a triazole, to three TPE units. The second molecule was compound **2TPE-(S)TATA**, in which two extremities bear the same TPEs, while the last one is constituted by a S-chiral branched amide chain. For the last compound, the two enantiomers were synthesized **1TPE-(S)TATA** and **1TPE-(R)TATA**, in which just one extremity terminates with a TPE moiety, while the others bear two chiral chains.

2.2.2 Synthesis of TATA derivatives

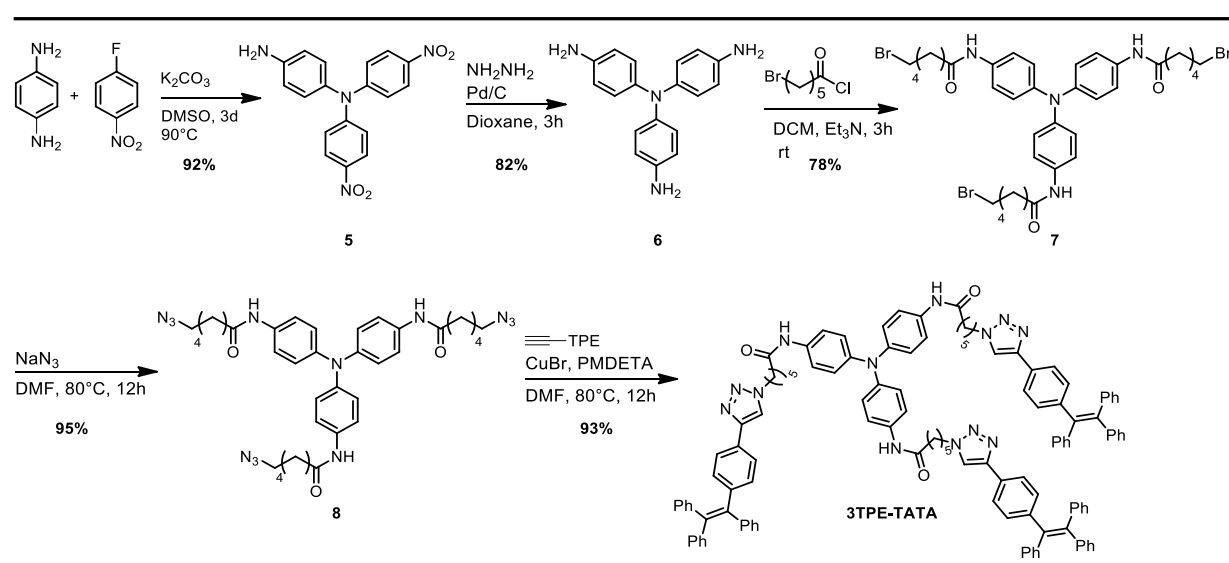
We approached the synthesis of **3TPE-TATA** by firstly synthesizing the TPE precursor with a pendent alkyne moiety (**4**) necessary for the click reaction with the TATA core. The synthesis of compound **4** was performed according to a protocol described in the literature (**Scheme 5**).¹⁷⁶ Upon adding a solution of 4-bromobenzophenone to a solution of benzophenone in THF with n-butyllithium, we synthesized alcohol **1** which eliminates water by refluxing it in toluene with a catalytic amount of *p*-toluenesulfonic acid (PTSA), forming alkene **2** in good yield. The

Sonogashira coupling of **2** with trimethylsilylacetylene (TMSA) affords compound **3** in excellent yield. Finally, the hydrolysis of compound **3** with potassium hydroxide allowed us to achieve the alkyne-TPE **4**.



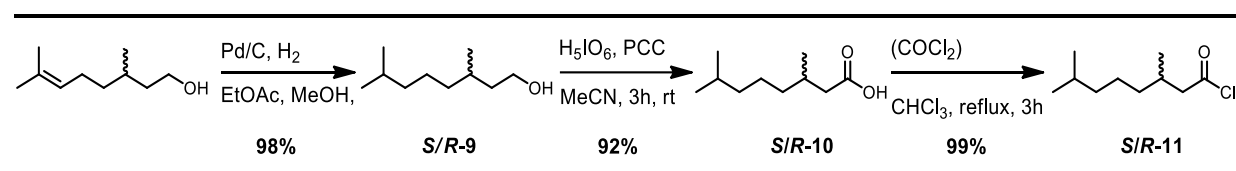
Scheme 5 | Synthetic route to compound **4**.

The triarylamine core was synthesized starting from commercial materials (**Scheme 6**), by the nucleophilic aromatic substitution between the 4-aminoaniline with 4-fluoro-nitrobenzene, we obtained compound **5**. The nitro groups were then reduced with hydrazine and palladium on carbon to obtain amine **6** in good yield. The subsequent acylation with 6-bromohexanoyl chloride allowed us to prepare TATA **7** which was successively reacted with sodium azide in DMF to obtain precursor **8**. Finally, in the last step, the click reaction, catalyzed by copper bromide, between **9** and the alkyne derivative of TPE **4**, gives access to **3TPE-TATA** in excellent yield.



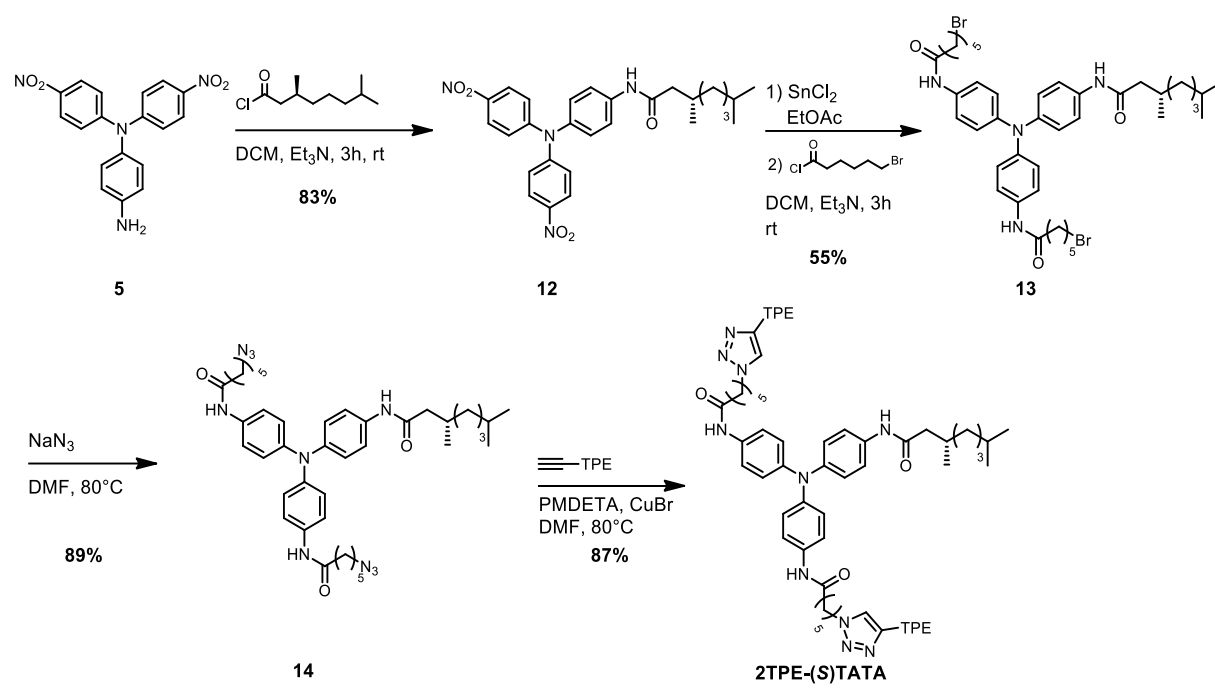
Scheme 6 | Synthetic pathway to compound **3TPE-TATA**.

The chiral chains, for the synthesis of compounds **2TPE-(S)TATA** and **1TPE-(S/R)TATA** were obtained starting from (*S*)-citronellol and (*R*)-citronellol, in few steps, according to a reported protocol (**Scheme 7**).¹⁷⁷



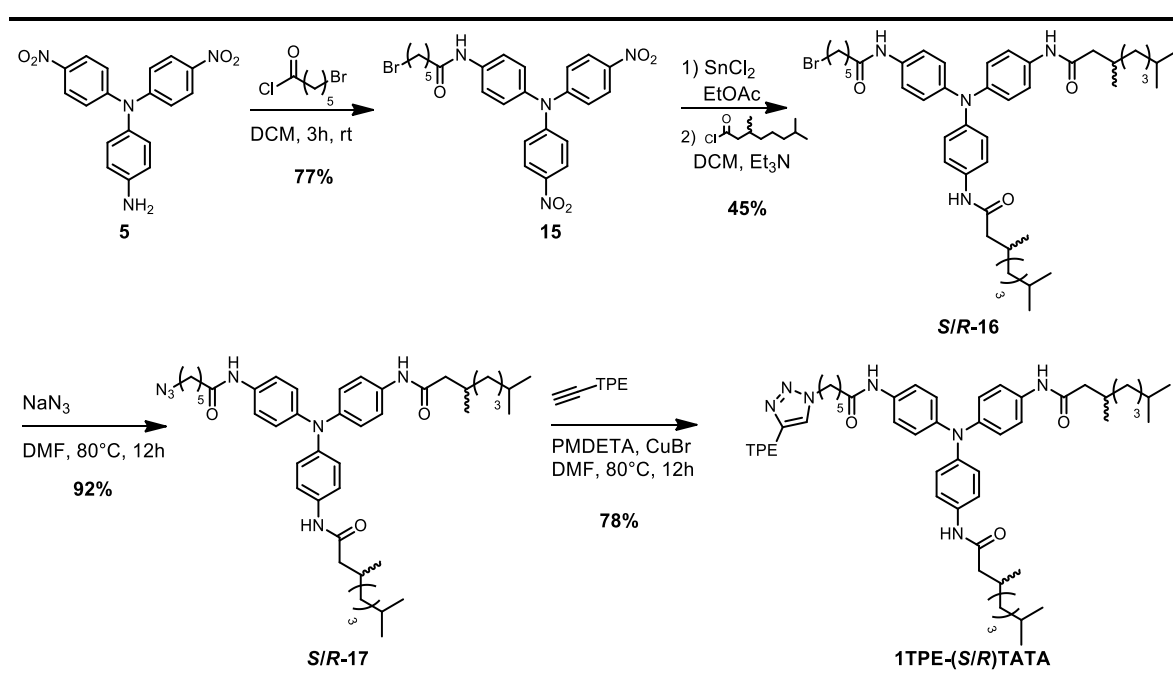
Scheme 7 | Synthesis of the chiral chains.

Compound **2TPE-(S)TATA** was synthesized starting from triarylamine **5**, by firstly acylating the amino group reacting it with **S-11** to obtain compound **12**. The nitro groups were then reduced by tin chloride and the generated amines were functionalized with 4-bromo-hexanoyl chloride to afford TATA **13**. The two bromo- groups of **13** are then substituted with azido-groups to obtain compound **14**, which is then coupled, *via* click reaction, with **4** to achieve the target molecule **2TPE-(S)TATA** (**Scheme 8**).



Scheme 8 | Synthetic route to compound **2TPE-(S)TATA**.

The last two compounds, the enantiomers **1TPE-(S)TATA** and **1TPE-(R)TATA**, were synthesized starting from triarylamine **5** with a similar pathway (Scheme 9) as for compound **2TPE-(S)TATA**. The amine **5** is firstly functionalized with 4-bromo-hexanoyl chloride and in a subsequent step, after reduction of the nitro groups, substituted with the chiral amidic chains to afford TATAs **S-16** and **R-16**. As for previous compounds, the click reaction with TPE **4**, allowed us to obtain the two final enantiomers.



Scheme 9 | Synthetic route to compounds 1TPE-(S)TATA and 1TPE-(R)TATA.

2.2.3 Properties of 3TPE-TATA

After the synthesis, compound **3TPE-TATA** was characterized by standard spectroscopic and spectrometric methods (mass by ESI and NMR spectroscopy; see experimental part). We then started to explore the properties of this derivative by testing its solubility in several organic solvents. Since the beginning, the compound showed a very limited solubility in most organic solvents, being insoluble in acetone, ethanol, DCM, toluene, acetonitrile, methanol, xylene, ethyl acetate, *etc.* Limited solubilities were observed in DMF and THF while only DMSO and mixtures toluene/methanol were able to fully solubilize the molecule. In a general way, low solubility may be advantageous towards the self-assembly and the formation of supramolecular networks, meaning that not negligible non-covalent forces take place between the monomers. Hence, we investigated whether the **3TPE-TATA** could form supramolecular assemblies and, in such case, if we could achieve a good control over the entire process and on the so formed morphologies. From our previous studies on triarylamine self-assembly, we knew that aromatic solvents are suitable for this task but, given the low solubility already showed in toluene even at high temperature, we chose more polar solvents with higher boiling points. Chlorobenzene turned out to be a good candidate since, upon cooling a hot solution to room temperature, the system showed a phase transition to form a gel at room temperature. Moreover, the gel showed

intense blue fluorescence when irradiated with UV light ($\lambda = 254$ nm), giving a fluorescent quantum yield (QY) of about 24% for a 1 mM gel ($\lambda_{\text{exc}} = 322$ nm). This confirmed, in a preliminary way, the SPIE properties of the system (**Figure 59a**). In order to observe the morphologies of the supramolecular architectures of the gel, we drop-casted it on copper TEM grids (covered by a carbon film) to direct observe the putative structures by microscopy. TEM analysis showed the formation of a dense network of fibers with a substantial presence of non-organized material (**Figure 59b**). Single fibers were observed even under fluorescence optical microscopy clearly assigning the origin of the fluorescence to the supramolecular polymers (**Figure 59c**).

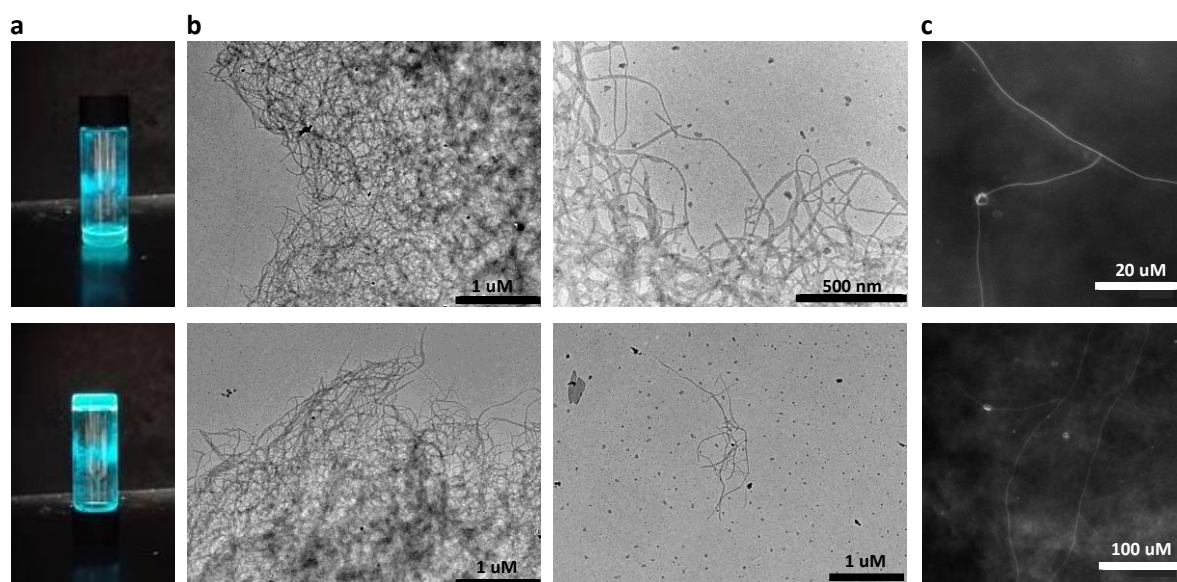


Figure 59 | a) Photographs of 1 mM gel of **3TPE-TATA** in chlorobenzene under UV irradiation ($\lambda_{\text{exc}} = 254$ nm); b) TEM images of drop-casted gels on copper TEM grids; c) Fluorescence optical microscopy images of isolated fibers ($\lambda_{\text{exc}} = 408$ nm).

In order to get a better overview on the gelation properties, like the temperature for the sol-gel transition and the minimum gelation concentration, we built a phase diagram by plotting the temperature for the sol/gel ($T_{\text{s/g}}$) and gel/sol ($T_{\text{g/s}}$) transition.

The first one was determined by using light diffusion techniques: the sample is constantly irradiated with a laser beam while cooling it down to room temperature. As long as no aggregation occurs, the intensity of the beam remains unaffected but, as soon as the $T_{\text{s/g}}$ is reached, the light is diffused by the sample and the intensity of the beam decrease. For the reverse process we adopted the tube test: several samples, at different concentrations, were

gradually heated until the $T_{g/s}$ is reached and the gel breaks and start to flow. The phase diagram shows high $T_{g/s}$ being close to 100 °C, and the $T_{s/g}$ values were even higher. This significant hysteresis underlines the cooperativity of the self-assembly process. The lowest gelation concentration was about 0.8 mM, thus we chose 1 mM as concentration for the following characterizations to ensure the system exhibits a gel state (see Annexes; **Figure A 1**) and the melting temperature lays within the measurable domain.

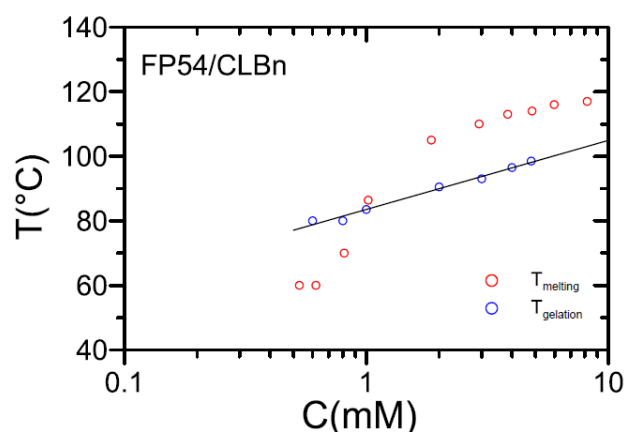


Figure 60 | Phase diagram for compound **3TPE-TATA** in chlorobenzene. The red dots correspond to $T_{g/s}$ obtained by the tube inversion test; the blue dots correspond to $T_{s/g}$ obtained by light diffusion.

Variable temperature UV-vis measurements of a solution of **3TPE-TATA** in toluene (1 mM) showed an hypsochromic shift of the absorbance together with a decrease in the intensity (**Figure 61a**) of the absorption band. This behavior has been already reported for other triarylamine trisamides derivatives and was ascribed to the π - π stacking interactions between piled triarylamine cores.¹³⁴ We further characterized the SPIE properties by variable temperature fluorescence of a 1 mM gel in chlorobenzene and, as shown in **Figure 61b**, we only observed the presence of a weak emission band at 400 nm at high temperature (105 °C). This can be explained by the aggregation induced emission properties of the triarylamino- core, suggesting that, even at high temperature, some nuclei are already assembled. Such nuclei are too small to freeze the rotors of the TPE units on the periphery but are big enough to restrict the conformation of the TATA cores in a stable propeller shape, activating its emission. As soon as the temperature is decreased, the supramolecular polymerization moves forward, and the growth of the polymer starts to block the intra-molecular rotation of the TPE moieties enhancing the observed fluorescence as an intense band with its maximum at 490 nm. The

decrease of the fluorescence, which occur between 55 °C and 20 °C is mainly due to a phase separation and precipitation of the material out of solution.

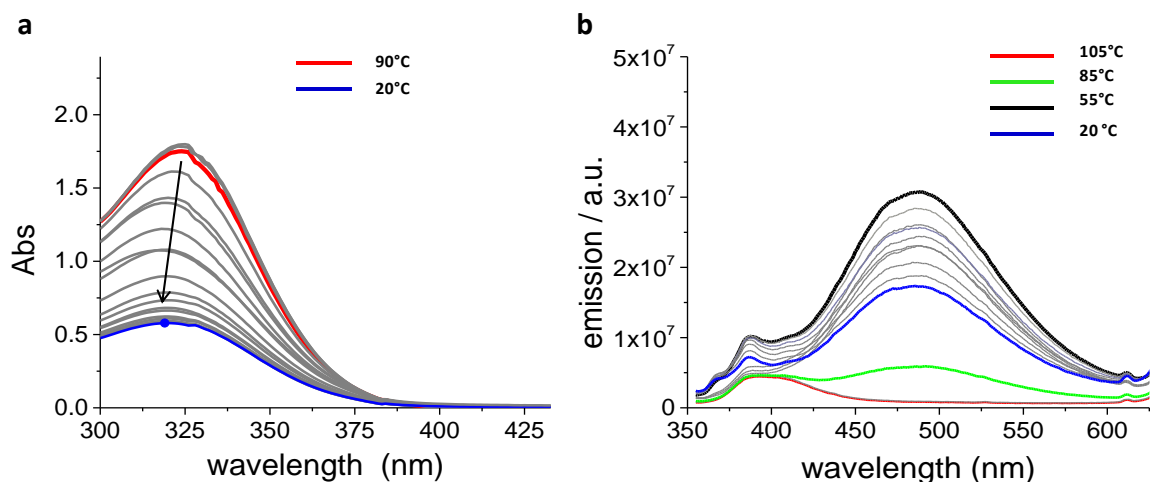


Figure 61 | a) Temperature-dependent absorption spectra of a 1 mM chlorobenzene solution of **3TPE-TATA** recorded during the cooling down process from 90 °C (red line) to 20 °C (blue line) at a rate of 5 °C/min; **b)** Temperature-dependent emission spectra of a 1 mM chlorobenzene solution of **3TPE-TATA** recorded during the cooling down process from 105 °C (red line) to 20 °C (blue line) ($\lambda_{\text{exc}} = 322 \text{ nm}$).

As a control experiment, we performed variable temperature fluorescence of two reference compounds for the TPE and the TATA units. We chose, respectively, the alkyne-substituted TPE (**4**) and the 3N₃-TATA (**8**). As reported below, compound **4** showed no fluorescence during the cooling of the solution to room temperature (**Figure 62a**). On the other hand, compound **8** showed an enhancement of the fluorescence as soon as the temperature is decreased, and the molecule assemble to form supramolecular fibers (**Figure 62b**). This test underlines the synergistic effect of the two moieties, with the TATA driving the self-assembly, and the TPE providing strong emission in *solid* state.

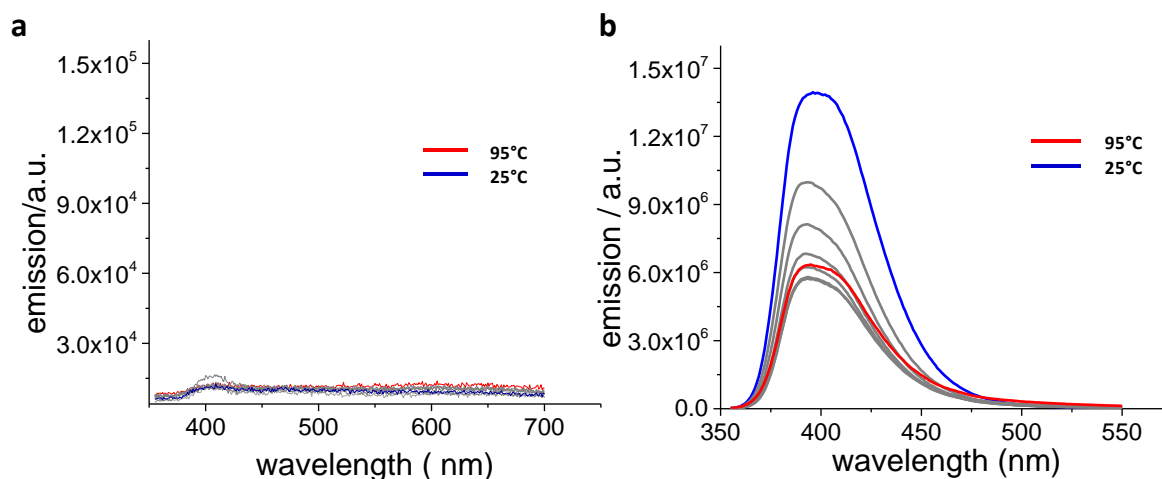


Figure 62 | **a**) Temperature-dependent emission spectra of a 1 mM chlorobenzene solution of **4** recorded during the cooling process from 95 °C (red line) to 25 °C (blue line); $\lambda_{\text{exc}} = 322$ nm; **b**) Temperature-dependent emission spectra of a 1 mM chlorobenzene solution of **8** recorded during the cooling process from 95 °C (red line) to 25 °C (blue line); $\lambda_{\text{exc}} = 322$ nm.

Despite the good results obtained with this molecule, we were never able to reach a good control on the self-assembly process which always occurred together with what appeared to be amorphous precipitation. The high tendency to precipitate for such a derivative can be explained by the number of TPE units per TATA molecule. The intrinsic nature of the AIE effect, the need for the fluorophore to aggregate in a disordered way preventing destructive π - π interactions, is effectively too well accomplished by the TPE moiety. In our derivatives, it is of utmost importance to reach a balance between the TPE-driven disorganized aggregation and the well-organized self-assembly of the TATA cores. It is apparent that the three TPEs on the periphery of compound **3TPE-TATA** make it almost impossible to achieve a high degree of organization and any kind of control on the supramolecular polymers which are formed.

2.2.4 Properties of chiral TPE-TATA derivatives

Since the presence of three TPEs units on the TATA core makes the aggregation of **3TPE-TATA** difficult to control, we hypothesized that the reduced number of TPEs on derivatives **2TPE-(S)TATA** and **1TPE-(S/R)TATA** would improve the degree of organization of the system. Moreover, the presence of branched chains should improve the solubility of the compounds, allowing us to obtain self-assembled structures in solvents with lower boiling points. The introduction of chiral moieties in the derivatives further provides us a common

methodology to follow the supramolecular polymerization, given the typical chirality transfer from monomers to assemblies should be accompanied by the appearance of a Cotton effect in the CD spectra. We first tested the self-assembling properties for **2TPE-(S)TATA** and **1TPE-(S)TATA** and, even if we observed the formation of a gel phase upon cooling a 1 mM solution in chlorobenzene, we decided to explore other solvents as well. We found that, for both the compounds, a good solubility in hot toluene and, upon cooling a 1 mM solution, we observed the formation of macroscopic aggregates. TEM analysis disclosed the presence of fibrillar structures for both samples with morphologies similar to **3TPE-TATA** (Figure 63).

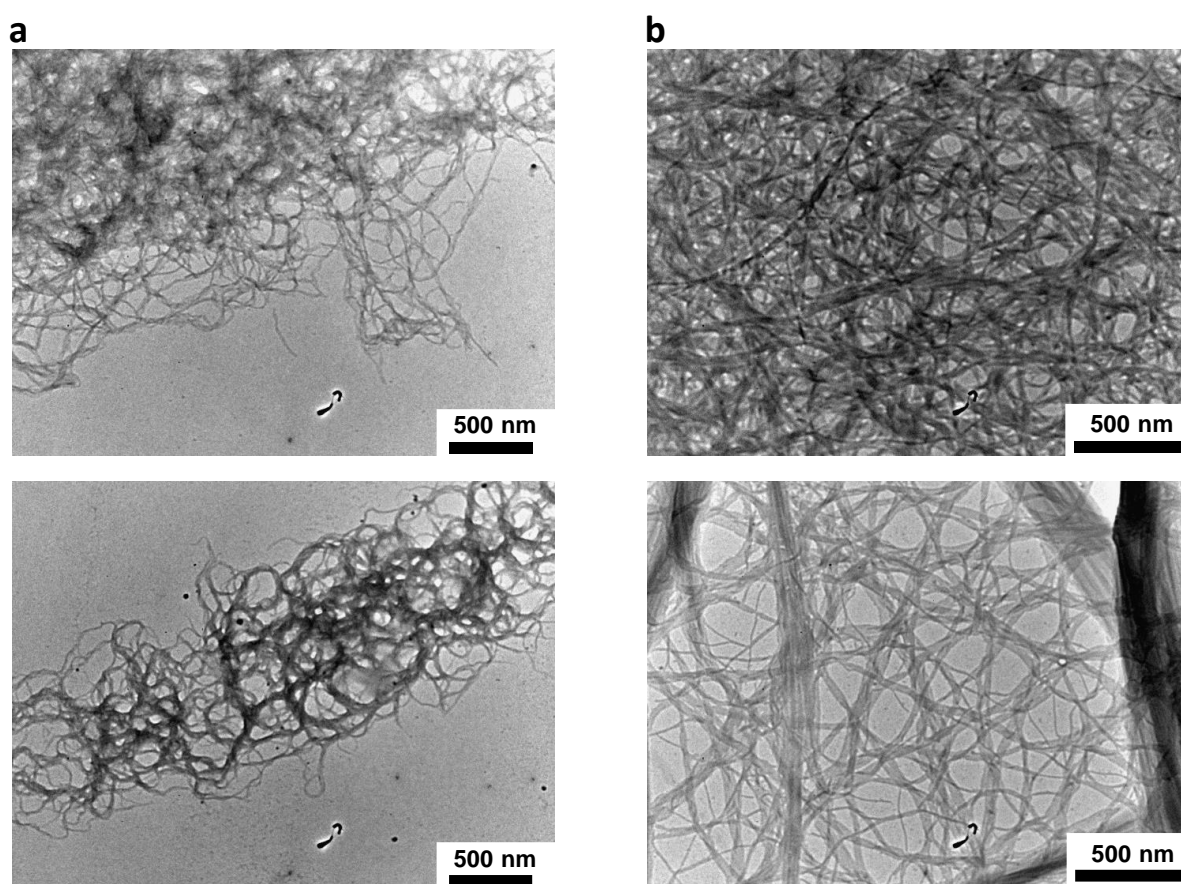


Figure 63 | a) TEM images obtained for a 1 mM solution of **2TPE-(S)TATA** in toluene; b) TEM images of a 1 mM solution of **1TPE-(S)TATA** in toluene.

Despite both the compounds showing excellent assembling properties, further tests demonstrated a higher degree of order and solubility for compound **1TPE-(S)TATA**. Thus, coherent with our goals, we decide to fully characterize the latter in priority. Fluorescence spectroscopy recorded upon cooling a 3 mM solution in toluene to room temperature, demonstrated the SPIE properties of **1TPE-(S)TATA**. In a similar way, we performed variable

temperature CD experiment on a 0.1 mM solution in toluene. As shown in fig, at 100 °C, no Cotton effect is detected, which means that the system is molecularly dispersed. As soon as the system is cooled to room temperature, a bisignate Cotton effect appears, indicating, that the system is polymerizing with a predominant helicity

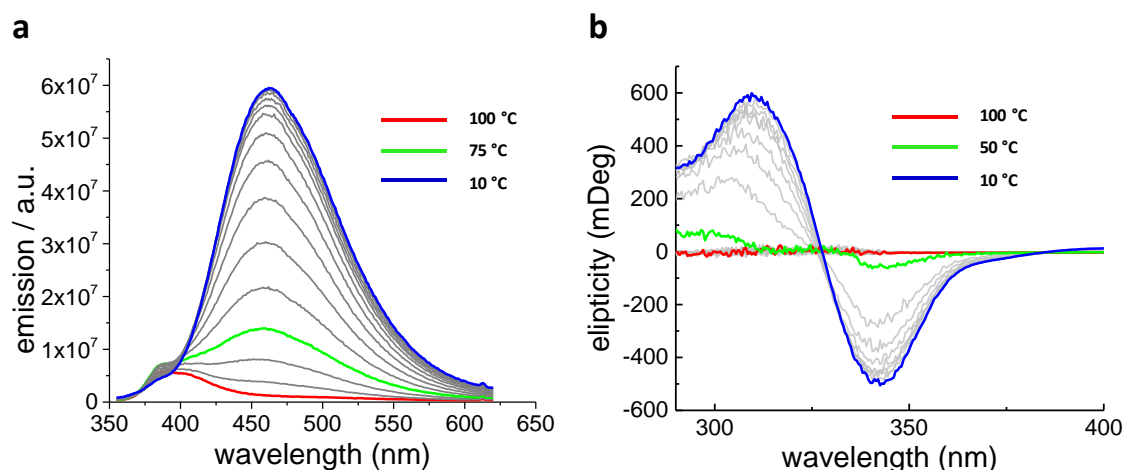


Figure 64 | a) Temperature-dependent emission spectra of a 3 mM solution in toluene of **1TPE-(S)TATA** recorded during the cooling process from 100 °C (red line) to 10 °C (blue line) ($\lambda_{exc} = 322$ nm); b) Temperature-dependent CD spectra of a 0.1 mM solution in toluene of **1TPE-(S)TATA** recorded during the cooling process from 100 °C (red line) to 10 °C (blue line).

Interestingly, we observed a great influence of the cooling rate adopted for the supramolecular polymerization process on the chiral response of the system. First, we performed a fast cooling (5 °C/min) of a 0.1 mM solution of **1TPE-(S)TATA** in toluene, and we followed the CD signal at 322 nm on a cooling/heating cycle. As shown below, we observed a very low Cotton effect, indicating only limited chirality transfer to the supramolecular structures. For a medium cooling rate (1 °C/min), the signal at 322 nm increase up to 60 mDeg at the end of the cooling process, indicating that the monomers assembled with a preferential helicity. Finally, for slow cooled sample (0.1 °C/min), we recorded very intense CD signal, up to 700 mDeg. The observation that, supramolecular polymers obtained through different cooling processes show different CD spectra, suggest that the morphologies of such polymers should show significant differences. Hence, we analyzed through TEM imaging the aggregates obtained from the three different cooling regimes, and we found that, fast cooled sample gave a network of thin, long and soft fibers with a certain amount of non-organized material. On the other hand, slow cooled

samples, showed thicker bundles of fibers with longer persistence length, and a minimization of the disorganized precipitation.

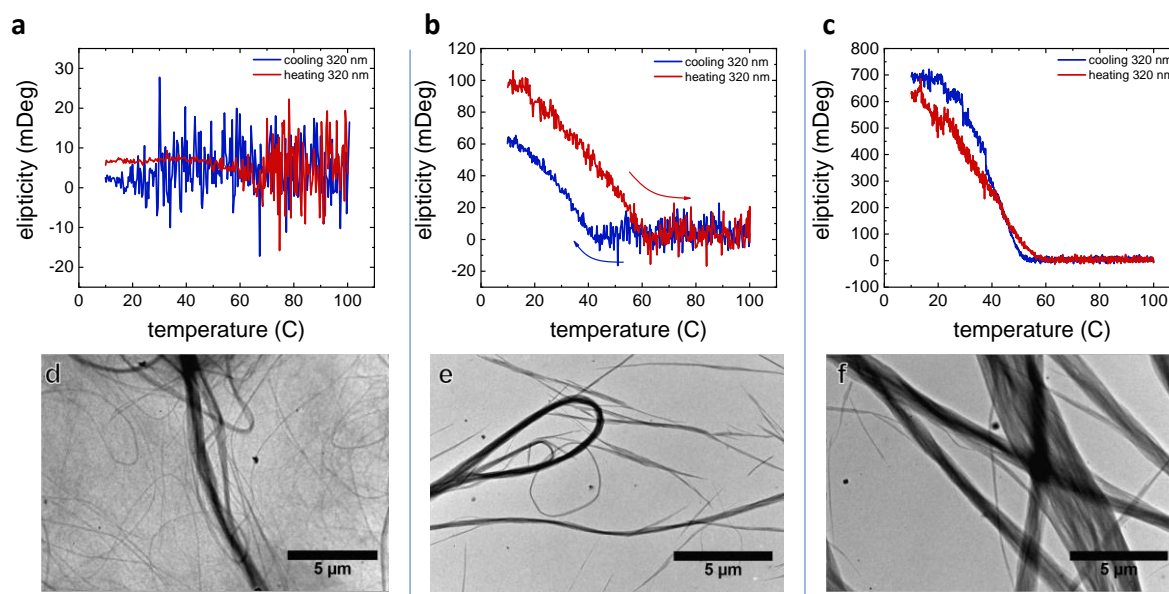


Figure 65 | Evolution of CD signal at 322 nm (top images) during a cooling/heating process for a 0.1 mM solution of **1TPE-(S)TATA** in toluene and related TEM sample of supramolecular polymers for three different cooling regimes: 5 °C/min (**a**; **d**); 1 °C/min (**b**; **e**); 0.1 °C/min (**c**; **f**).

Thus, CD and TEM analysis indicated that supramolecular polymers obtained after slow cooling, are organized in higher hierarchical levels compared to fast cooled ones. SAXS and WAXS analysis further confirmed the higher order of the assemblies for a slow cooled 1 mM solution compared to those of a fast cooled (see Annexes; **Figure A 2**).

Moreover, when the fluorescence properties of a slow cooled 0.1 mM solution of **1TPE-(S)TATA** in toluene were explored, it showed the highest quantum yield value, close to 37 % ($\lambda_{exc} = 322$ nm) that we have observed for this family of compounds. Indeed, when compared to the QY of the **3TPE-TATA** (QY = 24%) it is evident that the higher organization at a supramolecular level, as shown by the chiral compound, leads to a better molecular packing and a stronger restriction of the intramolecular motion, thus, enhanced fluorescence.

We further investigated the properties of the other enantiomer, compound **1TPE-(R)TATA**, and we performed variable temperature CD measurements to compare the results to those obtained from compound **1TPE-(S)TATA**. Since the chirality of the chains is reversed, we expected these supramolecular polymers to show an opposite helicity as compared to the polymers of **1TPE-(S)TATA**. This assumption was confirmed by the CD spectrum of a fast-

cooled sample of **1TPE-(R)TATA** which appears as the mirror image of its enantiomer (**Figure 66a**). This indicates that the monomers aggregate in fibers with an opposite helicity under the influence of the molecular chirality. Surprisingly, a different behavior was observed on the supramolecular polymers obtained through a slow cooling process. Here, the two enantiomers gave an almost identical CD spectrum which can be translated to supramolecular structures with the same chirality (**Figure 66b**). We hypothesized that, upon cooling a solution of molecularly dispersed monomers, the system first starts to nucleate in primary structures, whose helicity is controlled by the chirality of the lateral chains. These primary assemblies can further aggregate together, driven by lateral interactions, in hierarchical structures like superhelices, which are thermodynamically favored. At this stage, the chirality, showed by these polymers, is not anymore influenced by the molecular chirality but by the entanglement of the primary structures. Hence, during a fast cooling process, primary structures are formed which lack the time to self-organize in more complex architectures and result, thus, in the kinetically trapped structures. In addition, these assemblies turned out to be stable for several months. On the other hand, performing a slow cooling allows the primary structures to equilibrate and self-assemble in hierarchical superstructures.

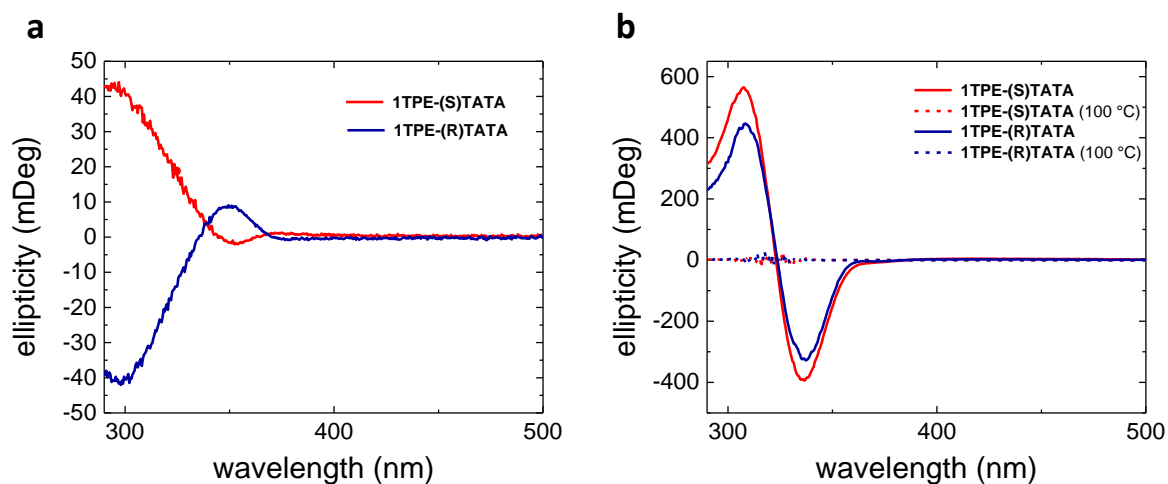


Figure 66 | a) CD spectra after fast cooling of 0.1 mM solutions of **1TPE-(S)TATA** (red) and **1TPE-(R)TATA** (blue); b) CD spectra for molecularly dispersed systems (dashed lines) and after slow cooling (0.1 °C/min; solid line) of 0.1 mM solutions of **1TPE-(S)TATA** (red) and **1TPE-(R)TATA** (blue).

When investigating the origin of the supramolecular chirality observed on slow cooled sample, we were able to exclude contributions from linear dichroism (LD), since we always detect LD values at least 1000 times lower than the CD values; furthermore, the two contributions appear

to be not correlated (i.e. depending on the sample preparation variations of more than 100 times the intensity of the LD are observed with only minor changes in CD signal). On the other hand, we have observed a correlation between the intensity of the signal and the stirring speed of the solution during the cooling down process. In particular, high values of CD were obtained only when the system was vigorously stirred (400 rpm). Thus, we wonder if the stirring could have a direct influence in entangling the fibers generating the observed chirality and whether a clockwise or anticlockwise rotation may generate the two different helicities. To clarify this hypothesis, a solution of **1TPE-(R)TATA** was fast cooled to generate the “kinetic” product and the CD spectrum acquired (**Figure 67**); then, the solution was left for 10 days at 40 °C degrees without stirring to see if the system would evolve towards the putative thermodynamic product. The CD signal did show an amplification of the original signal but without conversion to the more stable product. Next, we started to stir the system clockwise and we further waited for 5 days at 40°C. At the end of these experiment, the CD spectrum was measured again. Surprisingly, the CD signal showed a transition towards the “thermodynamic product”.

Repeating the previous experiment again but stirring on the opposite direction (i.e. anticlockwise) we obtained the same results, indicating, that, the stirring is not directly entangling the fibers and therefore not transferring its “chirality” but it is, in some way, necessary to determine or accelerate the formation of the supramolecular state showing the strongest helicity as observed by CD spectroscopy (**Figure 67**).

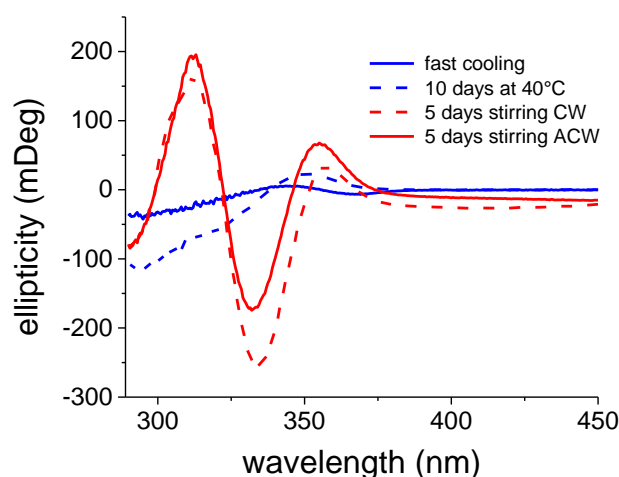


Figure 67 | Evolution of the CD spectrum for a fast cooled sample (solid blue line) after 10 days at 40 °C without stirring (dashed blue line), after 5 days stirring clockwise at 40 °C (dashed red line) and after 5 more days after stirring anticlockwise at 40 °C (solid red line) for 0.1 mM solution of **1TPE-(R)TATA** in toluene.

At the time of writing, we do not have a fully proven hypothesis on the way the stirring is affecting the formation of hierarchical structures. One alternative is that it could be due to a simple effect on the homogeneity of the solution, diminishing the local concentration gradient of monomers. Another possibility is to be found in the mechanism that leads to the hierarchical structures: we think that the primary assemblies coagulate together during an early stage of the supramolecular polymerization. Thus, when the primary assemblies exceed a certain length, the secondary nucleation become less favored. In such context, stirring would contribute to break the primary structures allowing the formation of the thermodynamically more stable superstructures.

2.2.5 Circularly polarized luminescence for **1TPE-(S)TATA** and **1TPE-(R)TATA**

Given both the strong emission and circular dichroism shown by **1TPE-(S)TATA** and **1TPE-(R)TATA**, we decided to investigate, in collaboration with the group of Professor D. Bassani in Bordeaux, the circularly polarized luminescence (CPL) for both compounds under the two extreme (slow and fast) regimes described to prepare the self-assembled materials. As can be seen from **Figure 68a**, a strong CPL signal was observed for slow cooled **1TPE-(S)TATA**, with g_{lum} values as high as $15 \cdot 10^{-3}$. Unfortunately, the same sample also showed a non-negligible value of linear polarized luminescence (LPL) (**Figure 68b**) probably due to the presence of long and thick bundles of fibers. The presence of such LPL indicates that the observed CPL may be, at least partially, due to an artefact of the measurement. On the other hand, supramolecular polymers obtained through slow cooling process of a **1TPE-(R)TATA** solution displayed a less important CPL signal but, on the bright side, a much lower intensity of the corresponding LPL. Both results combined indicate that, although we cannot neglect the contribution of the linearly polarized luminescence to the detected CPL, it is certain that our supramolecular polymers can act as circularly polarized emitters. Samples prepared following the fast cooling protocol, for both compounds **1TPE-(S)TATA** and **1TPE-(R)TATA**, showed weaker values of LPL and CPL, which is consistent with the lower degrees of organization leading to softer and thinner fibers with short persistence length.

It is important to mention that, as already observed in the CD experiments, the CPL spectra of the two enantiomers displayed the same sign and not, as expected, the mirror image of each other. This finding further confirmed our assumption of the factors that determine the supramolecular chirality: the helicity of the higher hierarchical structures (i.e. bundles of fibers)

is only poorly influenced by the molecular chirality, but mostly by the propeller-like conformation adopted by the triarylamine core in the assembly. Another important conclusion, obtained from our CD experiments, that should be stressed in the context of CPL, is that it is possible to reduce – or even invert – the detected LD of the sample by mechanical action (shacking, stirring) without significantly affecting the detected CD signal intensity.

Overall, we observed significant values of circularly polarized luminescence for slow cooled samples. It is not possible to exclude the presence of artefacts due to the linearly polarized luminescence and, thus, to extrapolate the precise values of $glum$. Nevertheless, the general trend is confirmed, namely, the presence of hierarchical assemblies in slow cooled samples leads to stronger CPL signals as compared to the supramolecular polymers of fast cooled ones.

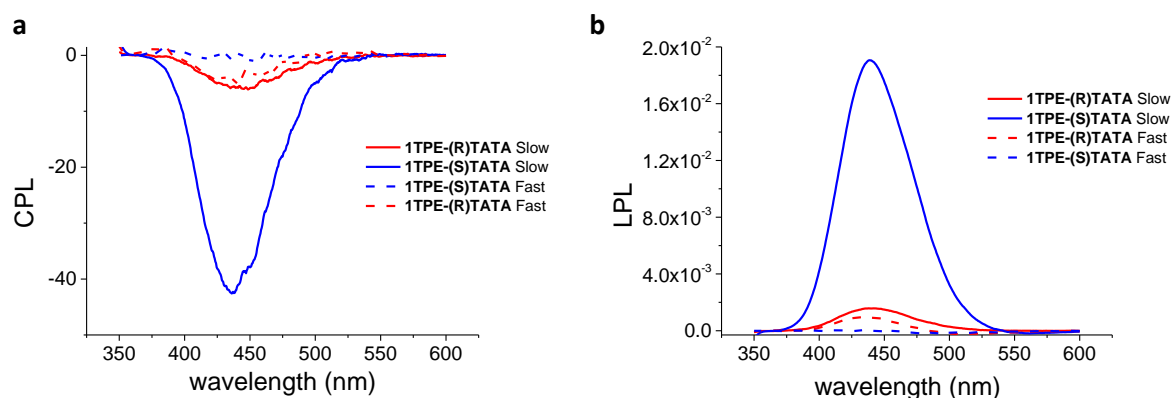


Figure 68 | a) Circular polarized emission for slow and fast cooled samples of **1TPE-(S)TATA** and **1TPE-(R)TATA** (0.2 mM, toluene); **b)** Linearly polarized luminescence for the same samples (see legends).

We then imaged the fibers by confocal polarized microscopy for both slow and fast cooled samples, by irradiating the samples at 375 nm and detecting above 405 nm. We observed strongly polarized light emitted from the bundles of fibers in all samples (**Figure 69a** ; **Figure 70a**), while the amorphous material showed no significant polarization (**Figure 72a**). Intriguingly, we detected two components for the light emitted by the assemblies as shown by the quantification of the polarization along the fibers (**Figure 69b**). To better understand the origin of these components, we measured FLIM under parallel and perpendicular detection (**Figure 72c** ; **Figure 69d**) observing that all the fibers show both of the components. This suggests that different parts of the molecule might be at the origin of the two components that we observe, and that each of these components has a preferential polarization. A similar behavior was observed for the slow cooled sample, which differs slightly on the morphologies

of the supramolecular polymers, and mainly on the amount of amorphous material present (Figure 70b ; Figure 70c).

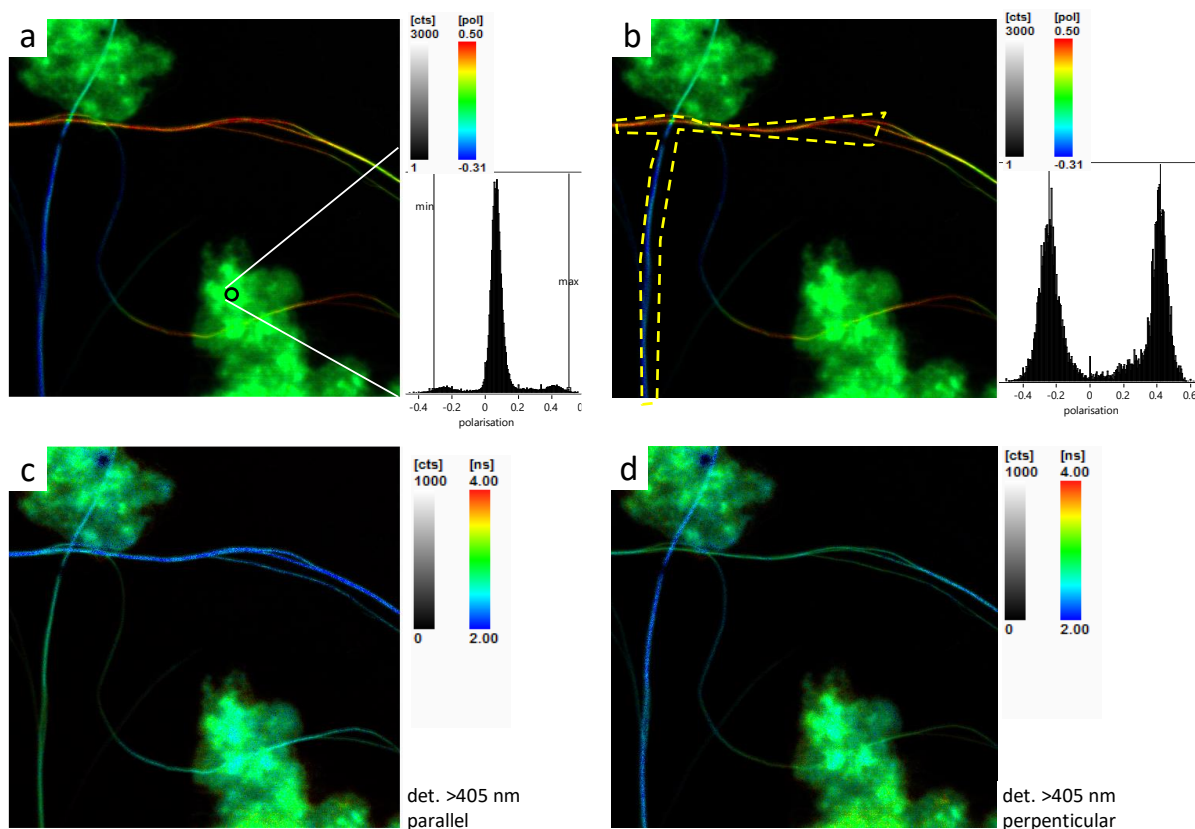


Figure 69 | a,b) Confocal polarized microscopy images obtained for a fast cooled sample of **1TPE-(S)TATA** (1 mM, toluene); The quantification of the observed polarization for amorphous material (a) and fibers (b) are depicted next to the image. FLIM images for the same samples at parallel (c) and perpendicular (d) polarization of the detection.

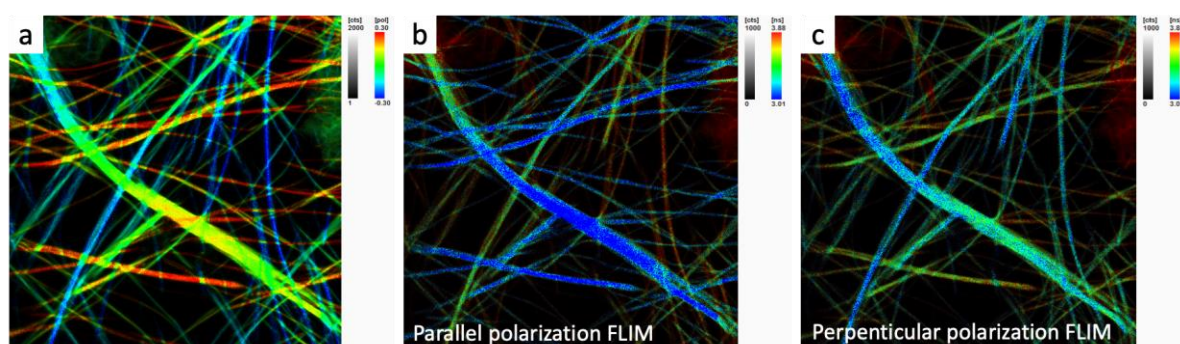


Figure 70 | a) Confocal polarized microscopy images obtained for a slow cooled sample of **1TPE-(S)TATA** (1 mM, toluene); FLIM images for the same samples at parallel (b) and perpendicular (c) polarization of the detection.

In light of these results, we hypothesize that the two components may be originated, independently, from the TATA core and the TPE motif. To further explore this assumption, we tried to selectively exclude one of the two components by detecting the emission at different wavelengths (**Figure 71**). Detection above 405 nm allowed to observed the sum of the contributions from both TATA and TPE as for previous experiments; detection above 490 nm allowed us to selectively exclude the emission from the TATA core, while detecting the polarized luminescence between 400 and 450 nm allowed us to focus on the TATA's contribution. As shown below, in all cases we detected polarized emission for all the fibers, suggesting that those two moieties are responsible for the different components. Moreover, the contribution coming from the TATA core appear more polarized than its counterpart but also a shorter fluorescence lifetime was observed when compared to the TPE component.

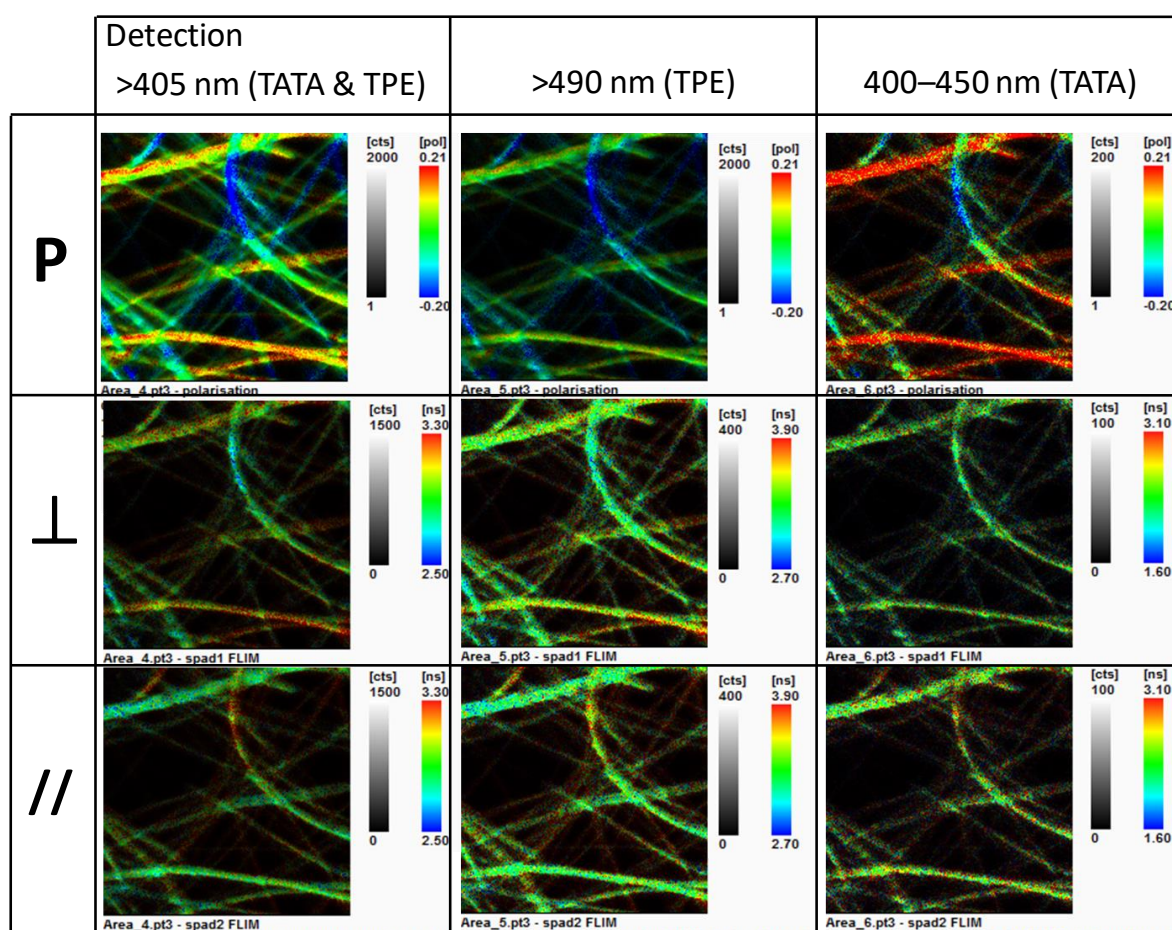


Figure 71 | FLIM images for a slow cooled sample of **1TPE-(S)TATA** (1 mM, toluene) under different polarizations of the detection: linear, perpendicular and parallel (rows), and for different detection wavelengths (columns).

2.2.6 Conductivity of **1TPE-(S)TATA** based supramolecular polymers

One of the main goals of this project is to develop supramolecular polymers with light emitting and hole transporting properties. In the first chapter we already described the hole transporting properties of the triarylamine core. Based on the published data, it is reasonable to postulate that the presence of a TATA unit in our derivatives should confer conductive properties to the materials. Moreover, it is well-known that the molecular arrangement within any conductive material has a big impact on its properties. Based on the findings described above, it is intriguing whether the change in luminescent properties is also correlated to charge mobility. Effectively, we wanted to investigate the consequences of the supramolecular architectures on the desired properties.

To test this hypothesis, we performed conductivity measurements, in ITO cells (see Annexes; **Figure A 9**), on fast and slow cooled solutions (0.1 mM) of **1TPE-(S)TATA**, in a mixture toluene/TCE (9:1). The presence of a small amount of TCE allows to oxidize the TATA part of the molecule by light irradiation, effectively doping with holes the supramolecular polymers, which greatly increases its conductivity. As shown below, (**Figure 72**) for slow (red lines) and fast (blue lines) cooled samples, before the light irradiation (solid lines), we measured only low currents, in the order of 10^{-11} A, for both samples which is consistent with our previous reports. After irradiation for 5 minutes, we observed a ten-fold increase in the measured current (dashed lines) for both the samples. Remarkably, when continuing the irradiating for further 25 minutes, the conductivity of the slow cooled sample increases dramatically while the other sample showed almost no significant changes (dotted lines). These results indicates that the well-organized supramolecular polymers obtained through slow cooling indeed behaves different that the less ordered sample.

Although these results are preliminary and there are technical and methodological issues to be addressed, their consistency with the observed supramolecular constructions and our understanding of the TATA conducting systems are extremely promising: Indeed, a higher electric conductance is perfectly in line with the presence of longer and stiffer bundles of fibers for slow cooled samples; A slower kinetic of photo-oxidation is also easily explained by densely-packed fibers is the same system; and a similar observation can be made for the less organized fast cooled sample, in which disorder leads to easier photo-oxidation but given only limited access to highly conducting materials.

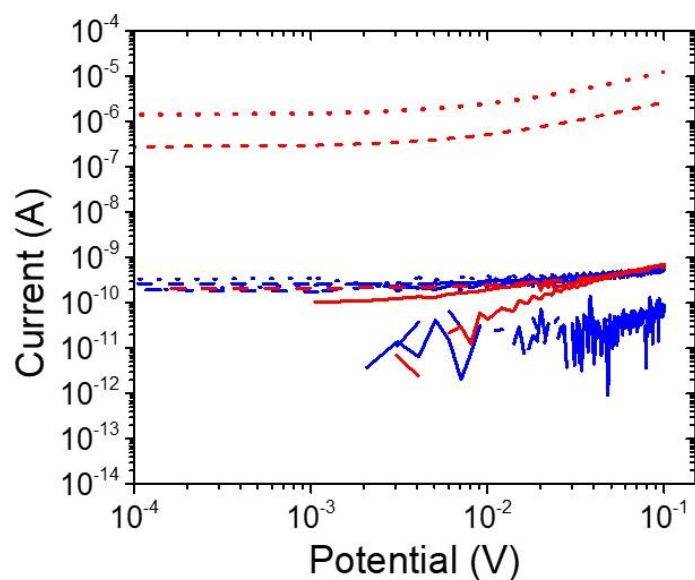


Figure 72 | I-V curves of fast (blue lines) and slow (red lines) cooled 0.1 mM solutions of **1TPE-(S)TATA** in toluene before light irradiation (solid lines), after 5 minutes irradiation (dashed lines) and after 30 minutes (dotted lines) of light irradiation.

2.2.7 OLED device based on **1TPE-(S)TATA** polymers

In order to test our supramolecular polymers in OLED applications, we built a multilayer device employing our polymers as active emitting layer. The geometry of the devices, reported below (**Figure 73a**), uses poly(3,4-ethylenedioxythiophene) polystyrene sulfonate (PEDOT:PSS) as interfacial layer, VB-FNPD as hole-transport layer (HTL), our polymer as emitting layer, and 2,2',2''-(1,3,5-Benzinetriyl)-tris(1-phenyl-1-H-benzimidazole) (TPBi) as electron-transport layer. Such devices showed very weak electroluminescence (EL), and mainly coming from the VB-FNPD which is probably due to the recombination of the charges occurring in that layer. This is not due to the absence of fibers, since we could easily confirm their abundant presence on the surface by UV irradiation showing brightly luminescence fibers (**Figure 73d**)

As stated before, the surface of the device, imaged by microscopy, showed weak EL coming from the background (**Figure 73c**), but when focusing on the black spots, which are most likely due to the solvent dissolving the VB-FNPD layer, we detected weak EL coming from the fibers (**Figure 73e** ; **Figure 73f**). Another confirmation came by imaging the EL and detecting the polarization of the emitted light: as shown in image **Figure A 3** (see Annexes) we observed polarized emission only from the supramolecular polymers which appear colored in red and

blue on the green unpolarized background of the HTL. This indicates that an optimization of the devices' structure, like removal of the VB-FNPD layer, may lead to stronger EL allowing the charges recombination to occur at the emitting layer.

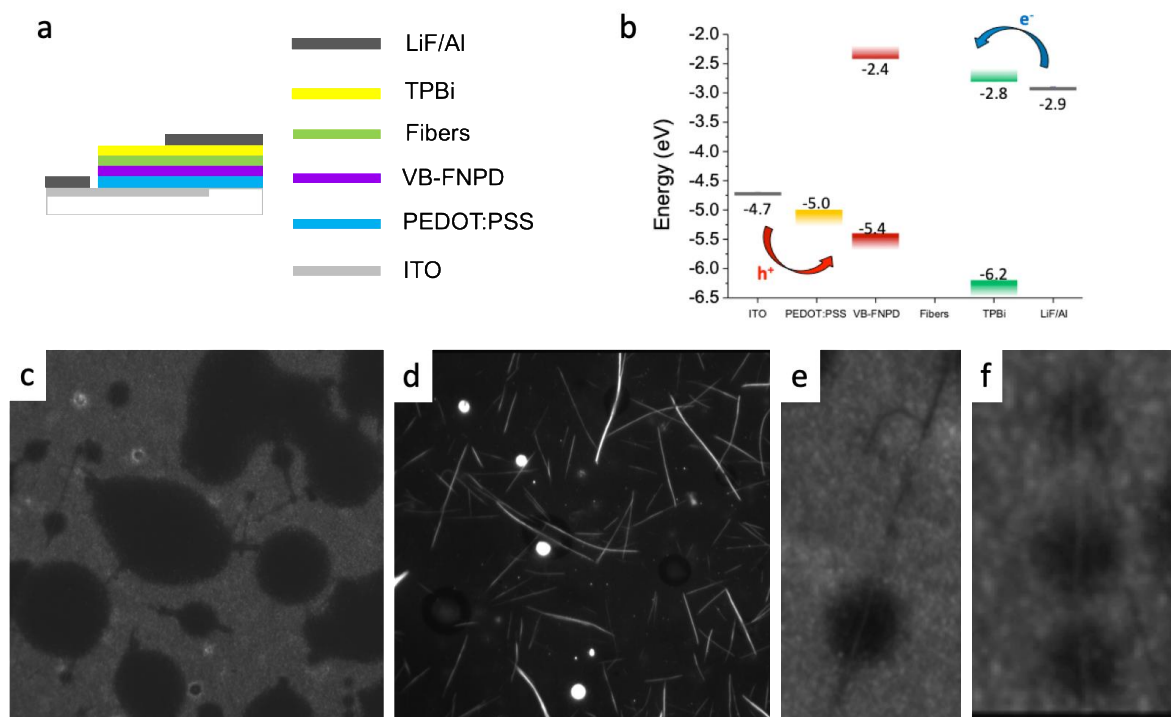


Figure 73 | a) Schematic structure of the multilayer device; b) Representation of the energetic levels for the different components of the device; c) Image of EL (4V) from the device built with **1TPE-(S)TATA** slow cooled polymers (78x78 μm); d) Image of PL ($\lambda_{exc} = 365$ nm) from the same area (detection with a long pass filter 405 nm); e,f) Images of the weak EL coming from the single fibers (zoom-in).

2.3 CONCLUSIONS AND PERSPECTIVES

In this chapter we prepared new triarylamine trisamides derivatives by combining TPE units and chiral chains to a central TATA core. As expected, the triarylamine motif endows the system to form supramolecular polymers upon cooling a molecularly dispersed solution. As consequence of the self-assembly, the intramolecular motion of the peripheric TPE moieties is restrained, switching on the fluorescence of these materials. Upon adjusting the architectures of the derivatives we found that, for compounds **1TPE-(S/R)TATA**, different morphologies can be achieved by changing the cooling rate. In particular, a kinetic product was obtained upon fast cooling while a thermodynamically, more stable, polymer was obtained by slow cooling. These different states showed significant differences under TEM microscopy and gave different CD signatures. The CD spectra, for the kinetic product, showed a direct influence of the molecular chirality while the thermodynamic one showed no correlation with the chirality of the monomer. This is mainly due to differences in the supramolecular polymerization processes, which requires a small nuclei in an initial stage. According to the cooling rate, this nuclei can undertake different pathways. Upon fast cooling, they only growth in primary structures, while in the case they are cooled down slowly, they can further assemble, by lateral interactions, leading to hierarchical architectures. The thermodynamic polymers obtained using compounds **1TPE-(R/S)TATA**, showed high fluorescent quantum yield together with the emission of circularly polarized luminescence. We further observed higher conductivity for the thermodynamic product as compared to that showed by the kinetic product.

Overall, we described triarylamine-based supramolecular polymers which show properties that make them promising for the implementation in optoelectronic devices. We demonstrated that we can control the supramolecular polymerization with the concomitant tuning of the functional characteristics showed by the materials.

In the next months, we will correlate the data from all the spectroscopic techniques (circular dichroism, fluorescence and UV-vis) which should allow us to fully understand the supramolecular polymerization mechanisms for compounds **1TPE-(S/R)TATA**. Further experiment will be addressed to optimize the geometry of the OLED devices to verify our hypothesis that by controlling the organization of the materials at the nanoscopic level, advantages can be obtained for the efficiencies of the devices.

CHAPTER III: TRIARYLAMINE BASED MACROCYCLE

3.1 INTRODUCTION

3.1.1 Self-assembly from conjugated macrocyclic units

Fully conjugated macrocyclic units represent a fundamental class of compounds with well-defined and persistent shape. Their intrinsic nature, as infinite π -conjugated system, allow them to show outstanding structural, optical and electronic properties.¹⁷⁸ Moreover, the intermolecular interactions between aromatic rings, or other functional groups, may allow the formation of self-assembled structures like: nanotubes, porous surfaces, fibers networks, etc.^{179,180,181}

Supramolecular polymers and materials based on conjugated macrocyclic units can show enhanced properties compared to those showed by their isolated monomers. This has increased the interest of the scientific community around the opportunities that such systems offer for the fabrication of nanoscaled optoelectronic devices.^{178,179} A few examples exemplifying the preceding will be discussed in the following.

The group of Mayor¹⁸¹ reported the synthesis and self-assembly of a series of shape-persistent macrocycles built by an alternating sequence of tetrafluorobenzene and benzene interconnected by diacetylene bridges (Figure 74a). The presence of fluorinated and non-fluorinated benzenes, enhances the π - π interactions between the monomers, leading to good self-assembling properties for these derivatives.¹⁸² The authors investigated the aggregation properties of six macrocycles by a combination of variable temperature ¹H-NMR and vapor pressure osmometry studies, in chloroform, finding a strong correlation between the number of fluorinated substituents of the derivatives and their self-assembling properties. For instance, the non-fluorinated macrocycle showed no aggregation tendency while all the fluorinated molecules showed self-assembling properties with a predominant formation of dimers. For compound **3**, upon cooling a hot solution in toluene, they observed the formation of rod-like crystallites which showed unique self-healing properties upon irradiation with the electron beam during SEM analysis (Figure 74b). Considering that, for most of the organic compounds, irradiation during SEM imaging charges the materials leading to its decomposition, the opposite behavior, showed by these aggregates, suggests an efficient charge transport mechanism within the rods. Further investigation demonstrated the presence of covalently linked dimers and trimers as

constituent monomers of the micro-rods. The authors hypothesized an oligomerization occurring in hot toluene between the diacetylene units of two stacked macrocycles.

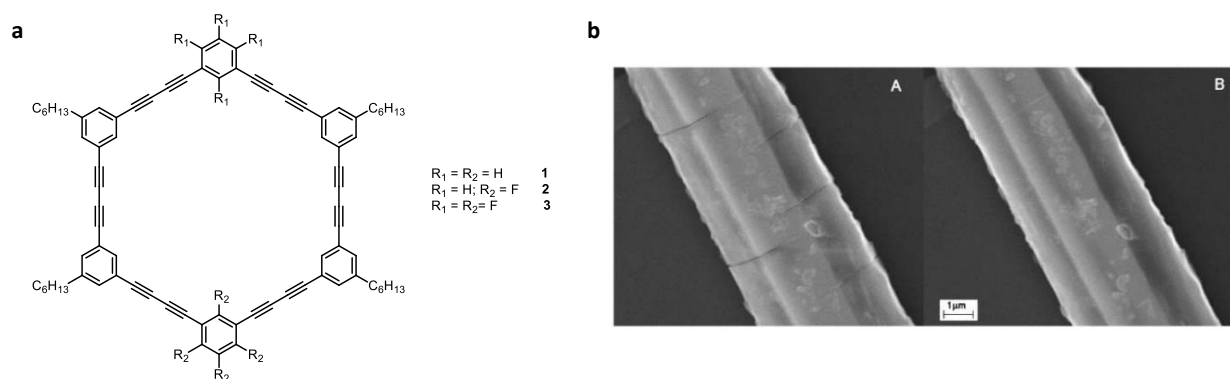


Figure 74 | a) Chemical structure of three out of six molecules object of the study; **b)** μ -rods obtained upon cooling a 50 °C solution of **3** in toluene, SEM images before (left) and after (right) irradiation with the electron beam; less defects are present after irradiation. (Reproduced from¹⁸¹).

In another example, Zang and coworkers successfully obtained 1D nanofibrillar assemblies from arylene ethynylene macrocycle (AEM) molecules. The flat nature of the macrocyclic core should promote, if balanced between the lateral interactions between alkyl chains, the stacking of several units in a one-dimensional aggregate. Moreover, the strong aromatic interactions between the aromatic rings may permit an efficient intermolecular electronic coupling. The authors succeeded in maximizing the growth along the main axis, over the lateral growth, by reducing the mobility of the molecules through the formation of a physical gel (**Figure 75**). Nanofibers, with a rigid structure, and well-defined internal channels, were then obtained, providing an interesting way to produced supramolecular materials for nanoscaled optoelectronic devices.¹⁷⁹

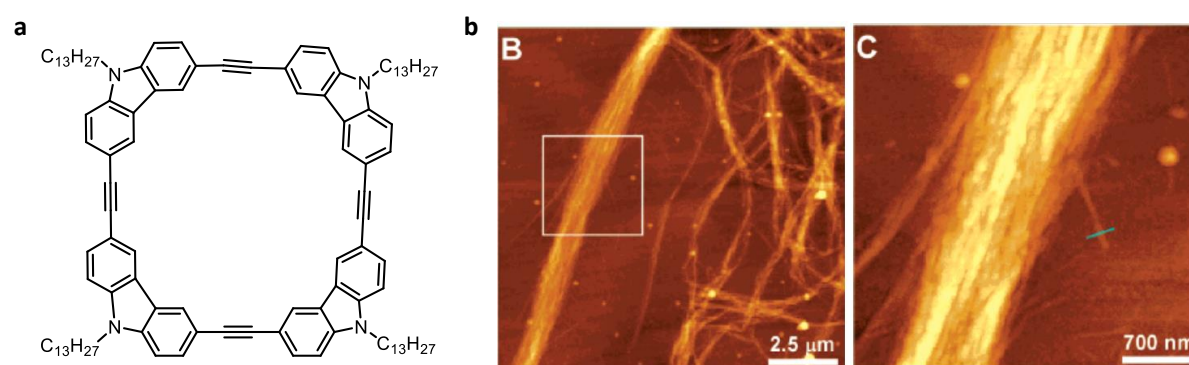


Figure 75 | a) Structure of the arylene ethynylene macrocycle (AEM); **b)** AFM images of the fibrous aggregates of the gel. (Reproduced from¹⁷⁹).

The magnetic properties of macrocyclic molecules can lead to powerful applications, as shown by Iyoda on a tetrathiafulvaleno[18]annulene system¹⁸³ (**Figure 76a**). Such derivative can self-assemble in THF/H₂O (1:1) mixture, by the means of S-S and π - π interactions, forming columnar architectures which show high charge mobility. Owing to the high magnetic anisotropy of the (supra)molecule, the authors succeed in orienting the fibers using a strong magnetic field. The induced ring current in the central annulene and the consequent diamagnetic response to the applied magnetic field, allows to obtain a parallel network of fibers aligned perpendicular to the applied magnetic field (\vec{B}) (**Figure 76b**). This bottom-up approach for the orientation in space of supramolecular, electronically active, materials is of particular interest for the construction of nanodevices.

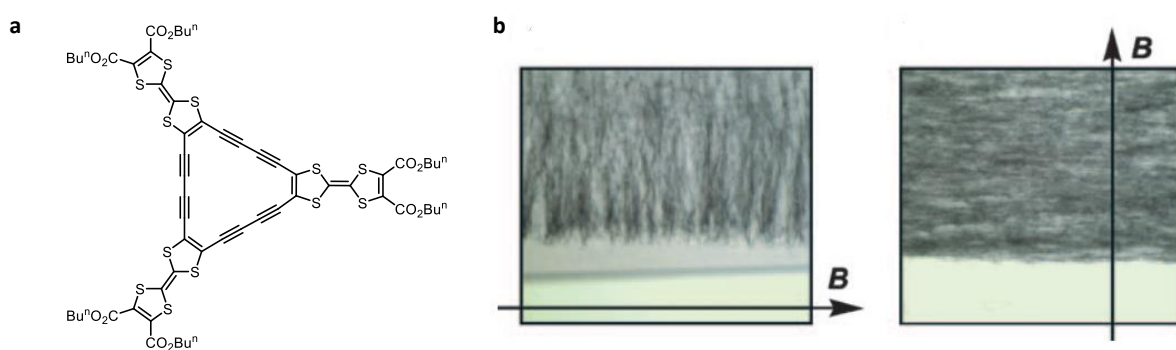


Figure 76 | a) Chemical structure of the tetrathiafulvaleno[18]annulene studied; b) Fibers oriented perpendicular to the magnetic field (5T). (Reproduced from¹⁸³).

3.1.2 Azacyclophanes

Conjugated macrocycles, in which aromatic rings are connected through nitrogen bridges, are called aza[1_n]cyclophanes. In this nomenclature, “1” represents the number of bridging atoms between the aromatic rings while “n” represents the total number of bridging atoms. The interest, around this class of compounds has increased during the last years in light of the possible applications in supramolecular and materials chemistry. In such cyclic oligoarylamines, the presence of multiple redox centers, constituted by the nitrogen nuclei, allows this materials to show peculiar electrochemical behaviors. The possibility to tune the size of the cavity, together with the different alternatives for the linking patterns between the aromatic rings and the nitrogen atoms, allows to differentiate the possible structures and the related properties. For instance, aza[1_n]meta-cyclophanes, in which the benzene units are interconnected by their *meta* position, enhances the ferromagnetic coupling between the radical

spin centers generated on the nitrogen nuclei. On the other hand, *aza*[1_n]*para*-cyclophanes show an extended π -conjugation over the macrocyclic structure.¹⁸⁴ In this context, the synthesis of macrocyclic oligoarylamines has represented, during last decades, a major challenge due to the absence of efficient synthetic strategies. The recent advances in palladium chemistry (as shown in *Chapter I*), boosted the study of this derivatives, provided an simpler approach to prepare various *aza*[1_n]*cyclophanes* with different arene-bridged patterns (**Figure 77**).

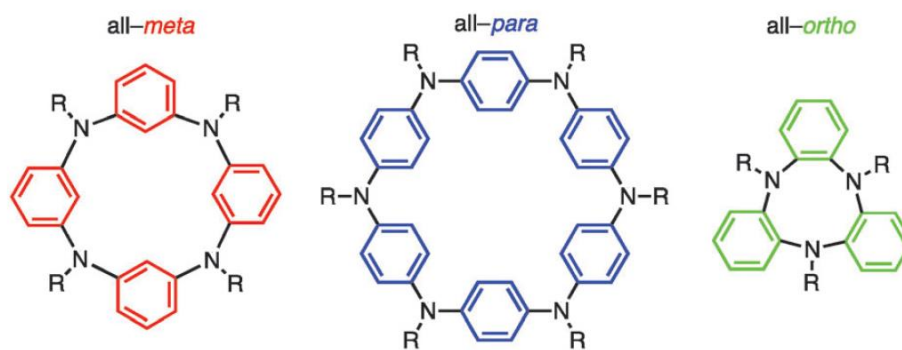
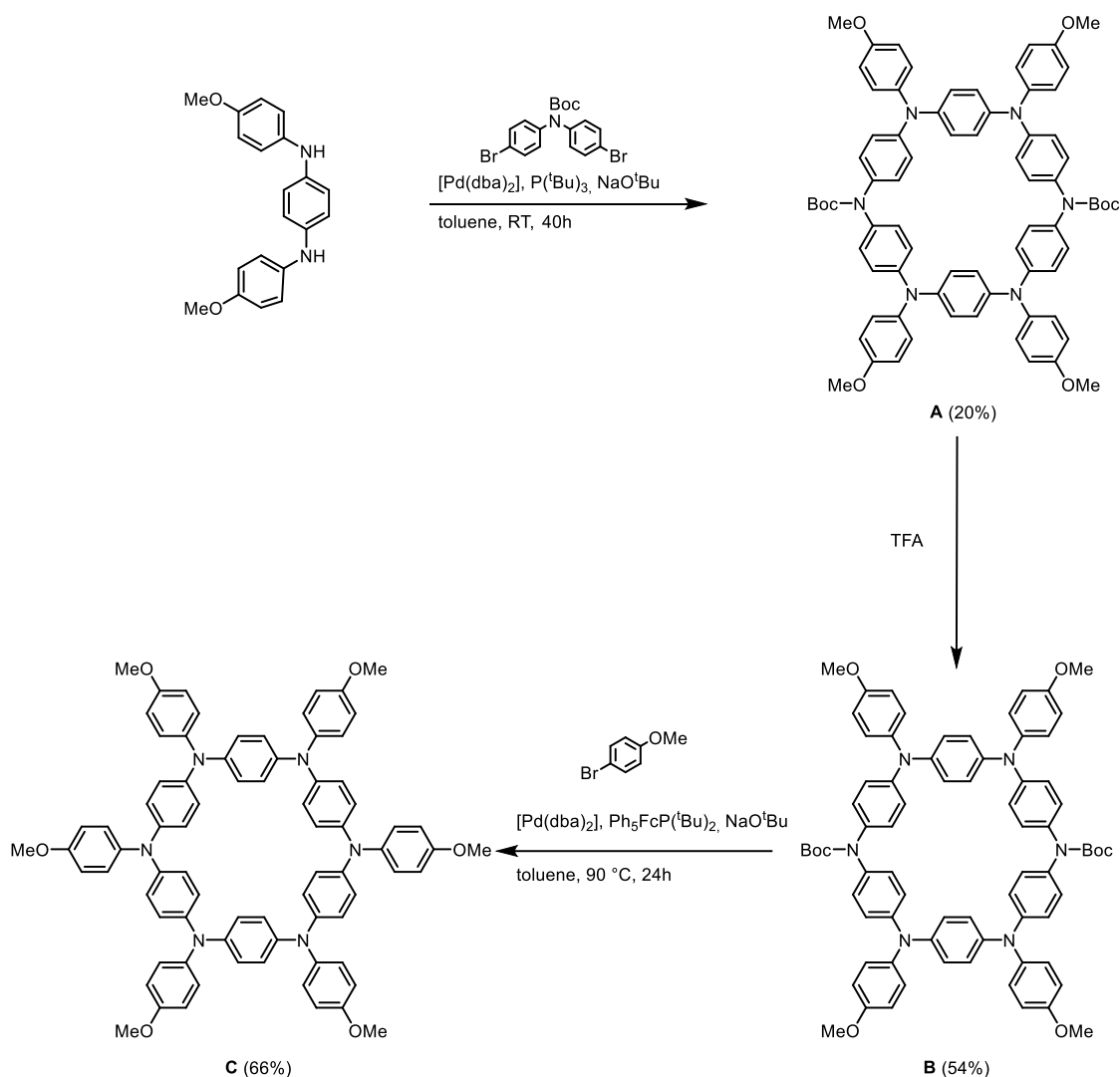


Figure 77 | Different arene-bridged patterns (from left to right): tetraaza[1₄]meta-cyclophane 1, hexaaza[1₆]para-cyclophane 2, triaza[1₃]ortho-cyclophane. (Reproduced from¹⁸⁴).

As we will show later, the main goal of the research described in this chapter is the synthesis and investigation of a amide-functionalized triarylamine based macrocycle whose core is constituted by a hexaaza[1₆]para-cyclophane. One of the first example of a macrocycle of this family was reported by the group of Tanaka. It described the synthesis of an N-anisyl-substituted hexaaza[1₆]para-cyclophane in three steps, with the first and the last ones being two palladium catalyzed couplings (**Scheme 10**).¹⁸⁵



Scheme 10 | Synthetic pathway for N-anisyl substituted hexaaza[1₆]paracyclophane **C**. (Reproduced from¹⁸⁵).

The Huckel molecular orbital (MO) calculation of the HOMO orbitals for the cyclic derivative and for a linear hexamer showed that in linear oligoaniline the HOMO is mostly localized on the central phenyldiamine unit, while in cyclic hexamer the MO coefficient is distributed equally on the six nitrogen atoms, leading to a completely delocalized HOMO. DFT calculations of the distribution of the spin density of the radical cation species predicted a delocalized character as well. cyclic voltammetry and differential pulse voltammetry showed five oxidation peaks for a total of six electrons removed from the macrocycle (the last peak accounting for 2 electrons). Interestingly, the potential of the first two oxidation peaks, is significantly lower for the macrocyclic derivative as compared to the linear one, suggesting a

stabilization of the radicals by delocalization. The authors confirmed their prediction by variable temperature (electron spin resonance) ESR analysis of the radical cation $C^{•+}$. The observation of a splitting pattern consistent with the presence of six equivalent nitrogen atoms, together with a hyperfine coupling which is unaffected by temperature changes, indicated that the spin of the radical is fully delocalized over the macrocyclic core at the time resolution of the technique (μs). Moreover, the appearance of an IV-CT band at 1630 nm (0.76 eV) in the UV-vis spectrum, obtained by electrochemical oxidation, provided a further evidence of the delocalized nature of the radical.

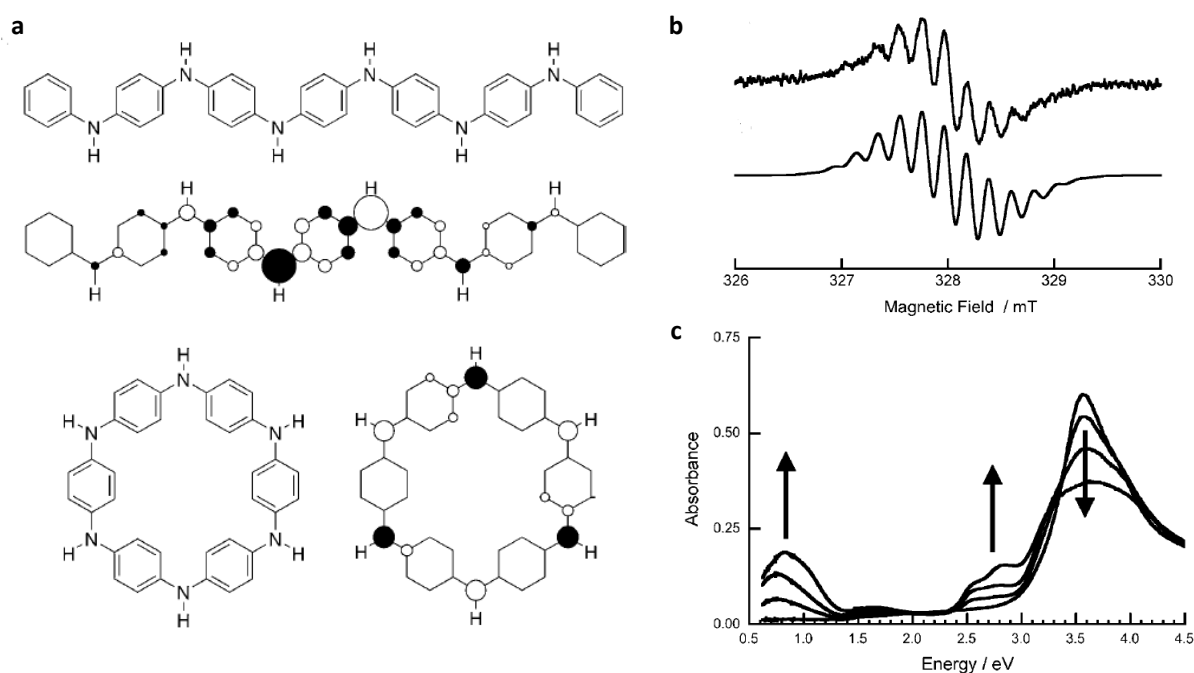
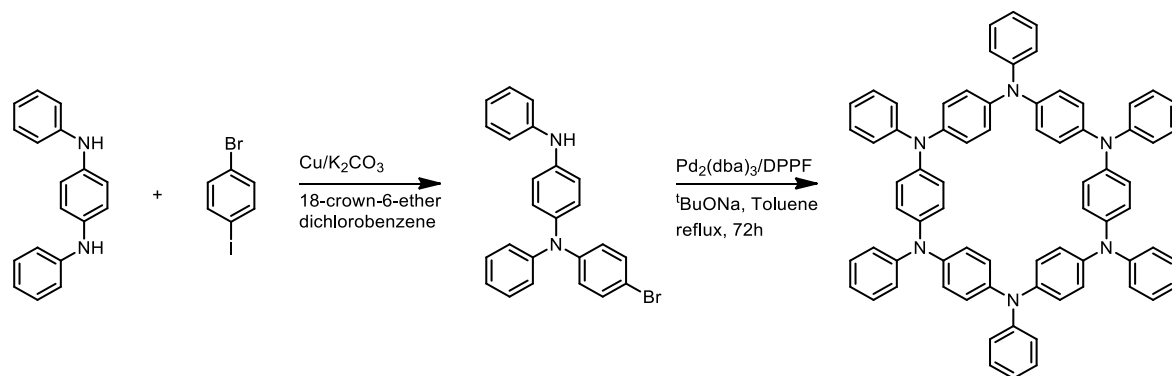


Figure 78 | a) Schematic representation of HOMO orbitals for linear (top) and cyclic (bottom) oligomers; b) ESR spectra of $C^{•+}$ in CH_2Cl_2 at 233 K (top) and simulated (bottom); c) Spectroelectrochemistry of C in CH_2Cl_2 (0.1 M $n\text{Bu}_4\text{N}^+\text{BF}_4^-$) at room temperature. (Reproduced from¹⁸⁵).

Two years later, Su and coworkers synthesized a similar derivative without methoxy-substituents on the periphery of the macrocycle.¹⁸⁶ The target molecule was prepared in two steps through a modified Ullmann coupling and a palladium catalyzed self-coupling (**Scheme 11**).



Scheme 11 | Synthetic scheme for non-functionalized macrocycle (Adapted from¹⁸⁶).

Cyclic voltammetry of the macrocycle showed two oxidation waves at 0.68 and 1.16 V. Furthermore, the integration areas of peaks, in differential pulse voltammetry, allowed them to estimate that each oxidation steps in cyclic voltammogram corresponded to a two-electron transfer, for a total of four electrons removed from the macrocycle (**Figure 79**). As compared to the oxidation of the N-anisyl substituted macrocycle from the previous example, the non-functionalized one shows a lower number of electrons removed, which can be due to the absence of the electron-donating methoxy- groups that makes the oxidation more difficult.

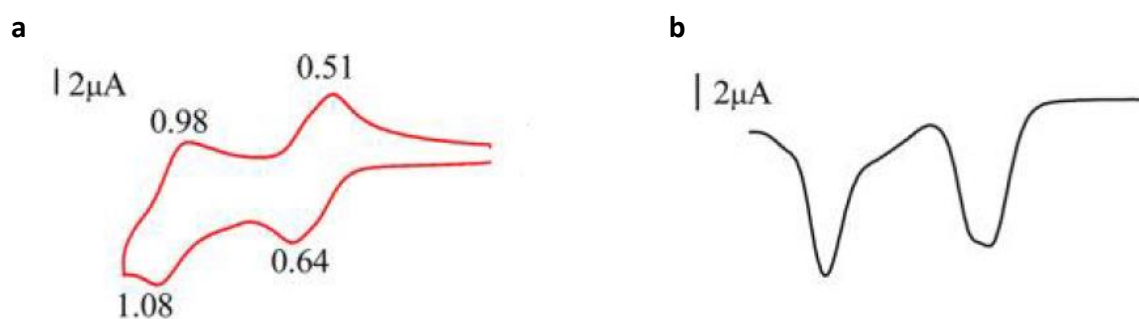


Figure 79 | a) Cyclic voltammogram of 1 mM solution of macrocycle in DCM (0.1 M TBABF₄); b) Differential pulse voltammogram for the same solution. (Reproduced from¹⁸⁶).

The authors further investigated this system by spectroelectrochemistry. Increasing the potential up to 0.67 V, they observed a decrease of the 322 nm absorption together with the appearance of a peak at 400 nm and an IV-CT band at 836 nm (**Figure 80a**). Moving the potential anodically up to 1.11 V, a third band grows at 586 nm while the 836 nm and 400 nm absorptions decrease dramatically (**Figure 80b**). They further observed an IV-CT band between 1200 nm and 1700 nm which decrease as soon as the one at 586 nm rises. The absence

of a strong IV-CT and, thus, of a large delocalization on the macrocycle, led the authors to further investigate the conformation by theoretical calculation. The optimized structures, obtained by DFT calculations indicated the non-coplanarity of the molecule, with two opposite aromatic rings almost perpendicular to the nitrogen plane (**Figure 80c**). Considering these results, the authors concluded that the two cation radicals were separately localized on two halves of the macrocycle and were not interacting with each other (**Figure 80d**).

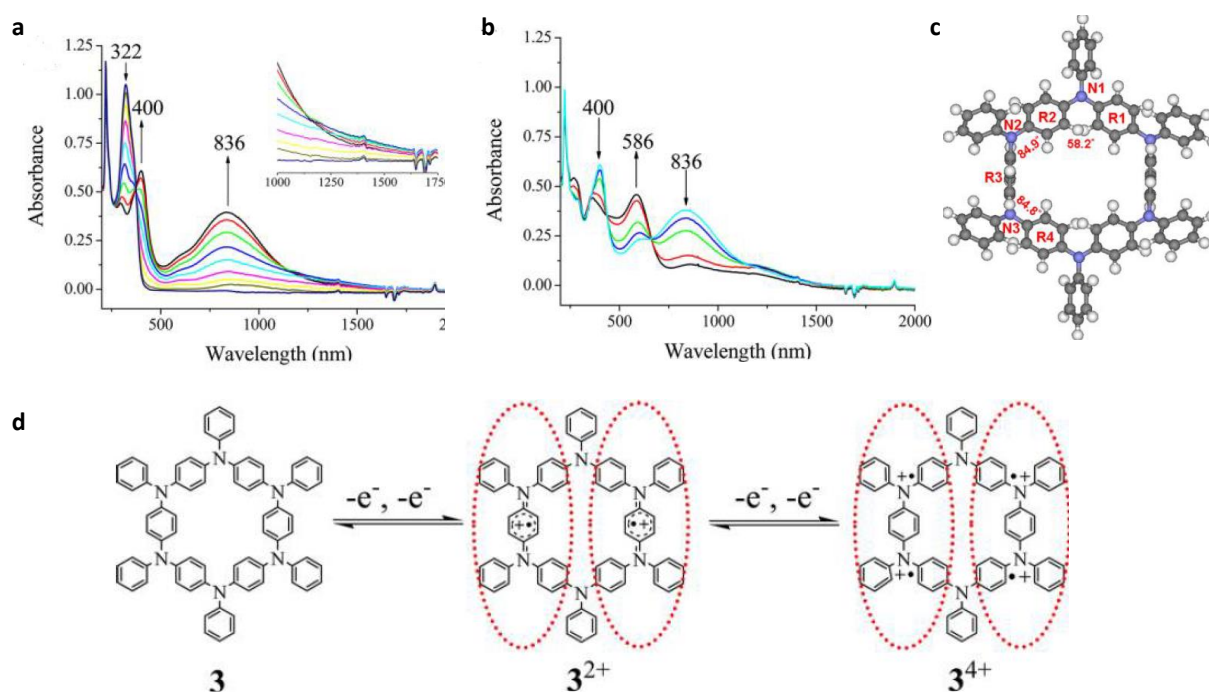


Figure 80 | a) Spectral changes of 2.5×10^{-4} M solution of macrocycle in DCM (0.1 M TBAP) upon increasing the potential from +0.00 to +0.67 V; b) Spectral changes of 2.5×10^{-4} M macrocycle solution in DCM (0.1 M TBAP) upon increasing the potential from +0.79 to +1.11 V. c) Optimized structure of the macrocycle calculated at the DFT B3LYP/6-31G** level of theory; d) Schematic representation of the oxidation process.

Summarizing, it has been showed that hexaazaparacyclophanes represent an intriguing class of compounds because of the extended π -conjugation, the rigidity of the structure and the presence of multiple redox centers. Nevertheless, the papers published so far on such systems are not only limited in number but also to the study of their redox and optical properties. Any kind of self-assembly has been reported for such systems and we think that, because of the already mentioned properties and the supramolecular characteristics of triarylamines, a self-assembling hexaaza[16]para-cyclophane would represent a unique materials with intriguing electromagnetic features.

3.2 TRIARYLAMINE BASED MACROCYCLE

3.2.1 General overview

Because of the excellent self-assembling properties showed by triarylamine derivatives, as reported in this manuscript and several publications^{128,130,134,187}, we were interested in combining the presence of multiple redox centers of hexaazaparacyclophanes with the self-assembling properties of amide substituted triarylamines, to obtain new electroactive materials. Thus, we proposed a triarylamine based macrocycle constituted by six nitrogen nuclei bridged through the para position of six aromatic rings and six amide chains on the periphery (**Figure 81a**). DFT molecular geometry optimization suggested that the proposed compounds can exist in a rather flat conformation with the inner aromatic rings slightly tilted with respect to each other. Moreover, the calculated HOMO orbitals showed a general electronic delocalization over the macrocyclic structure (**Figure 81b**). This flat conformation, together with the possibility of establishing six hydrogen bonding, should favor the self-assembly of this molecule in nanotubular structures over other possible morphologies. Furthermore, the expected double delocalization of the radicals, on both the macrocyclic core and along the assembled structure, should confer to the supramolecular polymers intriguing electromagnetic properties; the described double delocalization mode has not, to the best of our knowledge, been reported yet (**Figure 81c**).

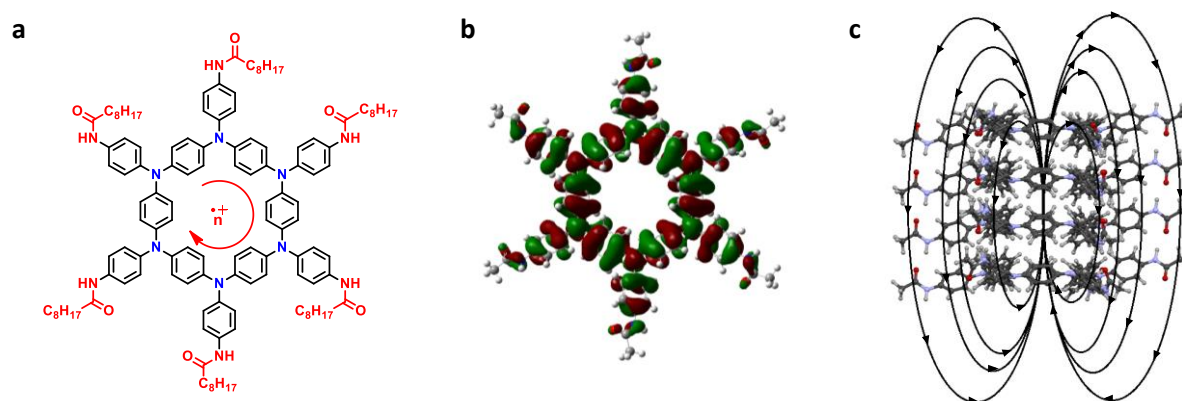


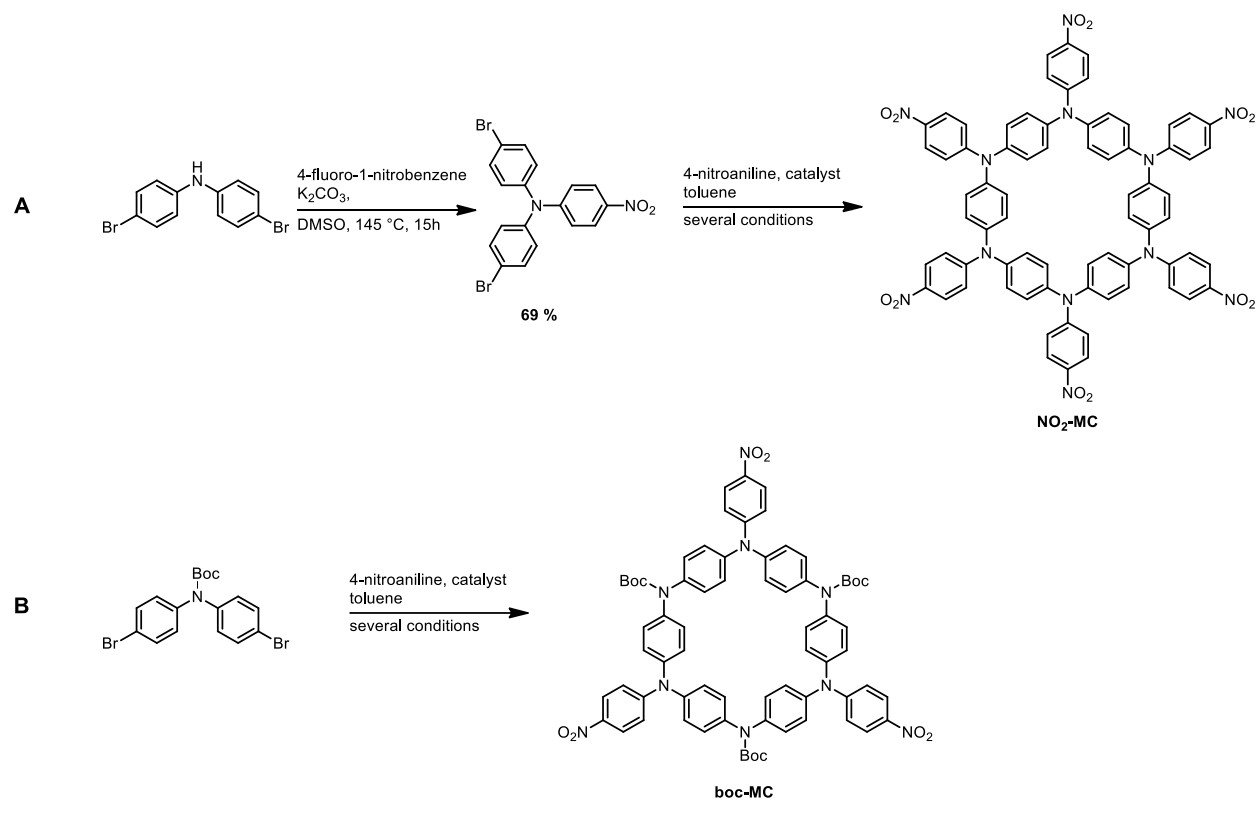
Figure 81 | a) Chemical structure of triarylamine based macrocycle; b) DFT calculation of the HOMO orbital of the macrocycle with short alkyl chains C2 using DFT at the M06-2X/6-31G level of theory; c) Simulated stacking of four macrocyclic units in unidirectional fashion and the expected magnetic field arising from double delocalization of the radicals.

3.3 RESULTS AND DISCUSSION

3.3.1 Synthesis of hexaaza[1₆]para-cyclophane hexakisamide (**HCHA**): Past attempts and current methodology

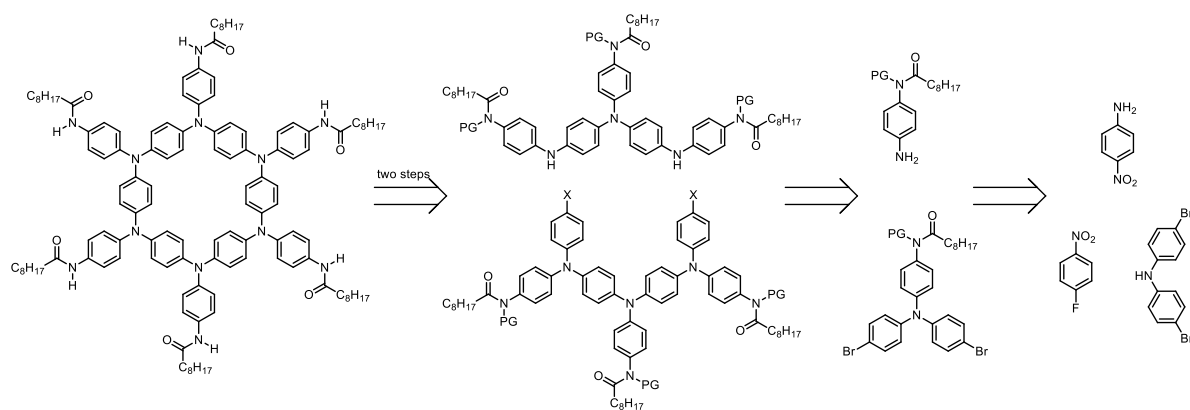
i) Past attempts

Before introducing the work object of this chapter, it is important to mention, briefly, the synthetic efforts undertaken previously by members of our research team, notably by a former PhD, Dr. Susanne Schneider, directly involved in this project. Aiming at the synthesis of the amide functionalized hexaazaparacyclophane, several different synthetic approaches have been proposed and tested. In a first attempt, she envisioned a one-pot and a sequential strategy in a similar way to the reported synthesis of hexaazaparacyclophanes.^{185,186} The synthesis of a nitro-modified macrocycle (**Scheme 12A**) would allow, after reduction of nitro groups to amino groups, the final functionalization with six amide chains. Despite these approaches having worked in good yields for other precursors, the methodology proved to be unsuccessful and the nitro-substituted macrocycle (**NO₂-MC**) could not be obtained by any variation of this procedure. This is probably due to the presence of several electron withdrawing nitro groups, which lower the activity of the palladium catalysts employed.^{188,189} Even reducing the number of nitro groups by replacing some *p*-nitrophenyl group with the boc protecting group (**Scheme 12B**) did not allow her to obtain the desired product.



Scheme 12 | A) Synthetic scheme towards the synthesis of nitro-functionalized macrocycle **NO₂-MC**; **B)** Synthetic scheme proposed for the synthesis of boc-functionalized macrocycle **boc-MC**.

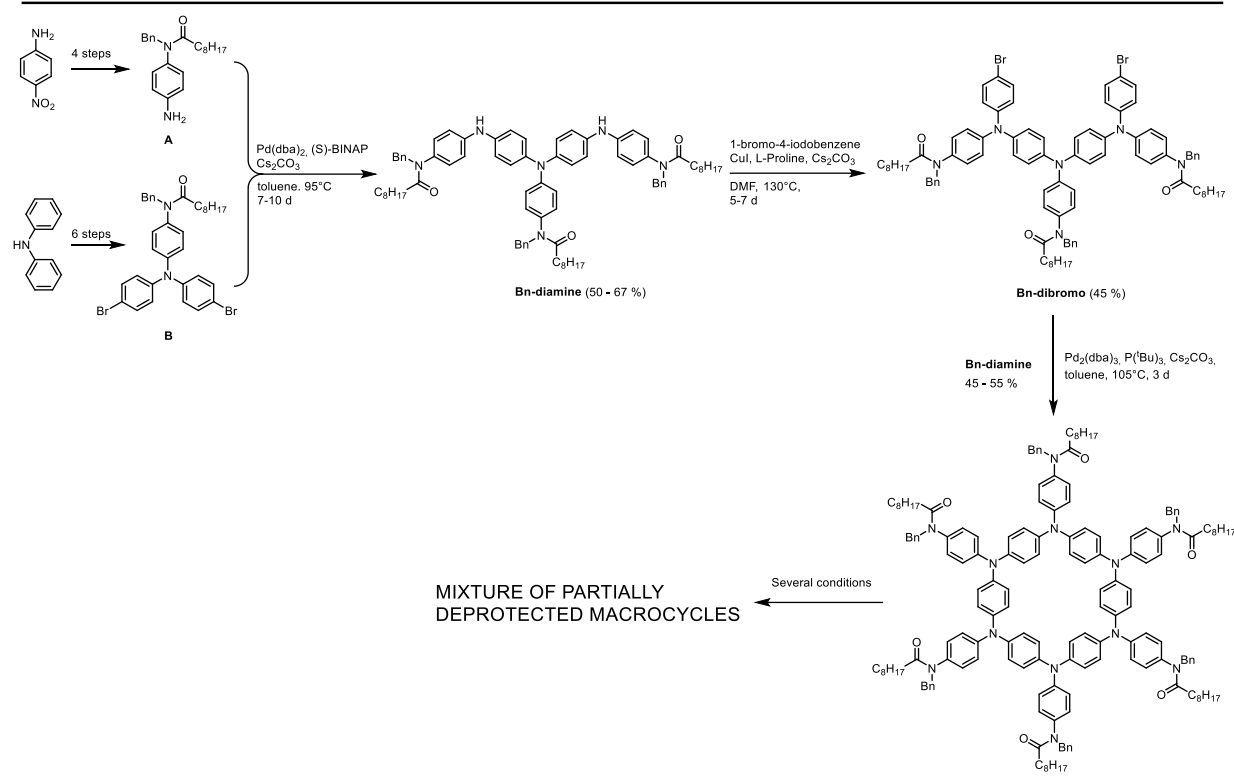
Beyond these attempts, some other strategies have been tested in order to obtain **NO₂-MC** but without obtaining encouraging results. Hence, a completely different approach was developed, in which she envisioned the synthesis of a macrocycle with all the amide groups protected by a selected protecting group. Towards this goal, she designed a multistep synthesis with a final deprotection step to afford the target molecule (**Scheme 13**).



Scheme 13 | Retrosynthetic scheme for the multistep synthesis of the **HCHA** (PG: protecting group).

The key element of this approach, is the proper choice of the protecting group which is introduced early in the synthesis and, thus, must to remain stable along the synthetic pathway. Furthermore, the protecting group, should be easily removable in the last step to afford the final compound. Hence, the choice of a protecting group is a critical point because of the mentioned balance in stability. That is, to harsh reaction conditions and an orthogonal lability for the final cleavage. As first choice, the boc group was employed to protect the amide groups but, along the synthesis, it showed some stability issues. Changing boc for phthalimido group did not improve the efficiency of the synthesis due to, probably, low reactivity of some intermediates. Finally, employing the benzyl group, she succeeded in obtaining the fully protected macrocycle after a multistep synthesis (**Scheme 14**). The precursors **A** and **B** were easily synthesized from commercial compounds, then three metal-catalyzed couplings allowed to synthesize the **Bn-diamine** through a Buchwald-Hartwig coupling, the **Bn-dibromo** after a modified Ullmann coupling, and the protected macrocycle by coupling the diamine with the dibromo via Buchwald-Hartwig coupling.

At this stage, different attempts were made in order to deprotect the derivative and obtain the final macrocycle. Unfortunately, the benzyl group, exhibited a good stability to many deprotection conditions. In fact, it was not possible to remove it without affecting the alkyl chains. From the many attempts, reduction with hydrogen on Pd/C gave the best results, allowing her to remove most of the benzyl groups preserving the lateral chains, but she never succeeded at removing all the protecting groups.

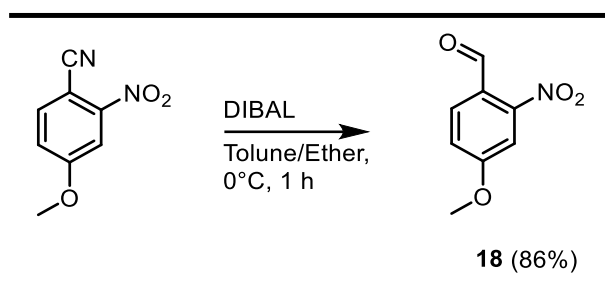


Scheme 14 | Synthetic pathway for the benzyl protected macrocycle.

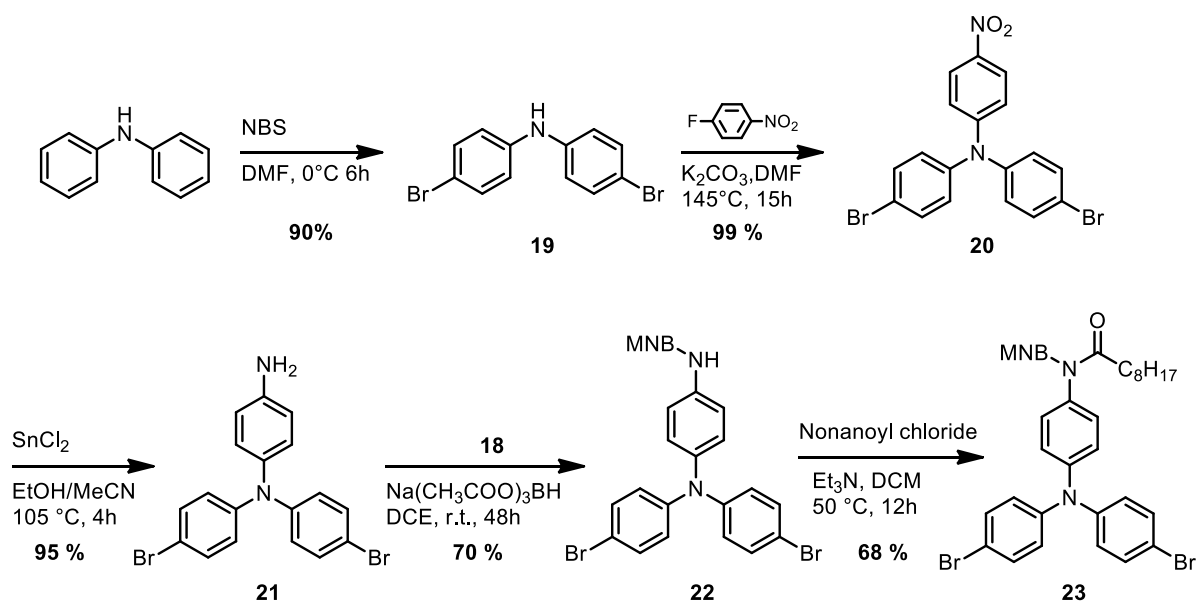
ii) *p*-methoxy-*o*-nitrobenzyl group

The previous short summary of the work of Dr. Susanne Schneider outlined how a multistep approach allows to obtain the precursor of the final macrocycle. However, we were not able to perform the deprotection in an efficient way, so the necessity of finding a suitable protecting group become the only reasonable option. In order to use the same synthetic approach, we looked for a protecting group structurally analog to the benzyl group. We finally choose the *p*-methoxy-*o*-nitrobenzyl group (MNB) which is described in literature to protect amide groups during the peptide synthesis to avoid H-bond driven aggregation.¹⁹⁰ Another interesting feature is that the MNB group is photoremovable under UV irradiation at $\lambda = 350$ nm,^{190,191} which would facilitate the last step, allowing an easier work-up and avoiding the use of strong reagents. Despite *o*-nitrobenzyl group having been described to fulfil the same role, we chose the *p*-methoxy-*o*-nitrobenzyl group because some studies indicate a faster deprotection rate for methoxy- substituted *o*-nitrobenzyl groups.¹⁹²

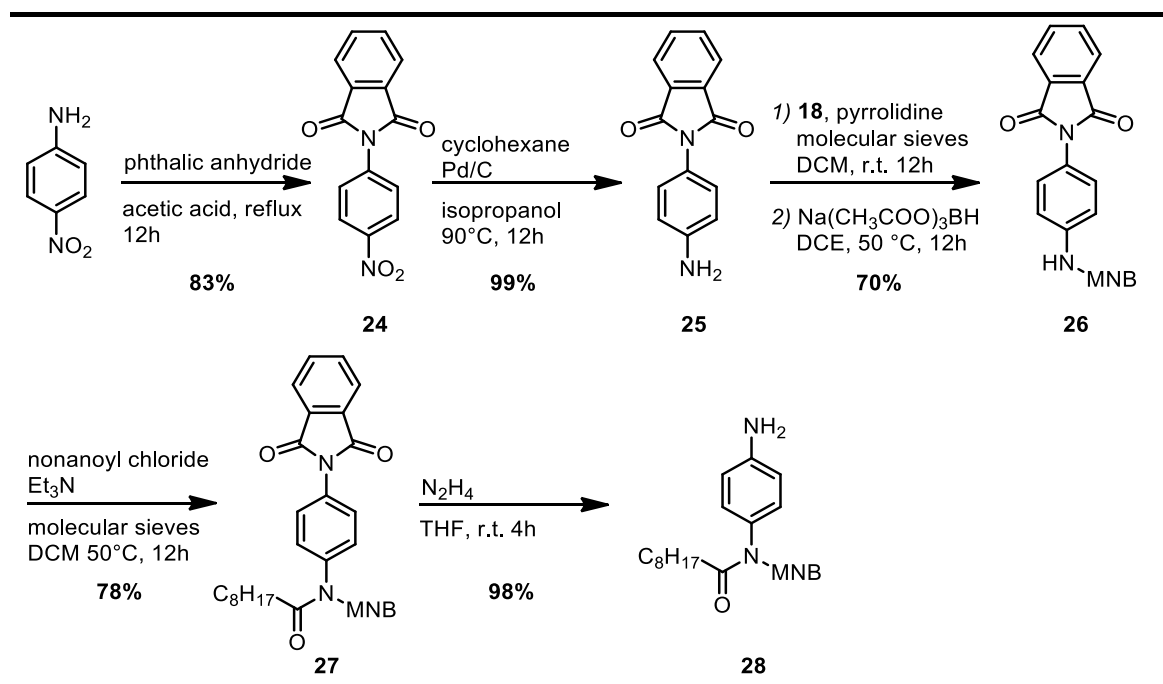
The protecting group was prepared by reduction with DIBAL of the commercially available 4-methoxy-2-nitrobenzotrile, according to a procedure reported in literature (**Scheme 15**).¹⁹³

**Scheme 15** | Synthesis of compound **18**

We then synthesized precursor **23** of the macrocycle. Starting from commercially available diphenylamine, by aromatic radical bromination with N-bromosuccinimide,¹⁹⁴ we obtained compound **19** in excellent yield. The nucleophilic aromatic substitution of *p*-fluoronitrobenzene with compound **19** in DMF allowed us to synthesize the substituted triarylamine **20** in quantitative yield.¹⁹⁴ Amine **21** was prepared by reducing the nitro group of **20** with tin chloride in an ethanol/acetonitrile mixture. At this stage, we introduced the protecting group (MNB) on the amine via reductive amination between **18** and **21**. For this step, we adopted a one pot approach in which, the formed imine was suddenly reduced *in-situ* by sodium triacetoxyborohydride in 1,2-dichloroethane (DCE). Thus, we obtained compound **22** in 70 % yield. As last step, compound **22** was reacted with nonanoyl chloride in DCM in presence of triethylamine to afford compound **23** in good yields (**Scheme 16**).

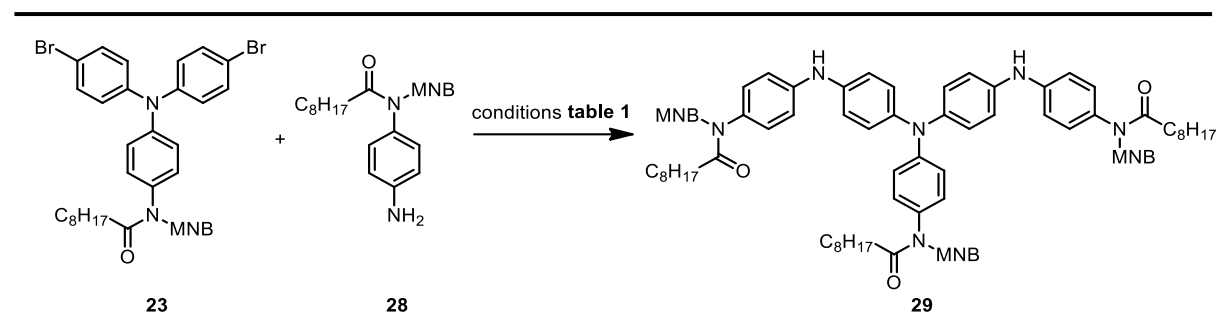
**Scheme 16** | Synthetic scheme towards compound **23**.

The other precursor, compound **28**, was synthesized starting from *p*-nitro-aniline. We firstly protected the amino group as phthalimido group by reaction with phthalic anhydride in acetic acid, then, hydrogenation of the nitro group with cyclohexane and palladium on carbon, allowed to obtain amine **25** in quantitative yield. At this stage, we introduced the protecting group, and, since the one-pot approach was unsuccessful, we performed it in two steps. Firstly, we synthesized the imine derivative by reacting aldehyde **18** with amine **25** in DCM in presence of pyrrolidine. The pyrrolidine acts as a catalyst maximizing the imine formation.¹⁹⁵ We then isolated the imine by reprecipitation from methanol and we reduced it with sodium triacetoxyborohydride in DCE. Stronger reducing agents, like sodium tetraborohydride, led to an over reduction of the phthalimido group. We obtained compound **26** in 70% yield over two steps. Amine **26** was then acylated with nonanoyl chloride in presence of triethylamine and molecular sieves to obtain compound **27** in good yield. The final deprotection of the amino group, mediated by hydrazine in THF, afforded compound **28** in almost quantitative yield (**Scheme 17**).



Scheme 17 | Synthetic route towards compound **28**.

For the first Buchwald-Hartwig coupling, between amine **28** and dibromo triarylamine **23** (**Scheme 18**), several conditions were tested, and the reactions were monitored by LC/MS analysis (**Table 9**).



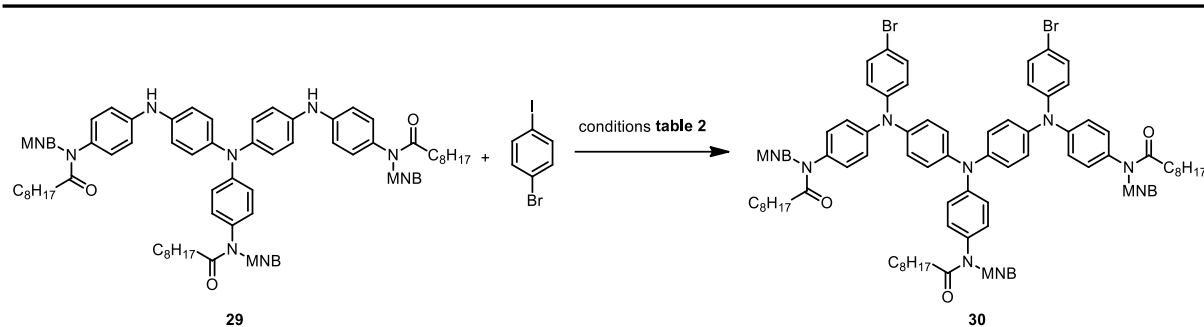
Scheme 18 | Synthesis of **29** via Buchwald-Hartwig coupling.

The first attempt, using the same conditions as employed for the benzyl-protected macrocycle, on a small scale (~ 20 mg of **23**), appeared to work in good yield, allowing us to isolate **29** in 55% yield. Unfortunately, as soon as the reaction was scaled up (~ 150 mg of **23**), we observed the partial cleavage of the protecting groups from **29** obtaining a complex mixture of side products. Shortening the reaction time and lowering the temperature did not increase the yields since not only the degradation was reduced but also the conversion to the desired product. Neither changing the base employed with sodium tert-butoxide or potassium carbonate allowed to reduce the degradation of the target molecule.

Entry	Catalytic system (Catalyst/Ligand/Base)	Reactant ratio 23/28/C/L/B	[23] mM	T (°C)	t (days)	LC/MS analysis
1	Pd(dba) ₂ /BINAP/Cs ₂ CO ₃	1/3/0.25/0.25/5	0.027	95	4	major peak of 29 (55%)
2	Pd(dba) ₂ /BINAP/Cs ₂ CO ₃	1/3/0.25/0.25/5	0.20	95	4	complex mixture of 29 and mono and bis deprotected
3	Pd(dba) ₂ /BINAP/Cs ₂ CO ₃	1/3/0.25/0.25/5	0.20	70	4	low conversion and degradation
4	Pd(dba) ₂ /BINAP/Na ^t BuO	1/3/0.25/0.25/5	0.20	95	2	complex mixture of 29 and mono and bis deprotected
5	Pd(dba) ₂ /BINAP/K ₂ CO ₃	1/3/0.25/0.25/5	0.20	95	2	complex mixture of 29 and mono and bis deprotected

Table 9 | Conditions tested for **Scheme 18**, solvent is toluene for all the entries.

The second coupling, according to the synthetic pathway, was the reaction of the diamine **29** with the 1-bromo-4-iodobenzene to afford the dibromo derivative **30** (Scheme 19).



Scheme 19 | Reaction scheme to afford compound **30**.

As for the benzylated molecule, a modified Ullmann coupling (**Table 10**; entry **1**) was employed but unfortunately, after 4 days of reaction, we did not observe any trace of our product. Furthermore, deprotected starting material was recovered. Changing the base for potassium carbonate, and reducing its quantity, led to similar results (**Table 10**; entry **2**). We then decided to change our approach and tried to run the coupling under Buchwald-Hartwig conditions, by using Pd(dba)₂ (**Table 10**; entry **3**). The results were not encouraging since we did not observe any product formation and evidence of starting material being deprotected. Finally, in a last attempt, we used a combination of Pd(OAc)₂ with Xantophos, which is an efficient ligand for the amination of arylhalide^{196,101} (**Table 10**; entry **4**). After three days of reaction, we found a small peak of the monofunctionalized product, some starting material and little degradation. The situation remains unchanged even after six days of reaction and we never observed the desired product. This is, in fact, not too surprising as palladium catalyzed couplings are less selective for halogens, thus, a mixture of products is expected in most cases and therefore we did not investigate this approach further.

Entry	Catalytic system (Catalyst/Ligand/Base)	Reactant ratio 29/dihalobenzene/C/L/B	[29] mM	T (°C)	t (days)	LC/MS analysis
1	CuI/L-Proline/Cs ₂ CO ₃	1/20/1/2/20	0.014	130	4	no product peak, deprotected starting material
2	CuI/L-Proline/K ₂ CO ₃	1/10/1/2/3	0.30	130	4	no product peak, deprotected starting material
3	Pd(dba) ₂ /BINAP/K ₂ CO ₃	1/10/0.5/0.5/5	0.014	95	1	no product peak, deprotected starting material
4	Pd(OAc) ₂ /Xantophos/Na ^t BuO	1/2/0.02/0.02/1.3	0.014	100	3	no product detection, low peak of monofunctionalized product, starting materials and low degradation

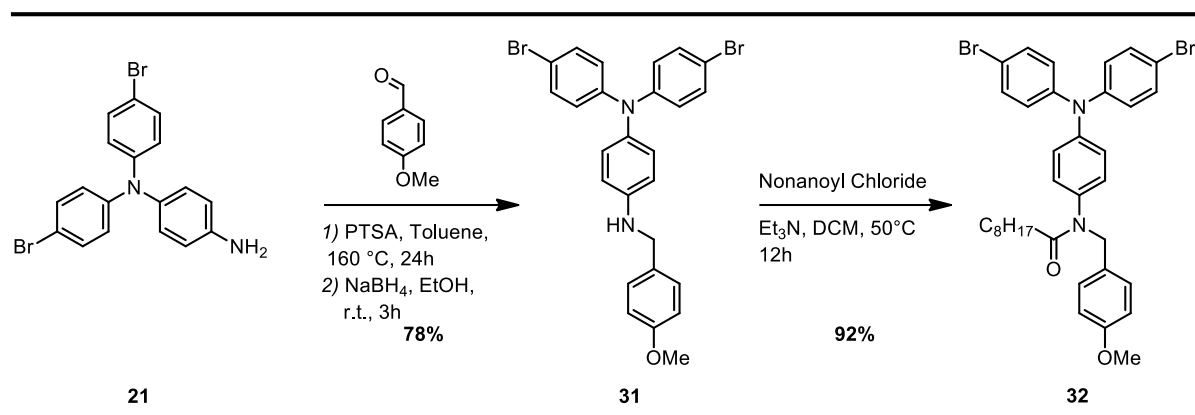
Table 10 | Conditions tested to synthesize compound **30**; solvent is DMF for entries 1, 2; toluene for entries 3, 4.

Considering these results, we concluded that the *p*-methoxy-*o*-nitrobenzyl group is quite instable in basic condition at high temperature and for long time reactions. This information added to the fact that the reactions employed, like the Buchwald-Hartwig coupling and especially the modified Ullmann coupling, require quite harsh conditions to show acceptable yields led us to decide to change approach and look for a more stable protecting group.

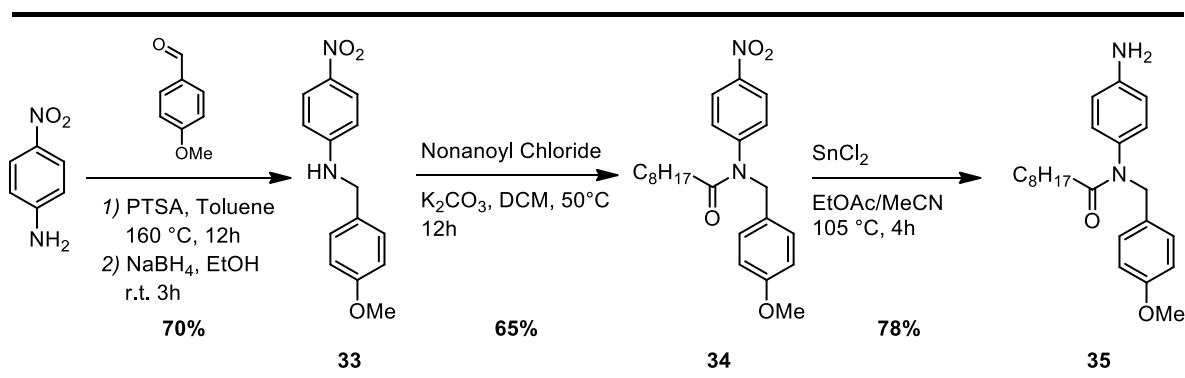
iii) *p*-methoxybenzyl group

Searching for a more stable alternative protecting group, we decided to test the *p*-methoxybenzyl group (PMB), which is a widely used and versatile protecting group. It has been successfully employed to protect alcohols,^{197,198,199} amines,^{200,201} amides,²⁰² and lactams^{203,204}; many deprotecting strategies, including cleavage by oxidation, acidic treatment, and photolysis, have been described so far.^{197-204,205,206}

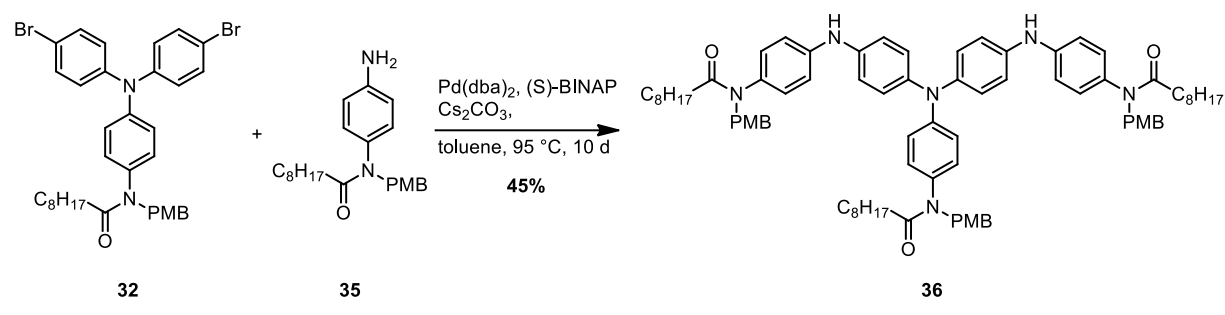
We started the synthesis by introducing the new protecting group on triarylamine **21** in two steps. In a first step, we formed the imine by condensation between the amine and the *p*-methoxybenzaldehyde in a Dean-Stark equipped set-up, with a catalytic amount of *p*-toluenesulfonic acid (PTSA). In a second step, we reduced *in-situ* the imine by adding carefully, at 0 °C, sodium borohydride. Thus, we obtained compound **31** in good yield. The subsequent reaction with nonanoyl chloride allowed to afford precursor **32** in 92% yield (**Scheme 20**).

Scheme 20 | Synthetic route towards precursor **32**.

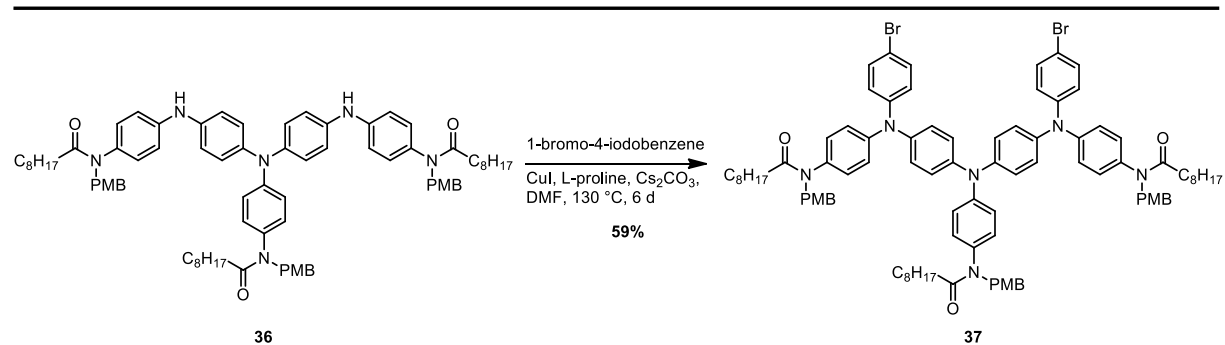
The second synthon was synthesized starting from *p*-nitroaniline, by protection with the *p*-methoxy benzyl group following the same procedure as for compound **31**, obtaining amine **33** in 70% yield. Acylation with nonanoyl chloride provided compound **34** and the final reduction, of nitro group into amino group mediated by tin chloride, afforded precursor **35** in good yield (Scheme 21).

Scheme 21 | Synthetic route towards amine **35**.

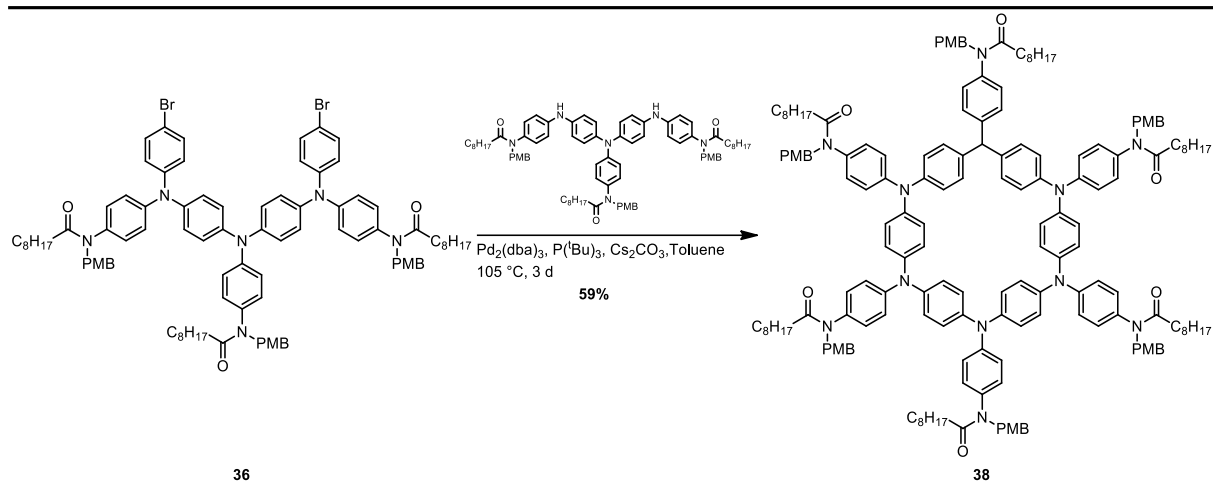
The coupling between amine **35** and triarylamine **32** was run under Buchwald-Hartwig conditions (Scheme 22) employing bis(dibenzylideneacetone)palladium(0) as catalyst, BINAP as ligand and cesium carbonate as base. After 10 days at 95 °C the LC/MS analysis showed a major peak corresponding to the diamine **36** which was isolated in 45 % yield after column chromatography.

**Scheme 22** | Synthetic route towards compound **36**

In order to prepare compound **37**, diamine **36** was reacted, under modified Ullmann conditions (**Scheme 23**), with 1-bromo-4-iodobenzene using copper (I) iodide as catalyst, L-proline as ligand and cesium carbonate as base. The reaction was stirred at $130\text{ }^\circ\text{C}$ and, after 6 days, LC/MS analysis showed the formation of dibromo compound **37**, and was isolated in 59% yield after purification.

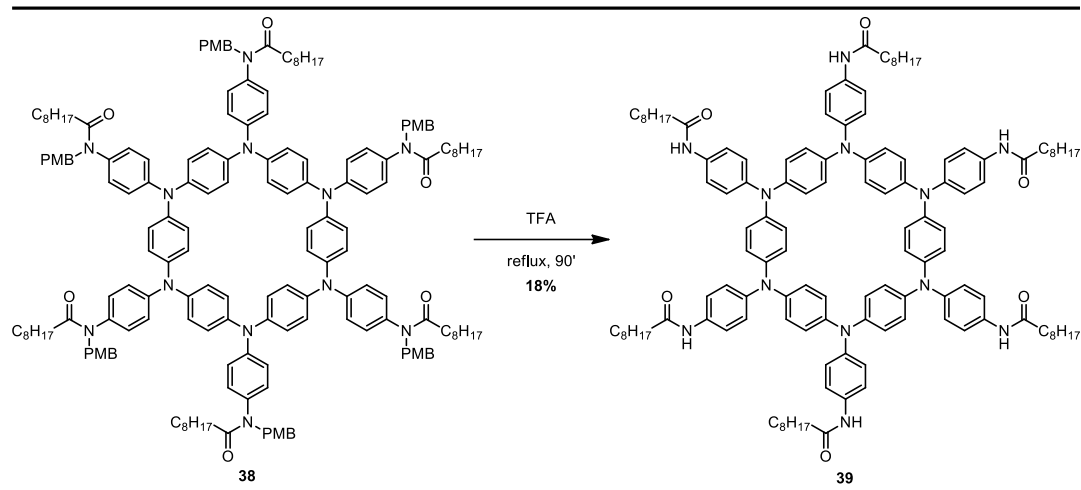
**Scheme 23** | Synthesis of compound **37**.

Macrocyclization was performed under Buchwald-Hartwig condition, by coupling diamine **36** and bromo derivate **37** (**Scheme 24**). As for the benzylated macrocycle, we used tris(dibenzylideneacetone)dipalladium(0) as catalyst, tri-tert-butylphosphine as ligand and cesium carbonate as catalyst. After 5 days at $105\text{ }^\circ\text{C}$ the reaction was quenched, the macrocycle precipitated from a mixture ethyl acetate/methanol, and characterized by MALDI and NMR analysis.



Scheme 24 | Macrocyclization under Buchwald-Hartwig conditions.

In order to deprotect compound **38** and, thus, obtain the final macrocycle **39** we tried, in parallel, two strategies: oxidation with DDQ in a DMF/water mixture, and removal by acidic treatment refluxing compound **38** in pure TFA. Following the reaction by MALDI analysis we observed, after one day, no product peaks for the reaction with DDQ, while for that in TFA, deprotection occurred, and we were able to detect compound **39**. Further optimization of the reaction conditions showed that the reaction was complete within 90 minutes, after which, degradation started to occur due to the harsh conditions (**Scheme 25**). After evaporation of the solvent, compound **39** was precipitated several times from hot ethyl acetate until a colorless supernatant was obtained. The collected precipitate was solubilized in a toluene/methanol mixture (1:1) and filtered through a short column of aluminum oxide. We obtained compound **39** in 18% yield, as shown by NMR and MALDI analysis (**Figure 82**; **Figure 83**).



Scheme 25 | Final deprotection to afford macrocycle **39**.

3.3.2 Characterization of triarylamine based macrocycle **39**

We confirmed the successful synthesis and purity of compound **39** by MALDI and NMR analysis. The reprecipitated compound showed a pattern of isotopic peaks between 1933 and 1938 m/z with the peak at 1934 m/z corresponding to the 100% of the intensity (exact mass of **39**: 1933.23). This result is consistent with the simulated distribution of isotopic peaks (**Figure 82**)

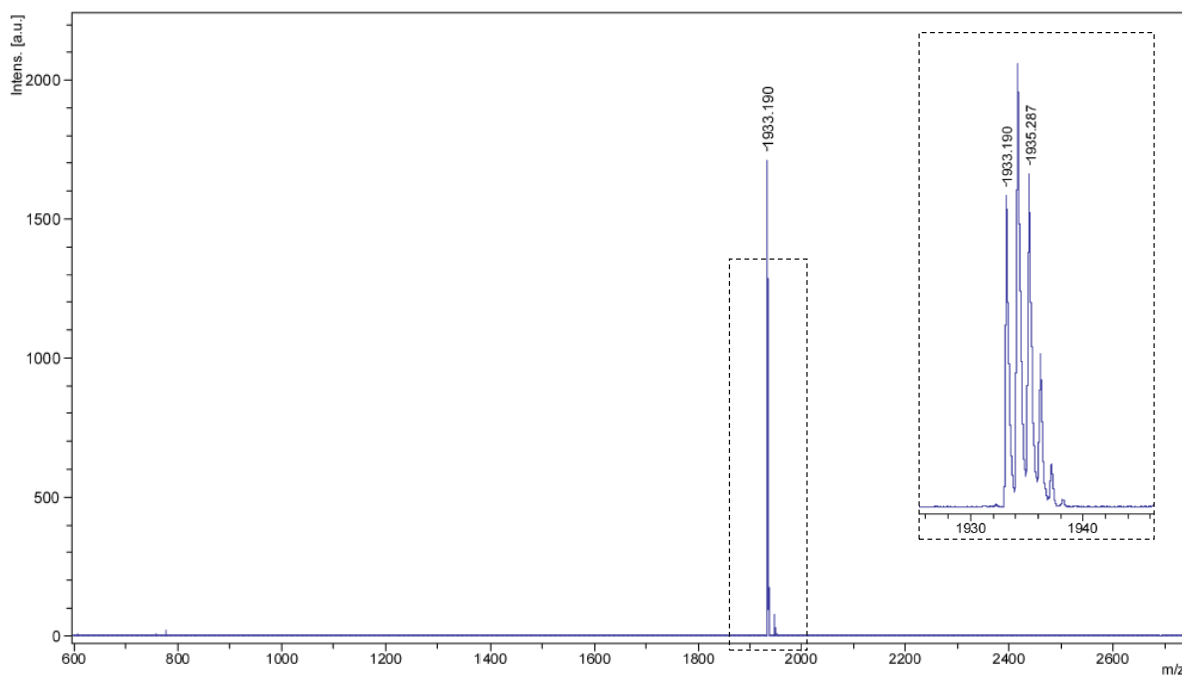


Figure 82 | MALDI analysis of compound **39** after reprecipitation with an enlargement of the peak at 1934 m/z; expected intensities: 1934.23 (100.0%), 1933.23 (73.4%), 1935.23 (36.2%), 1935.23 (31.4%), 1936.24 (21.6%), 1936.24 (8.6%), 1937.24 (5.8%), 1935.23 (4.4%), 1937.24 (3.3%), 1934.22 (3.3%), 1938.24 (2.1%).

The $^1\text{H-NMR}$ spectrum was recorded in DMF-d_7 , one of the few solvents able to solubilize the compound even at room temperature. All the peaks were assigned to the corresponding protons and the integrations fitted the expected number of hydrogens (**Figure 83**).

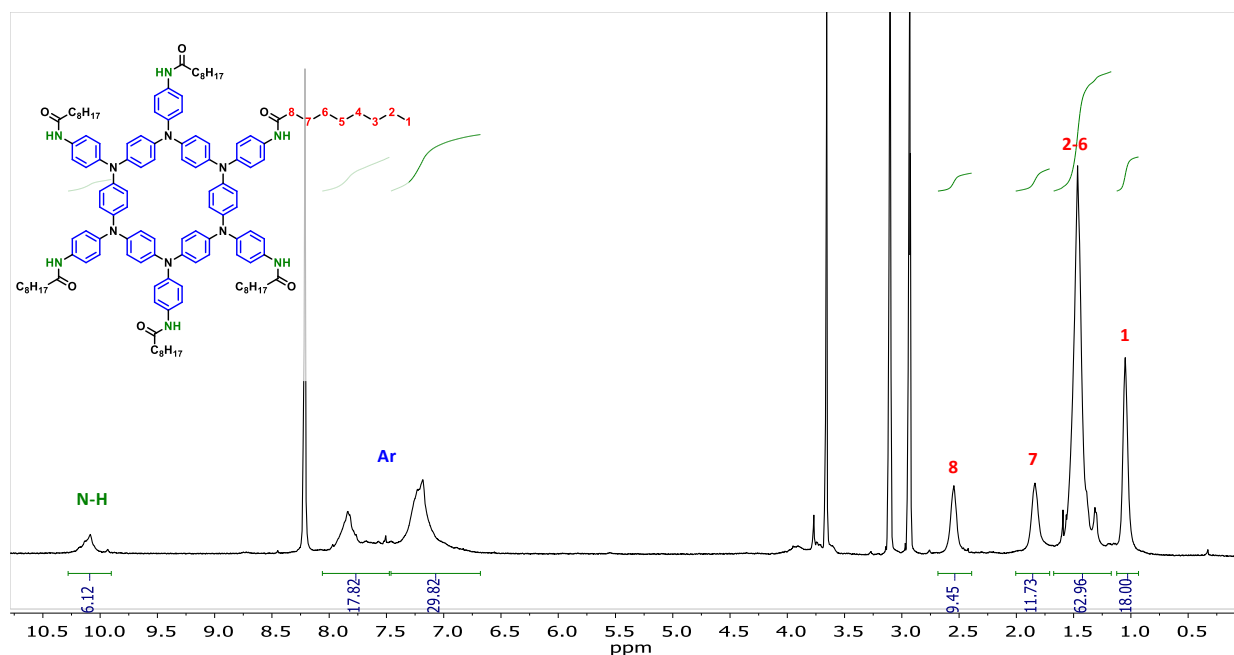


Figure 83 | $^1\text{H-NMR}$ spectrum of a 2 mM solution of **39** in DMF-d_7 (400 MHz).

i) Spectro-electrochemical analysis

In order to investigate the electrochemical properties of our molecule, we first investigated the behavior of compound **38**, the protected macrocycle, to determine whether the presence of free amides would have an influence on the redox process. This could lead to different oxidation pathways arising from the intrinsic structural differences between the molecules, and the possibility, for compound **39**, to establish hydrogen bonding and, thus, self-assemble. An eventual delocalization of the radical cation on the macrocyclic core and between stacked molecules would be visible by spectroelectrochemistry and would be a good indication of the need of further exploring the putative electromagnetic properties of compound **39**.

We performed cyclic voltammetry measurements in 1,1,2,2-tetrachloroethane (TCE), a solvent in which both molecules are soluble, and which show good stability between 0 and 1.8 V. The additional possibility to photo oxidize the triarylamine based macrocycle in such solvent, using UV light irradiation as shown before,¹³⁰ may enable, in the future, the direct comparison between the two oxidation methodologies. The cyclic voltammogram of compound **38** (**Figure 84a**) showed two reversible oxidation waves at 0.8 V ($E_{\text{pa},1}$) and 1.4 V ($E_{\text{pa},2}$), as confirmed also from square wave (SW) voltammetry (**Figure 84b**). Integrating the areas under the two SW peaks we obtained, for $E_{\text{pa},1}$, a value of 6.9×10^{-7} AV, while for $E_{\text{pa},2}$, a value of 7.1×10^{-7} AV. These values suggest that a total number of four electrons is removed from the macrocycle,

and that each oxidation wave corresponds to a two-electron transfer process. This result is similar to the one reported for unsubstituted hexaazaparacyclophane,¹⁸⁶ as discussed in the introduction of this chapter.

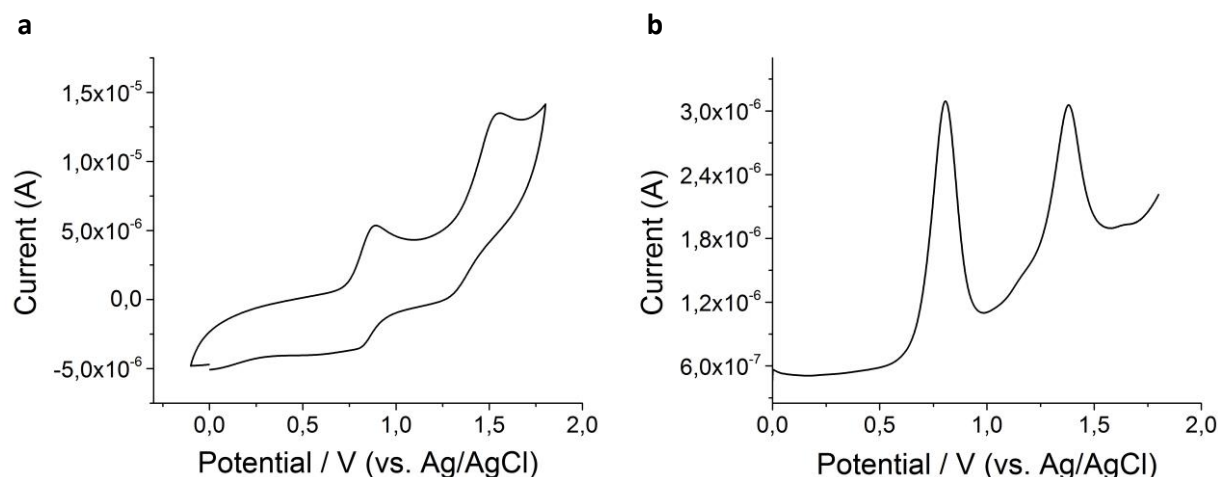


Figure 84 | **a**) Cyclic voltammogram of a 0.5 mM solution of **38** in TCE (0.1 M NBu₄PF₆), scanning rate: 0.1 Vs⁻¹; **b**) Square wave voltammogram of a 0.5 mM solution of **38** in TCE (0.1 M NBu₄PF₆).

Cyclic voltammetry of compound **39** showed a quite different behavior as compared to its precursor (**Figure 85a**). The number and potential of the oxidation peaks is not fully clear from CV analysis but, from the SW voltammetry measurement, we observed three main oxidation waves at 0.6 V ($E_{pa,1}$), 0.86 V ($E_{pa,2}$) and 0.96 V ($E_{pa,3}$) (**Figure 85b**). Integration of the first peak, corresponding to $E_{pa,1}$, gave a value of 6.4×10^{-7} VA while integrating the area under $E_{pa,2}$ and $E_{pa,3}$, we obtained a value of 1.04×10^{-6} VA. These results indicated that each peak correspond to a one-electron process, with the oxidation of compound **39** up to its trication radical **39**³⁺. A similar, mono-electronic oxidation pathway was observed in the case of the N-anisyl-substituted hexaazaparacyclophane described by Tanaka et al.¹⁸⁵

Moreover, the first oxidation occurred at a lower potential (0.6 V) for compound **39** when compared to protected macrocycle **38** (0.8 V). This is a good indication of a better stabilization of the radical cation within the macrocycle in the case of compound **39**, likely due to a better conjugated nature of the molecule, or potentially to delocalization along stacked charged and neutral molecules.

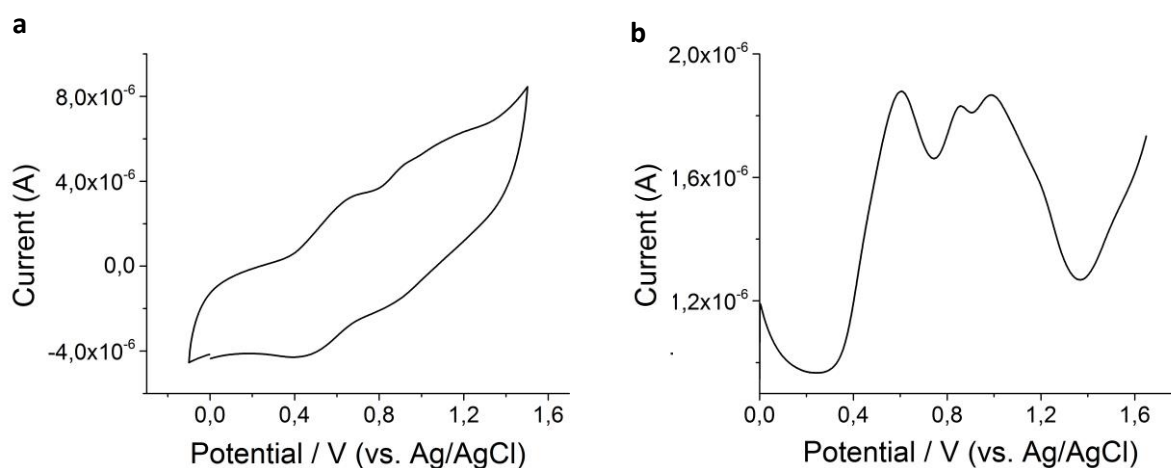


Figure 85 | a) Cyclic voltammogram of a 0.5 mM solution of **39** in TCE (0.1 M NBu_4PF_6), scanning rate: 0.1 Vs^{-1} ; **b)** Square wave voltammogram of a 0.5 mM solution of **39** in TCE (0.1 M NBu_4PF_6).

In order to get a better insight on the molecular process, we recorded the Vis-NIR electronic spectra of compounds **38** and **39** during a multistep oxidation. The electrooxidation was performed inside the spectrophotometer in a tin electrochemical cell (see Annexes; **Figure A 4**) by slowly increasing the potential applied to the cell during the acquisition of multiple spectra (one spectrum every 5 mins). The results, for compound **38** (**Figure 86a**) and **39** (**Figure 86b**), are shown below. When increasing the potential applied to the solution of **38** in TCE, we observed the increase of the shoulder at 450 nm and the generation of two new absorptions: a first one localized at 800 nm, and a second one at 1400 nm. The 800 nm band is assigned to the presence of localized triarylamine radical cations,¹³⁰ while the absorption at 1400 nm is the IV-CT band associated with an electron transfer from a neutral phenylamine nitrogen to the neighboring phenylamine radical cation. We can observe that when increasing the potential the shape of the spectrum remains essentially unchanged, while the intensities of the two red-shifted bands increase in response to the increased concentration of radicals that are generated. It appears that only one specie is generated during the oxidation process and should, thus, be assigned to the diradical **38**²⁺. The relative intensity of the localized and delocalized characteristic bands remain unaltered over the applied potentials we explored. It is also not clear why the oxidation to the tetracation **38**⁴⁺ is not observed. We hypothesized, though, that the kinetics for the formation of an analytical amount of the tetracation, is slower compared to the time scale of the experiment, or maybe, the potential needed to perform the second oxidation step, under these experimental conditions, is higher compared to that observed in the CV. Hence, it may necessitate an overpotential to produce a detectable amount

of $\mathbf{38}^{4+}$, but, considering that we were close to the oxidation potential of the solvent (2 V), we opted not to increase the potential.

On the other hand, compound $\mathbf{39}$, showed a different behavior: as soon as we increased the potential, two new absorptions are generated, a first one at 800 nm, for the localized radical, and a second one at 1700 nm corresponding to the delocalized radical. Comparing the IV-CT for compound $\mathbf{38}$ and $\mathbf{39}$ we observed that, for the latter, the band is significantly red-shifted ($\sim 1260\text{ cm}^{-1}$), suggesting a higher delocalization of the radical cation in compound $\mathbf{39}$. Increasing the potential, the IV-CT band undergoes a significant hypsochromic shift, together with the appearance of a shoulder at 605 nm. This absorption could be ascribed to a contribution of localized radical as soon as multiply charged species are formed ($\mathbf{39}^{2+}$, $\mathbf{39}^{3+}$), while the blue shift of the low energy IV-CT band could be explained in terms of intermolecular charge transfer. This is based on the observations, previously made, in triarylamine assemblies that show the a similar behavior following delocalization within stacks of triarylamines.¹³⁰ Unfortunately, as we will show in the following, we could not demonstrate the formation of large assemblies in TCE for the neutral macrocycle, but this does not exclude the formation of dimers and trimers, not the formation of larger aggregates induced by radical formation, and the partial delocalization of the charge within them.

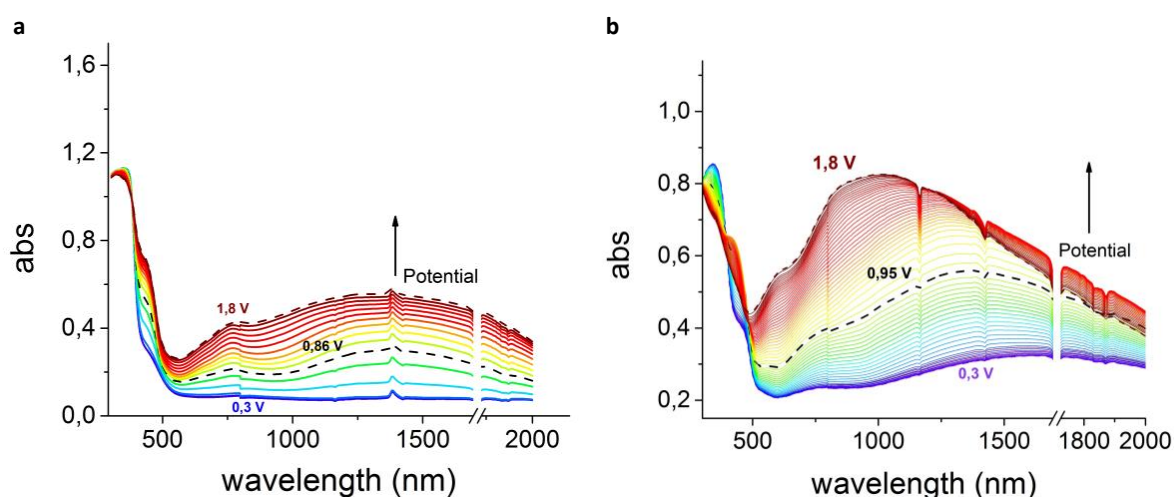


Figure 86 | Vis-NIR spectra recorded during the stepwise electrochemical oxidation of a 0.5 mM TCE solution of $\mathbf{38}$ (a) and $\mathbf{39}$ (b).

To confirm these results, we performed the chemical oxidation of both macrocycles. The titration of a solution of analyte in TCE with a solution of tris(4-bromophenyl)ammoniumyl hexachloroantimonate, a popular oxidant with a reduction potential of 1.4 V (vs Ag/AgCl), we

observed the same behavior as observed by spectroelectrochemistry for both the macrocycles (see Annexes; **Figure A 5**).

ii) Conformations

The evidence presented in the previous section strongly suggest a surprisingly different electrochemical by molecules **38** and **39**. This is not unexpected, a change in the substitution pattern, on the periphery of the macrocycle, can lead to drastic changes in the properties of these derivatives. We mention, in the introduction of this chapter, the differences between the unsubstituted macrocycle and the N-anisyl substituted one. One explanation to this observation can be found on the conformation adopted by the macrocycle under the influence of the substituents, or as a consequence of the synthetic methodology. The group of Tanaka, from DFT calculations, demonstrated that the methoxy substituted macrocycle adopted an almost coplanar conformation, with the aromatic rings tilted by 42° with respect to the nitrogen's plane.¹⁸⁵ On the other hand, the group of Su found a different conformation for the simplest hexaazaparacyclophane, with two aromatic rings almost perpendicular to the nitrogen's plane (**Figure 80c**).¹⁸⁶ Thus, we got interested in investigating if these conformations are always possible, and if further alternatives can exist for the hexaazaparacyclophanes. In all cases, there has to be a thermodynamically preferred structure and the related energies favoring any given structure.

As we mentioned in the general objects, DFT calculations for an acetamido substituted macrocycle show a flat structure as the most stable conformation. Nevertheless, other conformations are possible and, for certain substitution pattern, these might become the most stable. Hence, in order to explain the differences we observed between system **38** and **39**, and to explore the conformational freedom of the hexaazaparacyclophanes system, we did a conformational search (using the semi-empirical method PM6) based on several starting geometries of the simplest phenyl-substituted hexaazaparacyclophane. Then, the found geometries were optimized by DFT (M06-2X/6-31G) and the corresponding relative energy differences calculated. Only three stable geometries could be found. The first conformation (**Figure 87a**), represents the flat-macrocycle, is the thermodynamically most stable conformation and was used as reference for the energy calculations. the second one, named boat-macrocycle for its clear similarity to cyclohexane (**Figure 87b**), shows the aromatic rings are twisted with respect to each other and a relative energy is 21.18 kJ/mol; finally, the third one (**Figure 87c**) is the chair-macrocycle, and is the one reported by Su in the previous example; the relative energy in that case is about 32.90 kJ/mol. Needless to say, following a

Boltzmann distribution based on the relative energies, only the first conformation should be possible if, and only if, conformational interconversion is possible. Unfortunately, the calculation of the isomerization barrier proved to be technically unfeasible, but it is safe to assume that it has to be prohibitively high in energy.

Thus, we speculate that in our case, molecules **38** and **39** have adopted two different conformations. In particular, in light of the two examples reported in literature, we think that compound **38** would probably adopt a chair-like conformation, justifying the similarities with the electrochemical properties with the macrocycle described by Su. The bulkiness of the protecting group probably plays a role on the stabilization of this conformation. On the other hand, we postulate that compound **39** may assume a flat conformation (with an alternating pattern of Λ and Δ local conformation of the triarylamine propellers, resulting in an achiral macrocycle), like the methoxy substituted macrocycle, explaining the common features showed by these two substrates. It is noteworthy to mention that the eventual flat conformation of compound **39** would be necessary towards the stacking of several units in a columnar assembly, which is one of the main goals of this project. A flat conformation is also necessary to have a fully conjugated macrocycle.

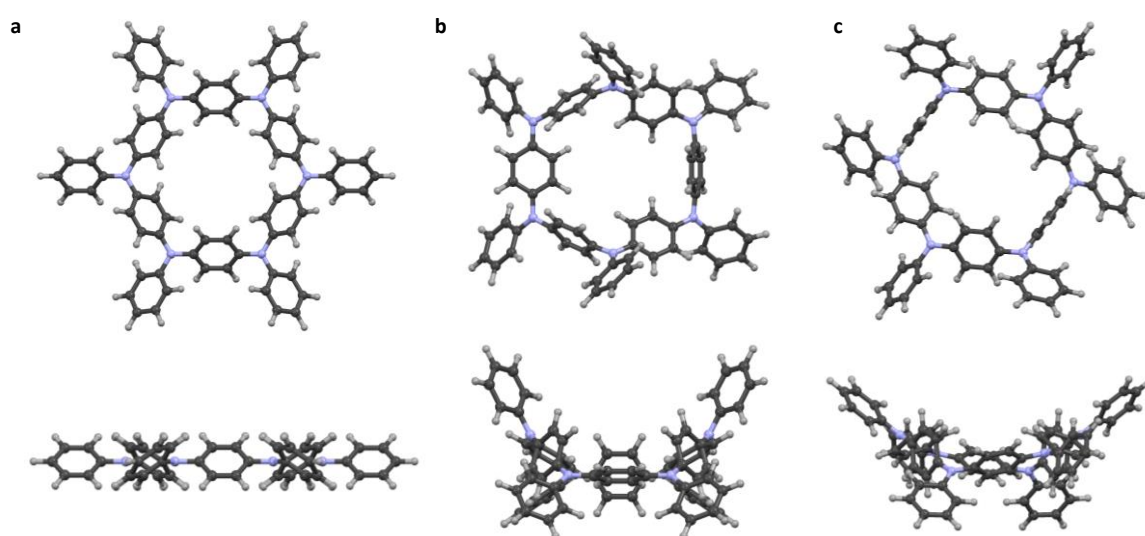


Figure 87 | DFT (M06-2X/6-31G) optimized conformations : top view (upper part), lateral view (bottom) for **a**) flat-macrocycle; **b**) boat-macrocycle; **c**) chair-macrocycle.

iii) Studies on the self-assembly of the macrocycle

In most of the common organic solvents, like acetone, ethyl acetate, toluene, methanol, ethanol, methylcyclohexane, dichloromethane, acetonitrile, *etc.*, macrocycle **39** was completely

insoluble, even heating up to the boiling point of the solvent. A good solubility could be achieved in hot chlorobenzene while, at room temperature, only DMF, dichlorobenzene, TCE and DMSO were able to solubilize it. At first, we investigated, whether the neutral molecule was assembled or molecular dispersed in pure TCE and DMF. Variable temperature $^1\text{H-NMR}$ spectra in DMF did not show any significant change in the shape and chemical shift of the aliphatic and aromatic peaks. The small shift of the amidic proton was explained, given its linear dependency with the temperature, by the interactions (hydrogen bonding) between the molecules and the solvent (**Figure 88a**). Transmission electron microscopy (TEM) further confirmed the absence of large self-assembled structures. In a similar way, variable temperature $^1\text{H-NMR}$ in TCE showed just a small broadening of the aromatic peaks at low temperature, suggesting that weak π - π stacking interactions take place (**Figure 88b**) (full spectra in Annexes; **Figure A 6**; **Figure A 7**). DOSY analysis, performed on protected (red spots in **Figure 88c**) and deprotected (blue spots in **Figure 88c**) macrocycle in TCE, showed similar diffusion coefficients for both the molecules, suggesting that, at room temperature and for neutral substrates, no self-assembly occurs.

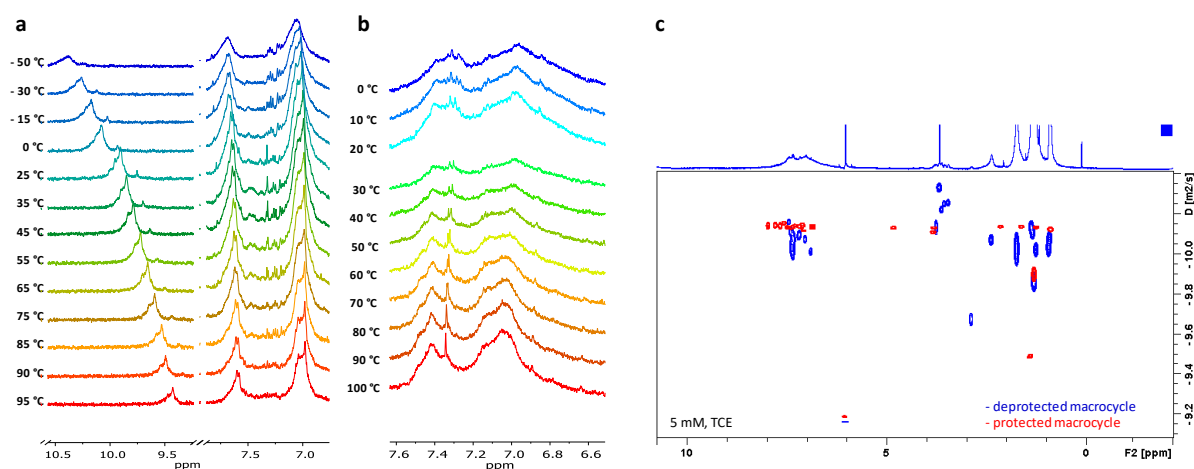


Figure 88 | a) Variable temperature $^1\text{H-NMR}$ of **39** in DMF- d_7 ; b) Variable temperature $^1\text{H-NMR}$ of **39** in TCE- d_2 ; c) Superimposed DOSY spectra for compounds **38** (red spots) and **39** (blue spots).

We further investigated the self-assembly of **39** by TEM in several other solvents. For this purpose, we tested three different concentrations (0.05 mM, 0.5 mM, 1 mM) in three different solvents toluene, chlorobenzene and dichlorobenzene. As shown in **Figure 89**, in toluene we observed amorphous aggregation for all the concentrations, mainly due to the low solubility of the macrocycle in this solvent. Chlorobenzene allowed to slightly improve the self-assembly of compound **39** since some fibers could be seen together with large amounts of amorphous

precipitation. Changing to the more polar *o*-dichlorobenzene, TEM images showed a quite important amount of self-organized material forming short fibrillar assemblies with some spots of non-organized precipitation. Unfortunately, for all the concentrations in *o*-dichlorobenzene, we were not able to minimize the amorphous aggregation. We believe that the monomers strongly interact with each other in solution. This makes it difficult to break the intermolecular forces before initiating the supramolecular polymerization, explaining the differences observed between the three different solvents, whose increasing boiling point (from toluene to *o*-dichlorobenzene), allow to reach a better solubility in *o*-dichlorobenzene, and thus higher degrees of organization. Several attempts were aimed at improving the order of the system in this solvent, like refluxing the solution for hours and performing slow cooling temperature ramps, but none of them gave any improvement.

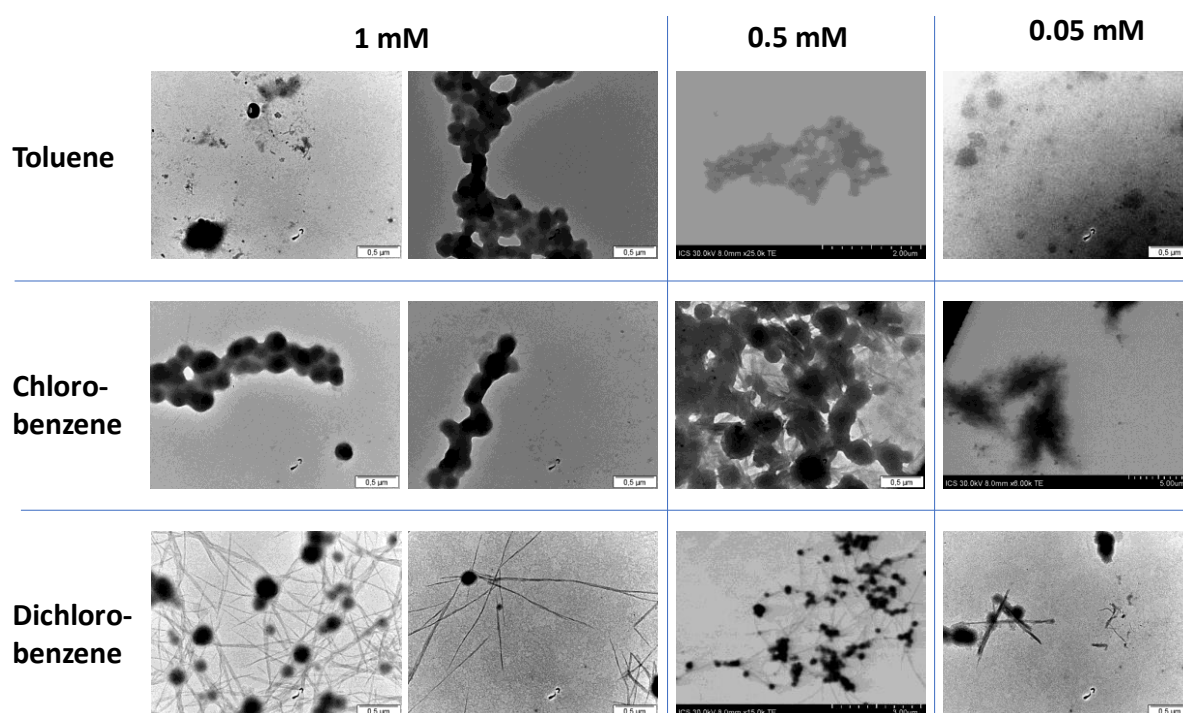


Figure 89 | TEM and STEM images for several solutions of **39** at different concentrations in various solvents.

In order to maximize the amount of self-assembled material, we tested other solvents and binary mixtures (all the conditions employed are summarized in Annexes; **Table A 1**). By employing solvent/non-solvent systems, we hoped to reduce the strength of the intermolecular interactions allowing the monomers to self-assemble in a controlled way. In light of the high solubility of **39** in toluene/methanol mixtures, we tried to obtain assemblies out of several samples with different toluene/methanol ratios. Unfortunately, this choice turned out to be

unsuccessful since no supramolecular structures were observed. We further tried to mix methanol and *o*-dichlorobenzene and we obtained small assemblies with still amorphous material, probably due to the low boiling point of the methanol which did not allow to heat the sample enough (see Annexes; **Figure A 8**). We decided to continue with *o*-dichlorobenzene as non-solvent, and we chose DMF as good solvent for its high boiling point. Upon cooling a 2 mM solution of **39** in *o*-dichlorobenzene/DMF (9:1), we finally observed the formation of supramolecular polymers with high degrees of organization. Imaging by AFM these fibers, we were able to identify single fibers with a diameter around 2.5 nm, coherent with the calculated diameter of the macrocycle which is about 2.1 nm (**Figure 90**). This result confirmed our expectation concerning the self-assembling of the macrocycle in nanocolumnar structures (see Annexes for modelling; **Figure A 10**).

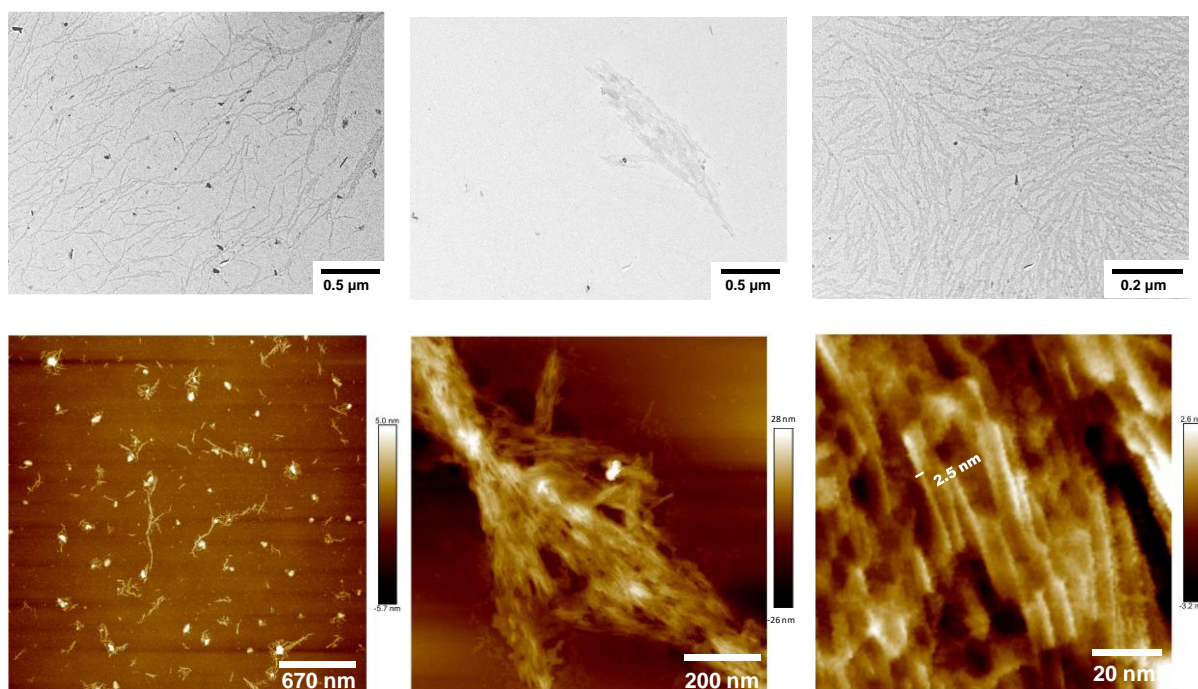


Figure 90 | TEM (top) and AFM (bottom) images of the supramolecular polymers obtained from a 2 mM solution of **39** in a mixture *o*-dichlorobenzene/DMF; Bottom right: image with the diameter of a single fiber.

3.4 CONCLUSIONS AND PERSPECTIVES

The synthesis of hexaazaparacyclophanes still represents a challenge as evidenced by the few papers reporting such structures. Moreover, the presence of functional groups on such molecules significantly complicates the synthetic methodologies by introducing stability issues, in particular during the metal-catalyzed couplings. Therefore, to succeed at the synthesis of a hexaaza[1₆]para-cyclophane bearing six terminal amides, the adoption of suitable protecting groups was necessary making the whole synthesis longer and more complex.

In this project, we developed a multistep synthesis which allows, starting from commercial materials, to synthesize hexaazaparacyclophanes with different substitution patterns on the periphery. After several attempts, we found that the *p*-methoxybenzyl group is the only protecting group that fulfilled the necessary condition: stable to all the reaction conditions employed and easily removable in the last step. Electrochemical measurements confirmed that the presence of multiple redox centers allow us to oxidize the macrocycle several times and, UV-vis analysis confirmed a large radical delocalization on the macrocyclic core, together with a putative delocalization between molecules in solutions/assemblies. The macrocycle showed the formation of supramolecular polymers in polar, high boiling aromatic solvents with the best results obtained in *o*-dichlorobenzene/DMF (9:1) mixture. In this system, we observed the formation of bundles of fibers with diameters for the individual fiber comparable to the size of the macrocycle.

Further studies will be addressed to investigate the supramolecular polymerization mechanism and to perform spectroelectrochemical measurements on the supramolecular polymers to investigate the delocalization along the stacking direction of the supramolecular polymer. We will characterize the hole transporting properties of this supramolecular materials through conductivity measurements in solution, and in solid state. Furthermore, EPR studies will be addressed to unravel the nature and stability of the radicals. In addition, in order to confirm the conformation of both compounds **38** and **39** we are currently trying to grow single crystals for X-ray analysis.

Related to this project, we envisioned the synthesis of other macrocyclic derivatives with different substitution patterns. In particular, we are synthesizing a chiral derivative to investigate the possibility to obtain chiral supramolecular structures and, thus, follow the supramolecular polymerization through CD spectroscopy. In another research direction, the use of this framework for prepare hexaazaparacyclophane derivatives expected to form a liquid crystalline phases is ongoing

GENERAL CONCLUSIONS AND PERSPECTIVES

In this work, we aimed to develop triarylamine based supramolecular systems able to show properties that are not accessible with simple triarylamine molecules. The knowledge we have gained during the past years on such systems can be exploited, now, to expand the field towards applications of triarylamine-based supramolecular polymers.

In *Chapter II*, we have investigated new triarylamine trisamide derivatives, bearing a variable number of tetraphenylethylene moieties and chiral chains, to obtain supramolecular polymers able to show both supramolecular polymerization induced emission and hole transporting properties. For the chiral compounds, we observed the formation of assemblies with a preferred helicity and, for one of them, we were able to achieve a high control of the morphologies of the supramolecular polymers by simply tuning the cooling rate applied to the system. High degrees of organization were reached for slow cooled samples, whose assemblies showed improved properties in term of circularly polarized luminescence and conductivity, compared to fast cooled samples. Further studies will be addressed to test these materials in optoelectronic devices to determine whether, a high level of organization, at the nanoscopic level, can lead to a major improvement in the efficiencies of the devices.

In *Chapter III* we described the synthesis of the first triarylamine based macrocycle able to form supramolecular polymers by means of six simultaneous hydrogen bonds. Owing to the presence of six triarylamine centers and its conjugated core, this macrocycle can be oxidized several times and the charge delocalized within the ring. The formation of nanoscopic assemblies should lead to a further delocalization of the radicals along the supramolecular polymer axis, conferring to this material intriguing electromagnetic properties. We hypothesize that the strong electron donating nature of this compound, together with the ability to assemble in supramolecular polymers, is advantageous towards its application as hole transporting materials. Further experiments will be addressed to unravel the electromagnetic properties of the macrocycle based supramolecular polymers and to test them for future applications.

To conclude, we have the strong conviction that the technological progress, which is more and more directed towards the downscaling of devices, can be boosted by the bottom up approach that only supramolecular chemistry provides, and which is not possible with classical approaches. In light of this, the search for supramolecular polymers with fascinating properties like luminescence, conductivity, plasmonic waveguiding, stimuli responsiveness,

piezoelectricity, *etc.* is of the greatest importance to discover new fields of application and advance those already existing.

EXPERIMENTAL PART

a. Solvents and Chemical Reagents

All reagents and solvents were purchased at the highest commercial quality and used without further purification unless otherwise noted. Dry solvents were obtained using a double column SolvTech purification system. Water was deionized by using a milli gradient system (Millipore, Molsheim). Bases for coupling reactions (Cs_2CO_3 , K_2CO_3 , NaOtBu) were dried under vacuum at 180°C for 24 h and then stored in a desiccator.

b. Chromatographic Methods

Thin Layer Chromatographies were performed using silica on TLC Aluminum foils (silica gel matrix with fluorescent indicator 254 nm, thickness: 500 μm , Sigma-Aldrich). In most cases, irradiation using a *Bioblock VL 4C* UV Lamp (6 W, 254 nm and/or 365 nm) as well as *p*-anisaldehydeanisaldehyde, phosphomolybdic acid and Cerium ammonium molybdate stainings, were used for visualization. *Preparative Adsorption Flash Column Chromatographies* were performed using silica gel (60 \AA , 230 - 400 mesh, 40 - 63 μm , Sigma-Aldrich) or aluminum oxide 90 (standardized activity II, 70 - 230 mesh, Merck). *Ultra-Performance Liquid Chromatographies coupled to Mass Spectroscopy (UPLC MS)* were carried out on a Waters Acquity UPLC SQD apparatus equipped with a PDA detector (190 500 nm, 80Hz and a SQD spectrometer), using a reverse phase column (Waters, BEH C_{18} 1.7 μm , 2.1 \times 50 mm or CSH Fluoro Phenyl Column, 130 \AA , 1.7 μm , 2.1 mm \times 100 mm), the MassLynx 4.1 XP software and a gradient (water acetonitrile + 0.1% TFA) as eluent.

c. Analytical Methods and Instruments

i. Nuclear Magnetic Resonance (NMR)

^1H NMR spectra were recorded on a *Bruker Avance 400* spectrometer at 400 MHz and ^{13}C NMR spectra at 101 MHz. The spectra were internally referenced to the residual solvent peaks (CDCl_3 : 7.26 ppm, DMSO-d_6 : 2.50 ppm, $(\text{CD}_3)_2\text{CO-d}_6$: 2.05 ppm, DMF-d_7 : 8.03, 2.92, 2.75 ppm, 1,1,2,2-Tetrachloroethane- d_2 : 6.0 ppm for ^1H spectrum; CDCl_3 : 77.16 ppm, DMSO-d_6 : 39.52 ppm, 1,1,2,2-Tetrachloroethane- d_2 73.7 ppm, DMF-d_7 : 163.15, 34.89, 26.76 ppm,

(CD₃)₂CO-*d*₆: 206.26 and 29.84 ppm for ¹³C spectrum). For ¹H NMR assignments, the chemical shifts are given in ppm. Coupling constants *J* are given in Hz. Peaks are described as singlet (s), doublet (d), triplet (t), quartet (q), septuplet (sept), multiplet (m) and broad (br).

ii. Mass Spectrometry

Electron Spray Ionization was recorded on a SQD mass spectrometer from Waters either by direct injection or after chromatography. *Matrix-Assisted Laser Desorption/Ionization* (MALDI) was performed on an Autoflex apparatus (Bruker). The sample matrix was dithranol dissolved in high purity CH₂Cl₂ and the sample solvent either in CH₂Cl₂ or DMF. Results were calibrated against a peptide calibration standard (Bruker) prepared in a mixture of CH₃CN and 0.1% TFA in ultrapure water in a volume ratio 1:2 and spotted with a 1,8-Diazabicyclo[5.4.0]undec-7ene (DBU) matrix in the same solvent system.

iii. UV-Vis-NIR

UV-Vis-NIR spectra were recorded either on a Varian Cary 5000 apparatus from Agilent Technologies (for far NIR region measurements or temperature dependent measurements); the same equipment was used to perform spectroelectrochemical measurements.

iv. Fluorescence Spectroscopy and Quantum Yield

Fluorescence emission spectra were recorded on a FluoroMax-4 (Horiba Jobin-Yvon) spectrofluorometer. Temperature was controlled using a Peltier system. *Quantum yield measurements* were performed by using an absolute photoluminescence quantum yield spectrometer Quantaaurus C11347 (Hamamatsu, Japan) exciting the sample at $\lambda_{\text{exc}} = 322$ nm.

v. Circular Dichroism Spectroscopy

CD spectra were recorded on a Jasco J-1700 spectropolarimeter. Quartz cell with a path length of 10 mm was used for the experiments. Temperature was controlled with a Peltier system (PTC-510).

vi. Circularly Polarized Luminescence (from the group of Professor D. Bassani)

Circularly polarized luminescence (CPL) was collected using a Jasco CPL-300 equipped with a xenon lamp (UXL-150S) and a head-on photomultiplier tube (Hamamatsu R376) as detector. The sample chamber is thermostated using a Peltier (PTC-517).

vii. Transmission Electron Microscopy (TEM)

TEM was performed using a CM12 Philips microscope equipped with a MVIII (SoftImaging System) CCD camera. Samples were analyzed in Bright Field Mode with a LaB₆ cathode and 120 kV tension. Image treatments were performed by using analySIS (Soft Imaging System) software. Samples were prepared by dropping a 0.1 mM chloroform solution of the compound onto a carbon-coated copper grid placed on a filter paper.

viii. Atomic Force Microscopy (AFM)

Atomic force microscopy (AFM) images were obtained by scanning the samples using a Nanoscope 8 (Bruker) operated in peak-force tapping mode. Ultra-sharp silicon cantilevers (ScanAsyst 0.4 N.m⁻¹) with a nominal tip radius < 5 nm were used. AFM images were acquired under an air atmosphere at room temperature. The force was reduced in order to avoid dragging of molecules by the tip. Integral gain was adjusted to give sharp images. Images were taken without on-line filtering and were subsequently processed only by flattening to remove the background slope.

ix. Rheology

The rheology measurement was taken with a conventional rheometer (Haake MARS-II) using a Couette geometry which is preferred to the plane–plane geometry because of its greater sensitivity. That makes easier acquiring reliable data in the liquid phase.

x Light diffusion

For light diffusion analysis a monochromatic light beam ($\lambda=632.8$ nm), provided by a HeNe laser (Melles Griot 05-LHP-151), successively passed through an attenuating filter (10^{-3}), a pinhole (50 μm), then through the sample over a 5 mm length and through a second pinhole (150 μm). At the end, the beam was focused onto the objective of a CCD camera (Retiga 2000R) to measure its intensity. The light intensity measurements were carried out while temperature was decreased from 115 °C to 25 °C at 0.2 °C/min. The sample temperature was controlled by an oven driven by a PID controller (SHINKO 100) (**Figure A 1**).

xi. Conductivity

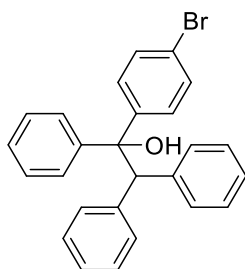
Conductivity experiments on solutions are performed on a Keithley 2400 source meter semiconductor characterization system as 2 point measurements. All experiments are performed under standard conditions (room temperature, air atmosphere). Commercial ITO electrochemical cells,

purchased from Instec, with an active ITO area of 10 x 10 mm, a 4 μm cell gap and no alignment layer (ref. S100A040uNOPI) were used (**Figure A 9**)

xii. Density Functional Theory (DFT) calculations

All the calculated molecular geometries were first optimised using the semi-empirical method PM6.²⁰⁷ The monomer and dimers geometries were then further optimised using the M06-2X functional and the 6-31G* all-electron basis set,²⁰⁸ as implemented in Gaussian09/D.01.²⁰⁹ In all cases, the absence of imaginary frequencies confirmed that the found geometries correspond to a local energy minima.

Compound 1

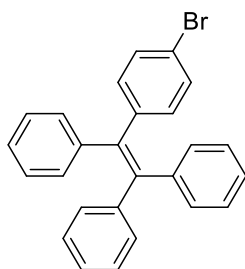


Compound 1 was synthesized according to a reported procedure.¹⁷⁶

To a two-necked round-bottom flask (250 mL) was added diphenylmethane (3.7 g, 22 mmol). After being evacuated and refilled with nitrogen three times, THF (40 mL) was injected. The mixture was cooled down to 0 °C and n-BuLi (1.6 M in hexanes, 13.8 mL, 22 mmol) was added dropwise. The resultant red solution was stirred at 0 °C for 1 h, then 4-bromobenzophenone (5.2 g, 20 mmol) dissolved in 10 mL THF was added slowly. The reaction mixture was warmed up to room temperature and left under stirring for 6 hours then quenched by addition of 300 mL of a saturated NH₄Cl solution. The solution was extracted by DCM (3 x 150 mL) and the combined organic layer was washed with water, brine and dried over Na₂SO₄. After solvent evaporation, the obtained solid was washed with hexane five times and purified by filtration to afford compound **1** (6.7 g) as a white powder.

The product is used in the next step without further characterization.

Compound 2



To a 100 mL round-bottom flask equipped with a condenser was placed the obtained alcohol **1** and a catalytic amount of *p*-toluenesulfonic acid (10 mg, 0.06 mmol). Toluene (20 mL) was added to the flask and the mixture was refluxed overnight. The reaction was allowed to regain room temperature, the solvent was evaporated and the crude product was purified by column chromatography (SiO₂, eluent: cyclohexane) to afford compound **2** (5.6 g) in 68% yield over two steps.

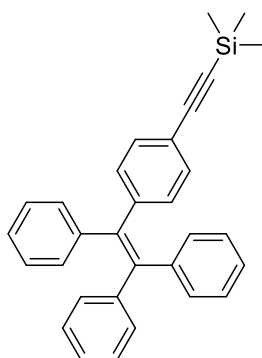
*Analyses were in accordance with the literature.*¹⁷⁶

¹H NMR (CDCl₃, 400 MHz, 298K): δ (ppm) = 7.22 (d, *J* = 8.2 Hz, 2H), 7.10 (m, 9H), 7.01 (m, 6H), 6.90 (d, *J* = 8.2 Hz, 2H).

¹³C NMR (CDCl₃, 101 MHz, 298K): δ (ppm) = 143.6, 143.5, 143.4, 142.9, 141.8, 139.9, 133.2, 131.5, 131.4, 131.1, 128.1, 128.0, 127.9, 126.9, 126.8, 120.6.

ESI-MS: *m/z* calculated for C₂₆H₁₉Br 411.07 [M+H]⁺; found 411.26

Compound 3



To a 250 mL round bottom flask was added $\text{PdCl}_2(\text{PPh}_3)_2$ (74 mg, 106 μmol), copper iodide (40 mg, 0.21 mmol), triphenylphosphine (83 mg, 0.32 mmol), compound **2** (2.2 g, 5.31 mmol), and a mixture of THF/TEA/piperidine (100 mL, 5:4:1 v/v/v) under nitrogen. After the catalyst was completely dissolved, trimethylsilylacetylene (626 mg, 6.38 mmol) was injected into the flask. The reaction was stirred at 50 °C for 24 h. The formed solid was removed by filtration and washed with diethyl ether. The filtrate was concentrated by a rotary evaporator and the crude product was purified by column chromatography (SiO_2 , eluent: cyclohexane) to afford compound **3** (2.23 g) as a white powder in 98 % yield.

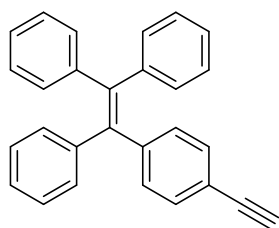
*Analyses were in accordance with the literature.*¹⁷⁶

^1H NMR (CDCl_3 , 400 MHz, 298K): δ (ppm) = 7.21 (d, J = 8.5 Hz, 2H), 7.10 (m, 9H), 7.01 (m, 6H), 6.96 (d, J = 8.5 Hz, 2H), 0.24 (s, 9H).

^{13}C NMR (CDCl_3 , 101 MHz, 298K): δ (ppm) = 144.5, 143.7, 143.6, 143.5, 141.9, 140.5, 131.6, 131.5, 131.45, 128.0, 127.94, 127.9, 126.9~126.8, 121.1, 105.5, 94.5, 0.2

ESI-MS: m/z calculated for $\text{C}_{31}\text{H}_{28}\text{Si}$ 429.20 $[\text{M}+\text{H}]^+$; found 429.32

Compound 4



To a 250 mL round-bottom flask was added compound **3** (532 mg, 1.24 mmol) and THF (15 mL). Then KOH (278 mg, 5 mmol) dissolved in methanol (5 mL) was added. The mixture was stirred at room temperature overnight. After most of the solvent was evaporated under reduced pressure, an HCl solution (1 M, 20 mL) was added, then extracted with DCM (3 x 50 ml). The organic layer was combined and washed with water (3 x 50 ml) and brine (1 x 50 ml), and then dried over Na₂SO₄. After filtration and solvent evaporation, the crude product was purified by column chromatography (SiO₂, eluent: cyclohexane) to afford compound **4** (398 mg) in 90% yield.

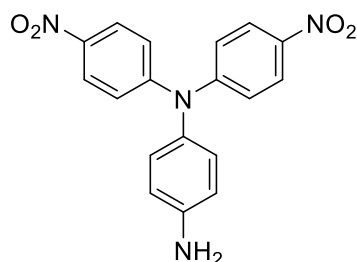
¹H NMR (CDCl₃, 400 MHz, 298K): δ (ppm) = 7.24 (d, J = 8.3 Hz, 2H), 7.11 (m, 9H), 7.02 - 6.94 (m, 8H), 3.05 (s, 1H).

¹³C NMR (CDCl₃, 101 MHz, 298K): δ (ppm) = 144.6, 143.6, 143.5, 143.4, 141.9, 140.2, 131.6, 131.4, 128.0, 127.9, 127.8, 126.8, 126.7, 120.0, 83.9, 77.4

ESI-MS: m/z calculated for C₂₈H₂₀ 357.16 [M+H]⁺; found 357.28

*Analyses were in accordance with the literature.*¹⁷⁶

Compound 5



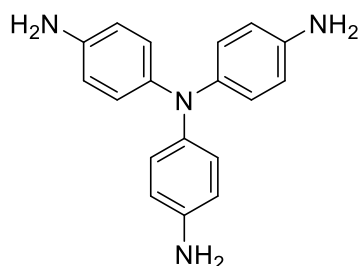
1,4-benzenediamine (3.5 g, 32.4 mmol) and potassium carbonate (17.9 g, 129 mmol) were dissolved in dry DMSO (50 mL) in a 250 mL Schleck flask. 4-fluoronitrobenzene (6.87 mL, 64.7 mmol) was added to the colorless reaction mixture and heated for 3 days at 90 °C. The color changed to dark-red. Upon completion, as monitored by UPLC-MS, the solution was allowed to cool down to room temperature and further diluted with water (300 mL) leading to the formation of a dark red precipitate. This solid was filtered, washed several times with water (5 × 50 mL) and then dried to afford compound **5** (10.4 g) in 92 % yield as a dark red solid.

¹H NMR (CDCl₃, 400 MHz, 298 K): δ (ppm) = 8.12 (d, *J* = 9.3 Hz, 4H), 7.13 (d, *J* = 9.3 Hz, 4H), 6.96 (d, *J* = 8.6 Hz, 2H), 6.73 (d, *J* = 8.6 Hz, 2H), 3.84 (br s, 2H).

¹³C NMR (CDCl₃, 101 MHz, 298 K): δ (ppm) = 152.2, 146.1, 142.3, 135.2, 129.1, 125.6, 121.6, 116.6.

ESI-MS: *m/z* calculated for C₁₈H₁₄N₄O₄ 351.10 [M+H]⁺; found 351.29

Compound 6



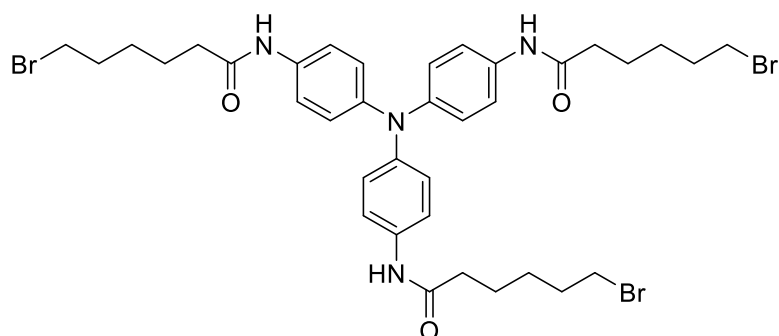
Compound **5** (10.5 g, 30 mmol) was dissolved in a mixture of ethanol (200 mL) and dioxane (100 mL) in a 500 mL round-bottom two-neck flask equipped with a reflux condenser. Palladium on charcoal (0.8 g) was added carefully under an atmosphere of argon. The reaction mixture was heated up to 80 °C. Hydrazine hydrate (35 mL, 719 mmol) was added dropwise under vigorous stirring over a period of 3 hours, and the reaction mixture was further stirred under reflux overnight. Then, the reaction was cooled down to room temperature. The catalyst was removed by filtration through a pad of celite, which was washed a few times with methanol (200 mL). The filtrate was poured into water (1 L). The precipitate was filtered off and dried to give the crude product which was recrystallized from boiling ethanol to obtain compound **6** (7.1 g) in 82 % yield as a grey solid.

¹H NMR (Acetone-*d*₆, 400 MHz, 298 K): δ (ppm) = 6.71 (d, J = 8.8 Hz, 6H), 6.55 (d, J = 8.8 Hz, 6H), 4.28 (br s, 6H).

¹³C NMR (Acetone-*d*₆, 101 MHz, 298 K): δ (ppm) = 143.9, 140.7, 125.3, 116.0.

ESI-MS: m/z calculated for C₁₈H₁₈N₄ 291.15 [M+H]⁺; found 291.38

Compound 7



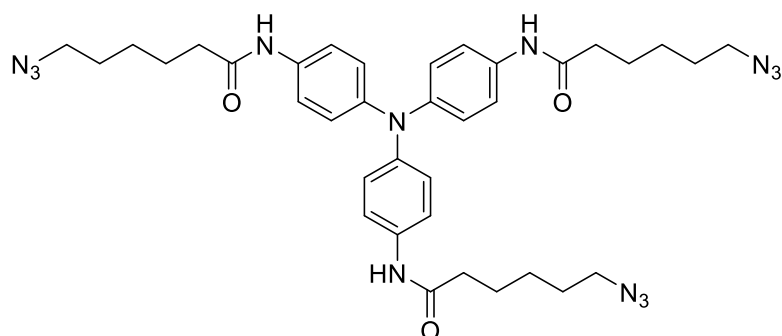
Compound **6** (520 mg, 1.79 mmol) was dissolved in a mixture of dichloromethane (70 mL) and THF (70 mL) in a round-bottom two-neck flask. Triethylamine (725 mg, 7.17 mmol) was added and the solution was cooled down to 0 °C on an ice bath. After that 6-bromohexanoyl chloride (1.26 mg, 5.91 mmol) was added dropwise to the stirred solution. The reaction was left to regain room temperature and was stirred for 1 hour. The solvent was evaporated and the crude solid was dissolved in THF (350 mL). The organic layer was washed subsequently with 1M HCl/brine (1:2; 100 mL), 1M NaOH/brine (1:2; 2 x 50 mL), saturated NH₄Cl (50 mL) and brine (100 mL). Then it was dried over anhydrous Na₂SO₄, which was removed by filtration. The solvent was evaporated under reduced pressure and the crude product was recrystallized from boiling ethanol. The precipitate was filtered using a glass filter, washed with cold ethanol and diethyl ether. After drying under vacuum, compound **7** (1.27 g) was obtained in 87% yield as white solid.

¹H NMR (DMSO-*d*₆, 400 MHz, 298 K): δ (ppm) = 9.80 (s, 3H), 7.47 (d, *J* = 8.3 Hz, 6H), 6.87 (d, *J* = 8.3 Hz, 6H), 3.53 (t, *J* = 6.8 Hz, 6H), 2.28 (t, *J* = 7.3 Hz, 6H), 1.82 (q, *J* = 6.8 Hz, 6H), 1.60 (q, *J* = 7.3 Hz, 6H), 1.41 (m, 6H);

¹³C NMR (DMSO-*d*₆, 101 MHz, 298 K): δ (ppm) = 171.2, 143.2, 134.7, 124.0, 120.7, 36.6, 35.6, 32.5, 27.7, 24.8;

ESI-MS: *m/z* calculated for C₃₆H₄₅Br₃N₄O₃ 821.10 [M+H]⁺; found 821.23

Compound 8

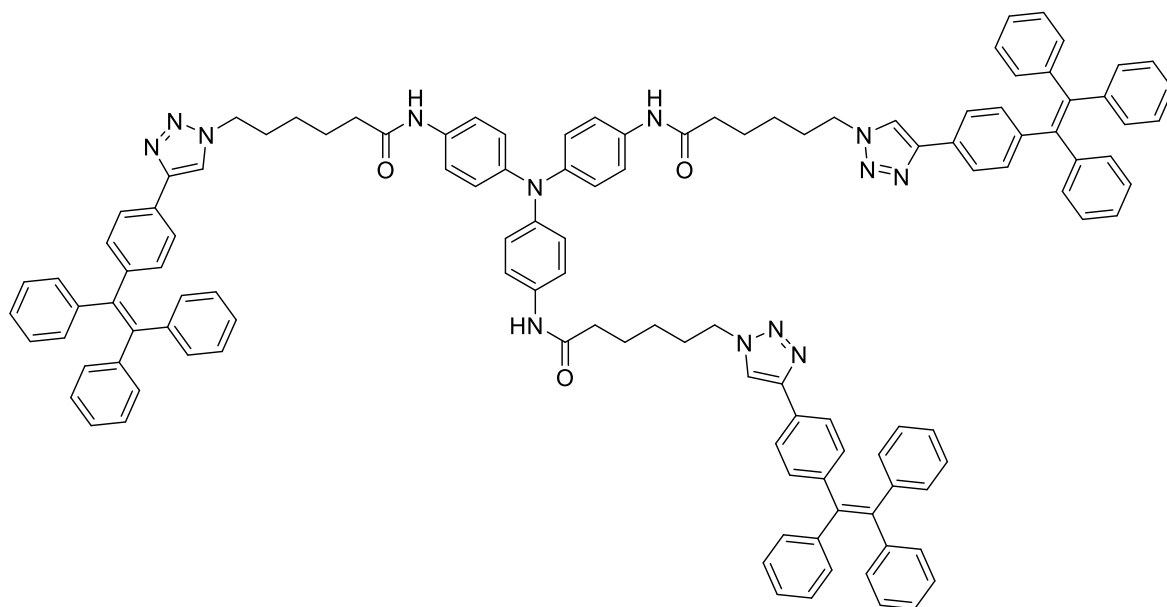


Compound **7** (512 mg, 0.623 mmol) was dissolved in DMF (9.64 mL) in a round-bottom two-neck flask equipped with a reflux condenser and sodium azide (243 mg, 3.74 mmol) was added under argon. The mixture was kept at 80°C overnight. Then, the reaction was left to cool down to room temperature and water (150 mL) was added. The aqueous phase was extracted four times with DCM (150 mL). Then the combined organic layers were washed several times with water (200 mL) and brine (200 mL), dried on Na₂SO₄ and the solvent evaporated. The crude product was recrystallized from boiling ethanol. The precipitate was filtered with a glass filter, washed with cold ethanol and diethyl ether. After drying under vacuum, compound **8** (427 g) was obtained in 97% yield as white solid.

¹H NMR (DMSO-d₆, 400 MHz, 298 K): δ (ppm) = 9.82 (s, 3H), 7.50 (d, *J* = 8.4 Hz, 6H), 6.89 (d, *J* = 8.4 Hz, 6H), 2.29 (t, *J* = 7.3 Hz, 6H), 1.63 (q, *J* = 7.3 Hz, 6H), 1.49 (t, *J* = 7.1 Hz, 6H) 1.32 - 1.27 (m, 12H),

¹³C NMR (DMSO-d₆, 101 MHz, 298 K): δ (ppm) = 171.4, 142.8, 134.1, 123.8, 120.8, 50.1, 36.3, 29.4, 25.7, 25.3;

ESI-MS: *m/z* calculated for C₃₆H₄₅N₁₃O₃ 708.38 [M+H]⁺; found 709.46

Compound **3TPE-TATA**

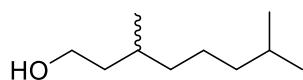
Compound **8** (330 mg, 0.46 mmol), compound **4** (531 mg, 1.49 mmol) and CuBr (214 mg, 1.49 mmol) were placed in a Schlenk under argon. Degassed DMF (15 mL) was added followed by N,N,N',N'',N''-Pentamethyldiethylenetriamine (258 mg, 1.49 mmol). The reaction was stirred overnight at 80 °C. After cooling down to room temperature, the reaction was poured into an EDTA solution (200 mL, 3 M, pH = 9 NaOH), stirred for 10 minutes and then extracted with DCM (3 x 150 mL). The collected organic layer were washed with saturated NH₄Cl (3 x 200 mL) and brine (200 mL). After solvent evaporation the solid was precipitated from ethyl acetate and then purified by column chromatography (SiO₂, dry loading from toluene/methanol 1:1, eluent: toluene/acetone 7/3) to afford compound **3TPE-TATA** (704 mg) in 85% yield.

¹H NMR (DMSO-d₆, 400 MHz, 298 K): δ (ppm) = 9.77 (s, 3H), 8.50 (s, 3H), 7.57 (d, *J* = 7.5 Hz, 6H), 7.44 (d, *J* = 8.3 Hz, 6H), 7.17 – 7.07 (m, 27H), 7.02 – 6.94 (m, 24H), 6.85 (d, *J* = 8.3 Hz, 6H), 4.37 (t, *J* = 6.3 Hz, 6H), 2.25 (t, *J* = 7.2 Hz, 6H), 1.86 (q, *J* = 7.4 Hz, 6H), 1.61 (q, *J* = 7.4 Hz, 6H), 1.26 (q, *J* = 7.2 Hz, 6H),

¹³C NMR (DMSO-d₆, 101 MHz, 298 K): δ (ppm) = 171.1, 146.4, 143.7, 143.6, 143.5, 143.1, 141.3, 140.7, 136.7, 131.7, 131.2, 131.1, 129.4, 128.4, 128.3, 128.2, 127.1, 125.0, 124.0, 121.8, 120.8, 49.9, 36.5, 29.8, 25.8, 25.0,

ESI-MS: *m/z* calculated for C₁₂₀H₁₀₅N₁₃O₃ [M+H]⁺ 1777.85, found 1777.90;

Compound (S)-9 and (R)-9



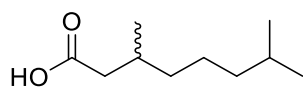
Compounds (S)-9 / (R)-9 were synthesized according to a reported procedure.¹⁷⁷

(3S)-3,7-dimethyloct-6-en-1-ol/(3R)-3,7-dimethyloctan-1-ol (5.0 g, 31.7 mmol) was dissolved in a mixture of ethyl acetate (50 mL) and methanol (50 mL) in a 250 mL round bottom flask. The solution is passed through an H-cube reactor (*THALESNANO H-Cube HC 2-SS Continuous Flow Hydrogenation Reactor With CatCart*) on a 10% Pd/C cartridge at 70°C, in full H₂ mode and with a 0.1 mL /min flow. The reaction is monitored by NMR and the process is repeated more times in case of some starting material is remaining. The solvent was evaporated under reduced pressure, and the resulting residue was dried in vacuo to give compound (S)-9 / (R)-9 (4.9 g, 98 %) as a colorless oily liquid, which was clean enough to be used in the next step without purification.

¹H NMR (CDCl₃, 400 MHz, 298 K): δ (ppm) = 3.74 – 3.60 (m, 2H), 1.65 – 1.45 (m, 3H), 1.42 – 1.33 (m, 1H), 1.33 – 1.20 (m, 4H), 1.19 – 1.06 (m, 3H), 0.92 – 0.80 (m, 9H).

¹³C NMR (CDCl₃, 101 MHz, 298 K): δ (ppm) = 61.4, 40.2, 39.4, 37.5, 29.6, 28.1, 24.8, 22.8, 22.7, 19.8.

Analyses were in accordance with the literature.¹⁷⁷

Compound (**S**)-**10** and (**R**)-**10**

Compounds (**S**)-**10** / (**R**)-**10** were synthesized according to a reported procedure.¹⁷⁷

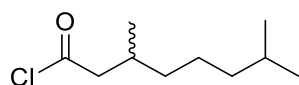
Periodic acid (7.2 g, 31.4 mmol) was dissolved in acetonitrile (100 mL) under vigorous stirring at room temperature for 40 min. Then, pyridinium chlorochromate (2 %, 60 mg, 0.278 mmol) was added. The solution was cooled down to 0 °C using an ice bath and compound (**S**)-**9** / (**R**)-**9** (2.2 g, 13.9 mmol) in acetonitrile (30 mL) was added dropwise. The reaction mixture was stirred for 1 hour at 0 °C and for 3 hours at room temperature. Following, acetonitrile was evaporated under reduced pressure. Ethyl acetate (200 mL) was added and the organic layer was extracted with water/brine 1:1 v/v (400 mL), saturated NaHSO₃ (300 mL) and brine (500 mL). The organic phase was dried over Na₂SO₄, filtered and evaporated under vacuum. The resulting crude liquid was distilled using the kugelrohr to give compound (**S**)-**10** / (**R**)-**10** (2.2 g, 92 %) as a colorless viscous liquid.

¹H NMR (CDCl₃, 400 MHz, 298 K): δ (ppm) = 2.35 (dd, *J* = 14.9, 5.8 Hz, 1H), 2.15 (dd, *J* = 14.9, 8.2 Hz, 1H), 2.01 – 1.90 (m, 1H), 1.60 – 1.46 (sept, *J* = 6.7 Hz, 1H), 1.38 – 1.10 (m, 6H), 0.97 (d, *J* = 6.7 Hz, 3H), 0.87 (d, *J* = 6.7 Hz, 6H).

¹³C NMR (CDCl₃, 101 MHz, 298 K): δ (ppm) = 179.5, 41.3, 39.1, 36.8, 30.1, 27.7, 24.5, 22.6, 22.3, 19.8;

*Analyses were in accordance with the literature.*¹⁷⁷

Compound (S)-11 and (R)-11



The synthetic procedure was adapted from ref.¹⁷⁷

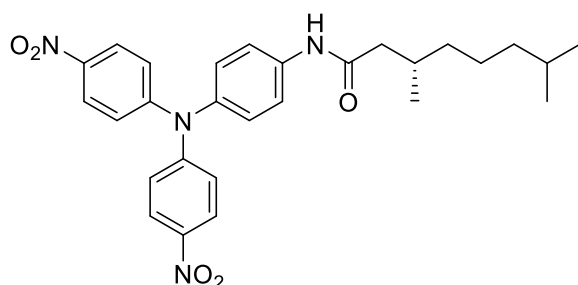
Compound (S)-10 / (R)-10 (2.2 g, 12.8 mmol) was dissolved in chloroform (10 mL) and thionyl chloride (5 mL, 68.9 mmol) was added. The reaction mixture was stirred at reflux for 3 hours. Next, it was cooled down to room temperature, solvent was removed under reduced pressure and compound (S)-11 / (R)-11 (2.4 g, 99 %) was obtained as a colorless oil after distillation using the kugelrohr.

¹H NMR (CDCl₃, 400 MHz, 298 K): δ (ppm) = 2.88 (dd, J = 16.0, 5.8 Hz, 1H), 2.68 (dd, J = 16.0, 8.0 Hz, 1H), 2.14 – 2.01 (m, 1H), 1.60 – 1.46 (sept, J = 6.7 Hz, 1H), 1.38 – 1.10 (m, 6H), 0.99 (d, J = 6.6 Hz, 3H), 0.87 (d, J = 6.6 Hz, 6H).

¹³C NMR (CDCl₃, 101 MHz, 298 K): δ (ppm) = 173.4, 54.4, 39.0, 36.5, 30.9, 3.03, 24.6, 22.8, 22.7, 19.4;

Analyses were in accordance with the literature.¹⁷⁷

Compound 12



Compound 5 (600 mg, 1.71 mmol) was placed in a round-bottom two-neck flask equipped with a reflux condenser and dissolved in dry dichloromethane (100 mL). Triethylamine (0.29 mL, 2.05 mmol) was added and the solution was cooled down to 0 °C in an ice bath. After that (S)-

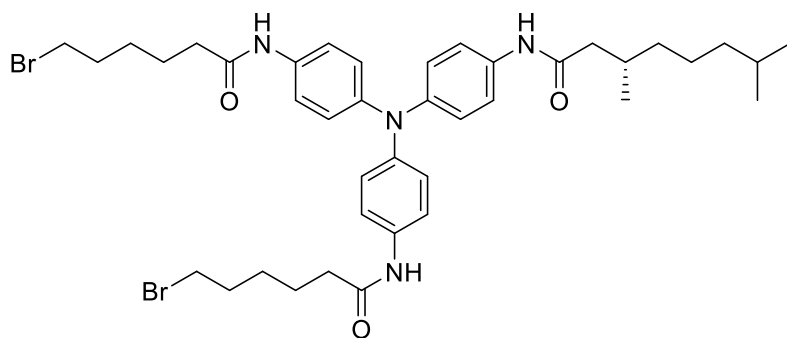
11 (360 mg, 1.88 mmol) was added dropwise to a stirred solution. The reaction was left to warm up and was stirred for 1 hour at room temperature. Following this step, additional DCM (100 ml) was added and the organic phase washed with a saturated solution of NaHCO₃ (3 x 200 ml) and brine (1 x 200 ml). The organic phase was dried over Na₂SO₄, filtered and evaporated under vacuum. The crude was then purified by column chromatography (SiO₂, eluent: cyclohexane/ethyl acetate 8/2) to afford compound **12** (760 mg) in 88% yield.

¹H NMR (CDCl₃, 400 MHz, 298 K): δ (ppm) = 8.09 (d, *J* = 8.9 Hz, 4H), 7.68 (d, *J* = 8.7 Hz, 2H), 7.35 (s, 1H), 7.05 (m, 6H), 2.30 (dd, *J* = 14.5, 5.5 Hz, 1H), 2.13 (dd, *J* = 14.5, 8.2 Hz, 1H), 2.05 – 1.88 (m, 1H), 1.61 – 1.45 (sept, *J* = 6.8 Hz, 1H), 1.38 – 1.10 (m, 6H), 0.97 (d, *J* = 6.8 Hz, 3H), 0.87 (d, *J* = 6.6 Hz, 6H).

¹³C NMR (CDCl₃, 101 MHz, 298 K): δ (ppm) = 171.2, 151.9, 142.9, 140.3, 136.9, 128.0, 125.6, 122.2, 121.6, 42.5, 39.3, 37.1, 30.2, 27.8, 24.5, 22.5, 22.4, 19.7;

ESI-MS: *m/z* calculated for C₂₈H₃₂N₄O₅ [M+H]⁺ 505.24 found 505.36

Compound 13



Compound **12** (691 mg, 1.37 mmol) was dissolved in ethyl acetate (50 mL) in a round-bottom two-neck flask equipped with a reflux condenser. Then tin chloride (2.6 g, 10 mmol) was added under argon and the reaction was stirred for 12h at 77 °C. Then, the solution was cooled to room temperature and more ethyl acetate (200 mL) was added. The organic phase was washed with saturated solution of NaHCO₃ (4 x 300 mL) and with brine (1 x 150 mL), dried over

Na₂SO₄, filtered and the solvent was concentrated to a reduced volume (~10 mL). This solution was used without any characterization in the next step.

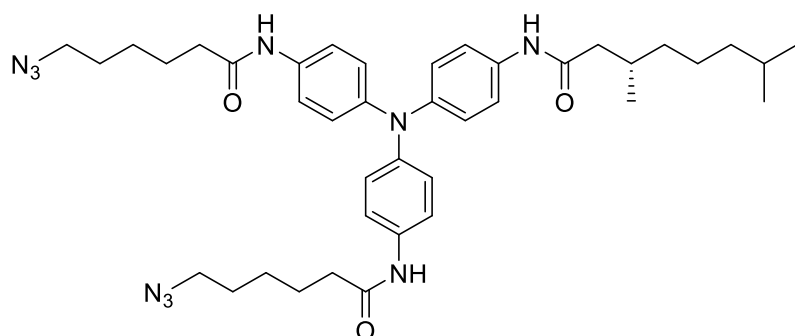
The solution from the previous step was diluted in dry DCM (40 mL) and placed in a round-bottom two-neck flask, then triethylamine (304 mg, 3.0 mmol) was added under argon and the mixture cooled to 0 °C on ice bath. To the stirred solution, 6-bromohexanoil chloride (643 mg, 3.0 mmol) was added dropwise after which the solution was allowed to regain room temperature. The mixture was stirred at room temperature for 4h. Once the reaction was complete, more DCM (50 ml) was added and the organic phase was washed with a saturated solution of NaHCO₃ (3 x 150 mL) and with brine (1 x 150 mL), dried over Na₂SO₄, filtered and the solvent evaporated under reduced pressure. The crude product was recrystallized from diethyl ether, the precipitate was filtered with a glass filter, washed with cold diethyl ether and dried under vacuum to obtain compound **13** (780 mg) in 71 % yield over two steps.

¹H NMR (DMSO-d₆, 400 MHz, 298 K): δ (ppm) = 9.82 (s, 1H), 9.79 (s, 2H), 7.47 (d, *J* = 8.9 Hz, 6H), 6.90 (d, *J* = 8.9 Hz, 6H), 3.53 (t, *J* = 6.8 Hz, 4H), 2.40 - 2.25 (m, 5H), 2.02 (m, 1H), 1.96 - 1.77 (m, 5H), 1.65 - 1.55 (m, 5H), 1.35 - 1.07 (m 10H), 0.89 (d, *J* = 6.7 Hz, 3H), 0.85 (d, *J* = 6.4 Hz, 6H)

¹³C NMR (DMSO-d₆, 101 MHz, 298 K): δ (ppm) = 171.4, 170.8, 143.4, 134.5, 124.3, 121.0, 43.8, 39.0, 36.9, 36.5, 35.5, 32.3, 27.8, 27.7, 24.9, 24.6, 23.1, 22.9, 19.9;

ESI-MS: *m/z* calculated for C₄₀H₅₄Br₂N₄O₃ [M+H]⁺ 799.25 found 799.40

Compound 14

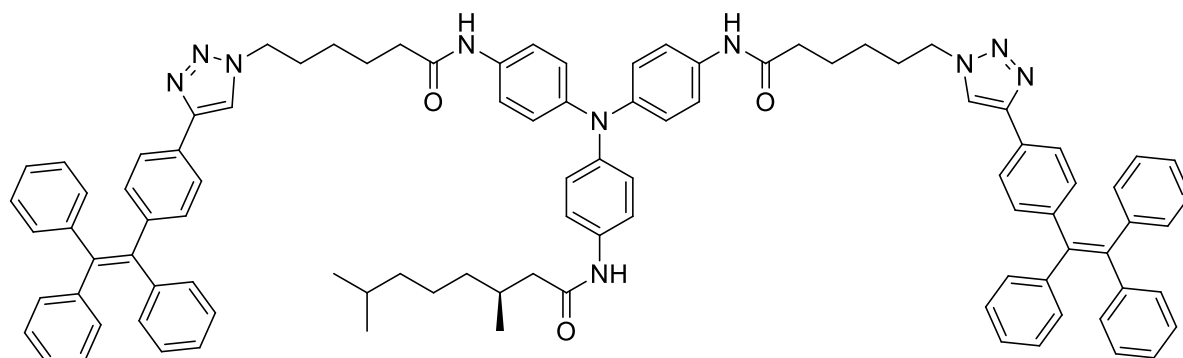


Compound **13** (500 mg, 0.7 mmol) was dissolved in DMF (10 mL) in a round-bottom two-neck flask equipped with a reflux condenser and sodium azide (260 mg, 4 mmol) was added under argon. The mixture was kept at 80 °C overnight. Then, the reaction was left to cool down at room temperature and water (150 mL) was added. Then the aqueous phase was extracted four times with DCM (150 mL). The combined organic phase was washed several times with water (200 mL) and brine (200 mL), dried on Na₂SO₄ and the solvent evaporated. The crude product was recrystallized from diethyl ether. The precipitate was filtered using a glass filter and washed with cold diethyl ether. After drying under vacuum, compound **14** (465 mg) was obtained in 92% yield as white solid.

¹H NMR (DMSO-d₆, 400 MHz, 298 K): δ (ppm) = 9.90 (s, 1H), 9.85 (s, 2H), 7.48 (d, *J* = 8.7 Hz, 6H), 6.90 (d, *J* = 8.7 Hz, 6H), 2.35 (t, *J* = 7.5 Hz, 4H), 2.27 (m, 1H), 2.02 (m, 1H), 1.80 (sept, *J* = 6.8 Hz, 1H), 1.71 - 1.63 (m, 5H), 1.55 - 1.47 (m, 4H), 1.35 - 1.08 (m, 14H), 0.89 (d, *J* = 6.8 Hz, 3H), 0.84 (d, *J* = 6.6 Hz, 6H)

¹³C NMR (DMSO-d₆, 101 MHz, 298 K): δ (ppm) = 171.2, 170.5, 143.1, 134.4, 124.1, 120.8, 50.0, 43.8, 39.0, 36.9, 36.5, 35.5, 27.8, 27.7, 24.9, 24.6, 23.1, 22.9, 19.9;

ESI-MS: *m/z* calculated for C₄₀H₅₄N₁₀O₃ [M+H]⁺ 723.44 found 723.54

Compound **2TPE-(S)TATA**

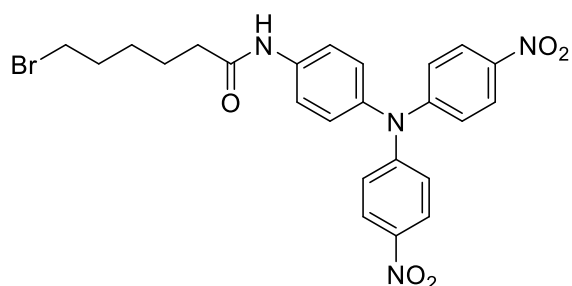
Compound **14** (160 mg, 0.22 mmol), compound **4** (173 mg, 0.49 mmol) and CuBr (70 mg, 0.49 mmol) were placed in a Schlenk under argon. Degassed DMF (7 mL) was added followed by N,N,N',N'',N''-Pentamethyldiethylenetriamine (84 mg, 0.49 mmol). The reaction was stirred overnight at 80 °C. After cooling down to room temperature, the reaction was poured over a solution of EDTA (200 mL, 3 M, pH = 9, NaOH), stirred for 10 minutes and then extracted with DCM (3 x 150 mL). The collected organic layer was washed with saturated NH₄Cl (3 x 200 mL) and brine (200 mL). After solvent evaporation the solid was precipitated from ethyl acetate and then purified by column chromatography (SiO₂, dry loading from toluene/methanol 1:1, eluent: toluene/ethyl acetate 7/3) to afford compound **2TPE-(S)TATA** (280 mg) in 89% yield.

¹H NMR (DMSO-d₆, 400 MHz, 298 K): δ (ppm) = 9.78 (s, 3H), 8.49 (s, 2H), 7.58 (d, *J* = 8.0 Hz, 4H), 7.51 - 7.41 (m, 6H), 7.20 - 7.07 (m, 20 H), 7.02 - 6.94 (m, 14H), 6.86 (m, 6H), 4.37 (t, *J* = 6.9 Hz, 4H), 2.26 (m, 6H), 1.98 - 1.80 (m, 5H), 1.61 (q, *J* = 7.4 Hz, 4H), 1.50 (sept, *J* = 6.3 Hz, 1H), 1.36 - 1.08 (m, 14H), 0.89 (d, *J* = 6.5 Hz, 3H), 0.84 (d, *J* = 6.8 Hz, 6H).

¹³C NMR (DMSO-d₆, 101 MHz, 298 K): δ (ppm) = 170.6, 170.3, 145.9, 143.2, 143.1, 143.0, 142.6, 140.7, 140.1, 134.2, 134.1, 131.2, 130.7, 130.6, 128.9, 128.2, 127.8, 127.7, 126.6, 126.5, 125.2, 124.5, 123.5, 121.4, 121.2, 120.3, 49.3, 44.0, 38.6, 36.4, 36.0, 30.1, 29.4, 27.3, 25.4, 24.5, 24.0, 22.6, 22.4, 21.0, 19.4;

ESI-MS: *m/z* calculated for C₉₆H₉₄N₁₀O₃ [M+H]⁺ 1436.75 found 1437.80

Compound 15

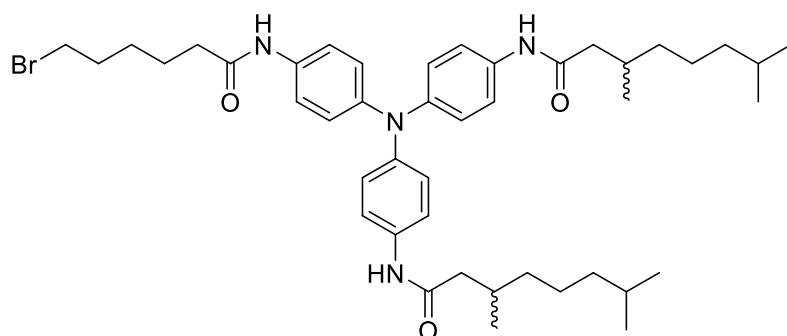


Compound **5** (520 mg, 1.48 mmol) was placed in a round-bottom two-neck flask equipped with a reflux condenser and dissolved in dry dichloromethane (50 mL). Triethylamine (0.248 mL, 1.78 mmol) was added and the solution was cooled down to 0 °C on an ice bath. Then, 6-bromohexanoyl chloride (348 mg, 1.63 mmol) was added dropwise to the stirred solution. The reaction was left to regain room temperature and was stirred for 1 hour. Then, additional DCM (50 ml) was added and the organic phase was washed with a saturated solution of NaHCO₃ (3 x 100 ml) and brine (1 x 150 ml). The organic phase was dried over Na₂SO₄, filtered and evaporated under vacuum. The crude was then purified by column chromatography (SiO₂, eluent: cyclohexane/ethyl acetate 8/2) to obtain compound **15** (670 mg) in 86% yield.

¹H NMR (CDCl₃, 400 MHz, 298 K): δ (ppm) = 8.11 (d, *J* = 9.2 Hz, 4H), 7.60 (d, *J* = 8.5 Hz, 2H), 7.45 (s, 1H), 7.11 (m, 6H), 3.40 (t, *J* = 6.8 Hz, 2H), 2.40 (t, *J* = 7.4 Hz, 2H), 1.89 (q, *J* = 7.4, 2H), 1.76 (q, *J* = 7.5 Hz, 2H), 1.52 (m, 2H);

¹³C NMR (CDCl₃, 101 MHz, 298 K): δ (ppm) = 171.3, 151.8, 142.7, 140.4, 137.0, 127.9, 125.5, 122.1, 121.6, 37.4, 33.7, 32.5, 27.7, 24.5;

ESI-MS: *m/z* calculated for C₂₄H₂₃BrN₄O₅ [M+H]⁺ 527.09, found 528.18

Compound (*S*)-**16** and (*R*)-**16**

Compound **15** (400 mg, 0.76 mmol) was dissolved in ethyl acetate (50 mL) in a round-bottom two-neck flask equipped with a reflux condenser and tin chloride (1.75 g, 7.58 mmol) was added under argon. The reaction was stirred for 12 h at 80 °C. Then, the solution was cooled to room temperature and more ethyl acetate (200 mL) was added. The organic phase was washed with saturated solution of NaHCO₃ (4 x 300 mL) and with brine (1 x 150 mL), dried over Na₂SO₄, filtered and solvent concentrated to a reduced volume (~10 ml). This solution was used without any characterization in the next step.

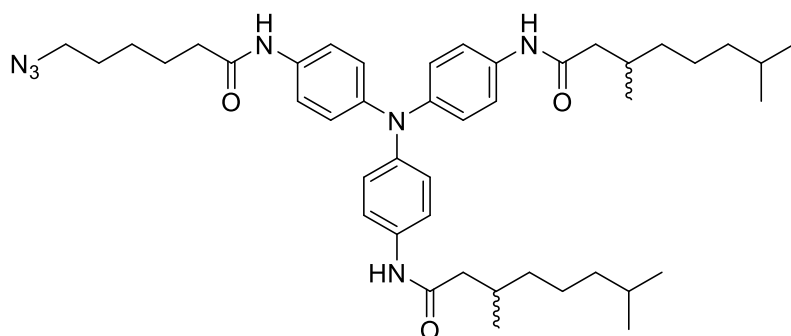
The solution from the previous step was diluted in dry DCM (40 mL) and placed in a round-bottom two-neck flask, then triethylamine (207 mg, 2.0 mmol) was added under argon and the mixture cooled down to 0°C on ice bath. To the stirred solution, (*S*)-**11** / (*R*)-**11** (391 mg, 2.0 mmol) was added dropwise after which the solution was allowed to regain room temperature. The mixture was stirred at room temperature for 4 h. Once the reaction was complete, additional DCM (50 ml) was added and the organic phase was washed with a saturated solution of NaHCO₃ (3 x 150 mL) and with brine (1 x 150 mL), dried over Na₂SO₄, filtered and the solvent evaporated under reduced pressure. The crude product was recrystallized from diethyl ether, the precipitate was filtered with a glass filter, washed with cold diethyl ether and dried under vacuum to obtain compound (*S*)-**16** / (*R*)-**16** (383 g) in 65 % yield after two steps.

¹H NMR (DMSO-d₆, 400 MHz, 298 K): δ (ppm) = 9.81 (s, 1H), 9.77 (s, 2H), 7.47 (d, *J* = 8.8 Hz, 6H), 6.88 (d, *J* = 8.8 Hz, 6H), 3.54 (t, *J* = 6.7 Hz, 2H), 2.26 (m, 4H), 2.08 (m, 2H), 1.92 (m, 2H), 1.82 (q, *J* = 7.0 Hz, 2H), 1.60 (q, *J* = 7.0 Hz, 2H), 1.50 (q, *J* = 6.5 Hz, 2H), 1.41 (m, 2H), 1.38 - 1.06 (m, 12H), 0.90 (d, *J* = 6.7 Hz, 6H), 0.84 (d, *J* = 6.7 Hz, 12H);

^{13}C NMR (DMSO- d_6 , 101 MHz, 298 K): δ (ppm) = 171.2, 170.8, 143.16, 134.7, 124.0, 120.7, 44.6, 39.2, 36.9, 36.6, 35.5, 32.5, 30.7, 27.9, 27.7, 24.8, 24.6, 23.1, 22.9, 20.0

ESI-MS: m/z calculated for $\text{C}_{44}\text{H}_{63}\text{BrN}_4\text{O}_3$ $[\text{M}+\text{H}]^+$ 775.41 found 775.53;

Compound (S)-17 and (R)-17

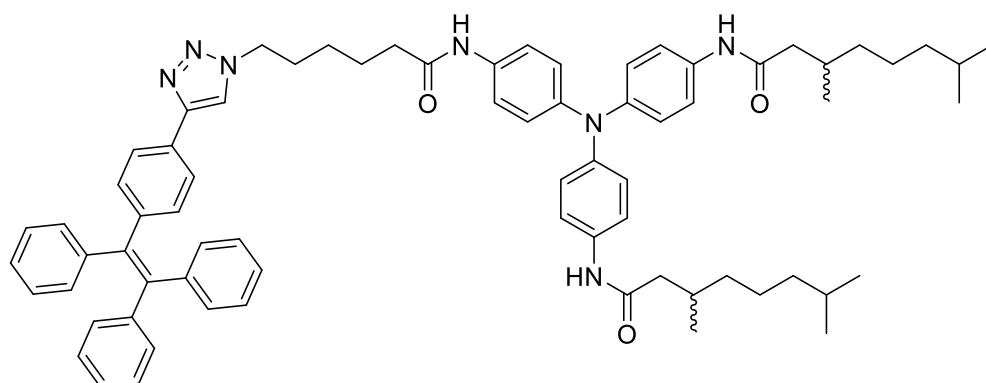


Compound (S)-16 / (R)-16 (900 mg, 1.16 mmol) was dissolved in DMF (10 mL) in a round-bottom two-neck flask equipped with a reflux condenser and sodium azide (260 mg, 4 mmol) was added under argon. The mixture was stirred at 80°C overnight. Then, the reaction was left to cool down and water (150 mL) was added. Next, the aqueous phase was extracted four times with DCM (150 mL). The combined organic layer was washed several times with water (200 mL) and brine (200 mL), dried on Na_2SO_4 and the solvent evaporated. The crude product was recrystallized from diethyl ether. The precipitate was filtered with a glass filter and washed with cold diethyl ether. After drying under vacuum, compound (S)-17 / (R)-17 (760 mg) was obtained in 89% yield as white solid.

^1H NMR (DMSO- d_6 , 400 MHz, 298 K): δ (ppm) = 9.80 (s, 1H), 9.78 (s, 2H), 7.48 (d, J = 8.8 Hz, 6H), 6.88 (d, J = 8.8 Hz, 6H), 2.25 (m, 4H), 2.08 (m, 2H), 1.93 (m, 2H), 1.65 – 1.45 (m, 7H), 1.39 – 1.06 (m, 15H), 0.90 (d, J = 6.6 Hz, 6H), 0.84 (d, J = 6.7 Hz, 12H),

^{13}C NMR (DMSO- d_6 , 101 MHz, 298 K): δ (ppm) = 171.2, 170.9, 143.1, 134.7, 124.0, 120.8, 51.0, 44.5, 39.1, 36.9, 36.6, 30.7, 30.6, 28.5, 27.7, 26.2, 25.2, 24.6, 23.0, 22.9, 20.0

ESI-MS: m/z calculated for $\text{C}_{44}\text{H}_{63}\text{N}_7\text{O}_3$ $[\text{M}+\text{H}]^+$ 738.50 found 738.61;

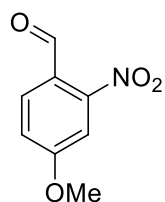
Compound **1TPE-(S)TATA** and **1TPE-(R)TATA**

Compound (**S**)-**17** / (**R**)-**17** (300 mg, 0.40 mmol), compound **4** (160 mg, 0.45 mmol) and CuBr (64 mg, 0.45 mmol) were placed in a Schlenk under argon. Degassed DMF (10 mL) was added followed by N,N,N',N'',N''-pentamethyldiethylenetriamine (77 mg, 0.45 mmol). The reaction was stirred overnight at 80 °C. After cooling down to room temperature, the reaction was poured in a solution of EDTA (200 mL, 3 M, pH = 9, NaOH), stirred for 10 minutes and then extracted with DCM (3 x 150 mL). The collected organic layer was washed with saturated NH₄Cl (3 x 200 mL) and brine (200 mL). After solvent evaporation, the solid was precipitated from ethyl acetate and then purified by column chromatography (SiO₂, dry loading from toluene/methanol 1:1, eluent: toluene/ethyl acetate 7/3) to afford compound **1TPE-(S)TATA** and **1TPE-(R)TATA** (390 mg) in 87% yield.

¹H NMR (DMSO-*d*₆, 400 MHz, 298 K): δ (ppm) = 9.78 (s, 3H), 8.49 (s, 1H), 7.58 (d, *J* = 8.4 Hz, 2H), 7.48 (d, *J* = 9.0 Hz, 4H), 7.44 (d, *J* = 9.0 Hz, 2H), 7.19 – 7.08 (m, 9H), 6.99 (m, 8H), 6.86 (m, 6H), 4.38 (t, *J* = 6.9 Hz, 2H), 2.25 (m, 4H), 2.07 (m, 2H), 1.99 – 1.80 (m, 4H), 1.61 (q, *J* = 7.4 Hz, 2H), 1.51 (sept, *J* = 6.3 Hz, 2H), 1.37 – 1.08 (m, 16H), 0.89 (d, *J* = 6.7 Hz, 6H), 0.85 (d, *J* = 6.6 Hz, 12H)

¹³C NMR (DMSO-*d*₆, 101 MHz, 298 K): δ (ppm) = 171.1, 170.9, 146.4, 143.7, 143.5, 143.1, 141.2, 140.7, 134.7, 131.7, 131.2, 131.1, 129.4, 128.7, 128.4, 128.3, 127.1, 125.0, 124.0, 121.8, 120.8, 49.8, 44.5, 39.1, 36.9, 36.5, 30.7, 29.8, 27.8, 25.8, 25.0, 24.6, 23.1, 22.9, 20.0;

ESI-MS: *m/z* calculated for C₇₂H₈₃N₇O₃ [M+H]⁺ 1094.66 found 1094.69

Compound **18**

Compound 18 was synthesized according to a reported procedure.²¹⁰

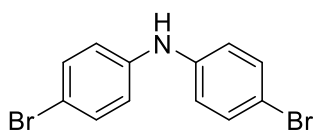
In a 2-necked round-bottom flask under Argon, a solution of DIBAL (5.15 mL, 1.2 M, 6.17 mmol) in toluene was added to a cold (0°C) solution of 4-Methoxy-2-nitrophenyl nitrile (1.0 g, 5.61 mmol) dissolved in a solution toluene/diethyl ether (1:1, 40 mL). The reaction mixture was stirred at 0 °C for 1 hour and then quenched with methanol (5 mL) and HCl (1 M, 5 mL). The reaction mixture was allowed to regain room temperature and further HCl (1 M, 20 mL) was added. The mixture was extracted with diethyl ether (4 x 100 mL) and the combined organic layer are washed with water (3 x 100 mL), brine (1 x 100 ml) and dried over Na₂SO₄. After solvent evaporation the crude compound was purified by flash chromatography (SiO₂, eluent: hexane / ethyl acetate 8/2) to afford compound **18** (86 mg) in 85% yield as yellow crystals.

¹H NMR (CDCl₃, 400 MHz, 298 K): δ (ppm) = 10.2 (s, 1 H), 7.90 (d, *J* = 8.7 Hz, 1 H), 7.45 (d, *J* = 2.5 Hz, 1H), 7.15 (dd, *J* = 9.7 Hz, 1.9 Hz, 1 H), 3.90 (s, 3 H);

¹³C NMR (CDCl₃, 101 MHz, 298 K): δ (ppm) = 187.0, 163.7, 151.4, 131.5, 123.2, 118.9, 109.7, 56.5;

ESI-MS: *m/z* calculated for C₈H₇NO₄ 182.04 [M+H]⁺; found 182.10.

*Analysis were in agreement with the literature.*²¹⁰

Compound **19**

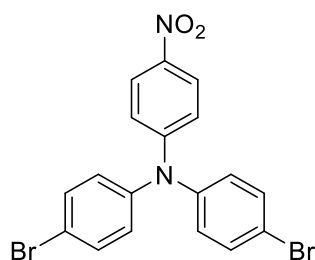
Compound **19** was synthesized according to a reported procedure.¹⁹⁴

To a stirred solution of diphenylamine (1.1 g, 6.4 mmol) in DMF (6 mL) under Argon at 0 °C a solution of N-bromosuccinimide (2.3 g, 13.0 mmol) in DMF (7 mL) was added dropwise over 30 minutes. The mixture was stirred at 0 °C for a further 5.5 hours. Then, water (100 mL) was added to the reaction mixture under vigorous stirring to afford the dibrominated compound as a white precipitate which was filtered off. The product was dissolved in DCM (200 mL) and dried over anhydrous Na₂SO₄. The solid was removed by filtration and the solvent evaporated under reduced pressure to obtain compound **19** (1.9 g) as a white powder, after drying *in vacuo*, in 90% yield.

¹H NMR (CDCl₃, 400 MHz, 298 K): δ (ppm)= 7.37 (d, J = 8.6 Hz, 4H), 6.91 (d, J = 8.6 Hz, 4H), 5.64 (s, NH);

ESI-MS: m/z calculated for C₁₂H₁₀Br₂N: 325.92 [M+H]⁺; found 325.91.

*Analysis were in agreement with the literature.*¹⁹⁴

Compound **20**

Compound **20** was synthesized according to a reported procedure¹⁹⁴

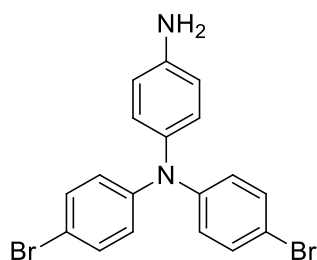
Compound **19** (1.8 g, 5.5 mmol), 4-fluoro-1-nitrobenzene (1.1 g, 8.2 mmol) and anhydrous K_2CO_3 (1.13 g, 8.2 mmol) were set under an Argon atmosphere and anhydrous DMF (11 mL) was added. The reaction mixture was heated for 15 hours at 145°C under vigorous stirring. After cooling to room temperature, the fine orange solid was filtered off and washed with cold EtOH (200 mL) and then cold water (200 mL). The product was then dissolved in DCM (400 mL) and anhydrous Na_2SO_4 was added. The solution was filtered and solvent was removed under reduced pressure to afford compound **20** (1.7 g) as a bright orange solid, after drying *in vacuo*, in 69% yield.

1H NMR (400 MHz, $CDCl_3$): δ = 8.06 (d, J = 9.4 Hz, 4H), 7.47 (d, J = 8.9 Hz, 2H), 7.03 (d, J = 8.9 Hz, 4H), 6.96 (d, J = 9.4 Hz, 2H);

^{13}C NMR (101 MHz, $CDCl_3$): δ = 152.7, 144.7, 141.3, 133.3, 127.8, 125.7, 119.4, 119.0;

ESI-MS: m/z calculated for $C_{18}H_{12}Br_2N_2O_2$ 446.93 $[M+H]^+$; found 446.98.

Analysis were in agreement with the literature.¹⁹⁴

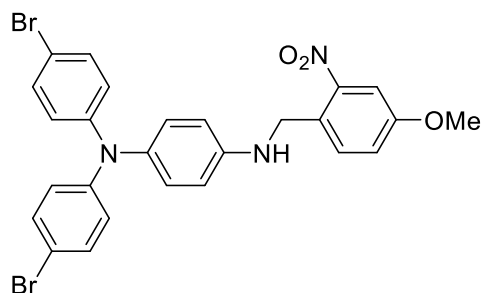
Compound **21**

To a 2-necked round-bottom flask equipped with a condenser and under Argon were added compound **20** (1.30 g, 2.91 mmol) and SnCl₂ (7.38 g, 38.11 mmol) followed by EtOH (12.7 mL) and CH₃CN (15.3 mL). The reaction mixture was then heated to 105°C for 4 hours. After cooling down to room temperature, the solvents were evaporated and CH₂Cl₂ (200 mL) was added. The solution was washed first with 3 M KOH (400 mL) and then with brine (200 mL) and anhydrous Na₂SO₄ was added. After filtration, the solvent was evaporated under reduced pressure to obtain compound **21** (1.17 g) as a grey solid, after drying *in vacuo*, in 95% yield. The compound was pure enough to be used as such in the next step.

¹H NMR (CDCl₃, 400 MHz, 298 K): δ (ppm) = 7.23 (d, *J* = 9.0 Hz, 4H), 6.92 – 6.71 (m, 6H), 6.61 (d, *J* = 8.9 Hz, 2H), 2.81 (s, 2H);

¹³C NMR (CDCl₃, 101 MHz, 298 K): δ (ppm) = 144.9, 142.1, 136.1, 135.9, 135.0, 132.7, 121.3, 117.3;

ESI-MS: *m/z* calculated for C₁₈H₁₄Br₂N₂ 416.96 [M+H]⁺; found 417.22.

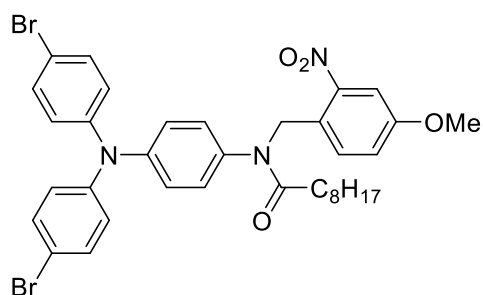
Compound **22**

In a round-bottom-flask compound **21** (1.50 g, 3.59 mmol) and 4-methoxy-2-nitrobenzaldehyde (649 mg, 3.59 mmol) were set under argon and solubilized in DCE (50 mL). Then, sodium triacetoxyborohydride (3.13 g, 14.3 mmol) was added and the mixture stirred for 48 h at room temperature. Next, 1 ml of HCl (0.1 M) was added to the solution followed by 10 ml of HCl (1 M) and 100 ml of DCM. The organic phase was washed three times with a saturated solution of Na₂CO₃ (150 mL), then with brine (150 mL), and dried over anhydrous Na₂SO₄. After evaporation of the solvent, the crude product was purified by column chromatography (SiO₂, eluent: cyclohexane/EtOAc: 90/10) to afford compound **22** (1.46 g) in 70% yield after drying *in vacuo*.

¹H NMR (CDCl₃, 400 MHz, 298 K): δ (ppm) = 7.51 (d, *J* = 2.8 Hz, 1H), 7.48 (d, *J* = 8.5 Hz, 1H), 7.07 (dd, *J* = 8.5 Hz, 2.8 Hz, 1H), 7.20 (d, *J* = 9.0 Hz, 4H), 6.77 - 6.87 (m, 6H), 6.46 (d, *J* = 8.9 Hz, 2H), 4.54 (s, 2H), 4.23 (s, 1H), 3.80 (s, 3H)

¹³C NMR (CDCl₃, 101 MHz, 298 K): δ (ppm) = 159.5, 148.5, 148.1, 144.9, 136.1, 134.8, 134.3, 132.4, 128.0, 121.1, 120.2, 118.6, 118.4, 109.6, 55.8, 41.5;

ESI-MS: *m/z* calculated for C₂₆H₂₁Br₂N₃O₃ 583.99 [M+H]⁺; found 583.98

Compound **23**

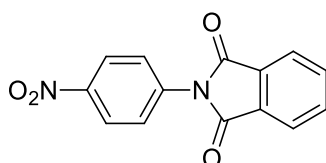
Compound **22** (1.4 g, 2.46 mmol) in a round-bottom-flask connected to a condenser was set under Argon and dichloromethane (44.5 mL) was added followed by triethylamine (298 mg, 2.95 mmol). Then, molecular sieves (4 Å) were added and the solution was let to stir for 30 minutes at 0 °C. Then, nonanoyl chloride (521 mg, 2.95 mmol) was added dropwise and the solution was heated to 50°C for 12 hours. Following, the reaction was cooled down and additional DCM (300 mL) was added, the organic layer was washed with saturated solution of NaHCO₃ (3 x 200 mL) and brine (200 mL), dried over anhydrous Na₂SO₄ and the organic layer evaporated to afford compound **23** (1.2 g) in 68% yield after purification by column chromatography (SiO₂, eluent: cyclohexane/EtOAc: 9/1)

¹H NMR (CDCl₃, 400 MHz, 298 K): δ (ppm) = 7.58 (d, *J* = 8.9 Hz, 1H), 7.42 - 7.36 (m, 5H), 7.15 (dd, *J* = 8.9 Hz, 2.6 Hz, 1H), 7.0 - 6.93 (m, 6H), 6.84 (d, *J* = 8.4 Hz, 2H), 5.22 (s, 2H), 3.87 (s, 3H), 2.17 (t, *J* = 7.4 Hz, 2H), 1.63 (q, *J* = 6.4 Hz, 2H), 1.39 - 1.17 (m, 10H), 0.89 (t, *J* = 7.1 Hz, 3H)

¹³C NMR (CDCl₃, 101 MHz, 298 K): δ (ppm) = 173.7, 159.0, 149.6, 146.7, 146.0, 136.7, 132.6, 132.0, 128.9, 126.0, 124.5, 124.1, 119.9, 116.3, 109.1, 55.8, 48.8, 34.3, 31.8, 29.3, 29.3, 29.1, 25.5, 22.7, 14.1;

ESI-MS: *m/z* calculated for C₃₅H₃₇Br₂N₃O₄ 724.11 [M+H]⁺; found 724.31

Compound 24



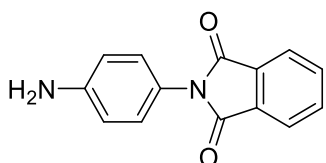
p-nitroaniline (10 g, 72.4 mmol) and phthalic anhydride (10.7 g, 72.4 mmol) in a round-bottom flask were dissolved in acetic acid (50 mL) and the mixture was heated to reflux for 12 h. Then, the solution was allowed to cool down to room temperature and water was added (150 mL) to afford the product as a precipitate which was filtered off. The precipitate was recrystallized twice from toluene (150 mL, each time) to obtain compound **24** (324 mg) in 83% yield after drying *in vacuo*.

¹H NMR (CDCl₃, 400 MHz, 298 K): δ (ppm) = 7.76 (d, J = 9 Hz, 2 H), 7.83 (dd, J = 6 Hz, 3 Hz, 2 H), 7.99 (dd, J = 6 Hz, 3 Hz, 2 H), 8.36 (d, J = 9 Hz, 2 H);

¹³C NMR (CDCl₃, 101 MHz, 298 K): δ (ppm) = 124.2, 124.4, 126.3, 131.3, 135.0, 137.5, 146.4, 166.4;

ESI-MS: m/z calculated for C₁₄H₈N₂O₄ 269.05 [M+H]⁺; found 269.51

Compound 25



In a round-bottom flask equipped with condenser and under Argon were added compound **24**, cyclohexene (60.8 g, 739 mmol) and isopropanol (150 mL). The solution was degassed with 3 freeze thaw cycle, followed by the addition of Pd on caracoral (10 %, 1.19 g, 11.2 mmol). The mixture was then refluxed at 90°C for 12h. Filtration of the solution over a pad of celite using

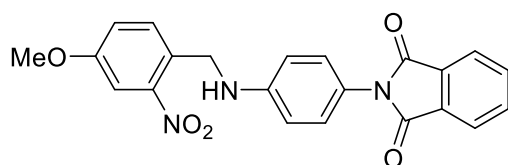
acetone and further evaporation of the solvent under reduced pressure afforded compound **25** (288 mg) in quantitative yield.

¹H NMR (DMSO-*d*₆, 400 MHz, 298 K): δ (ppm) = 7.97 – 7.83 (m, 4H), 7.01 (d, J = 8.9 Hz, 2H), 6.63 (d, J = 8.9 Hz, 2H), 5.33 (s, 2H);

¹³C NMR (DMSO-*d*₆, 101 MHz, 298 K): δ (ppm) = 167.6, 148.8, 134.5, 131.6, 128.2, 123.2, 119.5, 113.5;

ESI-MS: m/z calculated for C₁₄H₁₀N₂O₂ 239.07 [M+H]⁺; found 239.10

Compound 26



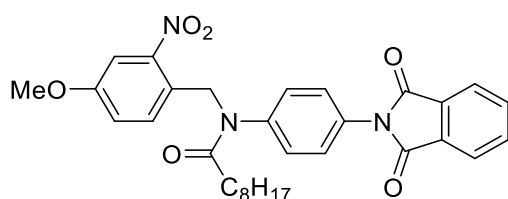
To a 2-neck round flask, compound **25** (2.1 g, 8.83 mmol), 4-methoxy-2-nitrobenzaldehyde (1.6 g, 8.83 mmol), and molecular sieves (4 Å) were added. To this mixture, DCM (20 mL) was added followed by pyrrolidine (10%, 62.8 mg, 0.88 mmol). The solution was stirred at room temperature overnight. After, the molecular sieves were removed and the solvent concentrated to small volume (5 mL). Then, methanol was added until a red precipitate was formed. The solution was decanted and the precipitate filtered, washed with a bit of methanol and dried under vacuum. The precipitate was solubilized in DCE (443 mL), under nitrogen, and sodium triacetoxyborohydride (5.6 g, 26.5 mmol) was added in one portion. The reaction was stirred overnight at 50°C and then quenched with NaHCO₃ and the amine extracted with DCM. The product was recrystallized in a mixture of DCM/cyclohexane (1:5) to afford compound **26** in 70% yield (2.5 g)

¹H NMR (CDCl₃, 400 MHz, 298 K): δ (ppm) = 7.85 (m, 2H), 7.69 (m, 2H), 7.54 (d, J = 2.8 Hz, 1H), 7.48 (d, J = 8.5 Hz, 1H), 7.10 (d, J = 8.9 Hz, 2H), 7.06 (dd, J = 8.5 Hz, 2.8 Hz, 1H), 6.58 (d, J = 8.9 Hz, 2H) 4.61 (s, 2H), 4.47 (s, 1H), 3.80 (s, 3H).

^{13}C NMR (CDCl₃, 101 MHz, 298 K): δ (ppm) = 167.1, 159.0, 149.6, 148.2, 132.2, 130.0, 128.8, 123.7, 122.4, 121.1, 120.2, 118.4, 117.9, 109.7, 55.8, 41.5;

ESI-MS: m/z calculated for C₂₂H₁₇N₃O₅ 404.12 [M+H]⁺; found 404.20

Compound 27

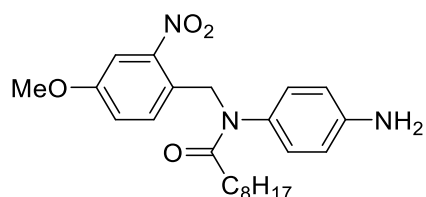


Compound **26** (2.67 g, 6.62 mmol) was placed in a round-bottom-flask connected to a condenser under Argon and DCM (119 mL) was added followed by triethylamine (803 mg, 7.94 mmol). Then, molecular sieves were added and the solution was let to stir for 30 minutes at 0 °C. Then nonanoyl chloride (1.40 g, 7.94 mmol) was added and the solution was heated to 50 °C for 12 hours. After cooling down to room temperature, the organic phase was washed first with a saturated solution of Na₂CO₃ (300 mL), then with brine (300 mL), and dried over anhydrous Na₂SO₄. After solvent evaporation, the crude product was purified by column chromatography (SiO₂, eluent: cyclohexane/EtOAc: 9/1) to obtain compound **27** as a yellow oil in 78% yield (2.8 g) after drying *in vacuo*.

^1H NMR (CDCl₃, 400 MHz, 298 K): δ (ppm) = 7.92 (m, 2H), 7.85 (m, 2H), 7.72 (d, J = 2.6 Hz, 1H), 7.55 (d, J = 8.5 Hz, 1H), 7.28 (dd, J = 8.5 Hz, 2.6 Hz, 1H), 7.18 (d, J = 8.9 Hz, 2H), 6.85 (d, J = 8.9 Hz, 2H) 5.15 (s, 2H), 3.85 (s, 3H), 2.12 (t, J = 7.4 Hz, 2H), 1.58 (q, J = 7.4 Hz, 2H), 1.35 - 1.11 (m, 10H), 0.85 (t, J = 7.0 Hz, 3H).

^{13}C NMR (CDCl₃, 101 MHz, 298 K): δ (ppm) = 175.0, 166.9, 158.7, 149.7, 148.4, 132.3, 130.1, 128.8, 123.6, 122.6, 121.4, 120.2, 118.4, 118.0, 109.5, 55.8, 41.5, 35.0, 32.9, 30.3, 30.2, 30.2, 26.7, 23.6, 14.4;

ESI-MS: m/z calculated for C₃₁H₃₃N₃O₆ 544.24 [M+H]⁺; found 544.26

Compound **28**

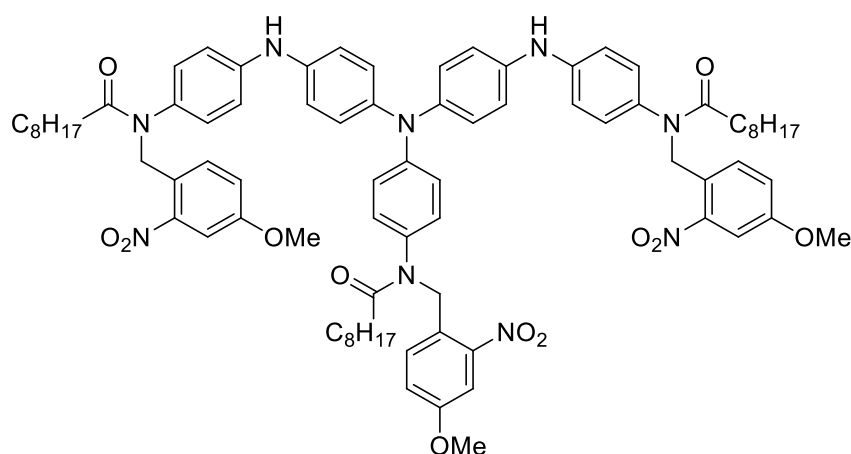
Compound **27** (1.77 g, 3.26 mmol) was placed in a round-bottom-flask under argon and solubilized in THF (50 mL). Then, a solution of hydrazine in water (130 mmol, 12 mL, 11 M) was added slowly. The mixture was stirred at room temperature for 4 h and followed by UPLC. After that period, the solvent was evaporated and DCM (300 mL) was added. The organic phase was washed first with water (150 mL), then with brine (150 mL), and dried over anhydrous Na₂SO₄. After evaporation of the solvent, the crude product was purified by column chromatography (SiO₂, eluent: toluene/EtOAc: 95/5 → toluene/EtOAc: 80/20) to afford compound **28** as a yellow oil in 98% yield (1.3 g) after drying *in vacuo*.

¹H NMR (CDCl₃, 400 MHz, 298 K): δ (ppm) = 7.50 (d, *J* = 8.65 Hz, 1H), 7.39 (d, *J* = 2.7 Hz, 1H), 7.13 (dd, *J* = 8.65 Hz, 2.7 Hz, 1H), 6.79 (d, *J* = 8.5 Hz, 2H), 6.62 (d, *J* = 8.5 Hz, 2H), 5.16 (s, 2H), 3.97 (s, 2H), 3.85 (s, 3H), 2.13 (t, *J* = 7.3 Hz, 2H), 1.59 (q, *J* = 7.3 Hz, 2H), 1.33 - 1.14 (m, 10H), 0.87 (t, *J* = 6.9 Hz, 3H).

¹³C NMR (CDCl₃, 101 MHz, 298 K): δ (ppm) = 174.3, 158.7, 149.5, 145.7, 133.2, 131.6, 128.8, 119.8, 115.8, 109.0, 55.8, 49.3, 34.1, 31.8, 29.4, 29.4, 29.0, 25.5, 22.6, 14.2;

ESI-MS: *m/z* calculated for C₂₃H₃₁N₃O₄ 414.23 [M+H]⁺; found 414.25

Compound 29



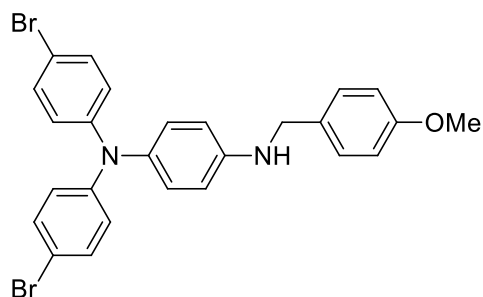
To compound **23** (20 mg, 0.028 mmol) and compound **28** (34 mg, 0.083 mmol) that have been vacuum dried in a Schlenk vessel at 55 °C under stirring for one night were added Cs₂CO₃ (47 mg, 0.14 mmol), Pd(dba)₂ (4 mg, 0.007 mmol) and BINAP (4.4 mg, 0.007 mmol). The flask was then set under Argon and dry toluene (1 mL) (which had been degassed by 5 freeze-thaw cycles in a separate flask) was added. The Schlenk flask was sealed with a Teflon wrapped glass stopper and the solution was heated to 95 °C for 10 days during which it was not opened. Then, the reaction was cooled down to room temperature, the reaction mixture was filtered over celite with additional acetone (100 mL) and the solvent evaporated under reduced pressure. The crude product was then purified by column chromatography (SiO₂, toluene/EtOAc: 45/5, 1% NEt₃) to obtain compound **29** (21 mg) in 55% yield.

¹H NMR (CDCl₃, 400 MHz, 298 K): δ (ppm) = 7.65 (d, *J* = 2.6 Hz, 3H), 7.40 (d, *J* = 8.8 Hz, 3H), 7.35 (dd, *J* = 8.8 Hz, 2.6 Hz, 3H), 7.20 (d, *J* = 8.9 Hz, 6H), 7.11 - 6.88 (m, 10H), 6.72 (d, *J* = 8.7 Hz, 4H), 5.20 (s, 6H), 4.0 (s, 2H), 3.85 (s, 9H), 2.45 (t, *J* = 7.3 Hz, 6H), 1.63 (q, *J* = 6.3 Hz, 6H), 1.39 - 1.17 (m, 30H), 0.88 (t, *J* = 7.2 Hz, 9H)

¹³C NMR (CDCl₃, 101 MHz, 298 K): δ (ppm) = 173.5, 159.5, 148.2, 141.5, 138.0, 136.8, 136.1, 135.4, 134.9, 134.2, 132.3, 131.1, 128.8, 121.2, 120.5, 120.2, 119.4, 109.2, 55.9, 48.5, 34.4, 31.8, 29.3, 29.2, 28.9, 25.9, 22.7, 14.1;

ESI-MS: *m/z* calculated for C₈₁H₉₇N₉O₁₂ 1388.73 [M+H]⁺; found 1388.79

Compound 31



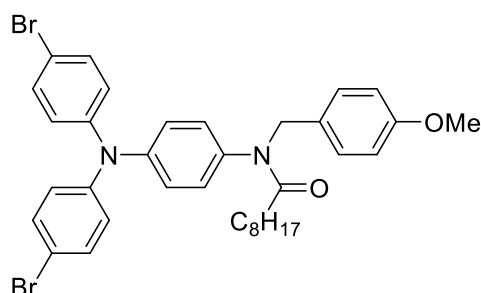
Compound **21** (13.9 g, 33.2 mmol), 4-methoxybenzaldehyde (4.52 g, 33.2 mmol), and a catalytic amount of *p*-toulen sulfonic acid (10 mg, 0.06 mmol) were placed in a large 2-necked round bottom flask equipped with a Dean-Stark, condenser and a CaCl₂ drying tube under Argon. To this mixture, dry toluene (140 mL) was added and the solution heated to 160°C for 24 h. Then, the solution was cooled down to room temperature, the Dean-Stark was replaced by a normal condenser and solid NaBH₄ (5 g, 132.8 mmol) was added, followed by EtOH (140 mL) (which had been dried over NaBH₄). The ice bath was removed and the reaction was stirred at room temperature. The progress of the reaction was followed by adding a small aliquot of the reaction to 1 M HCl, followed by MeOH (0.5 mL) and then monitored by UPLC. If no remaining primary amine was found, the reaction was stopped (usually 3 hours). The reaction was very slowly and very carefully quenched by adding first 1 M HCl (ca. 200 mL), then 3 M HCl (ca. 200 mL) whilst keeping the reaction mixture at 0°C and under Argon. (before quenching any possible heat source and organic solvents were removed from the fume hood). Once the mixture has reached an acidic pH (pH 1-2 by pH indicator paper), the solvent was evaporated under reduced pressure. The mixture was then diluted with DCM (400 mL) and washed first with pure water (2x 400 mL), then with brine (300 mL) and finally dried over Na₂SO₄. The solution was filtered and the solvent was removed under reduced pressure to afford compound **31** (1.4 g) as a yellow powder in 78% yield after drying in vacuo.

¹H NMR (CDCl₃, 400 MHz, 298 K): δ (ppm) = 7.35 - 7.27 (m, 6H), 6.98 – 6.89 (m, 6H), 6.62 (d, *J* = 8.8 Hz, 4H), 4.26 (s, 2H), 3.98 (br s, 1H), 3.84 (s, 3H).

¹³C NMR (CDCl₃, 101 MHz, 298 K): δ (ppm) = 158.9, 146.9, 145.7, 136.7, 132.0, 131.0, 129.3, 128.9, 127.9, 123.8, 123.8, 113.7, 55.1, 48.1.

ESI-MS: *m/z* calculated for C₂₆H₂₂Br₂N₂O 537.01 [M+H]⁺; found 538.55

Compound 32

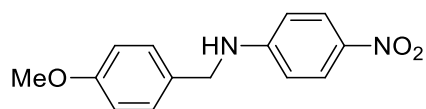


To compound **31** (2 g, 3.72 mmol) under Argon, was added dry DCM (30 mL) and the solution was cooled down to 0 °C using a water/ice bath. To this solution was added dropwise, first TEA (1.02 g, 10 mmol) and then nonanoyl chloride (1.12 g, 6.32 mmol). The reaction mixture was then heated to 60 °C for 3 hours. After cooling down to room temperature, the organic phase was diluted with more DCM (300 mL) and washed first with saturated NaHCO₃ (300 mL), then with brine (300 mL), and dried over anhydrous Na₂SO₄. After evaporation of the solvent, the crude product was purified by column chromatography (SiO₂, eluent: toluene/EtOAc: 95/5) to afford compound **32** (2.32 g) as a yellow oil in 92% yield after drying *in vacuo*.

¹H NMR (CDCl₃, 400 MHz, 298 K): δ (ppm) = 7.34 (d, *J* = 8.6 Hz, 4H), 7.1 (d, *J* = 8.5 Hz, 2H), 6.9 (m, 6H), 6.76 (m, 4H), 4.76 (s, 2H), 3.75 (s, 3H), 2.07 (t, *J* = 7.4 Hz, 2H), 1.58 (q, *J* = 7.4 Hz, 2H), 1.33 - 1.11 (m, 10H), 0.85 (t, *J* = 7.0 Hz, 3H).

¹³C NMR (CDCl₃, 101 MHz, 298 K): δ (ppm) = 173.3, 158.9, 146.3, 146.0, 137.2, 132.6, 132.6, 130.2, 130.2, 129.9, 126.0, 123.8, 113.7, 55.2, 52.3, 34.4, 31.9, 29.3, 29.3, 29.2, 25.6, 21.0, 14.1

ESI-MS: *m/z* calculated for C₃₅H₃₈Br₂N₂O₂ 679.13 [M+H]⁺; found 679.22

Compound **33**

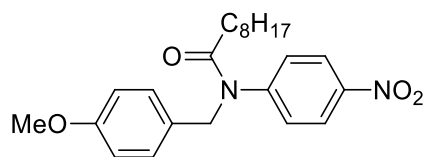
4-methoxybenzaldehyde (4.93 g, 36.2 mmol), p-nitroaniline (5 g, 36.2 mmol) and a catalytic amount of PTSA were placed in a large 2-necked round bottom flask equipped with a Dean-Stark, condenser and a CaCl₂ drying tube under Argon. To this mixture, toluene (140 mL) was added and the solution heated to 160 °C for 1 day. Then, the solution was cooled down to room temperature, the Dean-Stark was replaced by a normal condenser and solid NaBH₄ (5.5 g, 144.8 mmol) was added, followed by EtOH (140 mL) (which had been dried over NaBH₄). The ice bath was removed and the reaction was stirred at room temperature. The progress of the reaction was followed by adding a small aliquot of the reaction to 1 M HCl, followed by MeOH (0.5 mL) and then monitored by UPLC. If no further primary amine was found, the reaction was stopped (usually 3 hours). The reaction was very slowly and very carefully quenched by adding first 1M HCl (ca. 200 mL), then 3 M HCl (ca. 200 mL) whilst keeping the reaction mixture at 0°C and under Argon. (Before quenching any possible heat source and organic solvents were removed from the fumehood). Once the mixture had reached an acidic pH (pH 1-2 by paper), the solvent was evaporated under reduced pressure. The mixture was then diluted with DCM (400 mL) washed first with pure water (2x 400 mL), then with brine (300 mL) and finally dried over Na₂SO₄. The solution was filtered and the solvent was removed under reduced pressure to afford compound **33** (6.54 g) as a yellow powder in 70% yield after drying *in vacuo*.

¹H NMR (CDCl₃, 400 MHz, 298 K): δ (ppm) = 8.08 (d, *J* = 9 Hz, 2H), 7.24 (d, *J* = 8.6 Hz, 2H), 6.86 (d, *J* = 8.6 Hz, 2H), 6.66 (d, *J* = 9 Hz, 2H), 4.86 (s, 1H), 4.33 (s, 2H), 3.76 (s, 3H);

¹³C NMR (CDCl₃, 101 MHz, 298 K): δ (ppm) = 159.3, 152.7, 129.0, 126.2, 124.9, 114.3, 114.4, 111.8, 55.3, 47.4

ESI-MS: *m/z* calculated for C₁₄H₁₄N₂O₃ 259.10 [M+H]⁺; found 259.22

Compound 34



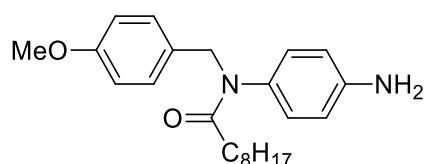
To a mixture of compound **33** (1.0 g, 3.87 mmol) and anhydrous potassium carbonate (2.27g, 16.4 mmol) under Argon was added first DCM (50 mL) followed by the addition of molecular sieves. Nonanoyl chloride (0.82 g, 4.65 mmol) was added dropwise at 0°C and the solution was then heated to 40 °C for 12 hours. After cooling down to room temperature, the solution was washed first with water (300 mL), then with brine (300 mL) and then dried over Na₂SO₄. After filtration, the solvent was evaporated under reduced pressure and the crude mixture was purified by column chromatography (SiO₂, toluene → toluene/EtOAc: 95/5) to afford compound **34** (1.0 g) as a yellow powder in 65% yield after drying *in vacuo*.

¹H NMR (CDCl₃, 400 MHz, 298 K): δ (ppm) = 8.13 (d, *J* = 9.0 Hz, 2H), 7.08 (d, *J* = 8.7 Hz, 2H), 7.00 (d, *J* = 8.7 Hz, 2H), 6.72 (d, *J* = 9 Hz, 2H), 4.79 (s, 2H), 3.70 (s, 3H), 2.01 (t, *J* = 7.2 Hz, 2H), 1.54 (q, *J* = 7.1 Hz, 2H), 1.25-1.09 (m, 10H), 0.79 (t, *J* = 6.3 Hz, 3H).

¹³C NMR (CDCl₃, 101 MHz, 298 K): δ (ppm) = 172.4, 159.0, 148.4, 146.7, 129.9, 129.2, 128.8, 124.8, 113.9, 55.1, 52.3, 34.7, 31.8, 29.3, 29.2, 29.1, 25.4, 22.6, 14.1

ESI-MS: *m/z* calculated for C₂₃H₃₀N₂O₄ 399.22 [M+H]⁺; found 399.52

Compound 35



To compound **34** (1.37 g, 3.44 mmol) and SnCl₂ (6.80 g, 30.94 mmol) in a 2-necked round-bottom flask equipped with a condenser and under Argon, were added EtOH (53 mL) and CH₃CN (58 mL). The reaction mixture was then heated to 105 °C for 4 hours. After cooling

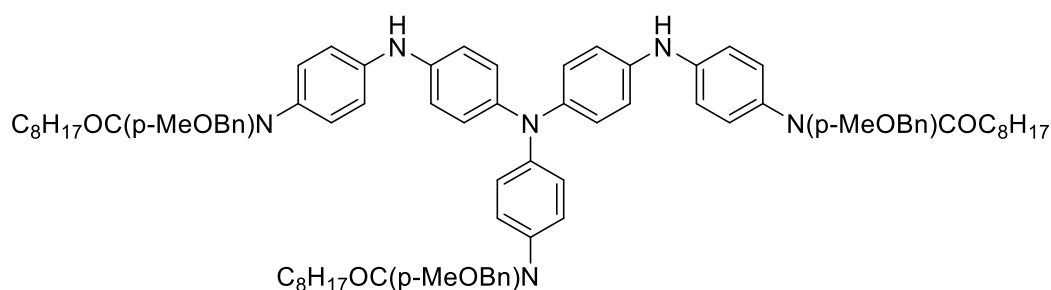
down to room temperature, the solvents were evaporated under reduced pressure and DCM (300 mL) was added. The solution was washed first with 3 M KOH (2x 300 mL) and then with brine (200 mL) followed by drying over Na₂SO₄. After filtration, residual SnCl₂ was removed by centrifugation (2 times at 14 °C, 9500 Tr/min, 20 minutes). Evaporation of the solvent under reduced pressure and drying *in vacuo* afforded compound **35** (988 mg) as a yellow oil in 78% yield.

¹H NMR (CDCl₃, 400 MHz, 298 K): δ (ppm) = 7.07 (d, *J* = 8.6 Hz, 2H), 6.74 (d, *J* = 8.6 Hz, 2H), 6.65 (d, *J* = 8.8 Hz, 2H), 6.55 (d, *J* = 8.8 Hz, 2H), 4.71 (s, 2H), 4.01 (s, 2H), 3.74 (s, 3H), 2.01 (t, *J* = 7.1 Hz, 2H), 1.53 (q, *J* = 7.1 Hz, 2H), 1.30 - 1.01 (m, 10H), 0.82 (t, *J* = 6.9 Hz, 3H);

¹³C NMR (CDCl₃, 101 MHz, 298 K): δ (ppm) = 173.51, 158.7, 145.7, 133.3, 130.2, 130.2, 129.4, 115.5, 113.5, 55.24, 52.35, 34.2, 31.8, 29.3, 29.3, 29.2, 25.6, 22.56, 14.1

ESI-MS: m/z calculated for C₂₃H₃₂N₂O₂ 369.25 [M+H]⁺; found 369.29

Compound 36



To a mixture of compound **32** (675 mg, 0.99 mmol) and compound **35** (1.155 g, 3.13 mmol) that had been vacuum dried in a Schlenk vessel at 55°C under stirring for one night, were added Cs₂CO₃ (1.7 g, 5.21 mmol), Pd(dba)₂ (177 mg, 0.308 mmol) and BINAP (192 mg, 0.308 mmol). The Schlenk was then set under Argon and dry toluene (8 mL) (which had been degassed by 5 freeze-thaw cycles in a separate flask) was added. The Schlenk flask was sealed with a Teflon wrapped glass stopper and the solution was heated to 95°C for 10 days during which it was not opened. After that period, the reaction was cooled down to room temperature and the mixture was filtered over celite with additional acetone (300 mL) and the solvent was evaporated under reduced pressure. The crude product was then purified by column

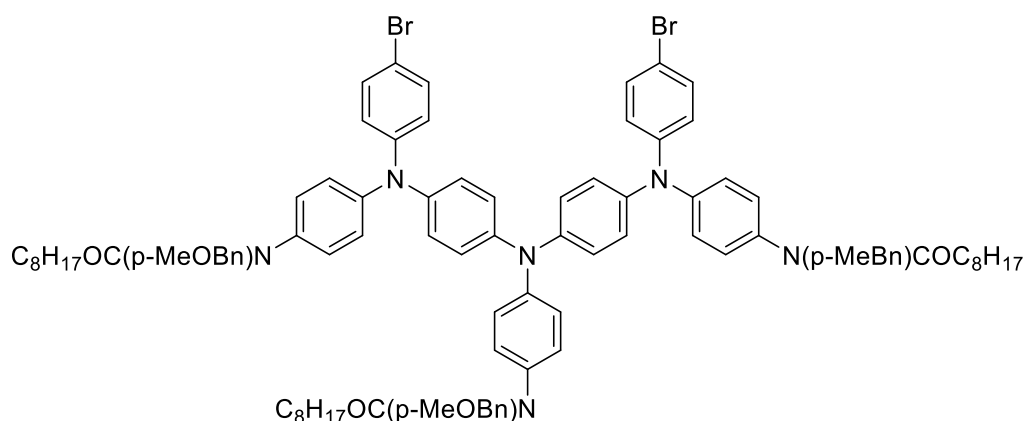
chromatography (SiO₂, toluene/EtOAc: 45/5, 1% NEt₃) to give compound **36** (561 mg) in 45% yield

¹H NMR (Acetone-d₆, 400 MHz, 298 K): δ (ppm) = 7.54 (s, 2H), 7.13 (m, 10H), 7.04 (d, J = 8.4 Hz, 8H), 6.88 (m, 8H), 6.81 (d, J = 8.4 Hz, 6H), 4.77 (s, 6H), 3.75 (s, 9H), 2.09 (m, 6H), 1.55 (m, 6H), 1.32 - 1.12 (m, 30H), 0.85 (m, 9H).

¹³C NMR (Acetone-d₆, 101 MHz, 298 K): δ (ppm) = 172.1, 172.0, 158.9, 147.9, 143.7, 143.6, 140.6, 139.3, 139.2, 135.0, 134.4, 130.6, 130.5, 129.8, 129.7, 129.4, 129.07, 126.5, 120.1, 119.5, 119.4, 116.5, 116.4, 113.5, 54.5, 51.7, 33.7, 31.7, (3 aliphatic carbons covered by the solvent) 25.3, 22.4, 13.5

ESI-MS: m/z calculated for C₈₁H₁₀₀N₆O₆ 1253.71 [M+H]⁺; found 1253.55

Compound 37



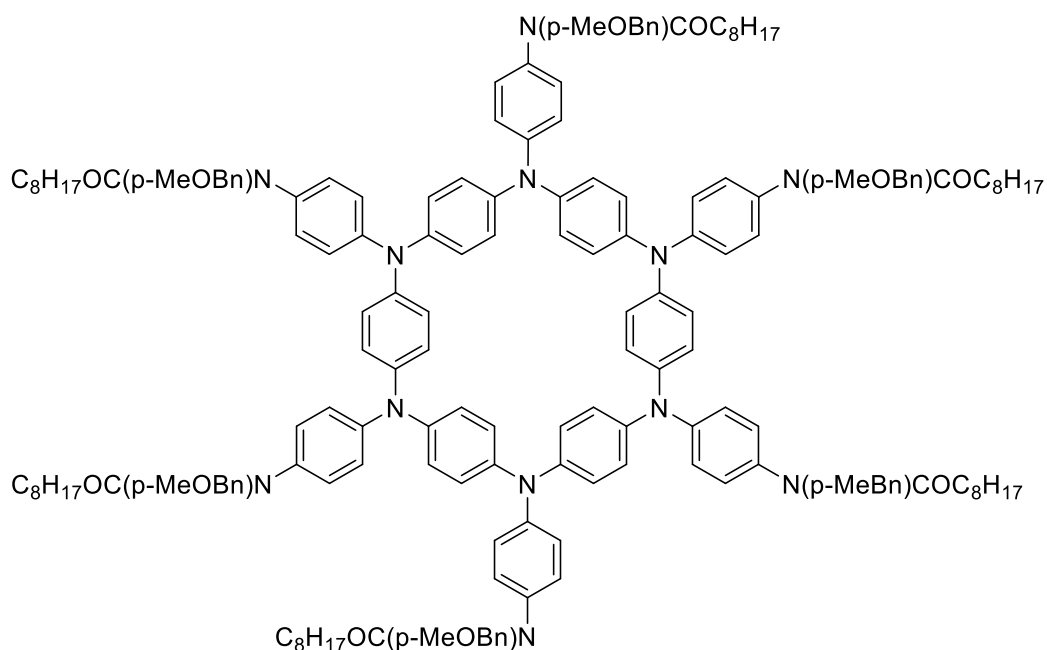
To a Schlenk tube was added compound **36** (500 mg, 0.4 mmol) and the compound was vacuum dried at 55 °C for one night under stirring followed by the addition of 1-bromo-4-iodo-benzene (2.26 g, 8.0 mmol), Cs₂CO₃ (2.6 g, 8.0 mmol), CuI (76 mg, 0.4 mmol) and L-Proline (92 mg, 0.8 mmol) and the Schlenk flask was set under Argon. In a separate round-bottom flask, dry DMF (6 mL) was degassed by 5 freeze-thaw cycles and was then added to the Schlenk which was then sealed with a Teflon wrapped glass stopper and the reaction heated to 130 °C and followed by UPLC-MS after at least 4 days of reaction. Then, the reaction was cooled down to room temperature and the mixture was filtered over celite with acetone (300 mL) and the

solvents were evaporated under reduced pressure. The crude product was then purified by column chromatography (SiO₂, dry loading from acetone, eluent: cyclohexane/EtOAc 4/1) to obtain compound **37** (370.0 mg) as a slightly purple oil in 59 % yield after drying *in vacuo*.

¹H NMR (Acetone-d₆, 400 MHz, 298 K): δ (ppm) = 7.29 (d, *J* = 8.8 Hz, 4H), 7.00 (m, 8H), 6.95 - 6.80 (m, 22H), 6.69 (d, *J* = 8.6 Hz, 6H), 4.66 (s, 6H), 3.61 (s, 9H), 1.98 (m, 6H), 1.43 (m, 6H), 1.18 - 1.00 (m, 30H), 0.72 (m, 9H).

¹³C NMR (Acetone-d₆, 101 MHz, 298 K): δ (ppm) = 171.8, 158.9, 146.8, 146.5, 143.1, 142.5, 138.3, 137.4, 132.2, 130.3, 129.7, 129.6, 129.5, 128.8, 126.2, 125.7, 125.3, 124.6, 123.6, 122.9, 113.5, 54.6, 51.6, 33.8, 31.7, 25.3, 22.4, 13.5 (3 aliphatic covered by the solvent)

ESI-MS: *m/z* calculated for C₉₃H₁₀₆Br₂N₆O₆ 1563.65 [M+H]⁺; found 1563.60

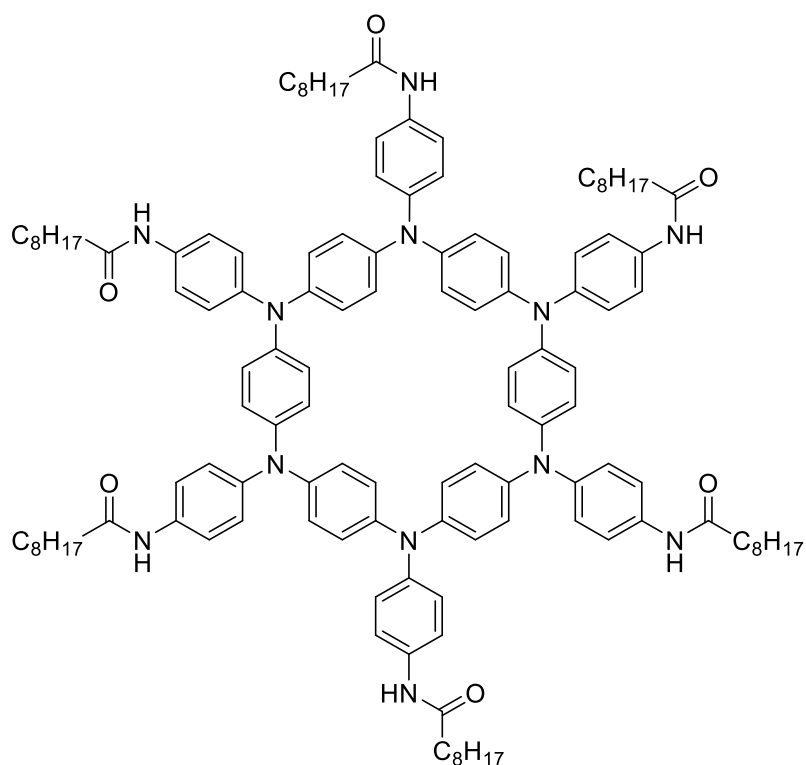
Compound **38**

To a mixture of compound **36** (202mg, 0.161mmol) and compound **37** (252 mg, 0.161 mmol) which had been dried overnight at 55 °C under vacuum in a Schlenk flask, were added Pd₂(dba)₃ (73.8 mg, 0.086 mmol) and Cs₂CO₃ (525mg, 1.61mmol) under an Argon atmosphere. Degassed toluene was added followed by tri-*tert*-butylphosphine in toluene (161 μL, 0.161 mmol, 1M). The Schlenk flask was sealed with Teflon ribbon and heated to 105 °C for five days. Then, the mixture was cooled down to room temperature and filtrated over a celite pad with additional acetone. The solvents were evaporated and the solid obtained was solubilized in ethyl acetate and precipitated 2 times by addition of an excess of methanol. After filtration and drying, we obtain **38** as a dark solid in 36 % yield (155mg, 0.073mmol).

¹H NMR (Acetone-d₆, 400 MHz, 298 K): δ (ppm) = 8.05 – 6.83 (m, 72H), 4.75 (s, 12H), 3.69 (s, 18H), 2.09 (m, 12H), 1.53 (m, 12H), 1.38 – 1.06 (m, 60H), 0.82 (m, 18H)

MALDI: m/z calculated for C₁₇₄H₂₀₄N₁₂O₁₂ 2654.57 [M+H]⁺; found 2653.72

Compound 39



Compound **38** (30 mg, 0.01 mmol), in a Schlenk flask, was stirred in refluxing TFA (1.85 mL) for 90 minutes. Then, the solvent was evaporated, the solid dried under high vacuum overnight and then dissolved in hot ethyl acetate (1.5 mL). The solution was allowed to cool down to room temperature, the precipitate decanted by centrifugation and the supernatant was removed. Then, fresh ethyl acetate was added, warmed at 60°C for 15 minutes and the whole process repeated 4 to 5 times as long as the supernatant was yellowish. After that, the precipitate was solubilized in a mixture toluene/methanol (1:1) and passed quickly through a short column of neutral aluminum oxide (eluent: toluene/methanol 1:1). The solvent was then evaporated to afford product **39** (4 mg) in 18% yield.

¹H NMR (DMF-d₇, 400 MHz, 298 K): δ (ppm) = 10.10 (s, 6H), 8.01 – 6.60 (m, 48H), 2.53 (m, 6H), 1.84 (m, 6H), 1.64 – 1.32 (m, 60H), 1.05 (m, 18H).

MALDI: m/z calculated for C₁₂₆H₁₅₆N₁₂O₆ 1934.23 [M+H]⁺; found 1933.19

ANNEXES

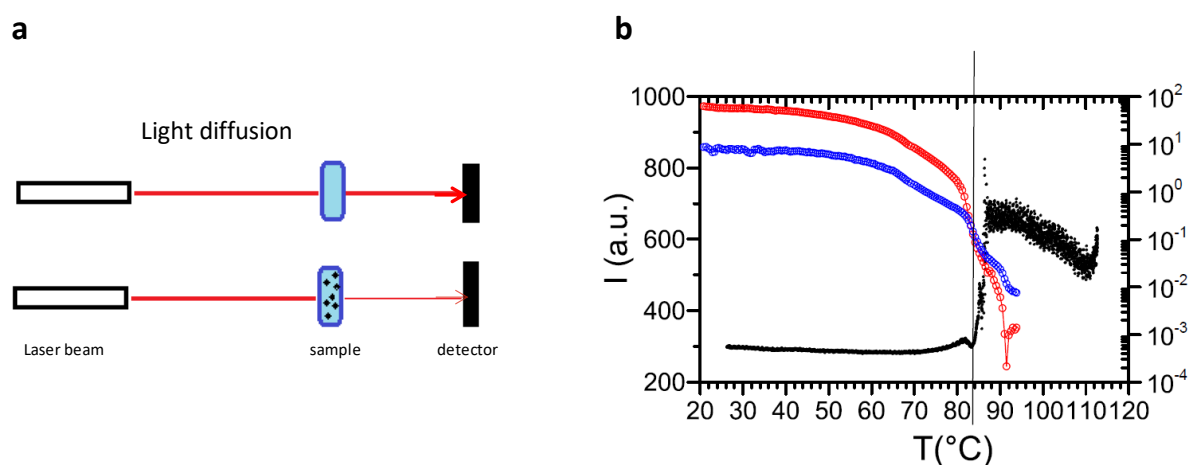


Figure A 1 | **a**) Schematic representation of the setup employed to determine the sol-gel transition: a light beam passes through a sample which is cooled at a constant rate. For temperatures higher than $T_{s/g}$ the intensity of the light beam remains unaffected since the sample is not diffusing it. As soon as the $T_{s/g}$ is reached, the light is diffused and the intensity decreases. When the gel is completely formed the intensity does not change anymore. **b**) Superimposition of light diffusion (black line) and rheology (G' red line, G'' blue line) upon cooling (0.2 °C/min for light diffusion and 1 °C/min for rheology) a 1 mM sample of **3TPE-TATA** in toluene (on the left y-axis is reported the intensity of the laser beam detected, on the right y-axis is reported the storage modulus [Pa]). For the two techniques we observed the sol/gel transition at 85°C.

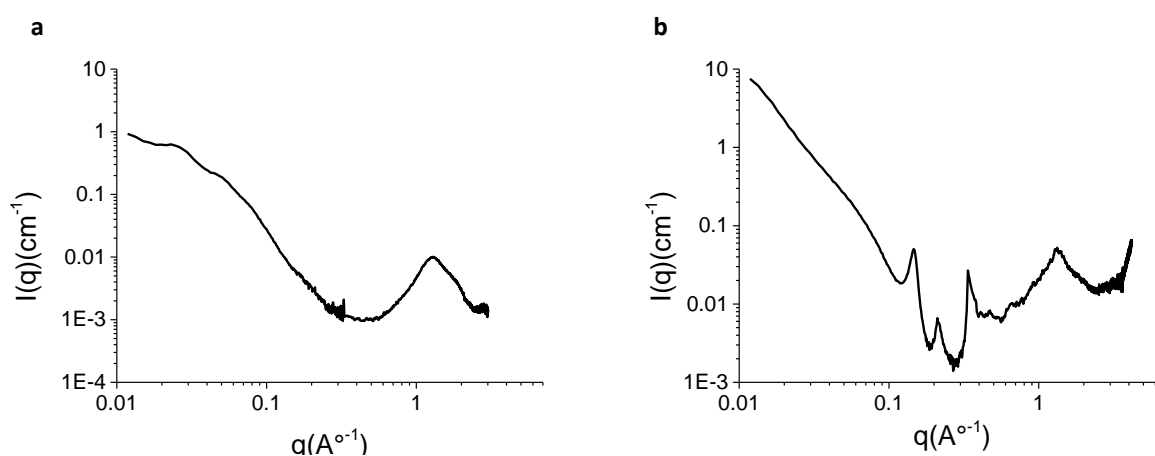


Figure A 2 | **a**) SAXS and WAXS trace obtained for a 1 mM fast cooled (5 °C/min) sample of **1TPE-(S)TATA** in toluene; **b**) SAXS and WAXS trace for a 1 mM slow cooled sample (0.1 °C/min) of **1TPE-(S)TATA** in toluene. The comparison between the two cooling regimes shows a higher degree of organization for slow cooled sample.

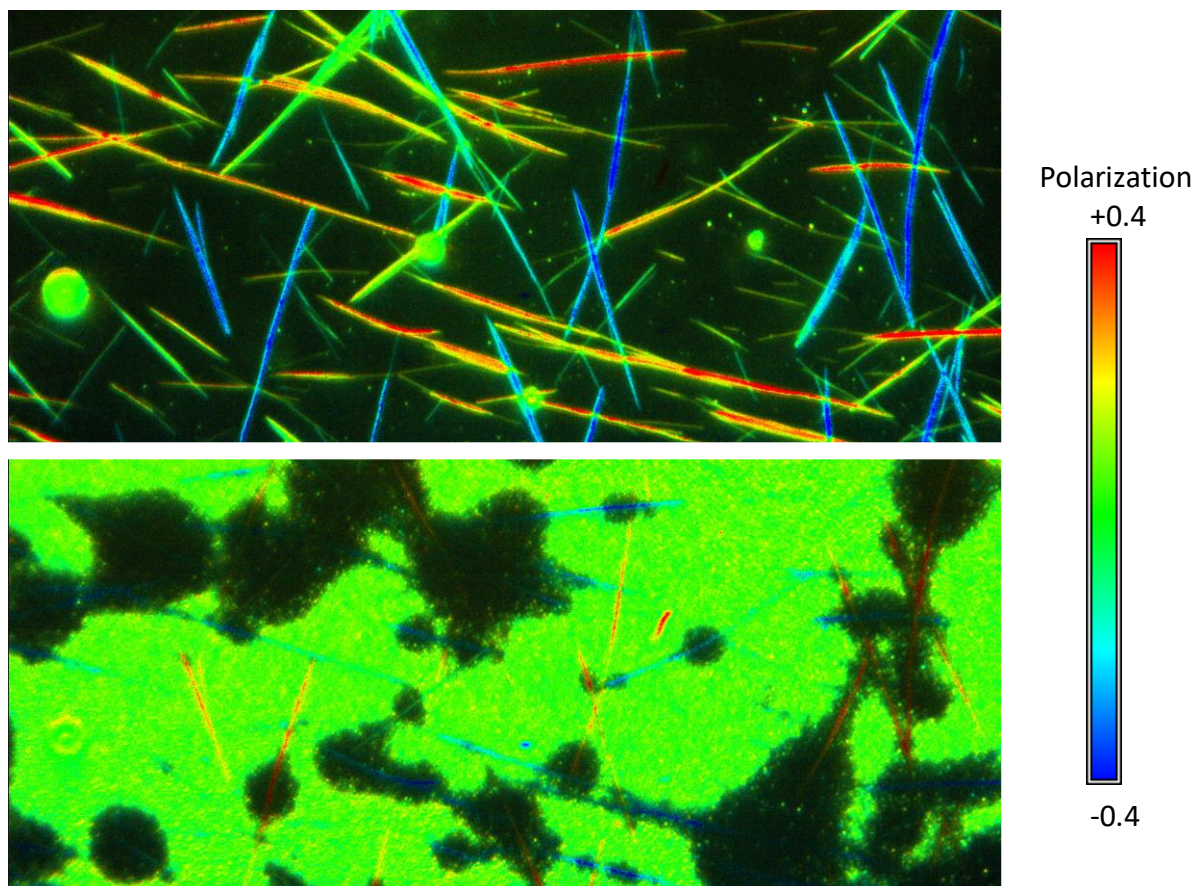


Figure A 3 | Top: image of photoluminescence from the OLEDs surface (**1TPE-(R)TATA** supramolecular polymers prepared from a slow cooled solution of 0.2 mM) under PL; Bottom: electroluminescence of the same area showing the fibers that emit weakly polarized light; the polarization of the PL is different from that observed in EL meaning that two different chromophores might be involved in the two processes.

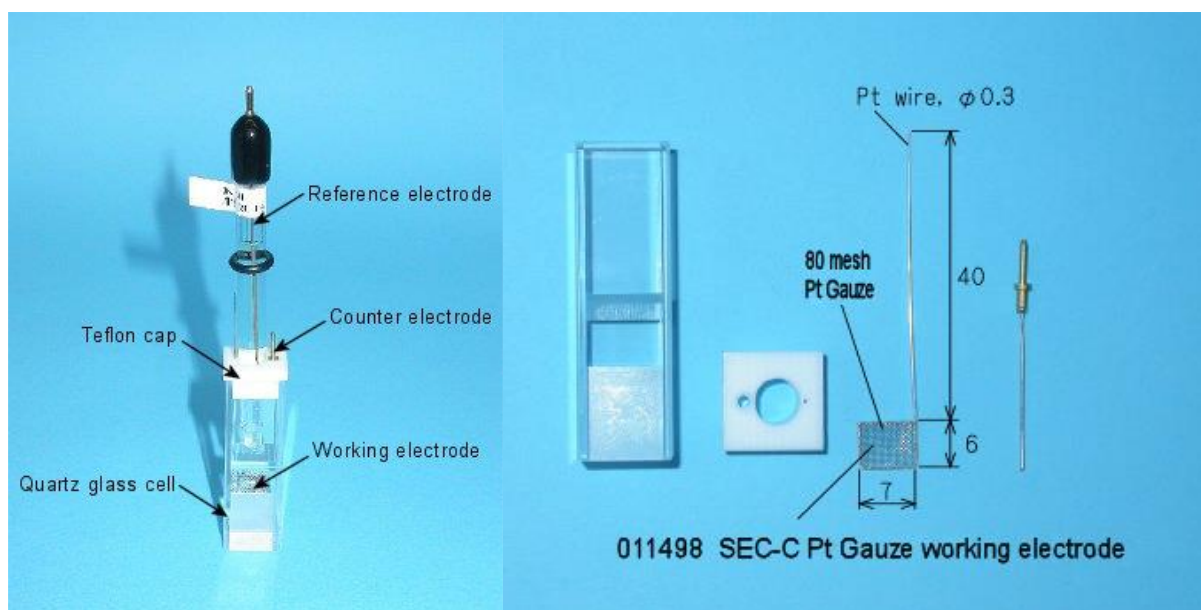


Figure A 4 | Quartz glass cell employed for electrochemical- and spectroelectrochemical experiments

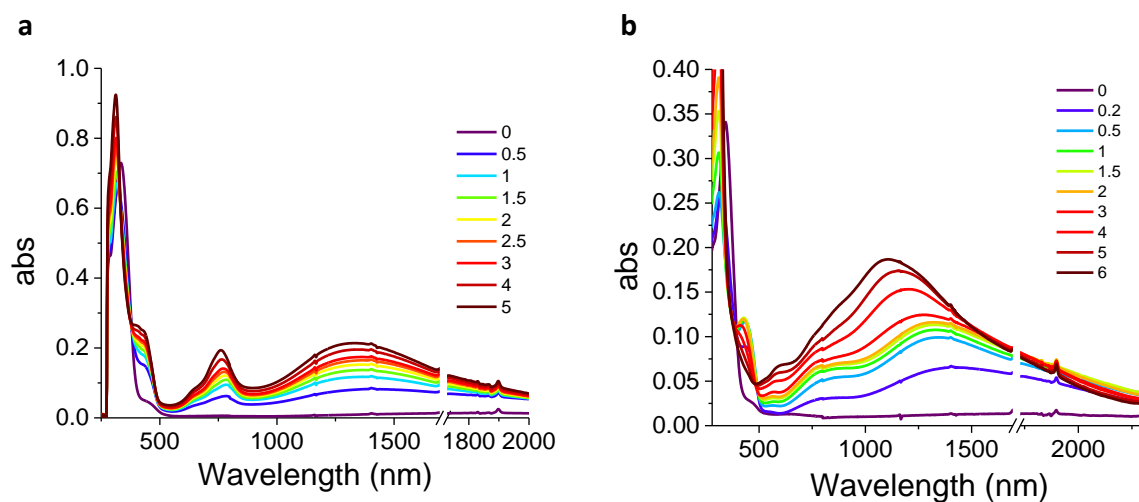


Figure A 5 | Titration of a 10^{-6} M solution of **38** (a) and **39** (b) in TCE with a $1,5 \cdot 10^{-3}$ M solution of tris(4-bromophenyl)ammoniumyl hexachloroantimonate in TCE (equivalents of oxidant added are reported in the legend)

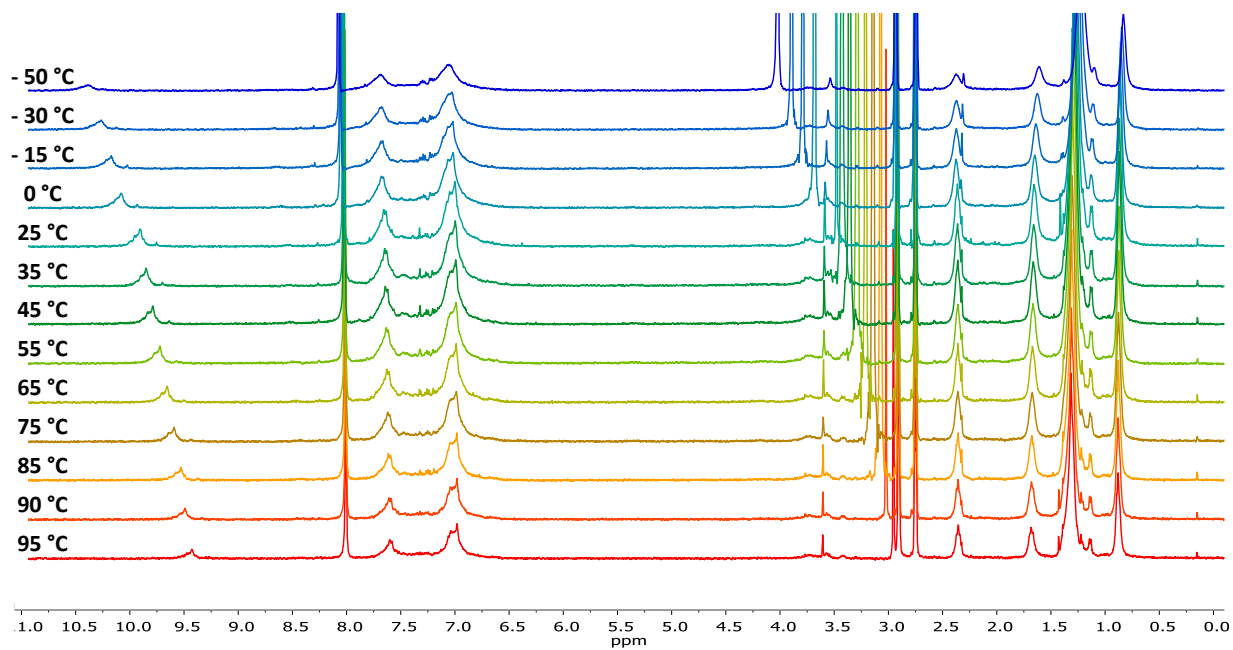


Figure A 6 | Variable temperature $^1\text{H-NMR}$ for a 1.5 mM solution of **39** in DMF-d_7 ;

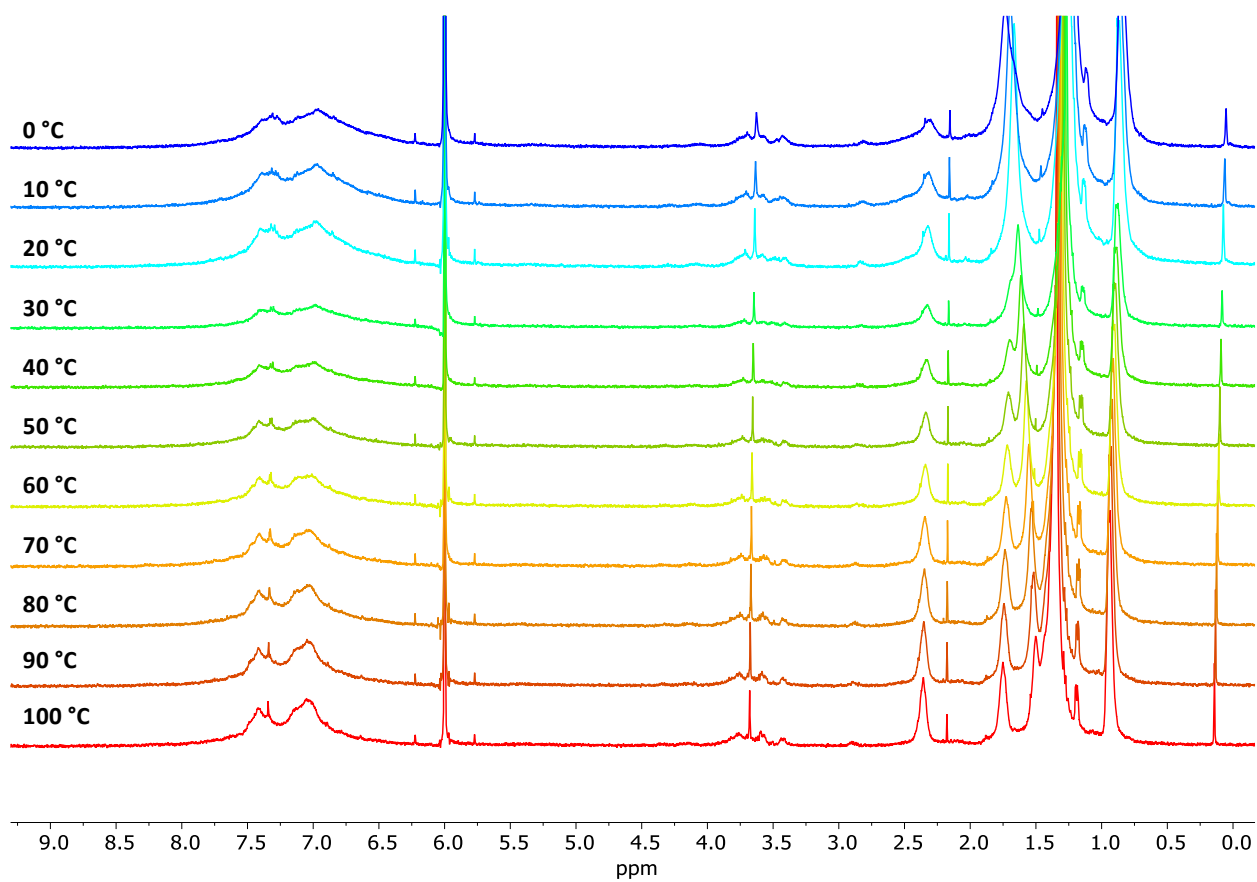


Figure A 7 | Variable temperature $^1\text{H-NMR}$ for a 1.5 mM solution of **39** in TCE-d_2 ;

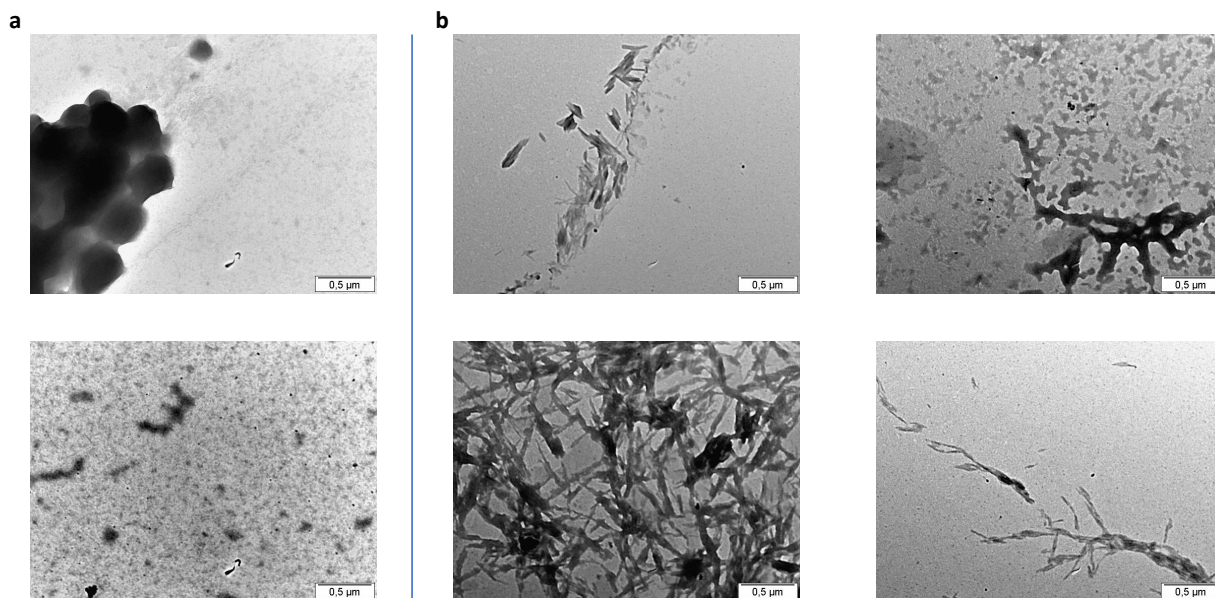


Figure A 8 | a) TEM images of the aggregates observed from a 1 mM solution of **39** in toluene/methanol (9:1); b) TEM images of the aggregates observed from a 1 mM solution of **39** in *o*-dichlorobenzene/methanol (9:1).

Solvent	Conc (mM)	Outcome
Toluene	0.05	Amorphous
	0.5	Amorphous
	1	Amorphous
Chlorobenzene	0.05	Amorphous / fibers
	0.5	Amorphous / fibers
	1	Amorphous / fibers
<i>o</i> -dichlorobenzene	0.05	Amorphous / fibers
	0.5	Amorphous / fibers
	1	Amorphous / fibers
	5	Amorphous / fibers
DMF	0.5	Amorphous
	1	Amorphous
	3	Amorphous
1,1,2,2-tetrachlorobenzene	1	Amorphous
	5	Amorphous
1,2,4-trichlorobenzene	1	Amorphous
Ethanol	1	Not soluble
Ethyl acetate	1	Not soluble
Methylcyclohexane	1	Not soluble
THF	1	Amorphous
THF / methylcyclohexane (85:15)	1	Amorphous
Tetrahydronaphthalene	1	Amorphous / fibers
Toluene / methanol	1	Amorphous
<i>o</i> -dichlorobenzene / methanol (90:10)	1	Amorphous / fibers
<i>o</i> -dichlorobenzene / DMF (90:10)	2	Fibers

Table A 1 | Conditions tested for the self-assembly of macrocycle **39**

Reference	ITO active area	Glass type	Cell gap	Alignment layer
<i>S100A040uNOPI (A35)</i>	10 x 10 mm	Soda-lime glass	4.0 μm	none

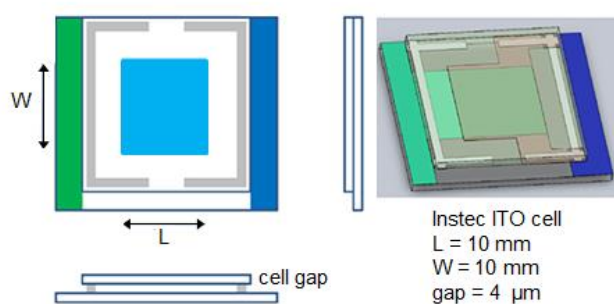


Figure A 9 | Representation of the ITO cell used for conductivity measurements.

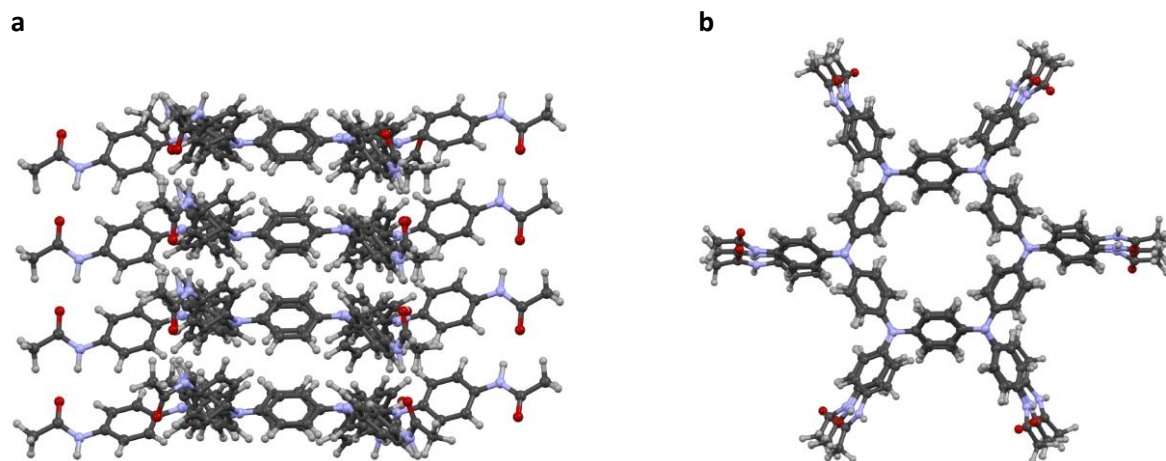


Figure A 10 | Simulated stacking of four macrocyclic units in unidirectional fashion (semi-empirical PM6; side (a) and top (b) view)

BIBLIOGRAPHY

- (1) Lehn, J. M. Supramolecular Chemistry - Scope and Perspectives: Molecules - Supermolecules - Molecular Devices. *J. Incl. Phenom.* **1987**, 6 (4), 351–396.
- (2) Cram, D. J. Preorganization-From Solvents to Spherands. *Angew. Chem. Int. Ed.* **1986**, 25 (12), 1039–1057.
- (3) Whitesides, G.; Grzybowski, B. Self-Assembly at All Scales. *Science (80-.)*. **2002**, 295 (5564), 2418–2421.
- (4) Sauvage, J. P.; Dietrich-Buchecker, C. *A Journey Through the World of Molecular Topology*; WILEY, Ed.; Wiley-VCH Verlag GmbH & Co. KGaA: Weinheim, Germany, 1999.
- (5) Lehn, J. M. Perspectives in Chemistry - Steps towards Complex Matter. *Angew. Chem. Int. Ed.* **2013**, 52 (10), 2836–2850.
- (6) Pieters, B. J. G. E.; Van Eldijk, M. B.; Nolte, R. J. M.; Mecinović, J. Natural Supramolecular Protein Assemblies. *Chem. Soc. Rev.* **2016**, 45 (1), 24–39.
- (7) McLaughlin, C. K.; Hamblin, G. D.; Sleiman, H. F. Supramolecular DNA Assembly. *Chem. Soc. Rev.* **2011**, 40 (12), 5647–5656.
- (8) Shiang, R.; Church, D. M.; Fielder, T. J.; Bocian, M.; Winokur, S. T.; Wasmuth, J. J. Mutations in the Transmembrane Domain of FGFR3 Cause the Most Common Genetic Form of Dwarfism , Achondroplasia. *Cell* **1994**, 79, 335–342.
- (9) Ajmal, M.; Mir, A.; Shoaib, M.; Malik, S. A.; Nasir, M. Identification and in Silico Characterization of p.G380R Substitution in FGFR3, Associated with Achondroplasia in a Non-Consanguineous Pakistani Family. *Cell* **1994**, 78, 335–342.
- (10) Müller-Dethlefs, K.; Hobza, P. Noncovalent Interactions: A Challenge for Experiment and Theory. *Chem. Rev.* **2000**, 100 (1), 143–168.
- (11) Steed, J. W.; Turner, D. R.; Wallace, K. *Core Concepts in Supramolecular Chemistry and Nanochemistry: From Supramolecules to Nanotechnology*; Wiley, 2007.
- (12) Yoder, C. H. Teaching Ion-Ion, Ion-Dipole, and Dipole-Dipole Interactions. *J. Chem. Educ.* **2009**, 54 (7), 402.
- (13) Yang, L.; Tan, X.; Wang, Z.; Zhang, X. Supramolecular Polymers: Historical Development, Preparation, Characterization, and Functions. *Chem. Rev.* **2015**, 115 (15), 7196–7239.
- (14) Brunsveld, L.; Folmer, J. B.; Meijer, E. W.; Sijbesma, R. P. Supramolecular Polymers.

- Chem. Rev.* **2001**, *101*, 4071–4097.
- (15) Matthews, R. P.; Welton, T.; Hunt, P. A. Competitive Pi Interactions and Hydrogen Bonding within Imidazolium Ionic Liquids. *Phys. Chem. Chem. Phys.* **2014**, *16* (7), 3238–3253.
- (16) Dhotel, A.; Chen, Z.; Delbreilh, L.; Youssef, B.; Saiter, J. M.; Tan, L. Molecular Motions in Functional Self-Assembled Nanostructures. *Int. J. Mol. Sci.* **2013**, *14* (2), 2303–2333.
- (17) Waters, M. L. Aromatic Interactions in Model Systems. *Curr. Opin. Chem. Biol.* **2002**, *6*, 736–741.
- (18) Sherrill, C. D. Energy Component Analysis of π Interactions. *Acc. Chem. Res.* **2013**, *46* (4), 1020–1028.
- (19) Biedermann, F.; Nau, W. M.; Schneider, H. J. The Hydrophobic Effect Revisited - Studies with Supramolecular Complexes Imply High-Energy Water as a Noncovalent Driving Force. *Angew. Chem. Int. Ed.* **2014**, *53*, 2–16.
- (20) Chandler, D. Interfaces and the Driving Force of Hydrophobic Assembly. *Nature* **2005**, *43*, 640–647.
- (21) Winter, A.; Hager, M. D.; Schubert, U. S. *Supramolecular Polymers*; 2012.
- (22) Herbst, F.; Döhler, D.; Michael, P.; Binder, W. H. Self-Healing Polymers via Supramolecular Forces. *Macromol. Rapid Commun.* **2013**, *34* (3), 203–220.
- (23) Brunsveld, L.; Folmer, B. J. B.; Meijer, E. W.; Sijbesma, R. P. Supramolecular Polymers. *Chem. Rev.* **2001**, *101*, 4071–4097.
- (24) Greef, T. F. A.; Smulders, M. M. J.; Wolffs, M.; Schenning, A. P. H. J.; Sijbesma, R. P.; Meijer, E. W. Supramolecular Polymerizations. *Chem. Rev.* **2009**, *109*, 5687–5754.
- (25) Fouquey, C.; Lehn, J. -M; Levelut, A. -M. Molecular Recognition Directed Self-assembly of Supramolecular Liquid Crystalline Polymers from Complementary Chiral Components. *Adv. Mater.* **1990**, *2* (5), 254–257.
- (26) Gulik-Krzywicki, T.; Fouquey, C.; Lehntt, J.-M. Electron Microscopic Study of Supramolecular Liquid Crystalline Polymers Formed by Molecular-Recognition-Directed Self-Assembly from Complementary Chiral Components (Helical Supramolecular Structures/Chiral Liquid Crystalline Species/Spontaneous Racemate. *Proc. Natl. Acad. Sci.* **1993**, *90*, 163–167.
- (27) Dobrawa, R.; Würthner, F. Metallosupramolecular Approach toward Functional Coordination Polymers. *J. Polym. Sci. Part A Polym. Chem.* **2005**, *43* (21), 4981–4995.
- (28) Winter, A.; Schubert, U. S. Synthesis and Characterization of Metallo-Supramolecular

- Polymers. *Chem. Soc. Rev.* **2016**, *45* (19), 5311–5357.
- (29) Schütte, M.; Kurth, D. G.; Linford, M. R.; Cölfen, H.; Möhwald, H. Metallosupramolecular Thin Polyelectrolyte Films. *Angew. Chem. Int. Ed.* **1998**, 2891–2893.
- (30) Zhang, Q.; Qu, D. H.; Wu, J.; Ma, X.; Wang, Q.; Tian, H. A Dual-Modality Photoswitchable Supramolecular Polymer. *Langmuir* **2013**, *29* (17), 5345–5350.
- (31) Sheu, E. Y.; Liang, K. S.; Chiang, L. Y. Self-Association of Disc-like Molecules in Hexadecane. *J. Phys.* **1989**, *50* (10), 1279–1295.
- (32) Monahan, A. R.; Brado, J. A.; DeLuca, A. F. The Dimerization of a Copper(II)-Phthalocyanine Dye in Carbon Tetrachloride and Benzene. *J. Phys. Chem.* **1972**, *76* (3), 446–449.
- (33) Kroon, J. M.; Koehorst, R. B. M.; Van Dijk, M.; Sanders, G. M.; Sudhölter, E. J. R. Self-Assembling Properties of Non-Ionic Tetraphenylporphyrins and Discotic Phthalocyanines Carrying Oligo(Ethylene Oxide) Alkyl or Alkoxy Units. *J. Mater. Chem.* **1997**, *7* (4), 615–624.
- (34) Nuckolls, C.; Katz, T. J. Synthesis, Structure, and Properties of a Helical Columnar Liquid Crystal. *J. Am. Chem. Soc.* **1998**, *120* (37), 9541–9544.
- (35) Prest, P. J.; Prince, R. B.; Moore, J. S. Supramolecular Organization of Oligo(m-Phenylene Ethynylene)s in the Solid-State. *J. Am. Chem. Soc.* **1999**, *121* (25), 5933–5939.
- (36) Katz, T. J. Syntheses of Functionalized and Aggregating Helical Conjugated Helical Conjugated Molecules. *Angew. Chem. Int. Ed.* **2000**, *39* (11), 1921–1923.
- (37) Kumar, M.; Venkata Rao, K.; George, S. J. Supramolecular Charge Transfer Nanostructures. *Phys. Chem. Chem. Phys.* **2014**, *16* (4), 1300–1313.
- (38) De Greef, T. F. A.; Meijer, E. W. Supramolecular Polymers. *Nanoscale* **2008**, *453*, 171–173.
- (39) Flory, P. J. *Principles of Polymer Chemistry*; Cornell University Press: Ithaca, New York, 1953.
- (40) Ciferri, A. Supramolecular Polymerizations. *Macromol. Rapid Commun.* **2002**, No. 23, 511–529.
- (41) Dudowicz, J.; Freed, K. F.; Douglas, J. F. Lattice Model of Equilibrium Polymerization. IV. Influence of Activation, Chemical Initiation, Chain Scission and Fusion, and Chain Stiffness on Polymerization and Phase Separation. *J. Chem. Phys.* **2003**, *119* (23), 12645–12666.

- (42) Martin, R. B. Comparisons of Indefinite Self-Association Models. *Chem. Rev.* **1996**, *96* (8), 3043–3063.
- (43) Henderson, J. R. Physics of Isodesmic Chemical Equilibria in Solution. *Phys. Rev. E* **1997**, *55* (5), 5731–5742.
- (44) Braswell, E. H. Sedimentation and Absorption Spectroscopy Studies of Some Self-Associating Cationic Dyes. *J. Phys. Chem.* **1984**, *88* (16), 3653–3658.
- (45) Coggeshall, N. D.; Saier, E. L. Infrared Absorption Study of Hydrogen Bonding Equilibria. *J. Am. Chem. Soc.* **1951**, *73* (11), 5414–5418.
- (46) Broom, A. D.; Schweizer, M. P.; Ts'o, P. O. P. Interaction and Association of Bases and Nucleosides in Aqueous Solutions. V. Studies of the Association of Purine Nucleosides by Vapor Pressure Osmometry and by Proton Magnetic Resonance. *J. Am. Chem. Soc.* **1967**, *89* (14), 3612–3622.
- (47) Wierzchowski, K. L.; Kozłowska, H.; Wierzchowski, K. L. Investigation on Purine and Pyrimidine Bases Stacking Associations in Aqueous Solutions by the Fluorescence Quenching Method. *Biophys. Chem.* **1977**, *6*, 213–222.
- (48) Gilligan, T. J.; Schwarz, G. The Self-Association of Adenosine-Triphosphate Studied by CD at Low Ionic Strengths. *Biophys. Chem.* **1967**, *4*, 55–63.
- (49) Chen, Z.; Fimmel, B.; Würthner, F. Solvent and Substituent Effects on Aggregation Constants of Perylene Bisimide π -Stacks - A Linear Free Energy Relationship Analysis. *Org. Biomol. Chem.* **2012**, *10* (30), 5845–5855.
- (50) Frieden, C. Protein Aggregation Processes: In Search of the Mechanism. *Protein Sci.* **2007**, *16* (11), 2334–2344.
- (51) De Young, L. R.; Fink, A. L.; Dill, K. A. Aggregation of Globular Proteins. *Acc. Chem. Res.* **1993**, *26* (12), 614–620.
- (52) Firestone, M. P.; De Levie, R.; Rangarajan, S. K. On One-Dimensional Nucleation and Growth of “Living” Polymers I. Homogeneous Nucleation. *J. Theor. Biol.* **1983**, *104* (4), 535–552.
- (53) Tanford, C. Theory of Micelle Formation in Aqueous Solutions. *J. Phys. Chem.* **1974**, *78* (24), 2469–2479.
- (54) Ogi, S.; Stepanenko, V.; Sugiyasu, K.; Takeuchi, M.; Würthner, F. Mechanism of Self-Assembly Process and Seeded Supramolecular Polymerization of Perylene Bisimide Organogelator. *J. Am. Chem. Soc.* **2015**, *137* (9), 3300–3307.
- (55) Hegstrom, R. A.; Kondepudi, D. K. The Handedness of the Universe. *Sci. Am.* **1990**, *262* (1), 108–115.

- (56) Liu, M.; Zhang, L.; Wang, T. Supramolecular Chirality in Self-Assembled Systems. *Chem. Rev.* **2015**, *115* (15), 7304–7397.
- (57) Rong, Y.; Chen, P.; Liu, M. Self-Assembly of Water-Soluble TPPS in Organic Solvents: From Nanofibers to Mirror Imaged Chiral Nanorods. *Chem. Commun.* **2013**, *49*, 10498–10500.
- (58) Gottarelli, G.; Lena, S.; Masiero, S.; Pieraccini, S.; Spada, G. P. The Use of Circular Dichroism Spectroscopy for Studying the Chiral Molecular Self-Assembly: An Overview. *Chirality* **2008**, *20*, 471–485.
- (59) Schenning, A. P. H. J.; Jonkheijm, P.; Peeters, E.; Meijer, E. W. Hierarchical Order in Supramolecular Assemblies of Hydrogen-Bonded Oligo(p-Phenylene Vinylene)S. *J. Am. Chem. Soc.* **2001**, *123*, 409–416.
- (60) Duan, P.; Zhu, X.; Liu, M. Isomeric Effect in the Self-Assembly of Pyridine-Containing L-Glutamic Lipid: Substituent Position Controlled Morphology and Supramolecular Chirality. *Chem. Commun.* **2011**, *47* (19), 5569–5571.
- (61) Shimizu, T.; Masuda, M.; Minamikawa, H. Supramolecular Nanotube Architectures Based on Amphiphilic Molecules Toshimi. *Chem. Rev.* **2005**, *105*, 1401–1443.
- (62) Duan, P.; Li, Y.; Li, L.; Deng, J.; Liu, M. Multiresponsive Chiroptical Switch of an Azobenzene-Containing Lipid: Solvent, Temperature, and Photoregulated Supramolecular Chirality. *J. Phys. Chem. B* **2011**, *115* (13), 3322–3329.
- (63) Wang, X.; Duan, P.; Liu, M. Universal Chiral Twist via Metal Ion Induction in the Organogel of Terephthalic Acid Substituted Amphiphilic L-Glutamide. *Chem. Commun.* **2012**, *48* (60), 7501–7503.
- (64) Jin, W.; Fukushima, T.; Niki, M.; Kosaka, A.; Ishii, N.; Aida, T. Self-Assembled Graphitic Nanotubes with One-Handed Helical Arrays of a Chiral Amphiphilic Molecular Graphene. *Proc. Natl. Acad. Sci. U. S. A.* **2005**, *102* (31), 10801–10806.
- (65) Wang, K. R.; An, H. W.; Wu, L.; Zhang, J. C.; Li, X. L. Chiral Self-Assembly of Lactose Functionalized Perylene Bisimides as Multivalent Glycoclusters. *Chem. Commun.* **2012**, *48* (45), 5644–5646.
- (66) Xie, Z.; Stepanenko, V.; Radacki, K.; Würthner, F. Chiral J-Aggregates of Atropo-Enantiomeric Perylene Bisimides and Their Self-Sorting Behavior. *Chem. Eur. J.* **2012**, *18* (23), 7060–7070.
- (67) Helmich, F.; Lee, C. C.; Nieuwenhuizen, M. M. L.; Gielen, J. C.; Christianen, P. C. M.; Larsen, A.; Fytas, G.; Leclère, P. E. L. G.; Schenning, A. P. H. J.; Meijer, E. W. Dilution-Induced Self-Assembly of Porphyrin Aggregates: A Consequence of Coupled

- Equilibria. *Angew. Chem. Int. Ed.* **2010**, *49* (23), 3939–3942.
- (68) Henze, O.; Feast, W. J.; Gardebien, F.; Jonkheijm, P.; Lazzaroni, R.; Leclère, P.; Meijer, E. W.; Scheming, A. P. H. J. Chiral Amphiphilic Self-Assembled α, α' -Linked Quinque-, Sexi-, and Septithiophenes: Synthesis, Stability and Odd-Even Effects. *J. Am. Chem. Soc.* **2006**, *128* (17), 5923–5929.
- (69) Stals, P. J. M.; Everts, J. C.; De Bruijn, R.; Filot, I. A. W.; Smulders, M. M. J.; Martín-Rapún, R.; Pidko, E. A.; De Greef, T. F. A.; Palmans, A. R. A.; Meijer, E. W. Dynamic Supramolecular Polymers Based on Benzene-1, 3, 5-Tricarboxamides: The Influence of Amide Connectivity on Aggregate Stability and Amplification of Chirality. *Chem. Eur. J.* **2010**, *16* (3), 810–821.
- (70) Aparicio, F.; García, F.; Sánchez, L. Supramolecular Polymerization of C₃-Symmetric Organogelators: Cooperativity, Solvent, and Gelation Relationship. *Chem. Eur. J.* **2013**, *19* (9), 3239–3248.
- (71) Wang, F.; Gillissen, M. A. J.; Stals, P. J. M.; Palmans, A. R. A.; Meijer, E. W. Hydrogen Bonding Directed Supramolecular Polymerisation of Oligo(Phenylene-Ethynylene)s: Cooperative Mechanism, Core Symmetry Effect and Chiral Amplification. *Chem. Eur. J.* **2012**, *18* (37), 11761–11770.
- (72) García, F.; Viruela, P. M.; Matesanz, E.; Ortí, E.; Sánchez, L. Cooperative Supramolecular Polymerization and Amplification of Chirality in C₃-Symmetrical OPE-Based Trisamides. *Chem. Eur. J.* **2011**, *17* (28), 7755–7759.
- (73) Zhang, W.; Fujiki, M.; Zhu, X. Chiroptical Nanofibers Generated from Achiral Metallophthalocyanines Induced by Diamine Homochirality. *Chem. Eur. J.* **2011**, *17* (38), 10628–10635.
- (74) George, S. J.; Tomović, Ž.; Schenning, A. P. H. J.; Meijer, E. W. Insight into the Chiral Induction in Supramolecular Stacks through Preferential Chiral Solvation. *Chem. Commun.* **2011**, *47* (12), 3451–3453.
- (75) Cui, J.; Liu, A.; Guan, Y.; Zheng, J.; Shen, Z.; Wan, X. Tuning the Helicity of Self-Assembled Structure of a Sugar-Based Organogelator by the Proper Choice of Cooling Rate. *Langmuir* **2010**, *26* (5), 3615–3622.
- (76) Kumar, J.; Nakashima, T.; Kawai, T. Inversion of Supramolecular Chirality in Bichromophoric Perylene Bisimides: Influence of Temperature and Ultrasound. *Langmuir* **2014**, *30* (21), 6030–6037.
- (77) Young, W. R.; Aviram, A.; Cox, R. J. Stilbene Derivatives. A New Class of Room Temperature Nematic Liquids. *J. Am. Chem. Soc.* **1972**, *94*, 3976–3981.

- (78) Keith, C.; Reddy, R. A.; Hauser, A.; Baumeister, U.; Tschierske, C. Silicon-Containing Polyphilic Bent-Core Molecules: The Importance of Nanosegregation for the Development of Chirality and Polar Order in Liquid Crystalline Phases Formed by Achiral Molecules. *J. Am. Chem. Soc.* **2006**, *128* (9), 3051–3066.
- (79) De Rossi, U.; Dähne, S.; Meskers, S. C. J.; Dekkers, H. P. J. M. Spontaneous Formation of Chirality in J-Aggregates Showing Davydov Splitting. *Angew. Chem. Int. Ed. Eng* **1996**, *35* (7), 760–763.
- (80) Stals, P. J. M.; Korevaar, P. A.; Gillissen, M. A. J.; De Greef, T. F. A.; Fitié, C. F. C.; Sijbesma, R. P.; Palmans, A. R. A.; Meijer, E. W. Symmetry Breaking in the Self-Assembly of Partially Fluorinated Benzene-1,3,5-Tricarboxamides. *Angew. Chem. Int. Ed.* **2012**, *51* (45), 11297–11301.
- (81) Shen, Z.; Jiang, Y.; Wang, T.; Liu, M. Symmetry Breaking in the Supramolecular Gels of an Achiral Gelator Exclusively Driven by π - π Stacking. *J. Am. Chem. Soc.* **2015**, *137* (51), 16109–16115.
- (82) Agarwala, P.; Kabra, D. A Review on Triphenylamine (TPA) Based Organic Hole Transport Materials (HTMs) for Dye Sensitized Solar Cells (DSSCs) and Perovskite Solar Cells (PSCs): Evolution and Molecular Engineering. *J. Mater. Chem. A* **2017**, *5* (4), 1348–1373.
- (83) Thelakkat, M. Star-Shaped, Dendrimeric and Polymeric Triarylamines as Photoconductors and Hole Transport Materials for Electro-Optical Applications. *Macromol. Mater. Eng.* **2002**, *287* (7), 442.
- (84) Jiang, Z.; Chen, Y.; Yang, C.; Cao, Y.; Tao, Y.; Qin, J.; Ma, D. A Fully Diarylmethylene-Bridged Triphenylamine Derivative as Novel Host for Highly Efficient Green Phosphorescent OLEDs. *Org. Lett.* **2009**, *11* (7), 1503–1506.
- (85) Wang, S.; Yan, X.; Cheng, Z.; Zhang, H.; Liu, Y.; Wang, Y. Highly Efficient Near-Infrared Delayed Fluorescence Organic Light Emitting Diodes Using a Phenanthrene-Based Charge-Transfer Compound. *Angew. Chemie - Int. Ed.* **2015**, *54* (44), 13068–13072.
- (86) Karam, R. E. Method for the Preparation of an Electrostatographic Photoreceptor. US4006019A, 1977.
- (87) Li, Y.; Zheng, M.; Wang, J.; Gao, Y.; Zhang, B.; Yang, W. Two-Photon Absorption and Fluorescence Fluoride-Sensing Properties of N-Octyl-3,6-Bis[4-(4-(Diphenylamino)Phenyl)Phenyl]-1,4-Diketo-Pyrrolo[3,4-c] Pyrrole. *Dye. Pigment.* **2014**, *104*, 97–101.

- (88) Merz, V.; Weith, W. Vermischte Mittheilungen. *Berichte der Dtsch. Chem. Gesellschaft* **1873**, 6 (2), 1511–1520.
- (89) Goldberg, I.; Nimerovsky, M. Über Triphenylamin Und Triphenylamin-carbonsäure. *Berichte der Dtsch. Chem. Gesellschaft* **1907**, 40 (2), 2448–2452.
- (90) Manifar, T.; Rohani, S. Synthesis and Analysis of Triphenylamine: A Review. *Can. J. Chem. Eng.* **2004**, 82 (2), 323–334.
- (91) Sung, S.; Sale, D.; Braddock, D. C.; Armstrong, A.; Brennan, C.; Davies, R. P. Mechanistic Studies on the Copper-Catalyzed N-Arylation of Alkylamines Promoted by Organic Soluble Ionic Bases. *ACS Catal.* **2016**, 6 (6), 3965–3974.
- (92) Moriwaki, K.; Satoh, K.; Takada, M.; Ishino, Y.; Ohno, T. Amination and Amidation of Aryl Iodides Catalyzed by Copper(I)-Phenanthroline Complexes. *Tetrahedron Lett.* **2005**, 46 (44), 7559–7562.
- (93) Gujadhur, R. K.; Bates, C. G.; Venkataraman, D. Formation of Aryl-Nitrogen, Aryl-Oxygen, and Aryl-Carbon Bonds Using Well-Defined Copper(I)-Based Catalysts. *Org. Lett.* **2001**, 3 (26), 4315–4317.
- (94) Qian, C.; Xu, S.; Zong, Q.; Fang, D. Copper-Catalyzed Synthesis of Triarylamine from Aryl Halides and Arylamines. *Chinese J. Chem.* **2012**, 30 (8), 1881–1885.
- (95) Goodbrand, H. B.; Hu, N. X. Ligand-Accelerated Catalysis of the Ullmann Condensation: Application to Hole Conducting Triarylamine. *J. Org. Chem.* **1999**, 64 (2), 670–674.
- (96) Liu, Y.; Yang, L. Efficient Synthesis of Triarylamine Catalyzed by Copper(I) Diazabutadiene Complexes. *Chinese J. Chem.* **2015**, 33 (4), 473–478.
- (97) Sambriago, C.; Marsden, S.; Blacker, J.; McGowan, P. Copper Catalysed Ullmann Type Chemistry: From Mechanistic Aspects to Modern Development. *Chem. Soc. Rev.* **2014**, 43, 3525–3550.
- (98) Wolfe, J. P.; Wagaw, S.; Buchwald, S. L. An Improved Catalyst System for Aromatic Carbon-Nitrogen Bond Formation: The Possible Involvement of Bis(Phosphine) Palladium Complexes as Key Intermediates. *J. Am. Chem. Soc.* **1996**, 118 (30), 7215–7216.
- (99) Driver, M. S.; Hartwig, J. F. A Second-Generation Catalyst for Aryl Halide Amination: Mixed Secondary Amines from Aryl Halides and Primary Amines Catalyzed by (DPPF)PdCl₂. *J. Am. Chem. Soc.* **1996**, 118 (30), 7217–7218.
- (100) Yamamoto, T.; Nishiyama, M.; Koie, Y. Palladium-Catalyzed Synthesis of Triarylamine from Aryl Halides and Diarylamines. *Tetrahedron Lett.* **1998**, 39 (16),

- 2367–2370.
- (101) Hartwig, J. F.; Kawatsura, M.; Hauck, S. I.; Shaughnessy, K. H.; Alcazar-Roman, L. M. Room-Temperature Palladium-Catalyzed Amination of Aryl Bromides and Chlorides and Extended Scope of Aromatic C-N Bond Formation with a Commercial Ligand. *J. Org. Chem.* **1999**, *64* (15), 5575–5580.
- (102) Harris, M. C.; Huang, X.; Buchwald, S. L. Improved Functional Group Compatibility in the Palladium-Catalyzed Synthesis of Aryl Amines. *Org. Lett.* **2002**, *4* (17), 2885–2888.
- (103) Old, D. W.; Wolfe, J. P.; Buchwald, S. L. A Highly Active Catalyst for the Room-Temperature Amination and Suzuki Coupling of Aryl Chlorides. *J. Am. Chem. Soc.* **1998**, *120*, 9722–9723.
- (104) Harris, M. C.; Buchwald, S. L. One-Pot Synthesis of Unsymmetrical Triarylamines from Aniline Precursors. *J. Org. Chem.* **2000**, *65* (17), 5327–5333.
- (105) Lee, W. Y.; Kurosawa, T.; Lin, S. T.; Higashihara, T.; Ueda, M.; Chen, W. C. New Donor-Acceptor Oligoimides for High-Performance Nonvolatile Memory Devices. *Chem. Mater.* **2011**, *23* (20), 4487–4497.
- (106) Ishow, E.; Brosseau, A.; Clavier, G.; Nakatani, K.; Pansu, R. B.; Vachon, J. J.; Tauc, P.; Chauvat, D.; Mendonça, C. R.; Piovesan, E. Two-Photon Fluorescent Holographic Rewritable Micropatterning. *J. Am. Chem. Soc.* **2007**, *129* (29), 8970–8971.
- (107) Tahara, K.; Nakakita, T.; Katao, S.; Kikuchi, J. I. Organic Mixed Valency in Quadruple Hydrogen-Bonded Triarylamine Dimers Bearing Ureido Pyrimidinedione Moieties. *Chem. Commun.* **2014**, *50* (95), 15071–15074.
- (108) Rozalska, I.; Kułyk, P.; Kulszewicz-Bajer, I. Linear 1,4-Coupled Oligoanilines of Defined Length: Preparation and Spectroscopic Properties. *New J. Chem.* **2004**, *28*, 1235–1243.
- (109) Branch, G. E. K.; Calvin, M. *The Theory of Organic Chemistry*; Prentice-Hall, I., Ed.; Englewood Cliffs, New Jersey, 1941.
- (110) Sasaki, Y.; Kimura, K.; Kubo, M. Electron Diffraction Investigation of Triphenylamine. *J. Chem. Phys.* **1959**, *31* (2), 477.
- (111) Sobolev, A. N.; Belsky, V. K.; Romm, I. P.; Chernikova, N. Y.; Guryanova, E. N. Structural Investigation of the Triaryl Derivatives of the Group V Elements. IX. Structure of Triphenylamine, C₁₈H₁₅N. *Acta Crystallogr. Sect. C Cryst. Struct. Commun.* **1985**, *41* (6), 967–971.
- (112) Pacansky, J.; Waltman, R. J.; Seki, H. Ab Initio Computational Studies on the Structures and Energetics of Hole Transport Molecules: Triphenylamine. *Bull. Chem. Soc. Jpn.*

- 1997**, 70 (1), 55–59.
- (113) Naumov, V. A.; Samdal, S.; Naumov, A. V.; Gundersen, S.; Volden, H. V. Molecular Structure of Triphenylamine in the Gas Phase. *Russ. J. Gen. Chem.* **2005**, 75 (12), 1956–1961.
- (114) Reva, I.; Lapinski, L.; Chattopadhyay, N.; Fausto, R. Vibrational Spectrum and Molecular Structure of Triphenylamine Monomer: A Combined Matrix-Isolation FTIR and Theoretical Study. *Phys. Chem. Chem. Phys.* **2003**, 5 (18), 3844–3850.
- (115) Amthor, S.; Noller, B.; Lambert, C. UV/Vis/NIR Spectral Properties of Triarylamines and Their Corresponding Radical Cations. *Chem. Phys.* **2005**, 316 (1–3), 141–152.
- (116) Quinton, C.; Alain-Rizzo, V.; Dumas-Verdes, C.; Miomandre, F.; Clavier, G.; Audebert, P. Redox-Controlled Fluorescence Modulation (Electrofluorochromism) in Triphenylamine Derivatives. *RSC Adv.* **2014**, 4 (65), 34332–34342.
- (117) Budyka, M. F.; Alfimov, M. V. Photochemical Reactions of Complexes of Aromatic Amines with Polyhalomethanes. *Russ. Chem. Rev.* **1995**, 64 (8), 705–717.
- (118) Meyer, W. C. Halogen-Sensitized Photoionization of N,N,N',N'-Tetramethyl-p-Phenylenediamine in Liquid Halogenomethanes. *J. Phys. Chem.* **1970**, 74 (10), 2118–2121.
- (119) Lambert, C.; Moos, M.; Schmiedel, A.; Holzappel, M.; Schäfer, J.; Kess, M.; Engel, V. How Fast Is Optically Induced Electron Transfer in Organic Mixed Valence Systems? *Phys. Chem. Chem. Phys.* **2016**, 18 (28), 19405–19411.
- (120) Heckmann, A.; Lambert, C. Organic Mixed-Valence Compounds: A Playground for Electrons and Holes. *Angew. Chem. Int. Ed.* **2012**, 51 (2), 326–392.
- (121) Lambert, C.; No, G. The Class II / III Transition in Triarylamine Redox Systems. *Chem. Commun.* **1999**, No. 1, 8434–8442.
- (122) Crutchley, R. J. Intervalence Charge Transfer and Electron Exchange Studies of Dinuclear Ruthenium Complexes. *Adv. Inorg. Chem.* **1994**, 41 (C), 273–325.
- (123) Hush, N. S. Homogeneous and Heterogeneous Optical and Thermal Electron Transfer. *Electrochim. Acta* **1968**, 13 (5), 1005–1023.
- (124) Renz, M.; Theilacker, K.; Lambert, C.; Kaupp, M. A Reliable Quantum-Chemical Protocol for the Characterization of Organic Mixed-Valence Compounds. *J. Am. Chem. Soc.* **2009**, 131 (44), 16292–16302.
- (125) Sun, D.; Ke, Y.; Mattox, T. M.; Ooro, B. A.; Zhou, H. C. Temperature-Dependent Supramolecular Stereoisomerism in Porous Copper Coordination Networks Based on a Designed Carboxylate Ligand. *Chem. Commun.* **2005**, No. 43, 5447–5449.

- (126) Field, J. E.; Combariza, M. Y.; Vachet, R. W.; Venkataraman, D. Spontaneous Assembly of a Hydrogen-Bonded Tetrahedron. *Chem. Commun.* **2002**, 2 (19), 2260–2261.
- (127) Moulin, E.; Niess, F.; Maaloum, M.; Buhler, E.; Nyrkova, I.; Giuseppone, N. The Hierarchical Self-Assembly of Charge Nanocarriers: A Highly Cooperative Process Promoted by Visible Light. *Angew. Chem. Int. Ed.* **2010**, 49 (39), 6974–6978.
- (128) Moulin, E.; Armao, J. J.; Giuseppone, N. Triarylamine-Based Supramolecular Polymers: Structures, Dynamics, and Functions. *Acc. Chem. Res.* **2019**, 52 (4), 975–983.
- (129) Nyrkova, I.; Moulin, E.; Armao, J. J.; Maaloum, M.; Heinrich, B.; Rawiso, M.; Niess, F.; Cid, J.-J.; Jouault, N.; Buhler, E.; et al. Supramolecular Self-Assembly and Radical Kinetics in Conducting. *ACS Nano* **2014**, 8 (10), 10111–10124.
- (130) Armao, J. J.; Maaloum, M.; Ellis, T.; Fuks, G.; Rawiso, M.; Moulin, E.; Giuseppone, N. Healable Supramolecular Polymers as Organic Metals. *J. Am. Chem. Soc.* **2014**, 136 (32), 11382–11388.
- (131) Kim, T.; Mori, T.; Aida, T.; Miyajima, D. Dynamic Propeller Conformation for the Unprecedentedly High Degree of Chiral Amplification of Supramolecular Helices. *Chem. Sci.* **2016**, 7 (11), 6689–6694.
- (132) Green, M. M.; Reidy, M. P.; Johnson, R. J.; Darling, G.; O’Leary, D. J.; Willson, G. Macromolecular Stereochemistry: The Out-of-Proportion Influence of Optically Active Comonomers on the Conformational Characteristics of Polyisocyanates. The Sergeants and Soldiers Experiment. *J. Am. Chem. Soc.* **1989**, 111 (16), 6452–6454.
- (133) Ishi-I, T.; Kuwahara, R.; Takata, A.; Jeong, Y.; Sakurai, K.; Mataka, S. An Enantiomeric Nanoscale Architecture Obtained from a Pseudoenantiomeric Aggregate: Covalent Fixation of Helical Chirality Formed in Self-Assembled Discotic Triazine Triamides by Chiral Amplification. *Chem. - A Eur. J.* **2006**, 12 (3), 763–776.
- (134) Osypenko, A.; Moulin, E.; Gavat, O.; Fuks, G.; Maaloum, M.; Koenis, M. A. J.; Buma, W. J.; Giuseppone, N. Temperature Control of Sequential Nucleation–Growth Mechanisms in Hierarchical Supramolecular Polymers. *Chem. Eur. J.* **2019**, 25, 1–10.
- (135) Mei, J.; Leung, N. L. C.; Kwok, R. T. K.; Lam, J. W. Y.; Tang, B. Z. Aggregation-Induced Emission: Together We Shine, United We Soar! *Chem. Rev.* **2015**, 115 (21), 11718–11940.
- (136) Luo, J.; Xie, Z.; Xie, Z.; Lam, J. W. Y.; Cheng, L.; Chen, H.; Qiu, C.; Kwok, H. S.; Zhan, X.; Liu, Y.; et al. Aggregation-Induced Emission of 1-Methyl-1,2,3,4,5-Pentaphenylsilole. *Chem. Commun.* **2001**, 18, 1740–1741.

- (137) Hong, Y.; Lam, J. W. Y.; Tang, B. Z. Aggregation-Induced Emission. *Chem. Soc. Rev.* **2011**, *40* (11), 5361–5388.
- (138) Hong, Y.; Lam, J. W. Y.; Tang, B. Z. Aggregation-Induced Emission: Phenomenon, Mechanism and Applications. *Chem. Commun.* **2009**, No. 29, 4332–4353.
- (139) Wu, Y. T.; Kuo, M. Y.; Chang, Y. T.; Shin, C. C.; Wu, T. C.; Tai, C. C.; Cheng, T. H.; Liu, W. S. Synthesis, Structure, and Photophysical Properties of Highly Substituted 8,8a-Dihydrocyclopenta[a]Indenes. *Angew. Chem. Int. Ed.* **2008**, *47* (51), 9891–9894.
- (140) Skardžiute, L.; Kazlauskas, K.; Dodonova, J.; Bucevičius, J.; Tumkevičius, S.; Juršenas, S. Optical Study of the Formation of Pyrrolo[2,3-d]Pyrimidine-Based Fluorescent Nanoaggregates. *Tetrahedron* **2013**, *69* (46), 9566–9572.
- (141) Gao, C.; Gao, G.; Lan, J.; You, J. An AIE Active Monoimidazolium Skeleton: High Selectivity and Fluorescence Turn-on for H₂PO₄-in Acetonitrile and ClO₄-in Water. *Chem. Commun.* **2014**, *50* (42), 5623–5625.
- (142) Cho, Y. J.; Kim, S. Y.; Cho, M.; Han, W. S.; Son, H. J.; Cho, D. W.; Kang, S. O. Aggregation-Induced Emission of Diarylamino- π -Carborane Triads: Effects of Charge Transfer and π -Conjugation. *Phys. Chem. Chem. Phys.* **2016**, *18* (14), 9702–9708.
- (143) Fukazawa, A.; Ichihashi, Y.; Yamaguchi, S. Intense Fluorescence of 1-Aryl-2,3,4,5-Tetraphenylphosphole Oxides in the Crystalline State. *New J. Chem.* **2010**, *34* (8), 1537–1540.
- (144) Pan, H.; Fu, G. L.; Zhao, Y. H.; Zhao, C. H. Through-Space Charge-Transfer Emitting Biphenyls Containing a Boryl and an Amino Group at the o, o'-Positions. *Org. Lett.* **2011**, *13* (18), 4830–4833.
- (145) Zhao, C. H.; Sakuda, E.; Wakamiya, A.; Yamaguchi, S. Highly Emissive Diborylphemele-Containing Bis(Phenylethynyl)Benzenes: Structure-Photophysical Property Correlations and Fluoride Ion Sensing. *Chem. Eur. J.* **2009**, *15* (40), 10603–10612.
- (146) Lai, C. T.; Hong, J. L. Aggregation-Induced Emission in Tetraphenylthiophene-Derived Organic Molecules and Vinyl Polymer. *J. Phys. Chem. B* **2010**, *114* (32), 10302–10310.
- (147) Mullin, J. L.; Tracy, H. J.; Ford, J. R.; Keenan, S. R.; Fridman, F. Characteristics of Aggregation Induced Emission in 1,1-Dimethyl-2,3,4,5-Tetraphenyl and 1,1,2,3,4,5-Hexaphenyl Siloles and Germoles. *J. Inorg. Organomet. Polym. Mater.* **2007**, *17* (1), 201–213.
- (148) Lau, J. S. Y.; Lee, P. K.; Tsang, K. H. K.; Ng, C. H. C.; Lam, Y. W.; Cheng, S. H.; Lo, K. K. W. Luminescent Cyclometalated Iridium(III) Polypyridine Indole Complexes-

- Synthesis, Photophysics, Electrochemistry, Protein-Binding Properties, Cytotoxicity, and Cellular Uptake. *Inorg. Chem.* **2009**, *48* (2), 708–718.
- (149) Zhu, M. X.; Lu, W.; Zhu, N.; Che, C. M. Structures and Solvatochromic Phosphorescence of Dicationic Terpyridyl-Platinum(II) Complexes with Foldable Oligo(Ortho-Phenyleneethynylene) Bridging Ligands. *Chem. Eur. J.* **2008**, *14* (31), 9736–9746.
- (150) Li, Y.; Li, F.; Zhang, H.; Xie, Z.; Xie, W.; Xu, H.; Li, B.; Shen, F.; Ye, L.; Hanif, M.; et al. Tight Intermolecular Packing through Supramolecular Interactions in Crystals of Cyano Substituted Oligo(Para-Phenylene Vinylene): A Key Factor for Aggregation-Induced Emission. *Chem. Commun.* **2007**, *1* (3), 231–233.
- (151) Zhao, X.; Xue, P.; Wang, K.; Chen, P.; Zhang, P.; Lu, R. Aggregation-Induced Emission of Triphenylamine Substituted Cyanostyrene Derivatives. *New J. Chem.* **2014**, *38* (3), 1045–1051.
- (152) Yu, Z.; Duan, Y.; Cheng, L.; Han, Z.; Zheng, Z.; Zhou, H.; Wu, J.; Tian, Y. Aggregation Induced Emission in the Rotatable Molecules: The Essential Role of Molecular Interaction. *J. Mater. Chem.* **2012**, *22* (33), 16927–16932.
- (153) Bernet, A.; Albuquerque, R. Q.; Behr, M.; Hoffmann, S. T.; Schmidt, H. W. Formation of a Supramolecular Chromophore: A Spectroscopic and Theoretical Study. *Soft Matter* **2012**, *8* (1), 66–69.
- (154) Liu, J.; Lam, J. W. Y.; Tang, B. Z. Acetylenic Polymers: Syntheses, Structures, and Functions. *Chem. Rev.* **2009**, *109* (11), 5799–5867.
- (155) Rananaware, A.; Abraham, A. N.; La, D. D.; Mistry, V.; Shukla, R.; Bhosale, S. V. Synthesis of a Tetraphenylethene-Substituted Tetrapyrindinium Salt with Multifunctionality: Mechanochromism, Cancer Cell Imaging, and DNA Marking. *Aust. J. Chem.* **2017**, *70* (6), 652–659.
- (156) Dong, Y.; Lam, J. W. Y.; Qin, A.; Liu, J.; Li, Z.; Tang, B. Z.; Sun, J.; Kwok, H. S. Aggregation-Induced Emissions of Tetraphenylethene Derivatives and Their Utilities as Chemical Vapor Sensors and in Organic Light-Emitting Diodes. *Appl. Phys. Lett.* **2007**, *91* (1), 1–4.
- (157) Zhao, Z.; W. Y. Lam, J.; Zhong Tang, B. Aggregation-Induced Emission of Tetraarylethene Luminogens. *Curr. Org. Chem.* **2010**, *14* (18), 2109–2132.
- (158) La, D. D.; Bhosale, S. V.; Jones, L. A.; Bhosale, S. V. Tetraphenylethylene-Based AIE-Active Probes for Sensing Applications. *ACS Appl. Mater. Interfaces* **2018**, *10* (15), 12189–12216.

- (159) Fu, G. L.; Zhao, C. H. An Aggregation-Induced Emissive Chromophore as a Ratiometric Fluorescent Sensor for Cyanide in Aqueous Media. *Tetrahedron* **2013**, *69* (6), 1700–1704.
- (160) Usuki, T.; Shimada, M.; Yamanoi, Y.; Ohto, T.; Tada, H.; Kasai, H.; Nishibori, E.; Nishihara, H. Aggregation-Induced Emission Enhancement from Disilane-Bridged Donor-Acceptor-Donor Luminogens Based on the Triarylamine Functionality. *ACS Appl. Mater. Interfaces* **2018**, *10* (15), 12164–12172.
- (161) Hu, R.; Lager, E.; Aguilar-Aguilar, A.; Liu, J.; Lam, J. W. Y.; Sung, H. H. Y.; Williams, I. D.; Zhong, Y.; Wong, K. S.; Peña-Cabrera, E.; et al. Twisted Intramolecular Charge Transfer and Aggregation-Induced Emission of BODIPY Derivatives. *J. Phys. Chem. C* **2009**, *113* (36), 15845–15853.
- (162) Hu, R.; Lam, J. W. Y.; Deng, H.; Song, Z.; Zheng, C.; Tang, B. Z. Fluorescent Self-Assembled Nanowires of AIE Fluorogens. *J. Mater. Chem. C* **2014**, *2* (31), 6326–6332.
- (163) Li, Y.; Dong, Y.; Miao, X.; Ren, Y.; Zhang, B.; Wang, P.; Yu, Y.; Li, B.; Isaacs, L.; Cao, L. Shape-Controllable and Fluorescent Supramolecular Organic Frameworks Through Aqueous Host–Guest Complexation. *Angew. Chem. Int. Ed.* **2018**, *57* (3), 729–733.
- (164) Thejo, K.; Swart, H.; Dhoble, S. J. *Principles and Applications of Organic Light Emission Diodes*; Woodhead Publishing: Kidlington, 2017.
- (165) Zhao, Z.; Chen, S.; Shen, X.; Mahtab, F.; Yu, Y.; Lu, P.; Lam, J. W. Y.; Kwok, H. S.; Tang, B. Z. Aggregation-Induced Emission, Self-Assembly, and Electroluminescence of 4,4'-Bis(1,2,2-Triphenylvinyl)Biphenyl. *Chem. Commun.* **2010**, *46* (5), 686–688.
- (166) Huang, J.; Sun, N.; Yang, J.; Tang, R.; Li, Q.; Ma, D.; Li, Z. Blue Aggregation-Induced Emission Luminogens: High External Quantum Efficiencies up to 3.99% in LED Device, and Restriction of the Conjugation Length through Rational Molecular Design. *Adv. Funct. Mater.* **2014**, *24* (48), 7645–7654.
- (167) Chan, C. Y. K.; Lam, J. W. Y.; Zhao, Z.; Chen, S.; Lu, P.; Sung, H. H. Y.; Kwok, H. S.; Ma, Y.; Williams, I. D.; Tang, B. Z. Aggregation-Induced Emission, Mechanochromism and Blue Electroluminescence of Carbazole and Triphenylamine-Substituted Ethenes. *J. Mater. Chem. C* **2014**, *2* (21), 4320–4327.
- (168) Liu, Y.; Chen, X.; Lv, Y.; Chen, S.; Lam, J. W. Y.; Mahtab, F.; Kwok, H. S.; Tao, X.; Tang, B. Z. Systemic Studies of Tetraphenylethene-Triphenylamine Oligomers and a Polymer: Achieving Both Efficient Solid-State Emissions and Hole-Transporting Capability. *Chem. Eur. J.* **2012**, *18* (32), 9929–9938.

- (169) Roose, J.; Tang, B. Z.; Wong, K. S. Circularly-Polarized Luminescence (CPL) from Chiral AIE Molecules and Macrostructures. *Small* **2016**, 1–18.
- (170) Sang, Y.; Han, J.; Zhao, T.; Duan, P.; Liu, M. Circularly Polarized Luminescence in Nanoassemblies: Generation, Amplification, and Application. *Adv. Mater.* **2019**, 1900110.
- (171) Liu, J.; Su, H.; Meng, L.; Zhao, Y.; Deng, C.; Ng, J. C. Y.; Lu, P.; Faisal, M.; Lam, J. W. Y.; Huang, X.; et al. What Makes Efficient Circularly Polarised Luminescence in the Condensed Phase: Aggregation-Induced Circular Dichroism and Light Emission. *Chem. Sci.* **2012**, 3 (9), 2737–2747.
- (172) Haedler, A. T.; Meskers, S. C. J.; Zha, R. H.; Kivala, M.; Schmidt, H. W.; Meijer, E. W. Pathway Complexity in the Enantioselective Self-Assembly of Functional Carbonyl-Bridged Triarylamine Trisamides. *J. Am. Chem. Soc.* **2016**, 138 (33), 10539–10545.
- (173) Feuillastre, S.; Pauton, M.; Gao, L.; Desmarchelier, A.; Riives, A. J.; Prim, D.; Tondelier, D.; Geffroy, B.; Muller, G.; Clavier, G.; et al. Design and Synthesis of New Circularly Polarized Thermally Activated Delayed Fluorescence Emitters. *J. Am. Chem. Soc.* **2016**, 138 (12), 3990–3993.
- (174) Tao, Y.; Yang, C.; Qin, J. Organic Host Materials for Phosphorescent Organic Light-Emitting Diodes. *Chem. Soc. Rev.* **2011**, 40 (5), 2943–2970.
- (175) Moulin, E.; Busseron, E.; Giuseppone, N. CHAPTER 1. Self-Assembled Supramolecular Materials in Organic Electronics. In *Supramolecular Materials for Opto-Electronics*; Koch, N., Ed.; 2015; pp 1–52.
- (176) Wang, J.; Mei, J.; Zhao, E.; Song, Z.; Qin, A.; Sun, J. Z.; Tang, B. Z. Ethynyl-Capped Hyperbranched Conjugated Polytriazole: Click Polymerization, Clickable Modification, and Aggregation-Enhanced Emission. *Macromolecules* **2012**, 45 (19), 7692–7703.
- (177) Appel, W. P. J.; Portale, G.; Wisse, E.; Dankers, P. Y. W.; Meijer, E. W. Aggregation of Ureido-Pyrimidinone Supramolecular Thermoplastic Elastomers into Nanofibers: A Kinetic Analysis. *Macromolecules* **2011**, 44 (17), 6776–6784.
- (178) Iyoda, M.; Yamakawa, J.; Rahman, M. J. Conjugated Macrocycles: Concepts and Applications. *Angew. Chem. Int. Ed.* **2011**, 50 (45), 10522–10553.
- (179) Yen, M.; Huang, J.; Zang, L.; Zhang, W.; Naddo, T.; Moore, J. S.; Balakrishnan, K.; Yang, X.; Zuo, J.; Datar, A. Nanofibril Self-Assembly of an Arylene Ethynylene Macrocyclic. *J. Am. Chem. Soc.* **2006**, 128 (20), 6576–6577.
- (180) Shimura, H.; Yoshio, M.; Kato, T. A Columnar Liquid-Crystalline Shape-Persistent Macrocyclic Having a Nanosegregated Structure. *Org. Biomol. Chem.* **2009**, 7 (16),

- 3205–3207.
- (181) Shu, L.; Müri, M.; Krupke, R.; Mayor, M. Shape-Persistent Macrocycles Comprising Perfluorinated Benzene Subunits: Synthesis, Aggregation Behaviour and Unexpected μ -Rod Formation. *Org. Biomol. Chem.* **2009**, *7* (6), 1081–1092.
- (182) Shu, L.; Mayor, M. Shape-Persistent Macrocyclic Self-Complementary Recognition Pattern Based on Diacetylene-Linked Alternating Hexylbenzene and Perfluorobenzene Rings. *Chem. Commun.* **2006**, No. 39, 4134–4136.
- (183) Enozawa, H.; Hasegawa, M.; Isomura, E.; Nishinaga, T.; Kato, T.; Yamato, M.; Kimura, T.; Iyoda, M. Magnetic Alignment in Solid State and Temperature Hysteresis in Aqueous Tetrahydrofuran Solution for Tetrathiafulvaleno[18]Annulenes. *ChemPhysChem* **2009**, *10* (15), 2607–2611.
- (184) Ito, A. Macrocyclic Oligoarylamines as Hole- and Spin-Containing Scaffolds for Molecule-Based Electronics. *J. Mater. Chem. C* **2016**, *4* (21), 4614–4625.
- (185) Ito, A.; Yokoyama, Y.; Aihara, R.; Fukui, K.; Eguchi, S.; Shizu, K.; Sato, T.; Tanaka, K. Preparation and Characterization of N-Anisyl-Substituted Hexaaza[16]Paracyclophane. *Angew. Chemie Int. Ed.* **2010**, *49* (44), 8205–8208.
- (186) Yang, T. F.; Chiu, K. Y.; Cheng, H. C.; Lee, Y. W.; Kuo, M. Y.; Su, Y. O. Studies on the Structure of N-Phenyl-Substituted Hexaaza[16] Paracyclophane: Synthesis, Electrochemical Properties, And Theoretical Calculation. *J. Org. Chem.* **2012**, *77* (19), 8627–8633.
- (187) Ellis, T. K.; Galerne, M.; Armao, J. J.; Osypenko, A.; Martel, D.; Maaloum, M.; Fuks, G.; Gavat, O.; Moulin, E.; Giuseppone, N. Supramolecular Electropolymerization. *Angew. Chem. Int. Ed.* **2018**, *57* (48), 15749–15753.
- (188) Kim, B. S.; Lee, S. Y.; Youn, S. W. Pd-Catalyzed Sequential C-C and C-N Bond Formations for the Synthesis of N-Heterocycles: Exploiting Protecting Group-Directed C-H Activation under Modified Reaction Conditions. *Chem. Asian J.* **2011**, *6* (8), 1952–1957.
- (189) Fairlamb, I. J. S.; Kapdi, A. R.; Lee, A. F. H₂-Dba Complexes of Pd(0): The Substituent Effect in Suzuki-Miyaura Coupling. *Org. Lett.* **2004**, *6* (24), 4435–4438.
- (190) Johnson, E. C. B.; Kent, S. B. H. Synthesis, Stability and Optimized Photolytic Cleavage of 4-Methoxy-2-Nitrobenzyl Backbone-Protected Peptides. *Chem. Commun.* **2006**, No. 14, 1557–1559.
- (191) Horspool, W.; Lenci, F. *CRC Handbook of Organic Photochemistry and Photobiology*; Press, C., Ed.; 2004.

- (192) Holmes, C. P. Model Studies for New O-Nitrobenzyl Photolabile Linkers: Substituent Effects on the Rates of Photochemical Cleavage. *J. Org. Chem.* **1997**, *62* (8), 2370–2380.
- (193) Gallou-Dagommer, I.; Gastaud, P.; RajanBabu, T. V. Asymmetric Synthesis of Functionalized 1,2,3,4-Tetrahydroquinolines. *Org. Lett.* **2001**, *3* (13), 2053–2056.
- (194) Ishow, E.; Camacho-Aguilera, R.; Guérin, J.; Brosseau, A.; Nakatani, K. Spontaneous Formation of Complex Periodic Superstructures under High Interferential Illumination of Small-Molecule-Based Photochromic Materials. *Adv. Funct. Mater.* **2009**, *19* (5), 796–804.
- (195) Morales, S.; Guijarro, F. G.; García Ruano, J. L.; Cid, M. B. A General Aminocatalytic Method for the Synthesis of Aldimines. *J. Am. Chem. Soc.* **2014**, *136* (3), 1082–1089.
- (196) Yin, J.; Buchwald, S. L. Pd-Catalyzed Intermolecular Amidation of Aryl Halides: The Discovery That Xantphos Can Be Trans-Chelating in a Palladium Complex. *J. Am. Chem. Soc.* **2002**, *124* (21), 6043–6048.
- (197) Ilangovan, A.; Saravanakumar, S.; Malayappasamy, S.; Manickam, G. A Convenient Approach for the Deprotection and Scavenging of the PMB Group Using POCl₃. *RSC Adv.* **2013**, *3* (34), 14814–14828.
- (198) Oikawa, Y.; Yoshioka, T.; Yonemitsu, O. Specific Removal of O-Methoxybenzyl Protection by DDQ Oxidation. *Tetrahedron Lett.* **1982**, *23* (8), 885–888.
- (199) Schmidt, W.; Steckhan, E. Mild Oxidative Removal of the Benzyl Ether Protecting Group by Homogeneous Electron Transfer. *Angew. Chem. Int. Ed. Eng* **1978**, *17* (9), 673–674.
- (200) Singh, S. B. Total Synthesis of Flutimide, a Novel Endonuclease Inhibitor of Influenza Virus. *Tetrahedron Lett.* **1995**, *36* (12), 2009–2012.
- (201) Choudhury, A.; Pierce, M. E.; Confalone, P. N. Oxidative Removal of P-Methoxybenzyl-Amino Protecting Group in the Presence of a Proximal Hydroxy Function: A Solution to a Process Problem in SUSTIVA® (Efavirenz) Synthesis. *Synth. Commun.* **2001**, *31* (23), 3707–3714.
- (202) Iqbal, N.; Cho, E. J. Formation of Carbonyl Compounds from Amines through Oxidative C-N Bond Cleavage Using Visible Light Photocatalysis and Applications to N -PMB-Amide Deprotection. *Adv. Synth. Catal.* **2015**, *357* (10), 2187–2192.
- (203) Annadi, K.; Wee, A. G. H. Ceric Ammonium Nitrate Oxidation of N - (p -Methoxybenzyl) Lactams : Competing Formation of N - (Hydroxymethyl) δ -Lactams. *Arkivoc* **2014**, *6* (vi), 108–126.

- (204) Smith, A. B.; Leahy, J. W.; Noda, I.; Remiszewski, S. W.; Liverton, N. J.; Zibuck, R. Total Synthesis of the Latrunculins. *J. Am. Chem. Soc.* **1992**, *114*, 2995–3007.
- (205) Jung, M. E.; Koch, P. Mild, Selective Deprotection of PMB Ethers with Triflic Acid/1,3-Dimethoxybenzene. *Tetrahedron Lett.* **2011**, *52* (46), 6051–6054.
- (206) Howard, K. T.; Chisholm, J. D. Preparation and Applications of 4-Methoxybenzyl Esters in Organic Synthesis. *Org. Prep. Proced. Int.* **2016**, *48* (1), 1–36.
- (207) Stewart, J. J. P. Optimization of Parameters for Semiempirical Methods V: Modification of NDDO Approximations and Application to 70 Elements. *J. Mol. Model* **2007**, *13* (12), 1173–1213.
- (208) Zhao, Y.; Truhlar, D. G. The M06 Suite of Density Functionals for Main Group Thermochemistry, Thermochemical Kinetics, Noncovalent Interactions, Excited States, and Transition Elements: Two New Functionals and Systematic Testing of Four M06-Class Functionals and 12 Other Function. *Theor. Chem. Accounts* **2008**, *120* (1–3), 215–241.
- (209) Frisch, M. J.; Al, E. Gaussian 09, Revision D.01; Gaussian, Inc., Wallingford CT, 2009, Ed.
- (210) Nakamura, K.; Okubo, H.; Yamaguchi, M. Synthesis and Self-Aggregation of Cyclic Alkynes Containing Helicene. *Org. Lett.* **2001**, *3* (8), 1097–1099.

Flavio PICINI

**TRIARYLAMINE BASED
SUPRAMOLECULAR POLYMERS:
INCREASING COMPLEXITY**

Résumé

Dans cette thèse, nous avons étudié de nouveaux polymères supramoléculaires à base de triarylamine. Dans un premier projet, en profitant du phénomène d'émission induite par agrégation, nous avons réussi à obtenir des polymères supramoléculaires fluorescents ayant des propriétés conductrices de trous. De plus, les composés chiraux, ont conduit à des polymères présentant une hélicité préférentielle et l'émission de luminescence à polarisation circulaire. En ajustant opportunément la structure chimique du monomère, nous avons obtenu un contrôle élevé sur le processus de polymérisation supramoléculaire, ce qui nous a permis d'ajuster les morphologies des assemblages, la chiralité supramoléculaire et les caractéristiques des matériaux finis. Nous avons démontré que l'augmentation du degré d'organisation du système est un moyen approprié pour optimiser les performances de ces matériaux. Dans un deuxième projet, nous avons réussi à mettre au point un moyen approprié de synthétiser un macrocycle à base de triarylamine par une synthèse convergente en plusieurs étapes. La molécule présentait des propriétés électromagnétiques intrigantes, avec l'oxydation en un radical polycationique. Nous avons également réussi à optimiser les conditions de formation des polymères supramoléculaires par l'empilement d'unités macrocycliques de manière unidirectionnelle.

Mots-clés : Chimie supramoléculaire, auto-assemblage, polymères supramoléculaires, chiralité supramoléculaire, triarylamine, émission induite par agrégation, luminescence à polarisation circulaire, macrocycle, délocalisation

Résumé en anglais

In this thesis we have investigated new triarylamine based supramolecular polymers. In a first project, by taking advantage from the aggregation-induced emission phenomenon, we succeeded in obtaining fluorescent supramolecular polymers with hole-conductive properties. Moreover, its chiral versions led to polymers showing a preferential helicity and showed circularly polarized luminescence. By adjusting the chemical structure of the monomer, we gained control on the supramolecular polymerization process, which allowed us to tune the morphologies of the assemblies, its supramolecular chirality, and the photo-physical characteristics of the final materials. We demonstrated that increasing the degree of organization of the system is a suitable path to optimize the performance of these materials. In a second project, we succeeded in developing a suitable synthetic methodology to prepare a triarylamine-based macrocycle through a convergent multistep synthesis. The macrocyclic compound, a hexaaza[16]para-cyclophane bearing six amide groups, exhibited intriguing electronic properties during its oxidation to polycationic radicals. We further succeeded in optimizing the conditions for the formation of supramolecular polymers driven by six simultaneous hydrogen bonds and the stacking of macrocyclic units in unidirectional fashion.

Keywords: Supramolecular chemistry, self-assembly, supramolecular polymers, supramolecular chirality, macromolecular chemistry, triarylamine, aggregation-induced emission, circularly polarized luminescence, electronic delocalization.